DEVELOPMENT OF NEW GRADES OF
ZINC COATED DIRECT PRESS-HARDENABLE STEEL
WITH ROBUST CATHODIC PROTECTION

DEVELOPMENT OF NEW GRADES OF ZINC COATED DIRECT PRESS-HARDENABLE STEEL WITH ROBUST CATHODIC PROTECTION

By

CHRISTOPHER THOMSEN, B.ENG.MGT

A Thesis

Submitted to the School of Graduate Studies

In Partial Fulfillment of the Requirements

For the Degree

Master of Science

McMaster University

McMaster University	Master of Science (2020)
Hamilton, Ontario	(Materials Science & Engineering)

TITLE:	DEVELOPMENT OF NEW GRADES OF ZINC COATED DIRECT PRESS-HARDENABLE STEEL WITH ROBUST CATHODIC PROTECTION
AUTHOR:	Christopher Thomsen, B.Eng.Mgt (McMaster University)
SUPERVISOR:	Dr. Joseph R. McDermid
NUMBER OF PAGES:	xvi, 194

ABSTRACT

Despite the high demand for press-hardenable steel (PHS) with coatings that provide sacrificial cathodic protection, Zn-based coatings have experienced limited use due to the significant challenges associated with avoiding liquid metal embrittlement (LME) while maintaining robust cathodic protection when using conventional PHS materials and processing techniques. The present research addresses these challenges by reducing the conventional direct hot press forming (DHPF) temperature to between 600–700 °C, such that forming and quenching occurs well below the $Zn(Fe)_{liq} \rightarrow \Gamma\text{-}Fe_3Zn_{10}$ peritectic temperature of 782 °C, thereby removing the conditions necessary for LME to occur while allowing for formation of the cathodically-protective $\Gamma\text{-}Fe_3Zn_{10}$ phase. The objective of this work was to define a process window for two galvanized prototype PHS alloys with compositions of 0.20C-2.01Mn-0.26Si-0.005B and 0.19C-2.5Mn-0.26Si-0.005B (wt%) that would result in fully martensitic microstructures, tensile strengths (TS) ≥ 1500 MPa, and robust cathodic protection, defined as attaining ≥ 15 vol% $\Gamma\text{-}Fe_3Zn_{10}$ in the coating microstructure, while avoiding LME. Accomplishing this task involved characterizing both grades as a function of austenization time, stamping temperature, and strain imposed by the forming process in order to define process windows that resulted in parts that met the aforementioned property requirements.

It was found that the approach of increasing the Mn content relative to conventional PHS grades was successful in improving the hardenability sufficiently to enable the formation of fully martensitic microstructures despite the lower effective cooling rates associated with the reduced DPHF temperatures. Microstructural imaging and tensile testing demonstrated that, for both prototype PHS grades, a process window exists for the production of parts that satisfy the targets of the formation of fully martensitic microstructures and TS ≥ 1500 MPa while exhibiting uniform elongation of about 0.05 followed by significant post-uniform elongation. The effect of DHPF temperature and strain imposed by the forming process on mechanical properties was found to be negligible. Tensile tests and fractography revealed that reducing the DHPF temperature to between 600–700 °C was successful in preventing LME, thereby allowing samples to fracture in a ductile manner. Micro-cracking in the coating of the DHPF part was observed; however, these cracks were arrested at the coating-substrate interface. For all tested conditions, the coating met the target of $\geq$ 15 vol% Γ-Fe_3Zn_{10}, implying that robust cathodic protection is expected. Based on the results of these experiments, it was concluded that DHPF process windows that meet all of the property targets include austenization times and DHPF temperatures of 120–180 s and 600–700 °C, respectively, for the 2Mn grade, and 60–180 s and 600–700 °C, respectively, for the 2.5Mn grade.

ACKNOWLEDGMENTS

Firstly, I would like to express my deepest gratitude to my supervisor, Dr. Joe McDermid. He has provided me with continuous support, guidance, and opportunities, and under his supervision my research skills have improved greatly. I also appreciate his patience when guiding me through complex problems and when giving me feedback my work. I would also like to thank Dr. Joey Kish and Dr. David Wilkinson for their helpful comments throughout this project. I am grateful for Dr. Beth McNally, who tirelessly works to facilitate the success of each student in the lab, whether it be by providing experimental support or general advice. I would also like to thank Dr. Mike Bruhis, with whom I spent many hours in the mechanical testing lab, performing experiments together and learning how to operate equipment. I am thankful for everyone at the CAMC, for their support, their friendship, and for making our lab an all-around excellent place to graduate research. It has been a pleasure to work with them all.

There are many others without whom this work would not have been possible. I extend thanks to John Thomson and Ray Fullerton, who spent a considerable amount of time galvanizing all of my steel and were always a joy to be around. I acknowledge Vicky Jarvis and Dr. Jim Britten whose assistance with XRD training and analysis is greatly appreciated. I would also like to thank Marta Aniolek at CanmetMATERIALS for assistance with dilatometry experiments.

I would also like to acknowledge the International Zinc Association – Galvanized Autobody Partnership (IZA-GAP) and the Natural Sciences and Engineering Research Council of Canada for their financial support. Additionally, I am appreciative of U. S. Steel for their in-kind support of the prototype steels used for this study.

Last but not least, I am grateful for my family and friends, who have always supported me, encouraged me, and been a source of inspiration throughout my journey at McMaster.

TABLE OF CONTENTS

LIST OF FIGURES

LIST OF TABLES

CHAPTER 1 INTRODUCTION

The automotive industry is under intense pressure to decrease vehicle emissions [1]. One of the best ways to accomplish this is to reduce the weight of the Body-in-White (BIW). This demand has motivated substantial research and development efforts in the steel industry geared towards the development of ultra-high strength steels (UHSS). The use of UHSSs enables downgauging, i.e. replacing existing components with higher strength components with thinner cross sections, resulting in reduced BIW weight. Direct hot press forming (DHPF), also known as press-hardening or hot stamping, is a commonly used technique to produce UHSS parts with high strength levels, complex geometries, and the tight dimensional tolerances required for automotive design while avoiding significant springback. The most common press-hardening steel (PHS) grade is known as 22MnB5. It has a range of compositions but most commonly contains about 0.22C–1.23Mn–0.23Si–0.003B (wt%) [2–4]. This grade has been carefully formulated to minimize cost while providing high yield and tensile strength after forming, reasonable hardenability, and weldability [3],[4]. DHPF involves three main steps: austenization, transfer, and forming and quenching. Austenization occurs in a furnace heated to between 850–950 °C, typically with heating rates of 10–12 °C/s and soaking times of 3–8 minutes [2–4,6]. The blank is then removed and transferred to the die set for forming and quenching using water cooled dies to ensure that the part is cooled at rates of at least −40 °C/s to ensure formation of a fully martensitic microstructure [6]. Transfer typically occurs as quickly as possible such that the blank temperature does not decrease significantly before forming and quenching commences.

Blanks are typically pre-coated for use in the DHPF process to prevent decarburization [7] and the formation of an oxide scale at the high temperatures in the austenization furnace [8,9]. The coating should also have good weldability, paintability, and corrosion resistance. Currently, the most common coating used is an Al-Si alloy containing near-eutectic compositions of 7–11 wt% Si [2]. This coating offers excellent barrier corrosion protection, but does not offer cathodic corrosion resistance [2,10,11]. During the austenization step, the Al-Si coating transforms into layers of brittle intermetallics that are prone to cracking during forming [12,13], creating gaps exposing the underlying steel. These gaps allow the steel to corrode, which prevents the use of PHS in more corrosion prone areas of the BIW where cathodic corrosion resistance is required. Therefore, a strong demand exists for coating systems that can provide both barrier and cathodic protection [4].

Zn-based coatings have long been the coating of choice for steel sheet, due mainly to their cathodic corrosion protection abilities. However, in the context of DHPF, the relatively low melting temperature of Zn leads to problems associated with liquid metal embrittlement (LME). During austenization, the coating transforms into a Zn-enriched ferrite (α-Fe(Zn)) solid solution layer at the substrate-coating interface, usually some amount of a liquid Zn phase ($Zn(Fe)_{liq}$), and an oxide layer at the outer surface of the coating [2]. When the coating is quenched, it passes through the peritectic reaction $\alpha\text{-Fe(Zn)} + \text{Zn(Fe)}_{liq} \rightarrow \alpha\text{-Fe(Zn)} + \Gamma\text{-Fe}_3\text{Zn}_{10}$ at 782 °C [2]. The Γ-Fe_3Zn_{10} is necessary for robust cathodic protection [14,15]; however increased austenization and transfer times will result in a higher percentage of α-Fe(Zn) in the coating. It has been found that once the volume fraction of Γ-Fe_3Zn_{10} becomes less than 15%, the extent of cathodic protection offered by the coating is drastically reduced [14]. In addition, the presence of $Zn(Fe)_{liq}$ during forming creates conditions known to cause LME, which can lead to catastrophic brittle failure [16]. These two problems can be avoided by completing almost all of the forming before the part enters the austenization furnace (indirect press-hardening) [4], increasing the austenization time to form a coating consisting solely of α-Fe(Zn) [17,18], or forming after the coating has solidified via pre-cooling or extended transfer time [19,20]. The third option maintains both the formability that is reduced by the first option and the cathodic corrosion resistance that is mostly lost in the second; however, the proposed extended transfer time results in a cooling rate that is too slow to allow 22MnB5 to achieve the fully martensitic microstructure required for optimum mechanical properties [19,21].

The objective of the research contained in this thesis was to characterize two Zn-coated PHS grades based on the 22MnB5 composition but containing 2.0 and 2.5 wt% Mn. The key objectives were to increase hardenability by increasing the substrate Mn content and to achieve an TS ≥ 1500 MPa, avoid LME by stamping below the peritectic temperature, and attain robust cathodic corrosion protection by meeting the target of ≥ 15 vol% Γ-Fe_3Zn_{10} in the final coating microstructure. This included determining the microstructural evolution of the substrate and coating as a function of three key process parameters: austenization time, stamping temperature, and strain imposed by the forming process. Later, the mechanical properties and cathodic corrosion protection potential of the coating were determined and related to their microstructures.

The outline of this sandwich thesis is as follows. Chapter 2 consists of a detailed literature review, where all relevant aspects of previous studies are covered. This includes alloy design, DHPF process parameters, microstructure and mechanical properties of PHS, coatings used on PHS and their microstructural development, proposed mechanisms of LME and methods to avoid it, and finally corrosion resistance evaluation of Zn-coated PHS. Chapter 3 includes an accepted peer-reviewed conference paper focusing on results for the 2Mn alloy to be published in the Galvatech 2020 proceedings. Chapter 4 includes a manuscript to be submitted to the journal “Materials Science and Engineering: A” which details all results and discussion on phase transformation kinetics, evolution of microstructure and properties of the substrate and the coating, and analysis of fracture surfaces and coating cracks for the 2Mn alloy. Chapter 5 includes a draft manuscript, similar to Chapter 4 but concentrating only on the 2.5Mn alloy. Chapter 6 contains a global discussion that includes a comparison of both prototype alloys framed in the context of meeting the objective of this thesis. Finally, Chapter 7 presents the main conclusions and recommendations for future work.

CHAPTER 2 LITERATURE REVIEW

2.1 PRESS-HARDENED STEELS FOR AUTOMOTIVE APPLICATIONS

Under intense pressure to decrease emissions by increasing fuel efficiency, the automotive industry has been looking for ways to decrease the weight of the body-in-white (BIW) [1–4]. This has motivated a significant research effort within the steel industry to create new grades that have superior mechanical properties, along with other properties such as corrosion resistance, formability, and weldability [1–5].

Press-hardening, also known as hot stamping, is a commonly used method of producing high strength formed steel parts [2,6,7]. The press-hardening process (explained in detail in § 2.4) involves austenizing a hardenable C-Mn-Si-B steel then simultaneously forming and quenching at rates −40 °C/s or faster to attain a fully martensitic part, thereby enabling the production of parts with extremely high strengths and complex geometries. Press-hardening is not a new technology; the first patent was issued in 1977 to Plannja HardTech AB, a subsidiary of the Swedish manufacturer Norrbottens Järnverks [8] which envisioned the technology mainly being used in the agricultural and construction industries [9]. However, it did not take long for the technology to cross over to automobiles. During the 1980s several automotive manufacturers began projects exploring press-hardened steel (PHS) and cars such as the 1984 Saab 9000 and the 1986 Jaguar XJ featured press-hardened door beams [10]. Throughout the early 1990s Plannja HardTech supplied parts to a variety of automotive manufacturers and expanded the market to include front and rear bumper reinforcements [2]. In 1995, the Plannja HardTech patent expired and other manufacturers such as Ford, Renault, and Volvo introduced PHS to their vehicles [10] and by the end of the decade over 9 million PHS parts were being produced globally per year. Research into a metallic coating on PHS [11] led to an ArcelorMittal patent issued in 1999 on Al-Si coated PHS and subsequently trademarked as Usibor™. This allowed automotive manufacturers to avoid substrate decarburization and the formation of Fe-based scale during austenization and to expand use of PHS into more corrosion-prone areas of the BIW [2]. Later innovations in PHS manufacturing techniques have made the application of PHS possible in areas outside of anti-intrusion areas of the BIW by adjusting or "tailoring" the final microstructure and properties. These include commercial application of tailored heating, tailor welded blanks, tailored quenching, and tailor rolled blanks [2,12,13]. PHS continue to proliferate in the automotive BIW. For example, the 2014 Volvo XC90 BIW contains as much as 38 wt% PHS parts and, by 2015, over 500 million PHS were being produced annually worldwide [2].

2.2 BORON STEELS FOR PRESS-HARDENING

The industry standard grade for press-hardening, known as 22MnB5, has a typical composition of 0.22C–1.23Mn–0.23Si–0.003B (wt%) [2,7,14]. This chemistry is chosen for press-hardening because of its combination of mechanical properties, hardenability, good weldability, and low cost [2]. A continuous cooling transformation (CCT) diagram for 22MnB5, annotated with the effects of alloying elements on phase transformation temperatures and kinetics, is shown in Fig. 2.1 [15]. The main alloying elements in 22MnB5 and other PHS grades are C, Mn, Si and B. C is well known to have a dramatic effect on hardenability and strength through interstitial solid solution strengthening. By lowering the martensitic transformation start temperature (M_s) and delaying the start of diffusional phase transformations (Fig. 2.1), C provides a larger process window for press-hardening [16]. The main disadvantages of adding larger amounts of C are reductions in the steel's weldability and ductility [17]. Mn is also added for hardenability and solid solution strengthening, though its effects are much less pronounced than those from C. Mn also increases hardenability by preventing austenite decomposition [6] thereby delaying phase transformations via a similar mechanism to C (Fig. 2.1). However, in addition to reducing weldability and ductility, a Mn content of over 2% has the potential to form segregation bands, which can reduce bendability and cause cracking after quenching [17,18]. Si is beneficial for solid solution strengthening and is typically added in amounts of 0.20-0.35 wt% [17]. If Si concentrations are too high it could selectively oxidize during galvanizing, which reduces reactive wetting of the Zn coating adherence [2]. Boron is a critical alloying element for PHS because concentrations between 20 and 50 ppm have been proven to increase hardenability dramatically, more than additions of other more expensive elements such as Cr, Mo, and Ni [19]. The exact mechanism behind this unique and impressive effect have been the subject of many studies. It is generally accepted that B segregates to austenite grain boundaries during cooling from high temperatures by non-equilibrium segregation [20–26]. B-vacancy complexes are formed within grains which then migrate to grain boundaries (being vacancy sinks) during cooling, leading to an enrichment of B at austenite grain boundaries [20,22–24,26]. The presence of B at grain boundaries reduces the grain boundary surface energy, which in turn decreases the thermodynamic driving force for ferrite nucleation [23]. Therefore, hardenability is increased by delaying ferrite and pearlite formation and enabling martensitic transformation [19,25,26]. Naderi et al. [27]studied many different C-Mn steels and those that did not contain B were insufficiently hardenable and did not result in fully martensitic microstructures under typical DHPF conditions. Other alloying elements that are often added to PHS grades in small amounts include Cr, Ti, Al, and sometimes Nb. Cr also improves hardenability, though not as effectively as C or Mn (Fig. 2.1). In order to prevent the formation of BN, Ti and Al are added to form the nitrides TiN and AlN instead [2]. It is necessary to keep B in solid solution so that its effectiveness as a hardenability improver can be maximized. Nb additions are not usually present in 22MnB5 but some recent studies have shown significant promise for Nb microalloying as it leads to refined prior austenite grain size (PAGS), improved toughness, and even reduced susceptibility of the PHS to hydrogen embrittlement by the formation of Nb(C, N) hydrogen traps [28–30].

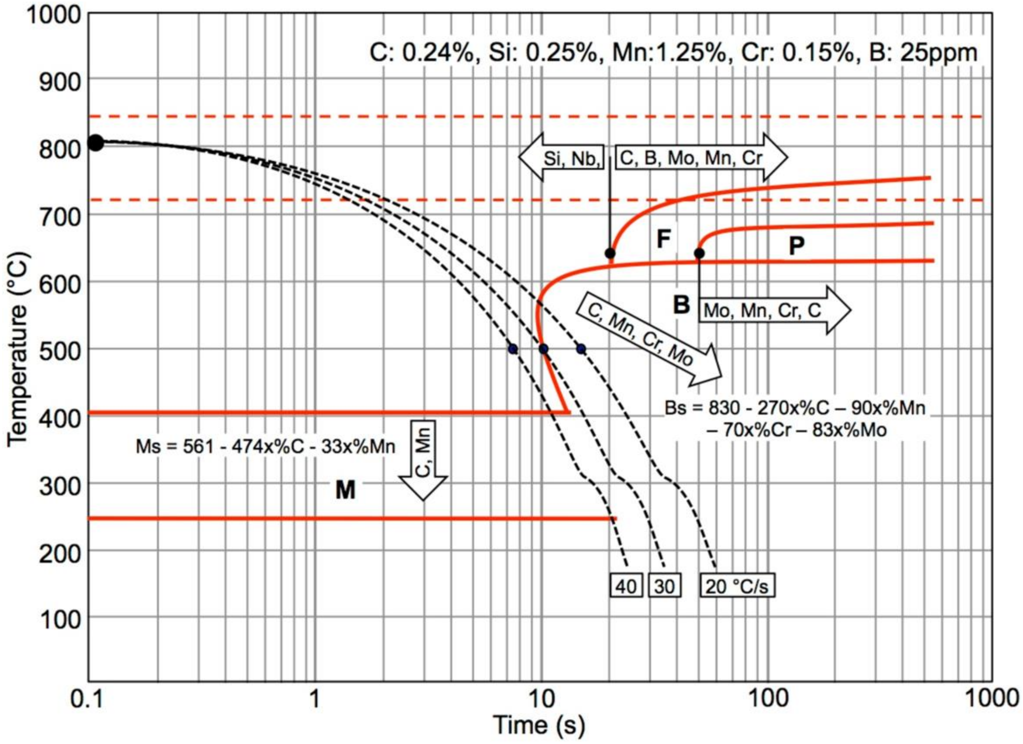

Fig. 2.1. CCT Diagram for 22MnB5 steel annotated with the effects of common alloying elements on phase transformation temperatures and kinetics [15].

2.3 THE CONTINUOUS GALVANIZING LINE

A continuous galvanizing line (CGL) is the most widely used technology used to produce metallic-coat sheet steel for corrosion protection. The process is described in depth in the classic review by Marder [31]. A partial schematic of a typical radiant tube heated CGL is shown in Fig. 2.2 [32]. The process begins by decoiling the strip steel and welding it into a continuous strip via resistance or laser welding, after which it is passed through several cleaning steps to remove oils, Fe fines and dirt on the surface. The strip then enters the annealing furnace where it is annealed to recrystallize the steel in order to produce the desired ferrite + pearlite microstructure and to reduce surface Fe oxides. In order to ensure reduction of Fe oxides, an N_2/5-20 vol% H_2 atmosphere with a controlled dewpoint – i.e. water vapour partial pressure (pH_2O) – is used to control the process atmosphere oxygen partial pressure (pO_2,) at the annealing temperature such that it is reducing to Fe oxides. The typical dewpoint in industrial CGL furnaces is −30 °C to −10 °C. An important consequence is that this pO_2 is actually oxidizing to many important alloying elements commonly found in advanced high strength steels, such as Mn, Si, and Cr. The strip then enters the gas jet cooling section of the line (Fig. 2.2), where it is cooled to the same temperature as the Zn bath. The strip then passes through the Zn bath for an immersion time of 2–4 s. The bath temperature itself depends on the composition of the coating; for galvanized coatings, the bath is kept at 460 °C [33]. A small amount of Al (typically 0.2 wt%) is added to the bath to promote the formation of the $Fe_2Al_5Zn_x$ interfacial or “inhibition layer” that is necessary to “inhibit” the formation of brittle Fe-Zn intermetallics. Upon exiting the bath, planar gas jet wipers (known as air knives) impinge on the strip with high-pressure air or nitrogen to create the desired coating thickness by returning the excess Zn to the bath. For galvanized coatings, the strip is allowed to cool, and the coating solidifies as it rises up the cooling tower. For galvannealed coatings, the strip is subsequently annealed (Fig. 2.2) to alloy the coating with Fe from the substrate prior to cooling. This is followed by several finishing steps including inspection, oiling, packaging of the coil.

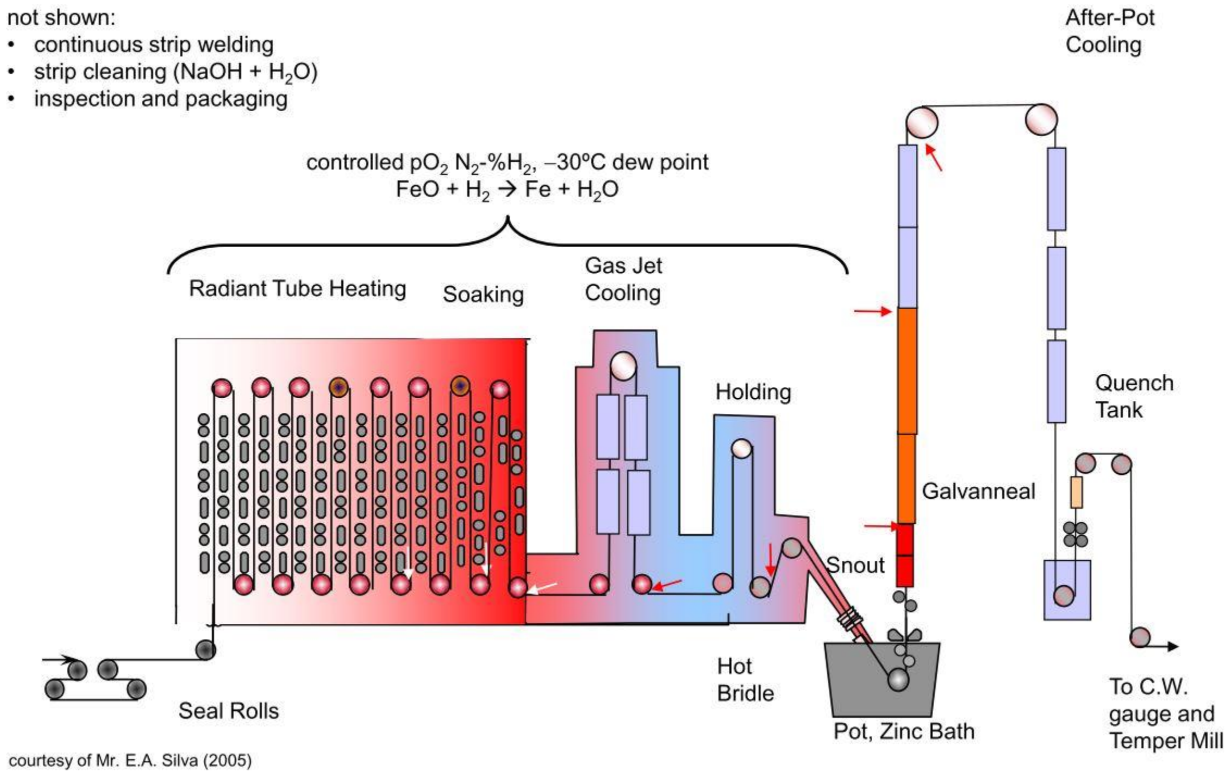

courtesy of Mr. E.A. Silva (2005)

Fig. 2.2. Schematic of a continuous galvanizing line [32].

2.4 THE DIRECT HOT PRESS-FORMING PROCESS

There are essentially two different versions of the press-hardening process: the direct method and the indirect method (discussed in § 2.9.1). The simplest of these methods is the direct hot press forming (DHPF) process, shown in Fig. 2.3.

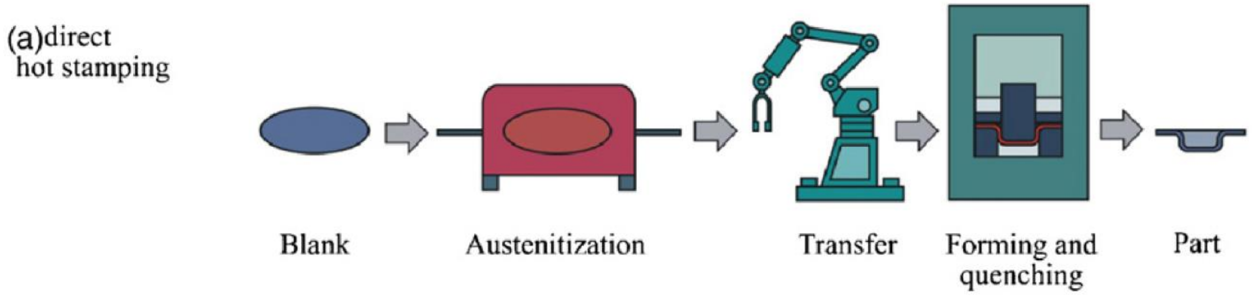

Fig. 2.3. Schematic of the direct press-hardening method [7].

DHPF typically begins with a cold-rolled steel coil (gauge <2 mm) that is cut into blanks. At this point in the process, the microstructure of the 22MnB5 typically consists of a ferrite + pearlite ($\alpha + Fe_3C$) microstructure that possesses a moderate tensile strength (TS) and high total elongation (TE) values of around 600 MPa and 25%, respectively [14]. The blanks are then austenized in roller hearth furnaces in ambient atmosphere, though an inert gas atmosphere is sometimes used [2,14]. When using uncoated substrates, an inert atmosphere is required to minimize decarburization and oxidation of the substrate and to avoid having to perform shot-blasting to remove the oxidation products [2]. When coated substrates are used, decarburization and oxidization of the substrate are mostly avoided and hence ambient atmospheres may be used. However, when using Zn-coated substrates, it is necessary to use an oxidizing environment to allow for the formation of an outer oxide layer of ZnO and Al_2O_3 which prevents evaporation of Zn [14]. Typical industrial practices involve heating the blank to between 850–950 °C at an average rate of 10–12 °C/s then holding for 3–8 minutes to ensure complete austenization [2]. In the fully austenitic state, the mechanical properties of the substrate become ideal for forming, i.e. very low TS of around 200 MPa and TE of up to 50 % [6]. The transfer from the furnace to the forming and quenching dies is typically accomplished as rapidly as possible using robotic arms to minimize exposure to ambient atmosphere and maximize the temperature of the blank when it enters the water-cooled die. Forming and quenching occur simultaneously between water-cooled dies that are held together for 8–12 s to rapidly cool the part to below the M_f temperature (about 230 °C) [2]. Cooling rates are on the order of −30 to −100 °C/s [2,6,14]. The necessity for a high cooling rate faster than −30 °C/s can be seen in Fig. 2.1, where the critical cooling rate for the formation of a fully martensitic microstructure is between −30 and −40 °C/s; other reports in the literature place the critical cooling rate between −27 and −35 ˚C/s [2,15,34,35]. After this step, the microstructure becomes fully or almost fully martensitic, except for some inter-lath retained austenite and perhaps some small ferrite islands, with high strength and low elongation values of 1500 MPa and 6% [14]. In some cases, there may be some post-processing required to remove oxide scales for weldability and paintability.

Recently, efforts have been made to make minor modifications to the DHPF process in order to accommodate Zn-coated PHS. A common misconception is that it is impossible to use Zn-based coatings with the DHPF method because of the risk of liquid metal embrittlement (LME) while forming. There are three methods that can make DHPF of Zn-coated steels possible, all of which work by ensuring no liquid phases are present during forming: 1) pre-forming before austenization (i.e. the indirect method), 2) increasing the austenization time, and 3) performing the stamping step below the Fe-Zn system peritectic temperature [14]. These methods will be discussed in § 2.9.

2.4.1 Influence of process parameters on microstructural and property development

Deformation has a pronounced effect on hardenability, which has been attributed to the mechanical stabilization of austenite [36–38]. Forming induced deformation substantially increases the dislocation density in the blank, which then act as barriers that impede the motion of glissile interfaces such martensitic transformation interfaces [39–41]. Several studies have specifically found that the deformation created during DHPF strongly reduces hardenability [36–38]. On a CCT curve, deformation widens the bainite phase field and shifts the onset of all diffusional phase transformations to shorter times (i.e. faster cooling rates), as seen in Fig. 2.4 [36]. For example, it has been found that the critical cooling rate for producing fully martensitic microstructures using 22MnB5 increases from −30 °C/s to −60 °C/s with a hot deformation of 40% [42].

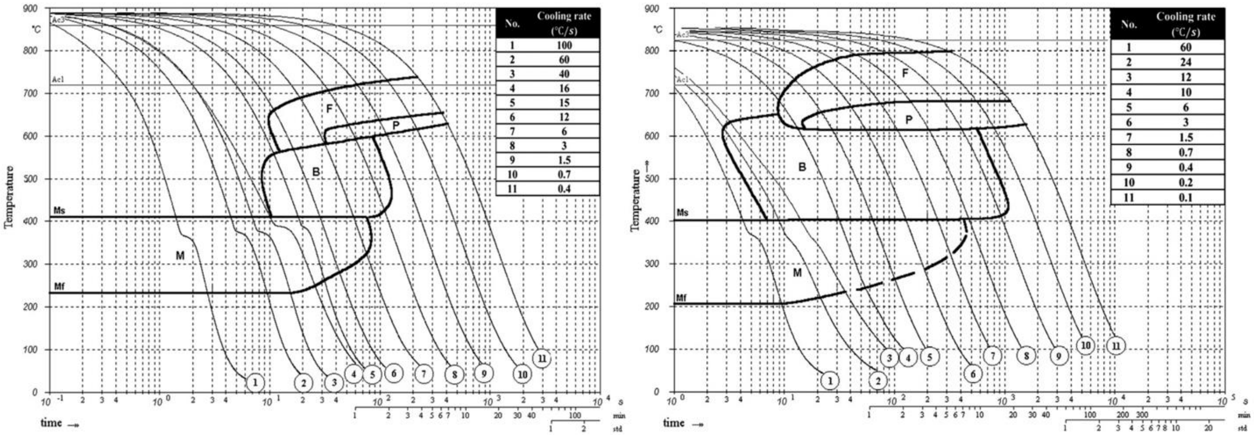

Fig. 2.4. Comparison of CCT curves for undeformed (left) and deformed by 40% (right) 22MnB5 [36].

Nikravesh et al. found that the M_s and M_f temperatures of 22MnB5 were a function of cooling rate [42] . Fig. 2.5 (a) shows that, in undeformed specimens, the dependence of M_s and M_f on cooling rate features an inflection point where the minimum values M_s and M_f are reached at a cooling rate of −20 °C/s. Above −20 °C/s, a reduction in cooling rate lead to lower M_s and M_f temperatures. The authors attributed this reduction to an increased time for rejection of C from austenite during cooling. Consequently, more C is rejected from the austenite at lower cooling rates, which increases the driving force required for the martensitic transformation. At cooling rates below the inflection point at −20 °C/s, a further reduction in cooling rate increased the M_s and M_f temperatures. This change was linked to the formation of bainite prior to the formation of martensite, i.e. above M_s and M_f. Bainite formation raises the M_s and M_f temperatures in two ways: 1) the presence of bainite promotes nucleation of martensite, and 2) the reduction of defects due to bainite formation decreases the shear strength of austenite, reducing the driving force required for the martensitic transformation [42].

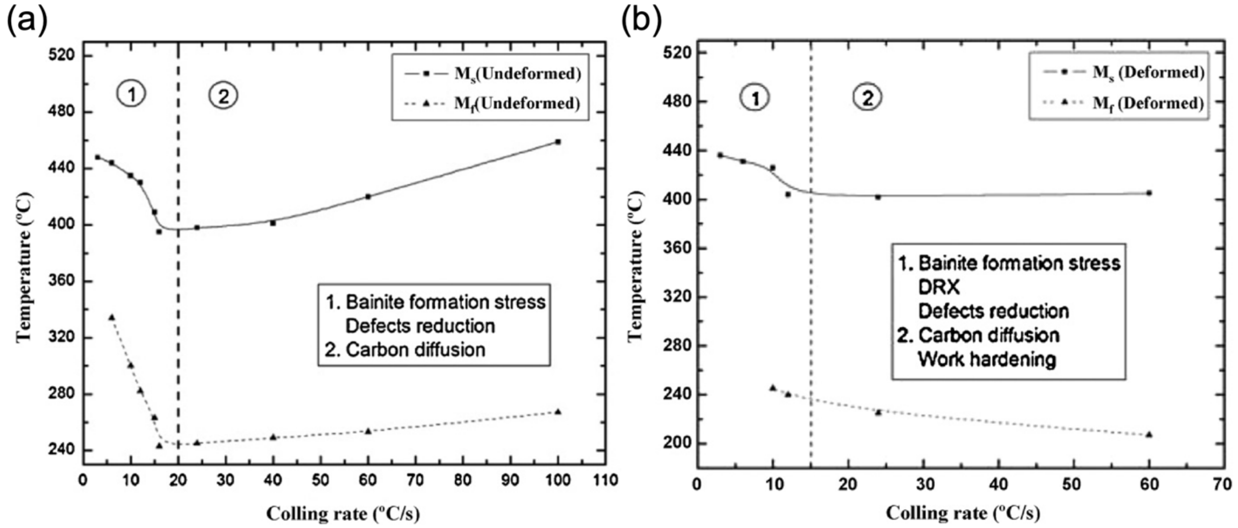

Fig. 2.5. Effect of cooling rate on M_s and M_f temperatures for (a) undeformed and (b) deformed 22MnB5 [42].

The M_s and M_f temperatures of deformed DPHF steels differ from those of undeformed steel cooled at the same rate. This indicates that different mechanisms, likely deformation induced, control the final microstructure of these deformed materials (Fig. 2.5 (b)). There are many factors introduced by deformation which result in a complex effect on M_s and M_f. Deformation increases dislocation density, which decreases the mean free path of dislocations. This raises the driving force for dynamic recrystallization; however, it is partially blocked due to the increase in dislocations in the austenite (mechanical stabilization). At a cooling rate of −60 °C/s, the M_s and M_f are significantly lower than for the undeformed specimens; this was attributed to mechanical stabilization of the austenite introduced by the deformation [42]. At cooling rates less than −15 °C/s, dynamic recrystallization was the dominant mechanism because deformation had been completed at higher temperatures. Because of an increase in thermal energy for dislocation motion and more time in the austenitic phase, dynamic recrystallization is promoted. This decreases the mechanical stabilization of austenite, decreases the driving force required for the martensitic transformation, thus increasing M_s relative to higher cooling rates [42]. It was also observed in this study that dynamic recrystallization lead to finer grain sizes at all cooling rates [42].

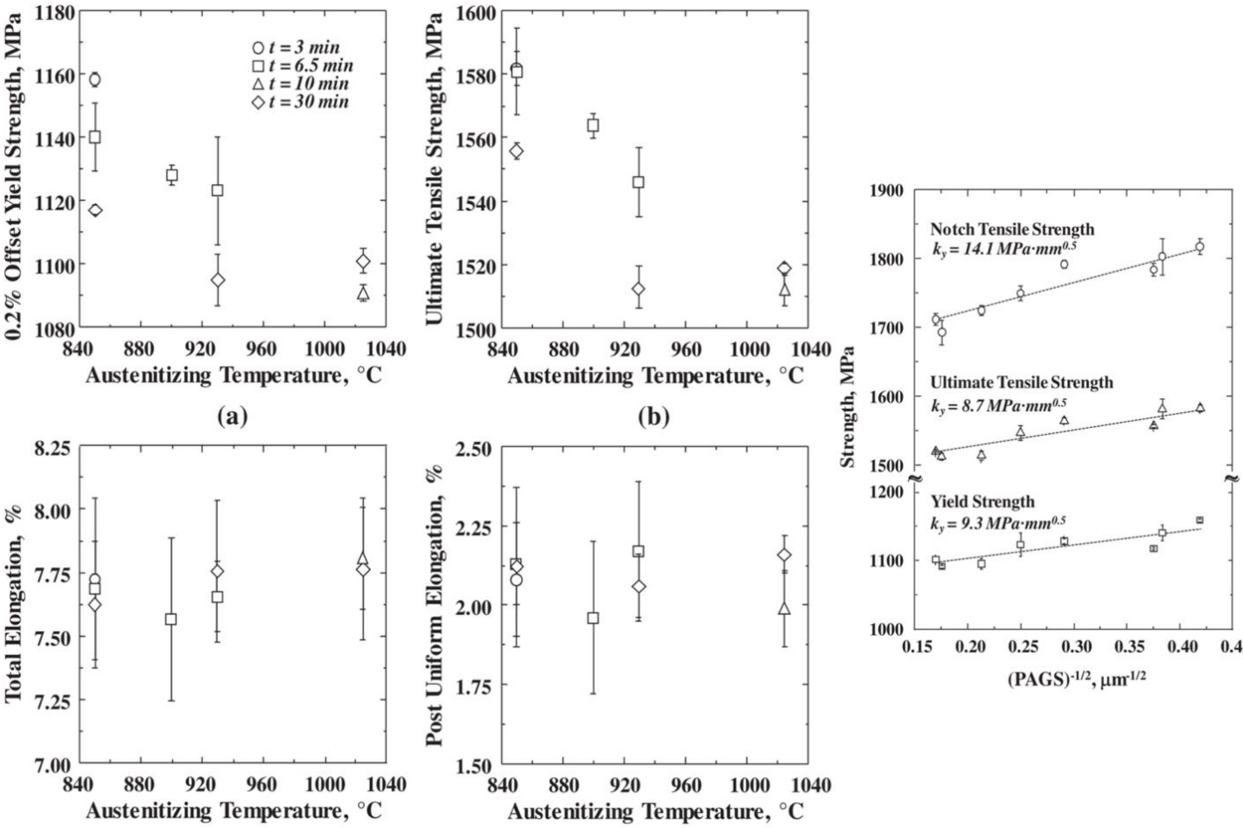

Fig. 2.6. Effect of austenization temperature and PAGS on mechanical properties of Al-Si coated 22MnB5 [43].

Golem et al. [43] studied the influence of austenization parameters on the mechanical properties of Al-Si coated 22MnB5. Unsurprisingly, it was found that increasing the austenization time and/or temperature enlarged the PAGS. A summary of the most relevant results is shown in Fig. 2.6 [43]. It can be seen that yield strength (YS) and TS followed a Hall-Petch type relationship with PAGS. The YS and TS decreased with increasing austenization time and temperature, i.e. increasing PAGS. However, the TE and post-uniform elongation (PUE) were not significantly influenced by PAGS. The main fracture mode was always ductile (Fig. 2.9), however, the authors noted some observations of flat features indicative of quasi-cleavage in the specimens with the largest PAGS (34 μm), which caused a loss of toughness. Coarsening of the PAGS causes both the YS and the brittle fracture stress of the substrate to decrease, however, the YS is reduced more than the brittle fracture stress, which shifts the ductile-brittle transition to lower temperatures [44]. Refinement of the PAGS improved YS and TS without affecting the amount of UE or PUE, so it can be concluded that prolonged austenization time or excessively high austenization temperatures should be avoided in order to minimize austenite grain growth, improve mechanical properties, and avoid brittle fracture [43].

2.5 MICROSTRUCTURE AND MECHANICAL PROPERTIES OF PRESS-HARDENED STEELS

The as-received condition of 22MnB5 consists of a cold-rolled microstructure of ferrite and pearlite, as seen in Fig. 2.7 (a) [6]. Because of the rolling process, the grains are often elongated in the rolling direction (RD) [45]. After the DHPF process, the microstructure becomes nearly or fully martensitic Fig. 2.7 (b) [6]. Typical properties of fully martensitic DHPF 22MnB5 in the RD consist of a YS of 1000–1200 MPa, TS 1400–1550 MPa, and TE of 5–7% [2,6,14,16,27,34,45–47].

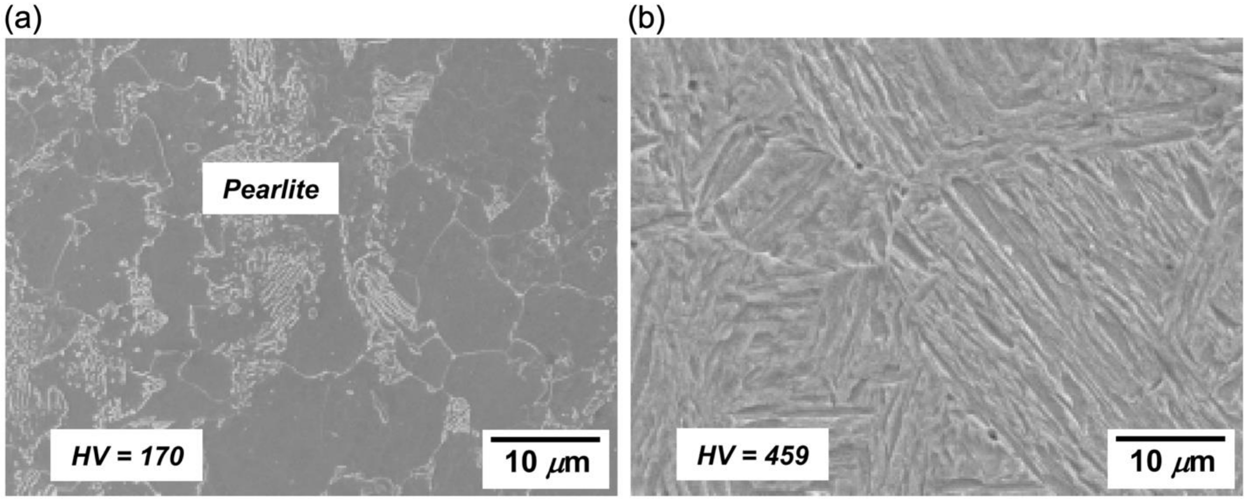

Fig. 2.7. Microstructure of 22MnB5 (a) before and (b) after press-hardening [6].

Lee et al. performed a study on uncoated and Zn-coated 22MnB5 and determined mechanical properties as a function of strain imposed by the forming process, both in the RD and transverse direction (TD) [48]. The authors employed a laboratory galvanizing simulator to coat the steel, using a Fe-saturated Zn-0.12 wt% Al bath held at 450 °C. The dipping time was 5 s and the coating thickness was approximately 10 μm. These parameters match typical industrial galvanizing conditions discussed in § 2.3. The blanks were austenized at 900 °C with a heating rate of 5 °C/s and a soak time of 120 s. The blanks were then simultaneously formed and quenched at 750 °C into a U-shaped channel. Engineering stress-strain curves for both uncoated and Zn-coated RD-oriented 22MnB5 samples taken from two areas of the U-shaped part (top and wall) are shown in Fig. 2.8 (a). The Zn-coated top sample had the minimum TS (1422 MPa) and the Zn-coated wall sample had the maximum TS (1519 MPa), with the TS of the two uncoated samples falling in between [48]. The Zn-coated samples had slightly higher TE than the uncoated samples. The uncoated top samples had the minimum TE (6.83%) and the Zn-coated wall sample had the maximum TE (7.60%) [48]. As seen in Fig. 2.8 (b) the TS of the TD-oriented samples was unchanged while a significant increase in PUE increased the TE to 10–12%. This increase in PUE was attributed to a smaller specimen geometry for the TD samples [48]. This agrees with other literature which states that TS, YS, and UE are relatively independent of specimen geometry, while the extent of PUE increases significantly as gauge length decreases [49,50]. Whether samples were tested in LD or TD direction, generally similar YS, TS, and TE results were obtained regardless of the coating or the region that the tensile coupon was taken from. Therefore, the authors concluded that the Zn coating did not influence mechanical properties and that the properties of the part were homogeneous [48].

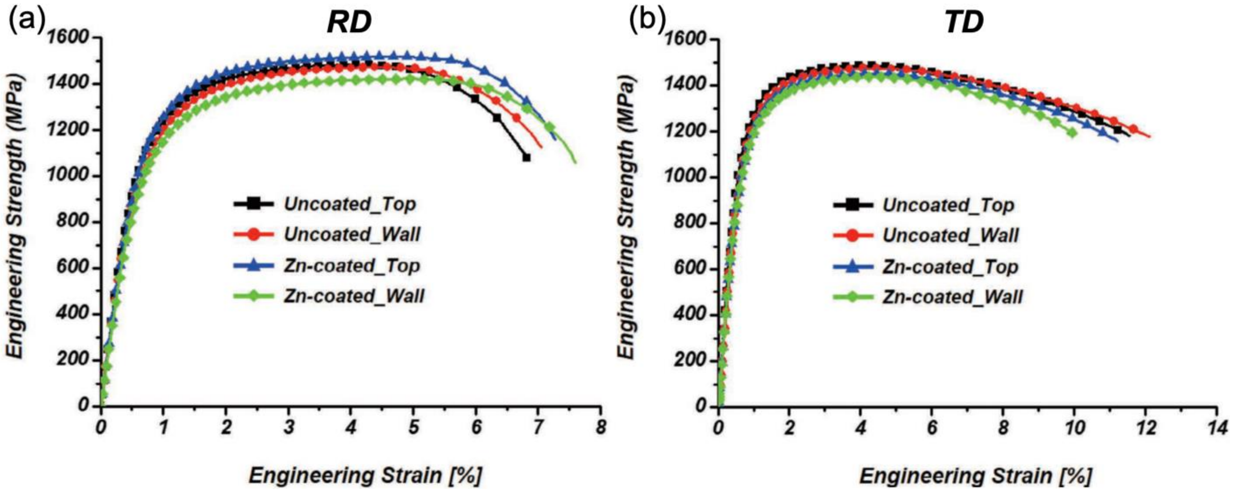

Fig. 2.8. Engineering stress-strain curves of RD and TD oriented tensile coupons from DHPF Zn-coated 22MnB5 [48].

Fig. 2.9 (a) shows the fracture surface of Al-Si coated 22MnB5 after a tensile test [43]. Despite the steel being fully martensitic, the fracture surface consists of the dimples and voids characteristic of ductile failure [43]. Fig. 2.9 (b) shows the fracture surface at the Zn coating-substrate interface, where the difference in fracture modes can clearly be seen. The coating fractured in a brittle intergranular manner, while the fracture of the steel matrix was ductile [48]. This is consistent with other observations in the literature [43,51,52].

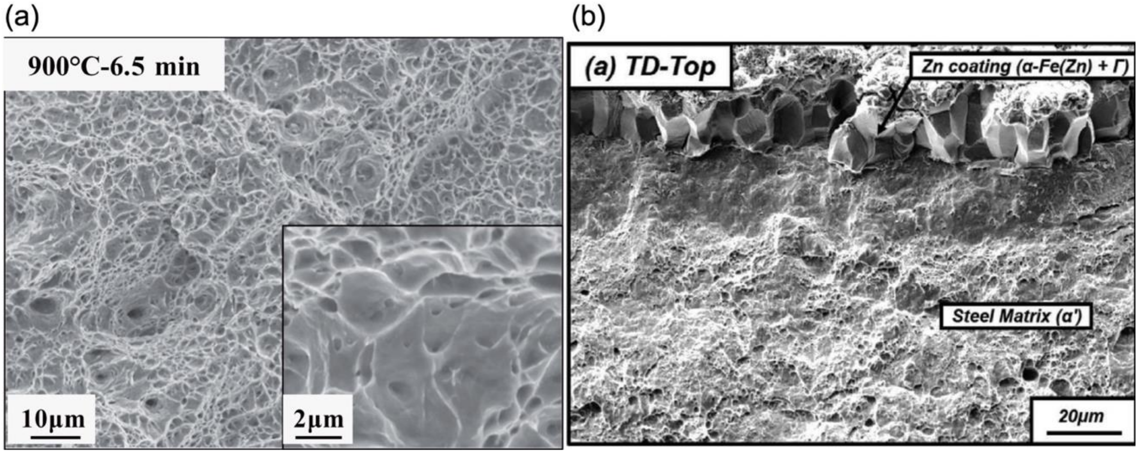

Fig. 2.9. Fracture surfaces at the mid thickness of Al-Si coated press-hardened 22MnB5 (a) [43] and substrate-coating interface of Zn-coated press-hardened 22MnB5 (b) [48].

2.6 METALLIC COATINGS FOR PRESS-HARDENED STEELS

2.6.1 Al-Si Coating

Al-Si coatings dominate the coated PHS industry and have experienced significant growth in recent years. ArcelorMittal began production of their patented Al-Si coated PHS (Usibor® AlSi) in 2006, and the following five years saw the world production increase by nearly a hundredfold, from 5000 tonnes to 480,000 tonnes annually [53]. Due to its ubiquity and technological importance, a significant body of literature on the properties of Al-Si coatings exists. The hot-stamped Al-Si coating offers excellent barrier corrosion protection, paintability [54], and weldability [54]. However, there are also several disadvantages, such as high friction coefficients due to surface roughness [55,56], brittleness [6,57], no cathodic corrosion resistance [14,53,58,59], higher cost than galvanized coatings [2], and market monopolization by ArcelorMittal [2].

The Al-Si coating composition is Al with a near-eutectic amount of Si, typically 7–11 wt% [14,60]. It is applied by continuous hot dipping in a bath of 88 wt % Al, 9 wt % Si and 3 % Fe held at approximately 675 °C. The composition of the bath is carefully chosen to promote the growth of an Fe_2SiAl_7 interfacial layer that prevents the run-away formation of Fe_2Al_5 [60]. The high temperature phase evolution of the coating has been the subject of several investigations [55,61–65] and is shown in Fig. 2.10 [55]. During austenization, the coating quickly forms an external surface oxide layer of Al_2O_3. At the coating-substrate interface, a reaction occurs causing the coating to thicken, become enriched with Fe, and to form a complex system of layered intermetallic phases such as the microstructure shown in Fig. 2.10 [55]. After 150 s at high temperature, a high fraction of voids near the coating-steel interface can be seen, as well as through-thickness cracks. The voids at this interface are thought to be due to Al atoms simultaneously diffusing outward (to form Al_2O_3) and inward (to react with the substrate). Inside the coating, it is believed that the voids are due to the Kirkendall effect, i.e. large differences between diffusivities of Fe and Al in the coating [14].

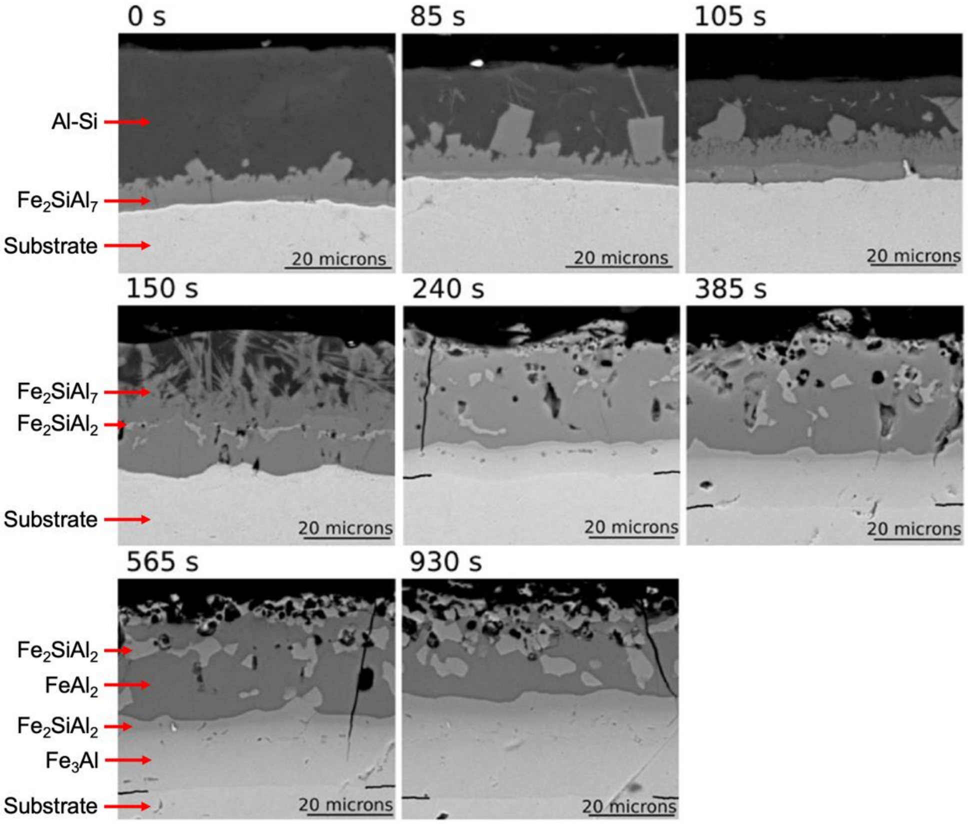

Fig. 2.10. Microstructural evolution of an Al-Si coating heated at 925 °C [55]. Note the presence of the multi-layered structure, voids, and cracks. Annotations added.

The most important conclusion is that the Al-Si coating after DHPF cannot offer cathodic corrosion protection to the steel substrate. The electrochemical potential of the coating is very similar to that of the steel [14,53,58,59] hence it cannot effectively act as a sacrificial anode. When combined with the many studies proving that the brittle nature of the coating's intermetallics lead to many through cracks after forming [14,57,65–67], the lack of corrosion protection provided by these coatings is a significant performance issue when in service. As applications of PHS spread to "wet zones" of the BIW (areas that are more susceptible to corrosion due to environmental exposure), it is necessary to either have a barrier coating that does not crack or a cathodically protective coating.

2.6.2 Zn-based coatings

Galvanized (GI) and galvannealed (GA) Zn-based coatings are widely used on sheet steels due to their excellent barrier and cathodic corrosion protection, formability, and appearance [14]. Other advantages of Zn coatings over Al-Si coatings are related to improved tribology characteristics and reduction of hydrogen embrittlement. Work by Kondratiuk and Kuhn [68] showed that, when compared to Al-Si coatings, the formation of ZnO leads to a reduction of the coefficient of friction and metallic build-up which lead to workpiece wear. Zn coatings appear to be more impervious to hydrogen embrittlement than Al-Si coatings, as shown by Jo et al. [69]. This finding was attributed to the prevention of the hydrogen generation reaction by ZnO and the slow transport rates of H through liquid Zn. However, Zn-based coatings have been found to suffer from LME during the DHPF process. As will be discussed in § 2.7, this has limited the use of Zn-coated PHS in industry.

The microstructural evolution of Zn coatings at the high temperatures used for DHPF has been the subject of many studies [70–78]. The addition of Al to the coating bath to slow the formation of Fe-Zn intermetallics during the continuous galvanizing process results in an essentially pure Zn coating with small amounts of Fe in solid solution (η-Zn) after continuous hot dip galvanizing [79]. Typical as-received galvanized coatings (such as GI70) have a coating weight of 70 g/m^2 which correlates to a coating thickness of about 10 μm. During the austenization step of the DHPF process, the coated blank is commonly held at 850–950 °C for 3–8 minutes [70]. This results in significant alloying of the coating with Fe from the substrate, leading to the formation of a number of intermetallic phases as shown in Fig. 2.11 [31,80].

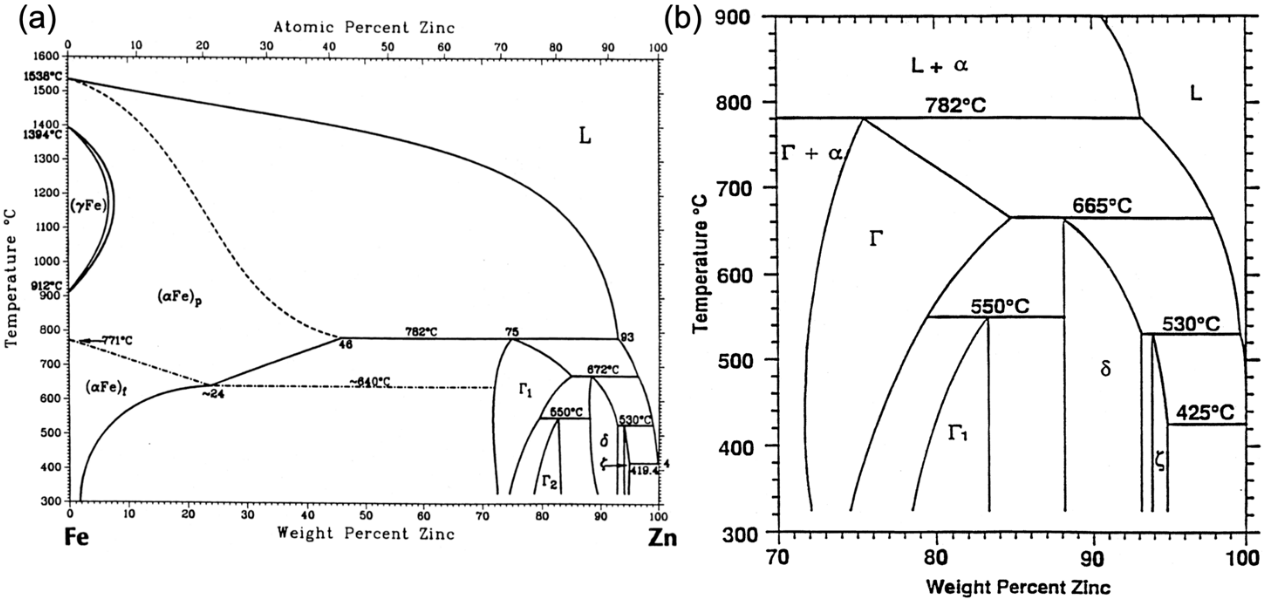

Fig. 2.11. The Fe-Zn phase diagram (a) [80] and the Zn-rich portion of the Fe-Zn diagram (b) [31].

The microstructural evolution of the coating focusing on the early stages of austenization has been summarized in the work of Autengruber et al. (Fig. 2.12), where galvanized panels with an initial coating weight of 70 gm^{-2} (thickness of 10 μm) were heated at 4–7 °C/s to the desired temperature in a conventional box furnace and subsequently quenched between cold plates [71]. The heating rate is relatively fast, so it is worth noting that the high-temperature phase evolution cannot be predicted by thermodynamics alone. The first intermetallic to form on heating was the ζ-$FeZn_{13}$ phase, which rapidly destroys the $Fe_2Al_{5-x}Zn_x$ inhibition layer. Although the ζ-$FeZn_{13}$ phase cannot be seen in Fig. 2.12 due to poor phase contrast, its presence was proven by X-ray diffraction (XRD) [71]. The Al from this layer segregates to the surface and oxidizes to form Al_2O_3 [14,75,81]. Along with ZnO, the Al_2O_3 mitigates Zn evaporation in the austenization furnace by forming an oxide layer [14,75]. By 550 °C (Fig. 2.12), the coating had transformed into a single phase that contained 11% Fe, corresponding to the δ-$FeZn_{10}$ phase field of the Fe-Zn phase diagram (Fig. 2.11). Further heating to 600 and then 650 °C brought the coating into the δ-$FeZn_{10}$ + Γ-Fe_3Zn_{10} phase field. At 700 °C the transformation to Γ-Fe_3Zn_{10} was complete. At 750 °C, an Fe-rich phase with Zn in solid solution (α-Fe(Zn)) formed at the coating/substrate interface, creating a two phase coating microstructure with Γ-Fe_3Zn_{10} at the surface and α-Fe(Zn) at the substrate interface. The Zn content of Γ-Fe_3Zn_{10} at this temperature is 28 wt%, which is near the solubility limit of Zn in Γ-Fe_3Zn_{10}. Further heating did not cause the Zn content of Γ-Fe_3Zn_{10} to change within ± 1% [71]. Because of the large difference in composition of these two phases, the two phases are easily discernable in backscatter electron images (Fig. 2.12). Above 782 °C, the Γ-Fe_3Zn_{10} phase transforms into liquid as the coating passes through the peritectic reaction: Γ-Fe_3Zn_{10} → Zn_{liq}(Fe) + α-Fe(Zn). However, when quenched, the coating goes back through the peritectic reaction and the liquid phase transforms back into Γ-Fe_3Zn_{10}, as seen in Fig. 2.12.

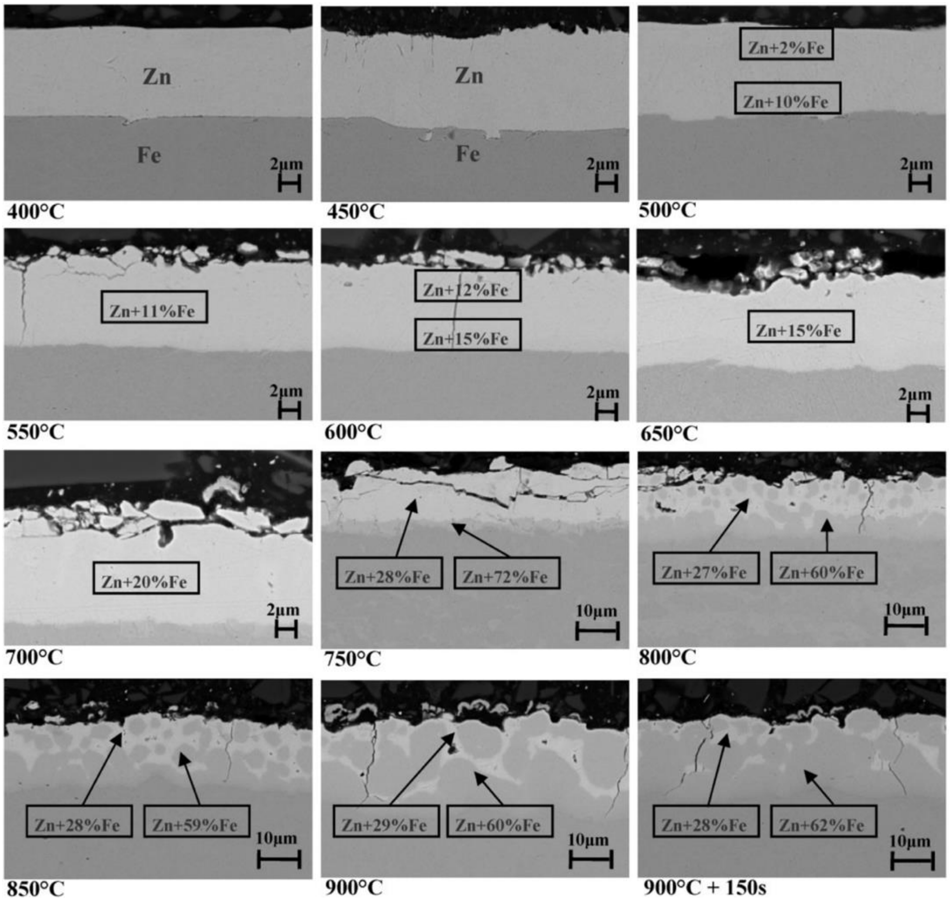

Fig. 2.12. Microstructural evolution of a Zn coating on 22MnB5 as the blank heats up to the austenization temperature of 900 °C [71]. Compositions given in wt. %.

The microstructural evolution data in Fig. 2.12 mostly focuses on the time from when the blank is inserted into the furnace to when the blank reaches the peak temperature (900 °C). While this is important, it is also very important to understand what happens throughout austenization, i.e. throughout the 3–8 minutes typically employed in industry. The work by Dever [78] captures this part of the process (Fig. 2.13–Fig. 2.15), using the same temperature and approximately the same heating rate as Autengruber et al.. In this study, austenization times were defined as starting once the blank reached 890 °C, which took 210 s. Higher temperatures and extended soak times lead to increased alloying of the coating with Fe and the growth of solid α-Fe(Zn), as seen in Fig. 2.13. The consequence of this is that in both Fig. 2.12 and Fig. 2.15 it can be seen that the fraction of Γ-Fe_3Zn_{10} decreases rapidly. The phase evolution with annealing time was quantified by XRD, as shown in Fig. 2.14 [78]. After 240 s at 900 °C, the coating completely transformed into α-Fe(Zn) (Fig. 2.15), one technique that is used to avoid LME as discussed in Section 2.7. Further austenization time did not alter the coating microstructure, but did cause an increase in coating thickness and Fe content (Fig. 2.15) [78].

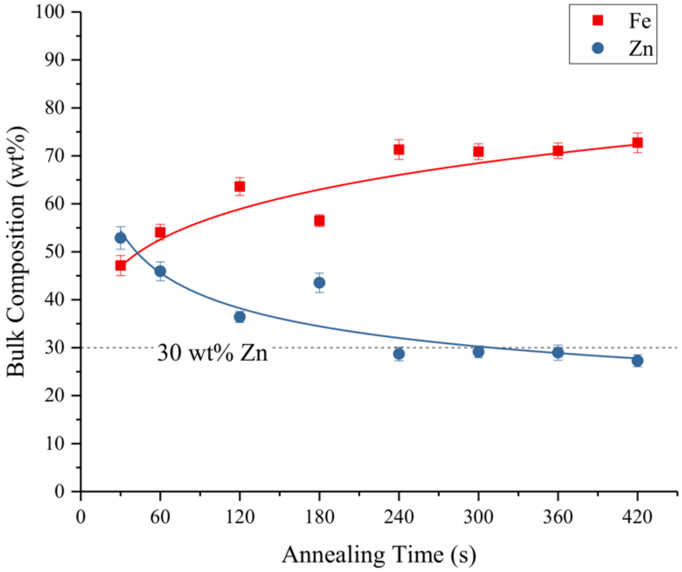

Fig. 2.13. Bulk composition of the coating as a function of austenization time at 900 °C, determined by XRD [78].

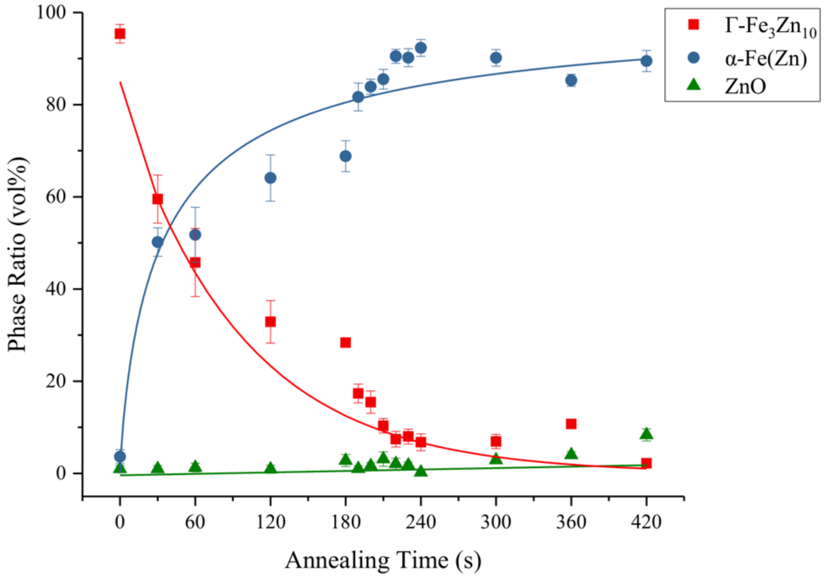

Fig. 2.14. Coating phase evolution as a function of austenization time at 900 °C measured by XRD [78].

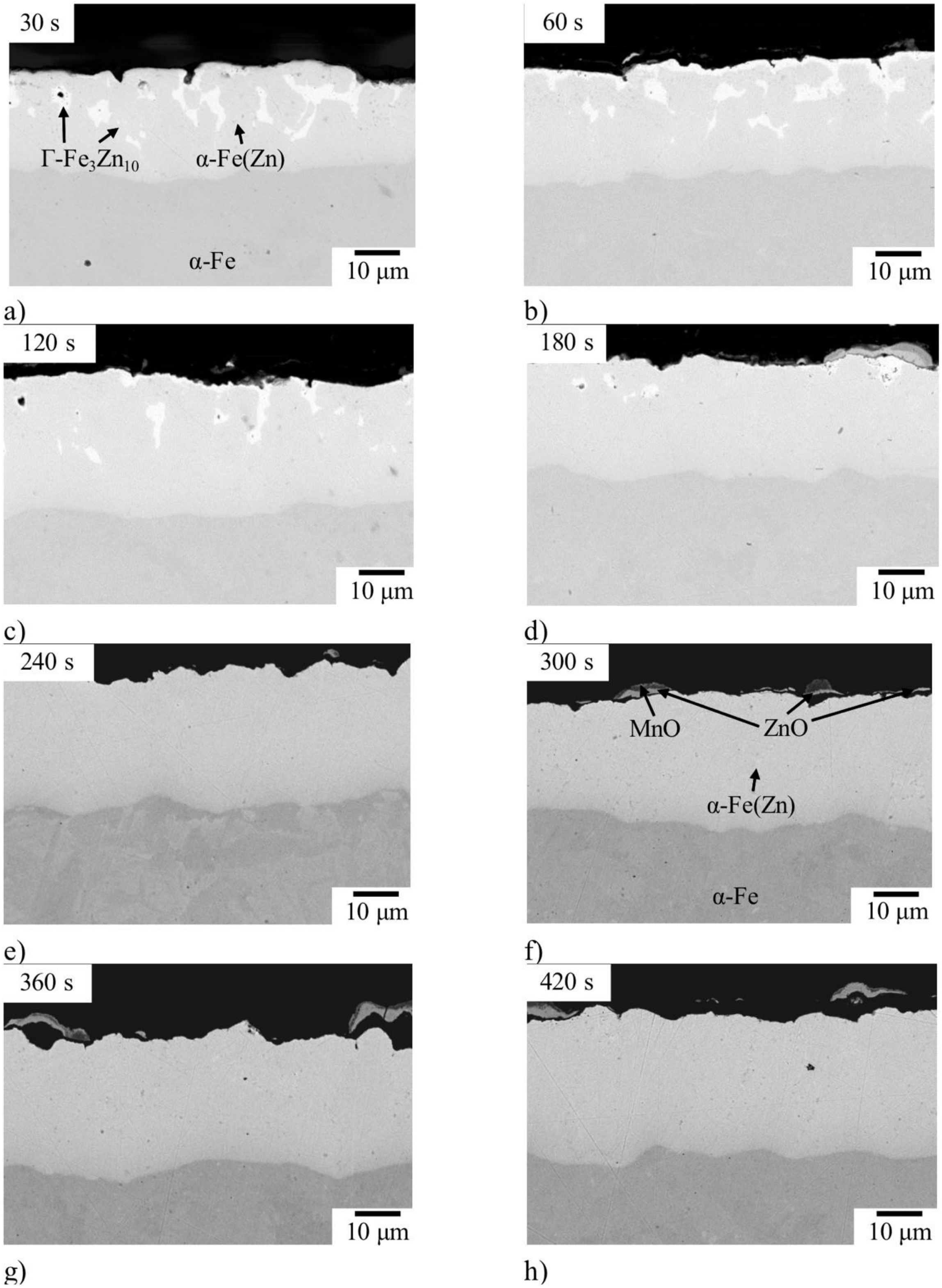

Fig. 2.15. Microstructural evolution of a Zn coating on 22MnB5 throughout austenization at 900 °C [78].

2.7 LIQUID METAL EMBRITTLEMENT

Liquid metal embrittlement (LME) is a type of environmentally assisted cracking. It is characterized by brittle failure, usually rapidly and along the grain boundaries of a normally ductile metal which is in contact with a liquid metal while exposed to tensile stresses [82–84]. The general phenomenon was first reported in studies that are now over a century old [85,86]. Many LME models have been proposed over the years, which fall into three general categories: crack tip brittle fracture propagation, dislocation activity, and diffusion at grain boundaries [87]. These have been summarized in Figure 13 [88].

2.7.1 Proposed LME Mechanisms

Crack tip brittle fracture propagation model

In this set of models, propagation of the cracks occurs by brittle fracture ahead of the crack tip. The Rostoker-Rehbinder model assumes that the embrittling liquid metal reduces the surface energy of the non-embrittling solid metal, which lowers fracture strength [89]. The Stoloff-Johnson-Westwood-Kamdar model [90,91] was developed to answer criticisms of the Rostoker-Rehbinder model, which the authors viewed as oversimplified. They chose to focus on what happens at the crack tip and suggested that atoms of the embrittling liquid reduce the cohesive strength of atomic bonds in the base metal just ahead at the crack tip. This reduction in cohesive strength makes it easier for the crack to advance by tensile decohesion instead of crack blunting by dislocation flow. The Robertson-Glickman model [92] assumes that the crack grows by stress-assisted dissolution of the base metal into the embrittling liquid metal at the crack tip. However, this model has no experimental validation and does not accurately predict the dependence of embrittlement degree on the liquid metal composition [87].

Dislocation activity model

In this set of models, the dislocation activity is affected by the embrittling metal ahead of the crack tip. There are again three major ones: the Lynch model, the Rehbinder-Popovich model, and the Hancock-Ives model. Lynch [93] used detailed metallographic and fractographic observations to prove that LME results from slip, not decohesion, as suggested by the brittle fracture propagation models. The Lynch model [93] suggests that LME occurs due to an adsorption-induced localized-slip process, where dislocations nucleating at the crack tip incrementally advance the crack by creating voids just ahead of the crack tip. The Rehbinder-Popovich model [94] states that adsorption of the liquid embrittling metal promotes dislocation nucleation and plastic deformation caused by a reduction in surface energy between the embrittling metal and the base metal. The Hancock-Ives model [95] builds on the Stoloff-Johnson-Westwood-Kamdar model [90,91]. It states that dislocation pileups at grain boundaries occur due to plastic deformation ahead of the crack tip. Embrittling atoms that diffuse a short distance ahead of the crack tip into this area of dislocation pileups cause rapid intergranular crack propagation.

Grain boundary diffusion models

Still other models focus on grain boundary diffusion. The Krishtal-Gordon-An model [84,96] argues that the cohesive strength reduction does not have the appropriate thermal characteristics to be the rate controlling step in LME crack formation (at least in the case of indium on steel), and disagrees with the brittle fracture propagation models because they do not explain delayed crack initiation. This model suggests that stress-assisted diffusion of the embrittling metal into grain boundaries of the base metal occurs, which lowers the resistance to crack nucleation and makes dislocation slip more difficult. When a critical concentration of embrittling atoms have diffused into the grain boundary, a crack will nucleate. The Rabkin model [97] suggests that the

Kirkendall effect generates tensile stresses at grain boundaries which leads to intergranular fracture. This allows liquid metal to penetrate into the separated grain boundary, which advances the crack. However, none of these models have become fully accepted.

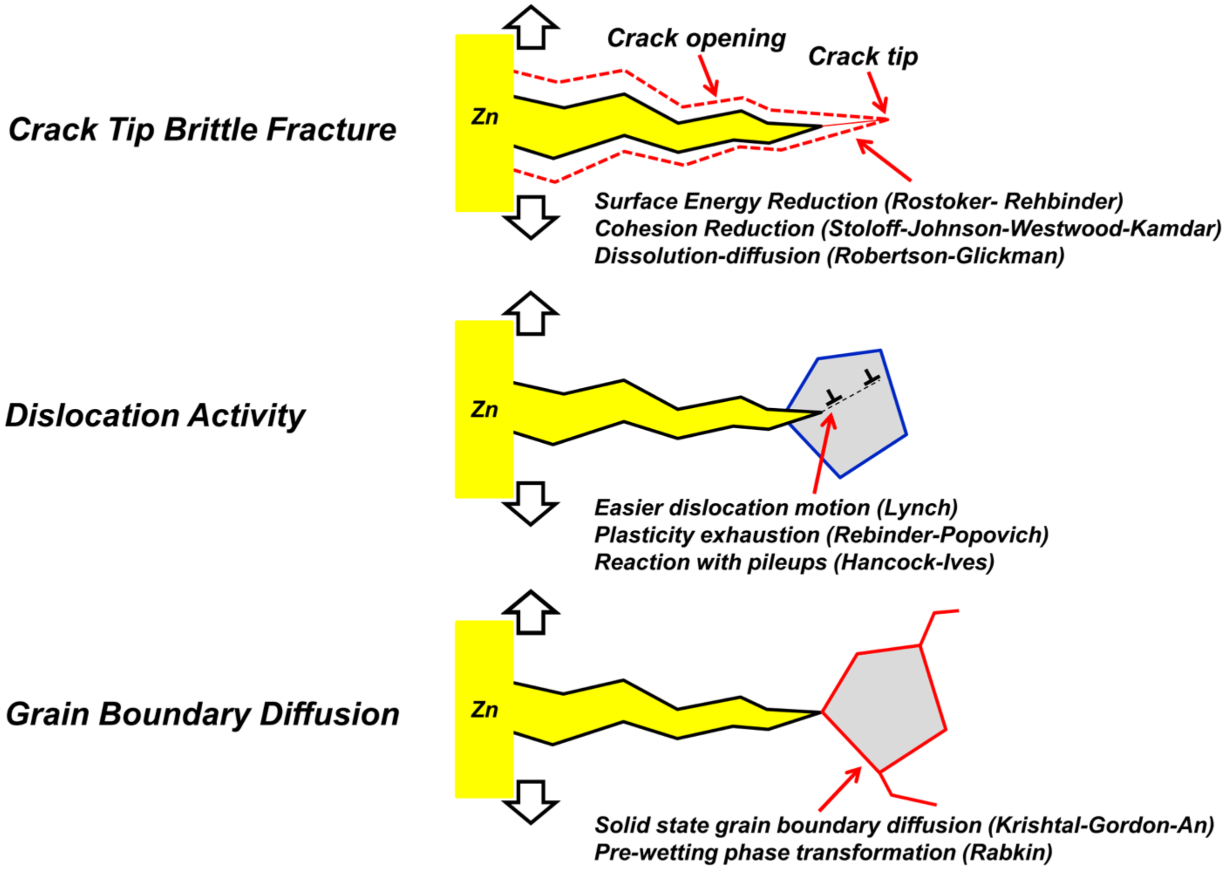

Fig. 2.16. Summary of LME mechanism models [88].

2.7.2 Observations of LME in Zn-Coated PHS

There have been many reports of LME in Zn-coated PHS during forming [48,76,87,98–100] and also in welding [101,102]. Cho et al. [98] studied LME in Zn-coated PHS and proposed the mechanism shown in Fig. 2.17. The process begins during the high temperature forming step of DHPF. Fig. 2.17 (a) shows cracks being initiated at α-Fe(Zn) coating grain boundaries during the application of tensile stress. Liquid Zn then fills these cracks and becomes in contact with the substrate. With the liquid Zn in contact, Zn diffuses very quickly through austenite grain boundaries in the substrate, as shown in Fig. 2.17 (b). However, Zn has limited solubility in austenite at 900 °C, so it acts as a ferrite stabilizer and transforms the grain boundary region into α-Fe(Zn). This accelerates Zn diffusion as the solubility of Zn in α-Fe(Zn) is higher than it is in austenite. This α-Fe(Zn) grain boundary layer is also weaker than the surrounding matrix, which causes cracking through this transformed region as shown in Fig. 2.17 (c). Once the crack is opened, liquid Zn penetrates and wets the crack through capillary action, introducing a fresh supply of Zn to continue this diffusion-assisted process. In Fig. 2.17 (d), the crack is shown advancing through repetition of steps (b) and (c). Fig. 2.17 (e) shows the liquid Zn transforming into Γ-Fe_3Zn_{10} upon quenching, demonstrating how it is possible to accurately determine the position of liquid Zn during the crack propagation process. In summary, it was concluded that it is not the liquid Zn itself that propagates cracks, but the continuous transformation of a thin region around grain boundaries that weakens the crack tip and allows the crack to advance [98].

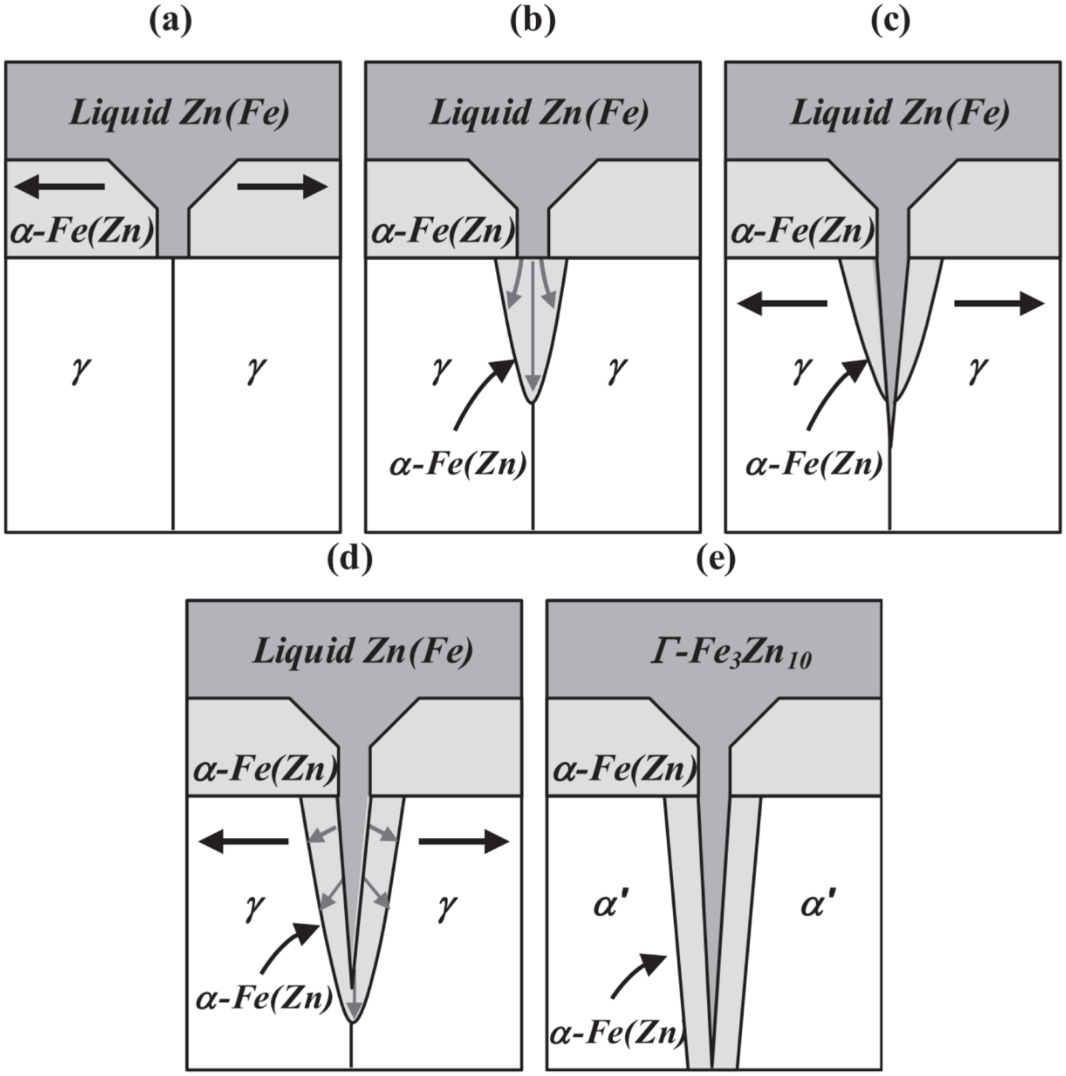

Fig. 2.17. Schematic showing the diffusion-assisted grain boundary phase transformation crack propagation mechanism, γ: austenite, α’: martensite [98].

In 2015, Lee et al. [48] performed a detailed cross-sectional analysis of the coating-substrate interface at each region of a DHPF U-shaped channel (Fig. 2.18). It can be seen that only a small amount of Γ-Fe_3Zn_{10} phase exists in the final coating, i.e. only a small amount of liquid Zn was present at the time of forming and quenching. The top surface (1) experienced minimal amounts of strain during the forming process, leading to a crack-free coating. Additionally, no cracks were observed in areas (3) and (6) which were deformed in compression. The outer corners

(2) and (7) were deformed in tension, and showed cracks through the thickness of the coating along α-Fe(Zn) grain boundaries. The inner wall (5) showed some cracks, but less than at the corners. The outer wall (4) showed LME cracks penetrating about 10 μm into the substrate. The authors attributed this finding to the forming history of the outer wall. During forming, the outer wall is subjected first to compression and then tension as it unbends, and finally to fraction by the forming die. The LME model that these authors proposed is essentially the same as Cho et al. [98], shown in Fig. 2.17. It is worth noting that the mechanical properties as measured by uniaxial tensile testing were seemingly unaffected by this cracking in the wall region, i.e. (4) and (5) (Fig. 2.8). However, bendability was dramatically reduced [48].

In 2016, Kang et al [87] studied LME using a twinning-induced plasticity grade with a composition of 0.44C-17.4Mn-1.4Al-0.6Si, a 22MnB5 grade, and an interstitial-free grade with a composition of 0.007C-0.8Mn-0.3Al-0.006Si. It was found that the TWIP grade was the most prone to LME, followed by 22MnB5, and then by the IF grade, which appeared to be resistant to LME. The Krishtal-Gordon-An model and the Stoloff-Johnson-Westwood-Kamdar model most closely matched their microstructural observations. Dislocation activity models did not apply, as no evidence was found for increased dislocation density near LME cracks.

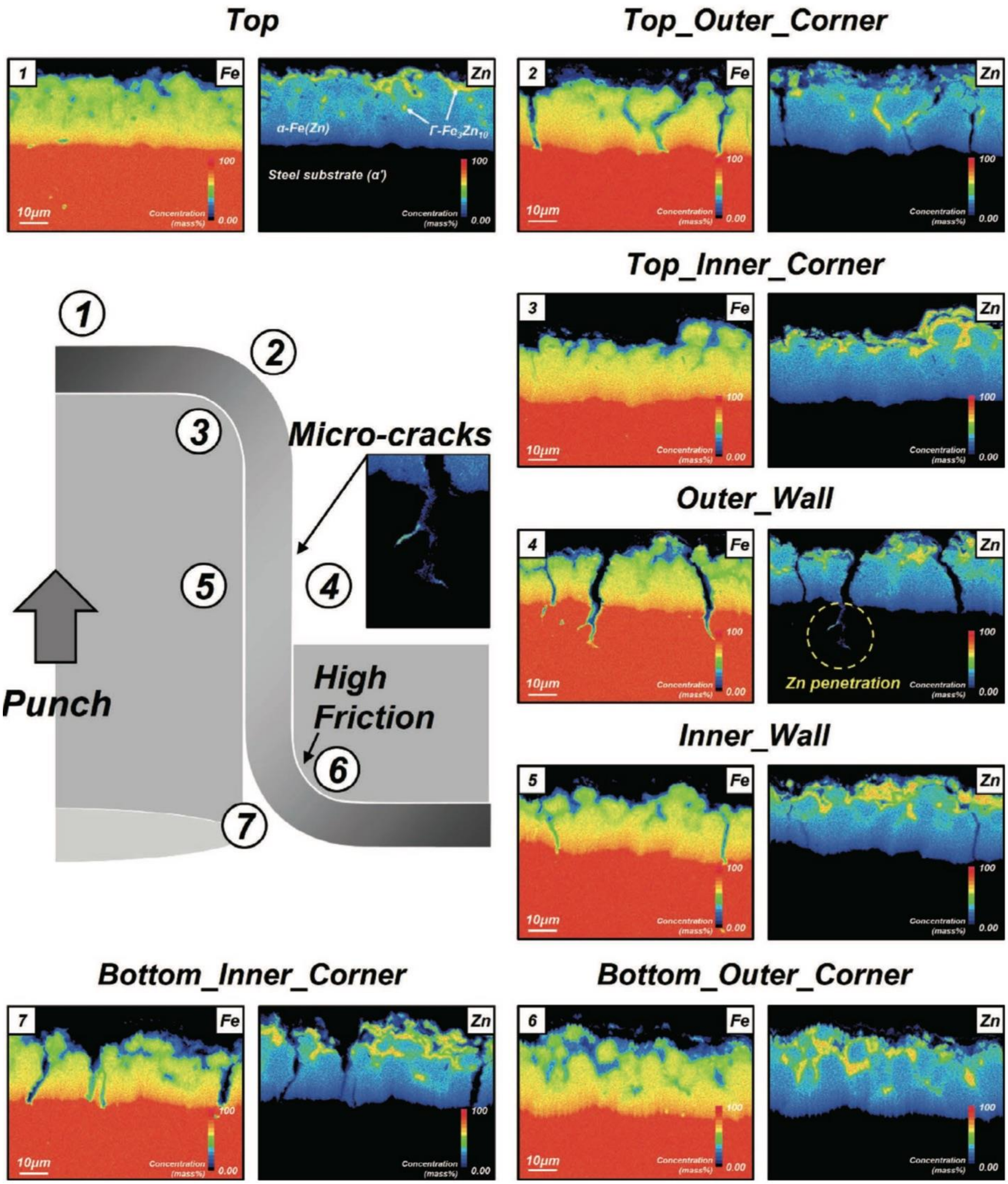

Fig. 2.18. Cross-sectional analysis showing the Fe and Zn distribution at the substrate-coating interface for each area of the Zn-coated 22MnB5 DHPF part [48].

2.8 SOLID METAL EMBRITTLEMENT

While LME has been well studied and widely reported in Zn-coated steels, there have also been reports of solid metal embrittlement (SME), also referred to as solid metal induced embrittlement (SMIE). SME is very similar to LME, the main difference being that SME can occur below the melting point of the embrittling metal [103]; in the case of Zn on steel the embrittling effect was shown to activate at approximately $0.75T/T_m$ (~315 °C) [104]. More specifically, the difference lies in the rate-controlling process for each embrittling mechanism – in LME, the embrittling atoms are transferred by capillary flow of the liquid metal, whereas the rate controlling step for SME is transport of atoms to the crack tip by diffusion [103]. This assumption that diffusion controls the crack kinetics agrees with experimental observations that the rate of crack growth increases with increasing temperature due to increased diffusion distances, and decreases with increasing crack length (distance from the source of embrittling metal) due to longer times required to transport the embrittling metal to the crack tip [103]. Therefore, cracking rates are much lower for SME than for LME [84,103–106], perhaps one reason why SME has received much less research attention than LME. An excellent demonstration of these claims is provided by Gordon and An through their study of pure indium on a commercial 4140 grade steel, where it was found that once the melting point of indium was passed and LME became the operating embrittlement mechanism instead of SME, the crack initiation time dropped by a factor of 6.5 times and the crack propagation time dropped by four orders of magnitude [84]. Thus, while SME may be unavoidable, LME must be avoided at all costs as it is significantly more destructive.

There have been a limited number of studies of the SME of Zn-coated PHS. Janik et al. [70] studied the embrittlement of Zn-coated 22MnB5 during DHPF and modelled the growth of the α-Fe(Zn) coating into the austenitic substrate using a finite difference model. A mechanism based on the general model of SME was proposed and is shown in Fig. 2.19, where Fig. 2.19 (a) shows the state of the coating as it is being heated, at which time the coating has mostly transformed into α-Fe(Zn) with some liquid Γ-Fe_3Zn_{10} present. Fig. 2.19 (b) shows that after 240 s of annealing the coating has completely transformed into solid α-Fe(Zn) with some through-thickness cracks, and there are Zn-rich pockets present where α-Fe(Zn) grain boundaries meet the substrate-coating interface (a unique feature of this proposed mechanism not found elsewhere in the literature). If a tensile stress is then applied, Fig. 2.19 (c) shows that the Zn-rich pockets assist SME and cause the propagation of deep, sharp microcracks. If austenization is extended to 600 s as in Fig. 2.19 (d), the α-Fe(Zn) coating grows deeper into the substrate resulting in reduced Zn concentration in the coating and the Zn-rich pockets homogenize, causing an overall reduction in the availability of Zn atoms to cause SME. When DHPF is performed after this extended austenization time, the microcracks barely penetrate into the substrate and are blunted, apparently because the amount of Zn in the region does not meet the critical concentration to promote SME (Fig. 2.19 (e)).

The origin of microcracking in Zn-coated DHPF 22MnB5 steel was also studied in detail by Maleki et al. [107,108]. A Zn-enriched martensite “transition layer” was detected by EBSD at the interface between the coating and the substrate, which agrees with previous reports in the literature [72,109]. Semi-quantitative electron energy loss spectroscopy (EELS) analysis determined that both α-Fe(Zn) grain boundaries and prior austenite grain boundaries (PAGBs) were enriched with Zn [108] by approximately a factor of 2 versus the bulk composition. This Zn enrichment causes the formation of α-Fe(Zn) along the α-Fe(Zn) and PAGBs, which weakens the substrate and allows the crack to propagate. Furthermore, the crack tip was observed to blunt and stop propagating once the PAGB Zn enrichment was no longer observed [108]. Based on these observations, the mechanism in Fig. 2.20 was proposed. According to this model, the Zn coating and substrate system after 780 s of annealing at 900 °C consisted of an outer α-Fe(Zn) layer, a thin Zn-enriched austenite layer (Zn-γ), and the austenitic substrate (Fig. 2.20 (a)). The coincident grain boundary in all three layers became enriched with Zn relative to the surrounding matrix with the extent of enrichment decreasing towards the substrate, as illustrated by the shade of red in Fig. 2.20 (a). As Zn diffused into the area surrounding the grain boundaries, a thin layer of brittle α-Fe(Zn) was formed. Then, as tension was applied during DHPF or afterwards in a tensile test (Fig. 2.20 (b)), cracks which initiated in the outer α-Fe(Zn) layer propagated downward along the coincident PAGBs that had become embrittled due to Zn-enrichment and the subsequent formation of α-Fe(Zn). The crack propagated until it had reached the extent of Zn enrichment, at which point it stopped and the tip blunted [107,108].

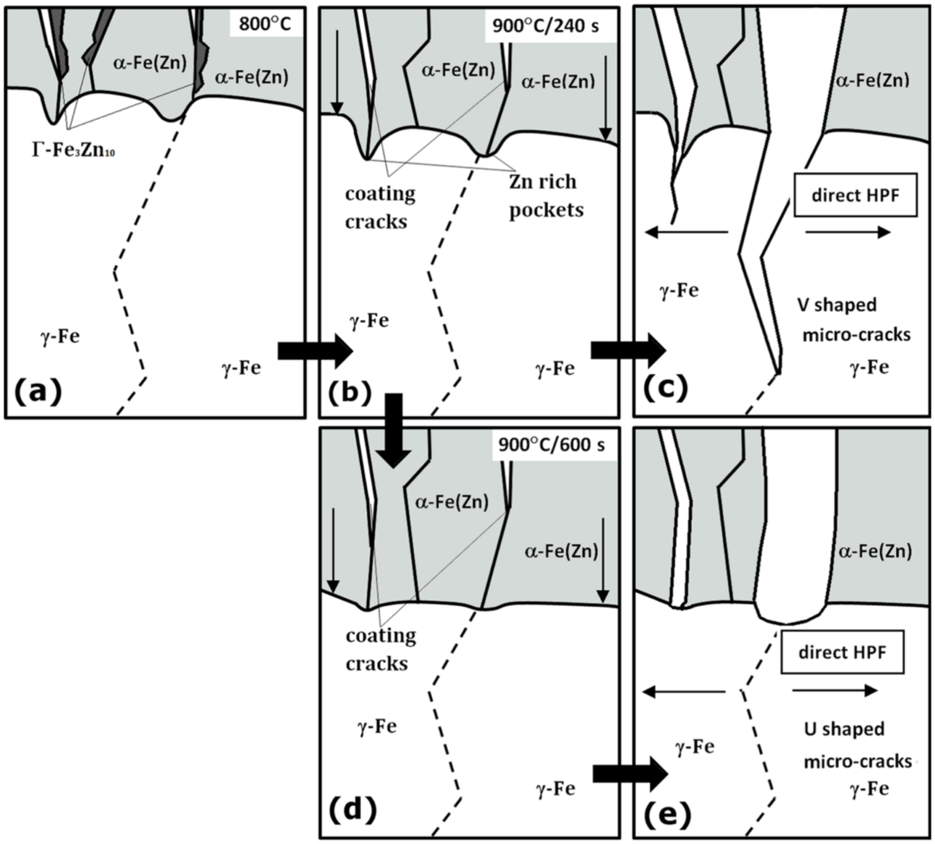

Fig. 2.19. Schematic of solid-metal induced microcracking mechanism in Zn-coated PHS proposed by Janik et al. [70].

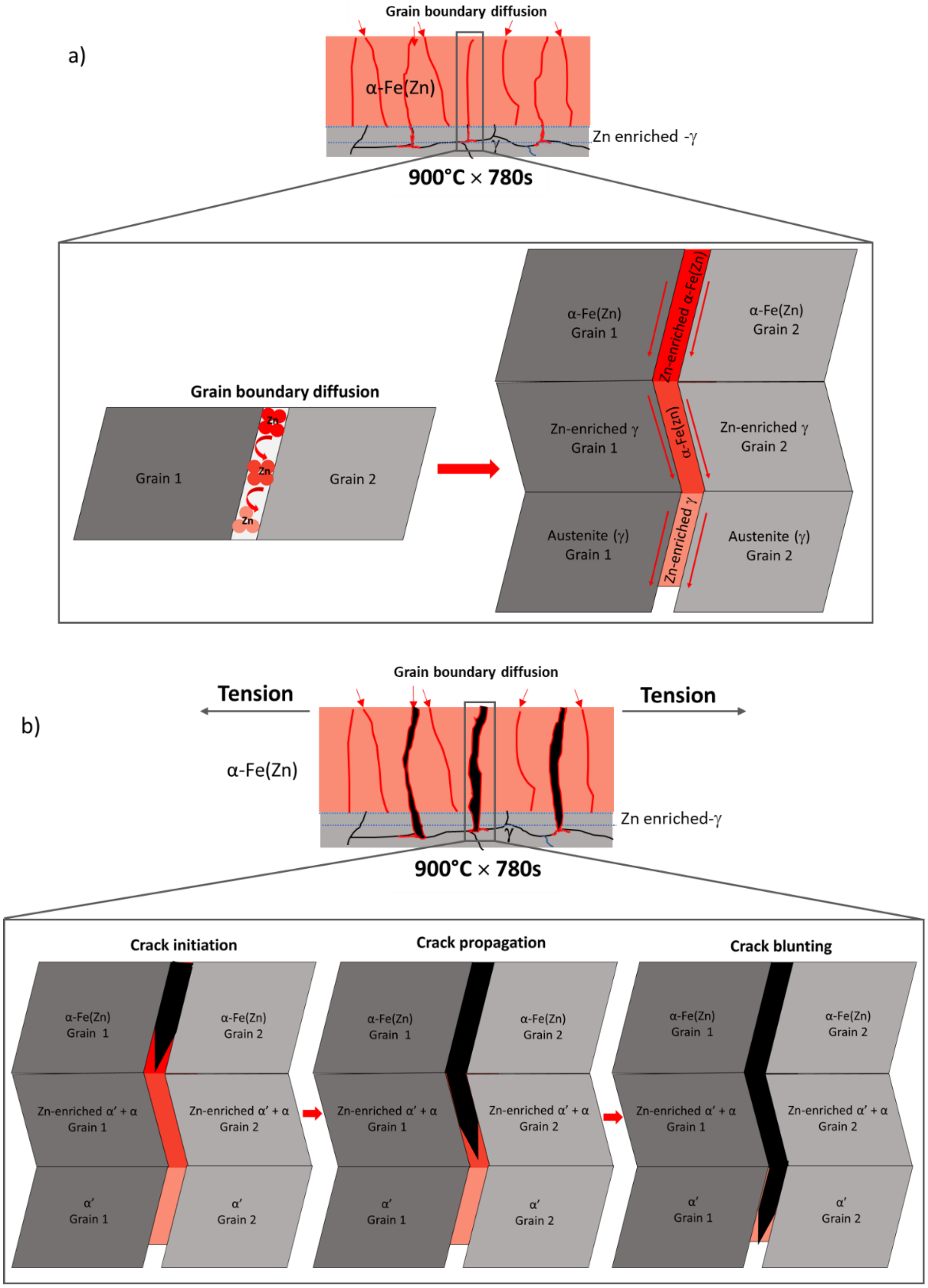

Fig. 2.20. Schematic of microcracking mechanism in Zn-coated PHS proposed by Maleki et al., (a) before the application of tension, (b) after simultaneous forming and quenching [108].

2.9 APPROACHES TO MITIGATING LIQUID METAL EMBRITTLEMENT IN ZN-COATED PRESS-HARDENED STEEL

There have been many reports of LME during press-hardening of Zn-coated steel [75,88,98,110,111]. The Al-Si coating is one way of eliminating LME, but it is not without disadvantages (§ 2.6). Attempts to minimize or avoid the LME of Zn-coated PHS generally take three forms. As defined earlier, LME may occur when a solid metal is in contact with a liquid metal while simultaneously exposed to tensile stresses. Since tensile stress is an unavoidable consequence of forming, the only option to mitigate LME is to have no liquid phases during forming.

2.9.1 The Indirect Press-Hardening Method

The indirect press-hardening method is rarely used but warrants discussion as it is a viable means of producing Zn coated PHS. In this method, the part is cold-formed to within 90–95% of its final geometry before entering the austenization furnace [6] (Fig. 2.21). Perhaps the most important advantage of the indirect method is that nearly all of the deformation is performed at room temperature and is performed on the highly ductile pure Zn coating. This removes the liquid during forming, so LME cannot occur. The pre-forming step also allows for larger, more complicated parts to be formed. Because the part is nearly fully formed when it enters the forming and quenching dies, contact and heat conduction is improved, thus improving the temperature homogeneity during quenching, allowing optimization of the material’s microstructure [6]. Furthermore, the indirect method creates less high-temperature deformation of the coating, which may reduce the severity of coating cracks [14]. However, there are significant disadvantages which negate the advantages of this method. The extra forming step requires extra time and significantly more cost because it is necessary to manufacture and maintain another die set [2]. Performing the forming step at room temperature confines the material to conventional cold-forming limits, eliminating one of the major benefits of press-hardening [112].

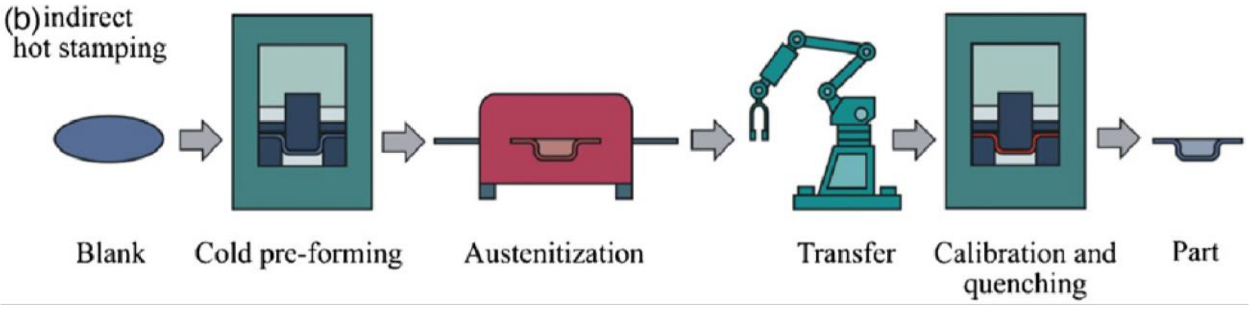

Fig. 2.21. Schematic of the indirect press-hardening method [7].

2.9.2 Complete formation of α-Fe(Zn)

Another method used to avoid LME is to increase the austenization time or use a thinner initial coating so that the coating is fully transformed into α-Fe(Zn) before it is formed and quenched [70,76,110,113,114]. Janik et al. [70] studied the effect of increasing annealing time on cracking within Zn-coated 22MnB5 steel. The authors found that after annealing 240 s at 900 °C the liquid phase in the coating had completely transformed into α-Fe(Zn), in agreement with other studies [71,76,115]. By transforming the entire coating into a solid phase, the acting embrittlement mechanism transitions from LME to SME, which as discussed in § 2.8, is highly desirable as it results in crack propagation rates several orders of magnitude slower than LME. While this prevented LME, through-thickness coating cracks were still seen penetrating into the substrate. It was assumed that since no Fe-Zn liquid was present these coating cracks must have come from die friction [70]. Other works suggest that cracks occur due to differences in thermal expansion coefficients of the brittle intermetallic phases. Janik et al. [70] also noted a clear relationship between the Zn concentration in the coating after austenization and the shape and maximum depth of micro-crack propagation into the substrate (Fig. 2.22), yet concluded that micro-crack propagation was not controlled by Zn diffusion into γ-Fe(Zn). Clearly, these researchers had some success in limiting microcracking, as shown in Fig. 2.22. However, microcracking was not completely eliminated and the low Zn concentration of the coating likely will cause it to have a electrochemical potential close to that of the substrate, negating the main advantage that Zn-based coatings have over Al-Si coatings, as will be discussed in § 2.10.

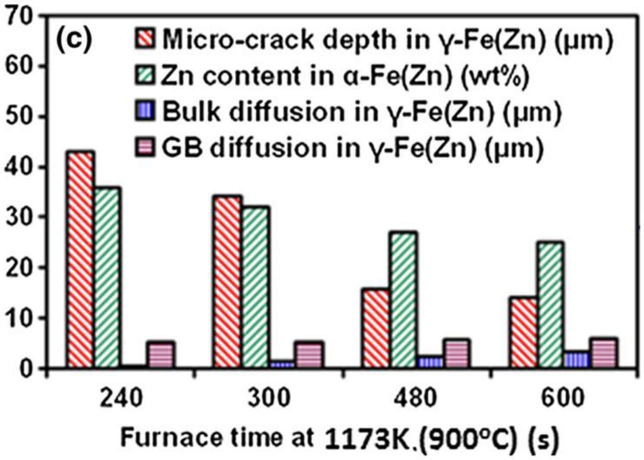

Fig. 2.22. Relationship between Zn content in the coating, microcrack depth, and diffusion into γ-Fe(Zn) [70].

2.9.3 Pre-cooling

Finally, the steel can be pre-cooled before press-hardening [14,116–118]. By allowing the steel to cool below the peritectic temperature of 782 °C, the peritectic reaction $Zn_{liq}(Fe) \rightarrow \Gamma\text{-}Fe_3Zn_{10} + \alpha\text{-}Fe(Zn)$ will occur and solidify the coating, removing the liquid necessary for LME to occur. The pre-cooling method should provide the most desirable results as it maintains the formability that is lost when forming at cold temperatures (indirect method) and is compatible with producing $\Gamma\text{-}Fe_3Zn_{10}$ and generally higher Zn contents in the final coating, which allow for potential cathodic corrosion resistance. In addition, since the coated blank is annealed for much shorter times than it takes for complete formation of α-Fe(Zn) (§ 2.9.2), the extent of solid-state Zn diffusion and hence the extent of SME should be reduced. The pre-cooling step can be accomplished by a dedicated cooling furnace [116,117] or simply by extending the transfer time to allow the steel to cool in ambient air before press-hardening.

One of the disadvantages with this method is that it is not entirely compatible with the standard 22MnB5 grade. When cooling rates are decreased, 22MnB5 is not sufficiently hardenable to achieve a fully martensitic microstructure upon quenching [116]. For example, in the study by Hu et al. [119] the "critical transfer time" was 11 s for a stamping temperature of 742 ˚C, beyond which the microstructure was no longer fully martensitic. Similarly, in a study by Chiuhuang et al. [120], a 15 s transfer time, −19.6 ˚C/s cooling rate and 576 ˚C stamping temperature resulted in some ferrite in the microstructure, reducing the final TS of the material.

To solve this problem, it is necessary to improve the hardenability of the steel substrate. Kurz et al. [116] used a 20MnB8 grade with a composition 0.195C-1.98Mn-0.19Si-0.003B (wt%). The grade is basically 22MnB5 with added Mn to increase hardenability, and slightly less C to keep TS levels around 1500 MPa. The authors found that the critical cooling rate was just −20 ˚C/s for the 20MnB8 alloy (Fig. 2.23) compared to −40 to −50 ˚C/s for 22MnB5 [116]. It is worth noting that the critical cooling rate for 22MnB5 determined by these authors is much higher than the −27 to −35 ˚C/s reported by others [2,15,34,35]. Therefore, it is possible that the actual critical cooling rate for the 20MnB8 alloy with 2% Mn is even lower than −20 ˚C/s. The results from the study by Kurz et al. [116] are promising, but this pre-cooling method is relatively new and the available literature remains scarce.

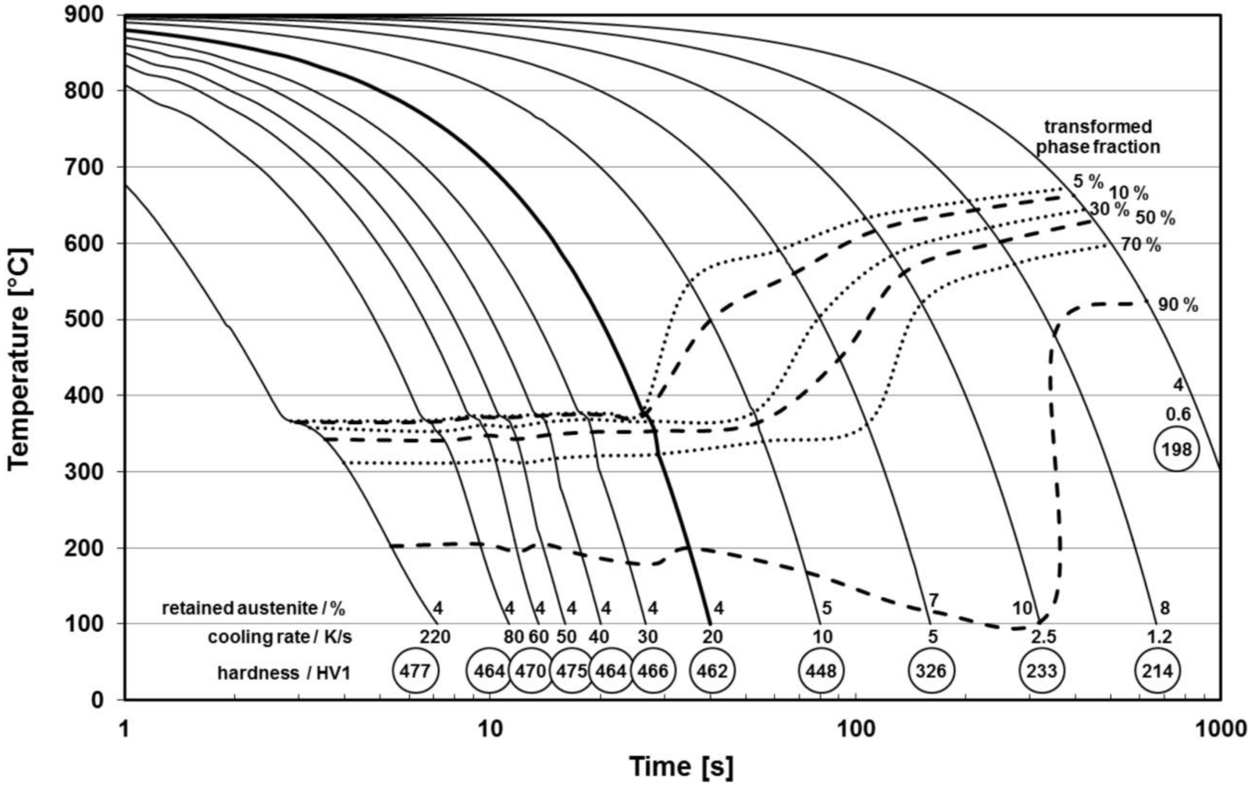

Fig. 2.23. CCT curve for 20MnB8 [116].

2.10 ELECTROCHEMICAL PROPERTIES AND CORROSION OF ZN-COATED PRESS HARDENED STEEL

During DHPF, the Zn coating undergoes extensive transformations as described in § 2.6.2. As the steel is austenized, the coating grows into the substrate *via* counter-diffusion with Fe. The electrochemical potential of the coating becomes more noble with increasing Fe content. Because the electrochemical potential of the coating becomes less negative and closer to that of the substrate itself, increased austenization time generally means that the thermodynamic driving force for cathodic protection is reduced.

The corrosion resistance of coated steels has typically been conducted using accelerated cyclic corrosion tests consisting of alternating salt spray tests or alternating climate tests, such as the VDA 621-415, ASTM G85 or SAE J2334 standard tests. A VDA test cycle is one week long and consists of three subcycles. First is a 24 h salt spray test with 5 wt% NaCl at 35 °C, then a 96 h condensing climate test at 40 °C and 95% relative humidity, followed by 48 hours at ambient atmosphere [121]. This cycle is then repeated over the 7 days of the test. Results for this test performed on Zn-coated PHS are shown in Fig. 2.24 [121]. It can be seen that the Γ-Fe_3Zn_{10} (bright phase) dissolves first, as it has the most negative electrochemical potential. Once Γ-Fe_3Zn_{10} was depleted, α-Fe(Zn) was attacked. However, after 10 testing cycles, there was still no attack into the substrate.

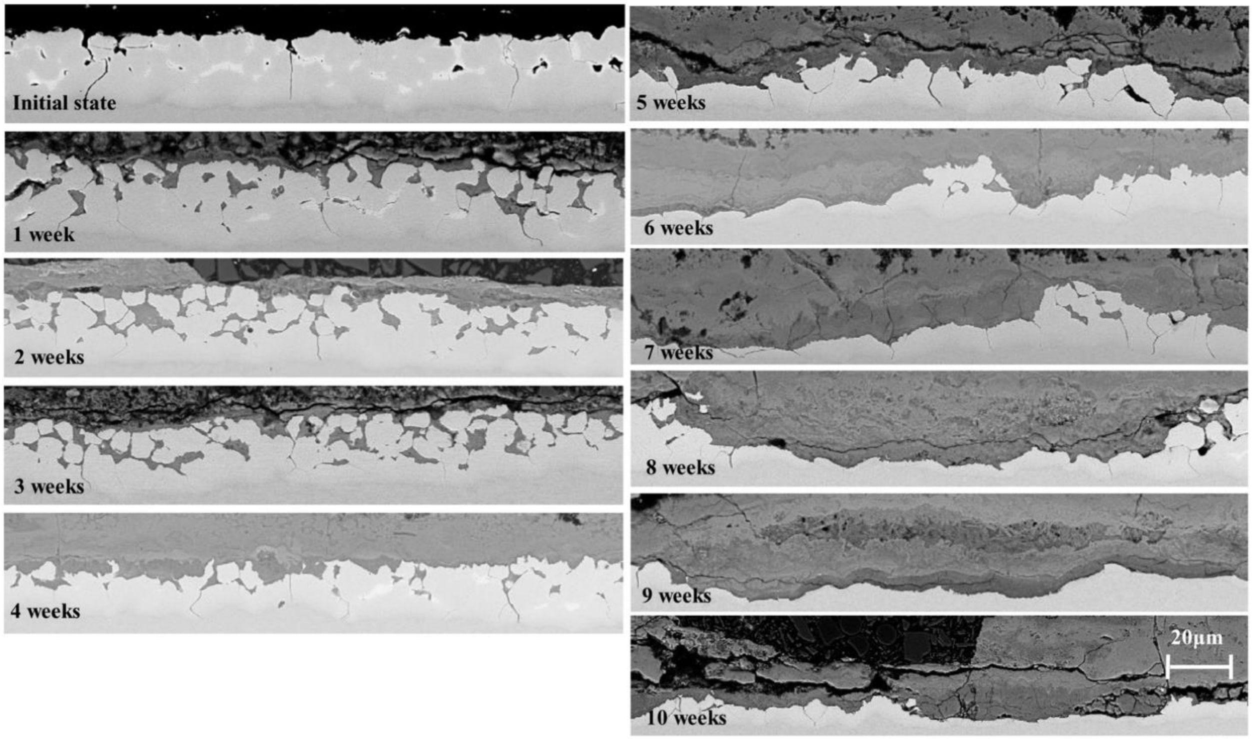

Fig. 2.24. SEM images of the press-hardened Zn coating after different times during an accelerated corrosion test [121].

This result proves that the corrosion resistance of Zn coatings actually improves after DHPF, since the galvanized coating before DHPF began to show substrate attack after only 2 weeks. This finding was attributed to the increased coating thickness after DHPF as well as the lower potential difference between the coating and the substrate that led to a decreased corrosion rate [121]. Dosdat et al. [58] found that Zn-coated PHS showed better cosmetic appearance and corrosion resistance at cut edges as well as offered cathodic corrosion resistance unlike the Al-Si coating. However, the authors also noted that the Al-Si coating provided better perforation resistance and a larger process window.

The coating can also be tested electrochemically using open circuit potential, potentiostatic polarization, or galvanostatic polarization tests [71,78,115,122]. The work by Dever et al. [78,115] included an extensive study on Zn-coated 22MnB5 subject to different austenization times. The study employed a naturally aerated salt solution consisting of 100 g $ZnSO_4{\cdot}7H_2O$ and 200 g NaCl in 1000 mL of DI water, as was used by Autengruber et al. [121]. All electrochemical tests were conducted in a classic three electrode cell using a saturated calomel electrode (SCE) reference electrode and using a carbon counter-electrode. Results of some galvanostatic tests are presented in Fig. 2.25, where Zn-coated 22MnB5 was tested after a variety of austenization times [78]. Clearly, the as-galvanized GI70 coating had the largest potential difference compared to the substrate. However, it also experienced full dissolution much faster than the press-hardened coatings (in agreement with Fig. 2.24 [121]). The press-hardened coatings show two distinct dissolution potentials corresponding to the intermetallic phases Γ-Fe_3Zn_{10} and α-Fe(Zn). The dissolution potentials of Γ-Fe_3Zn_{10}, α-Fe(Zn), and the substrate were -0.835 V_{SCE}, -0.655 V_{SCE}, and -0.54 V_{SCE}, respectively.

The dissolution time of a phase is related to its volume, which can be seen either directly on Fig. 2.25 as a function of austenization time, or in more detail in Fig. 2.26 as a function of fraction of Γ-Fe_3Zn_{10}. Observation of Fig. 2.26 shows that there is a linear relationship between dissolution time and fraction of Γ-Fe_3Zn_{10}. Based on the time spent at each voltage during the galvanostatic tests, the amount of Γ-Fe_3Zn_{10} decreases from a maximum at the 700 °C–60 s condition and at the 900 °C–240 s condition the coating had transformed completely to α-Fe(Zn), in agreement with the microstructural evolution discussed in § 2.6.2. The electrochemical potential of the Γ-Fe_3Zn_{10} phase also becomes more noble as austenization time and temperature are increased. This finding was linked to the lower Zn concentration in Γ-Fe_3Zn_{10} in samples that were austenized for longer times. Once Γ-Fe_3Zn_{10} had fully dissolved, the α-Fe(Zn) phase began to dissolve. The electrochemical potential of the α-Fe(Zn) phase slightly increased with testing time, due to a compositional gradient with increasing Fe content closer to the substrate. The last dissolution potential to be reached is that of the substrate itself. The time it took for the substrate to be attacked clearly increases with austenization time and temperature, which was linked to the growth of the coating from 10 μm in the as-received condition to 25–40 μm after austenization.

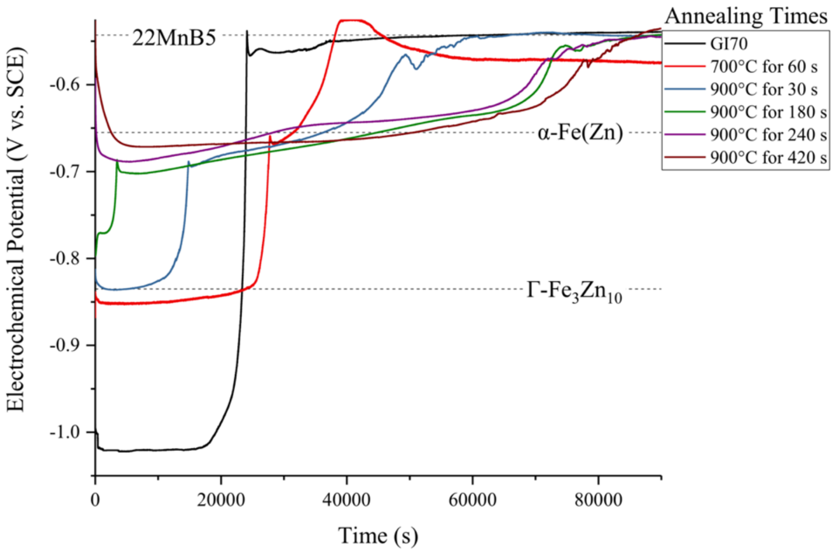

Fig. 2.25. Galvanostatic tests of Zn-coated DHPF 22MnB5 at an applied current density of +1 mA/cm^2 [78].

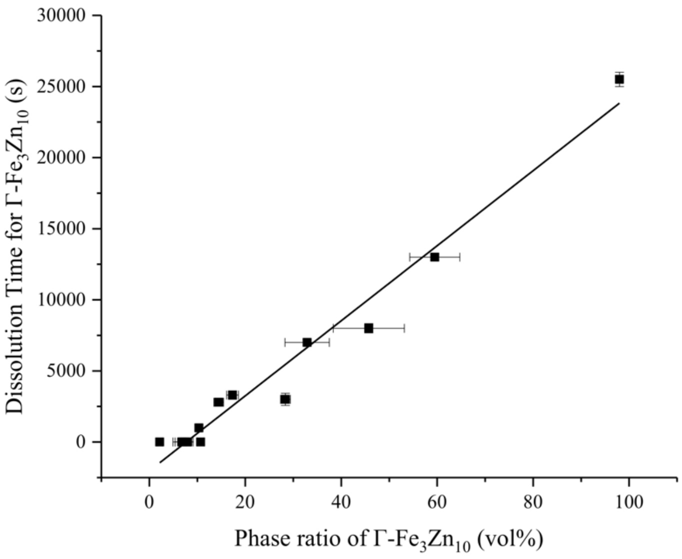

Fig. 2.26. Dissolution time of Γ-Fe_3Zn_{10} as a function of the fraction of Γ-Fe_3Zn_{10} within the coating [78].

Dever also determined the corrosion products formed as the various phases were dissolved during galvanostatic testing [78]. Galvanostatic tests were run until the dissolution of Γ-Fe_3Zn_{10} had completely finished, then the corrosion products on the surface were analyzed by XRD. These measurements are plotted in Fig. 2.27, which shows the fraction of corrosion products that were formed during galvanostatic tests. It was found that three corrosion products formed: 1) hydrozincite, which formed as a result of high Zn conents in the coating and the naturally aerated test environment; 2) simonkolleite, which formed due to high Zn content and the chloride-containing environment; and 3) akaganeite, which formed at high Fe contents in the coating [78]. These results are consistent with other available literature [121,123]. As shown in Fig. 2.27, a dramatic increase in the formation of corrosion products, specifically the Fe-based akageneite, occurred once the fraction of Γ-Fe_3Zn_{10} dropped below 15 vol%. On the other hand, at higher fractions of Γ-Fe_3Zn_{10}, the dominant corrosion product transitioned to simonkolleite and hydrozincite [78]. These trends have also been shown by others in the literature [122,124]. This finding is important because simonkolleite and hydrozincite are stable and passivating Zn-based corrosion products that assist in further decreasing the corrosion rate [78].

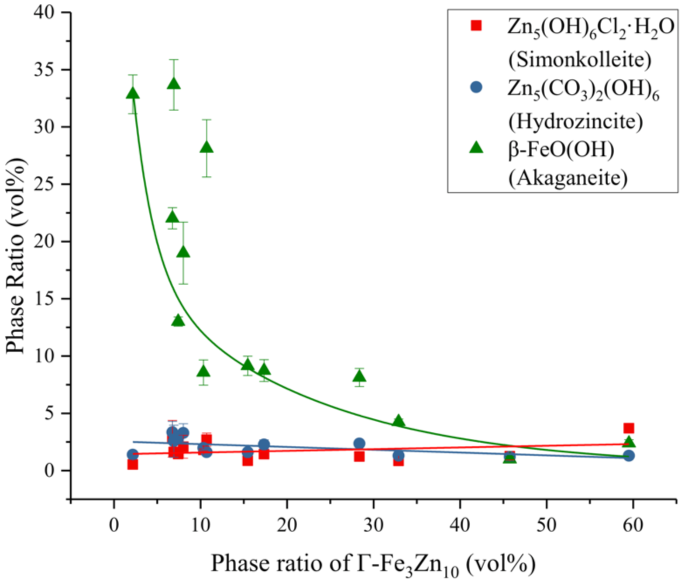

Fig. 2.27. Phase ratio of corrosion products as a function of global Zn content within the coating layer.

The ability of the coating to provide cathodic protection was assessed directly by Dever [78] by performing galvanostatic tests with a sample with an annealed coating coupled to a bare substrate sample through the electrolyte. The results of these tests are presented in Fig. 2.28 as a function of annealing time [78]. All coatings exhibited a positive current density, indicating active cathodic protection for the substrate material [78]. This plot shows that compared to the samples annealed for more than 180 s (corresponding to approximately 10% Γ-Fe_3Zn_{10}), the samples annealed for less than 180 s experience a lower current density and that this constant current density was reached more quickly. This finding was linked to the formation of passivating corrosion products (Fig. 2.27). The electrochemical noise (current density fluctuations) in Fig. 2.28 was also observed to be less in samples annealed for less than 180 s, and a lesser extent of electrochemical noise was linked to less corrosion activity [125]. The current density fluctuations have been attributed to repassivation and initiation of local corrosion [126].

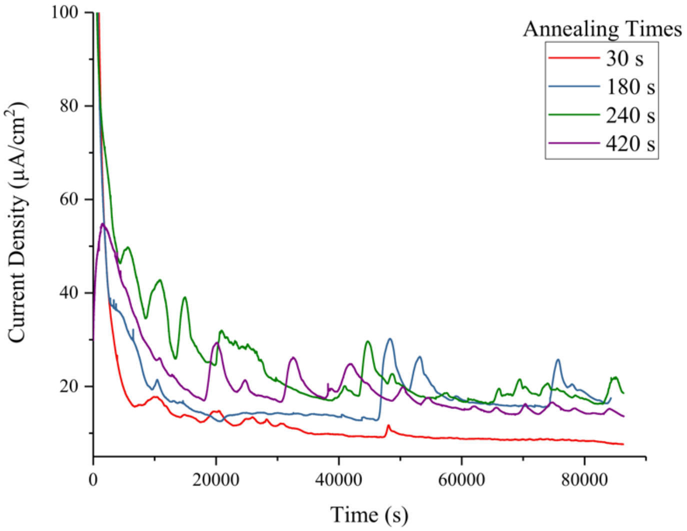

Fig. 2.28. Galvanic corrosion scans for galvanized samples annealed at 900 °C.

Fig. 2.29 presents the electrochemical potential of the E_{corr} and the initial dissolution arrest as a function of fraction of Γ-Fe_3Zn_{10} in the coating. For both curves, it is clear that once the fraction of Γ-Fe_3Zn_{10} drops below 15 vol%, the electrochemical potential increases sharply. The E_{corr} of the bare substrate was measured to be -0.675 V_{SCE} [78], and as seen in Fig. 2.29 the electrochemical potential of the α-Fe(Zn)-only coatings come to approaching this value. Likewise, the dissolution arrest of the substrate was measured to be -0.54 V_{SCE} (Fig. 2.25) [78], and the initial dissolution arrest of the α-Fe(Zn)-only coatings approached this as well. Thus, using the difference in electrochemical potential as a measure of driving force for cathodic corrosion protection, it is clear that the driving force becomes dramatically reduced when Γ-Fe_3Zn_{10} fractions drop below 15 vol%.

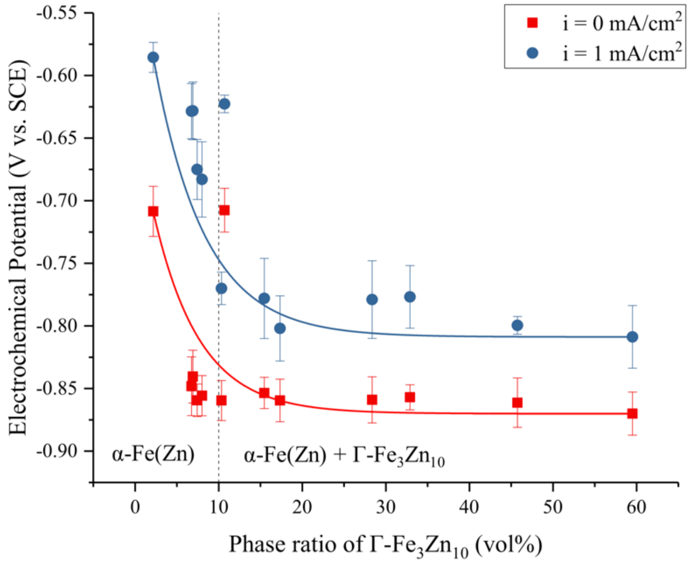

Fig. 2.29. Effect of the fraction of Γ-Fe_3Zn_{10} on the E_{corr} (i = 0 mA/cm^2) and initial dissolution potential arrest (i = +1 mA/cm^2).

In summary, the electrochemical testing performed by Dever [78] on Zn-coated 22MnB5 proved the benefits of having Γ-Fe_3Zn_{10} in the coating microstructure in a number of ways. In Fig. 2.25, it was shown that the breakdown of the coating consists of three dissolutions arrests, corresponding to first Γ-Fe_3Zn_{10}, then α-Fe(Zn), and finally the steel substrate. It is clear that the Γ-Fe_3Zn_{10} dissolution potential is the most negative, providing the greatest driving force for cathodic protection. It is desirable to maintain this driving force for as long as possible, and Fig. 2.26 demonstrates that the amount of time for dissolution of Γ-Fe_3Zn_{10} is linearly related to its volume fraction. Additionally, it was found that coatings containing above 15 vol % Γ-Fe_3Zn_{10} formed significantly less corrosion products, especially Fe-rich akageneite. In coatings containing a high amount of Γ-Fe_3Zn_{10}, the formation of corrosion products shifted to Zn-based ones that are able to passivate and further reduce the corrosion rate. Furthermore, the reduction of current density noise for coatings with high amounts of Γ-Fe_3Zn_{10} (Fig. 2.28) suggests that high amounts of Γ-Fe_3Zn_{10} reduce corrosion activity by preventing passivation breakdown and the current density spikes observed in the higher Fe content coatings. Finally, it is observed in Fig. 2.29 that the driving force for cathodic protection nearly disappears completely with Γ-Fe_3Zn_{10} fractions less than 15 vol %. Therefore, the target that must be reached in order to attain robust cathodic corrosion protection for PHS is a minimum of 15 vol % Γ-Fe_3Zn_{10} in the coating microstructure after DHPF [78].

OBJECTIVE STATEMENT

Based on the literature survey, there is a demand for cathodically protective PHS that cannot be met using conventional materials and processing techniques [2,6,14]. The use of Zn-coated PHS has been very limited due to the prospect of LME, which results in a catastrophic loss of ductility [2,48,98]. A promising method of avoiding LME during DHPF involves stamping below the peritectic temperature of 782 °C—the temperature at which the liquid phase solidifies into Γ-Fe_3Zn_{10}—to remove the liquid necessary for LME to occur [14,116–118]. It has also been shown that at least 15 vol% Γ-Fe_3Zn_{10} is required in the coating microstructure to provide robust cathodic protection [78,115]. However, studies have shown that the industry standard grade 22MnB5 is not sufficiently hardenable to attain fully martensitic microstructures when slowing the cooling rate to stamp at temperatures below 782 °C [116,119,120]. It is hypothesized that it will be possible to make DHPF parts with fully martensitic microstructures and robust cathodic protection while avoiding LME by increasing the hardenability of the substrate and stamping below the peritectic temperature.

To test this objective, two prototype PHS grades were developed based on the chemistry of 22MnB5. To improve the hardenability, the wt% of Mn was increased from 1.2 to 2.0 and 2.5, resulting in compositions for the two alloys of 0.20C-2.01Mn-0.26Si-0.0046B and 0.19C-2.5Mn-0.26Si-0.005B (wt. %). The phase transformation kinetics will be determined by dilatometry, with a specific focus on determining the critical cooling rate for complete martensitic transformation. The microstructural and mechanical property evolution of the substrate as a function of austenization time, stamping temperature, and strain imposed by the forming process will be determined by SEM, microhardness, and tensile tests, with the objective attaining fully martensitic microstructures and TS ≥ 1500 MPa. Coating cracking and fracture surfaces will be analyzed to verify the absence of LME-type cracks and confirm ductile fracture. The microstructural evolution of the coating as a function of austenization temperature, stamping temperature, and region of the DHPF part will be determined by SEM and XRD, with the objective of attaining ≥ 15 vol% Γ-Fe_3Zn_{10}.

REFERENCES

[1] S. Keeler, M. Kimchi, P. J. Mooney, Advanced High-Strength Steels Apllication Guidelines Version 6.0, World Auto Steel. 6 (2017) 314. http://www.worldautosteel.org/download_files/AHSS Guidelines V6/00_AHSSGuidelines_V6_20170430.pdf.

[2] T. Taylor, A. Clough, Critical review of automotive hot-stamped sheet steel from an industrial perspective, Mater. Sci. Technol. 0836 (2018) 1–53. https://doi.org/10.1080/02670836.2018.1425239.

[3] O. Bouaziz, H. Zurob, M. Huang, Driving force and logic of development of advanced high strength steels for automotive applications, Steel Res. Int. 84 (2013) 937–947. https://doi.org/10.1002/srin.201200288.

[4] P. Hu, L. Ying, B. He, Hot Stamping Advanced Manufacturing Technology of Lightweight Car Body, Springer Singapore, 2017. https://doi.org/10.1007/978-981-10-2401-6_10.

[5] M. Pouranvari, S.P.H. Marashi, Critical review of automotive steels spot welding: process, structure and properties, Sci. Technol. Weld. Join. 18 (2013) 361–403. https://doi.org/10.1179/1362171813Y.0000000120.

[6] D.W. Fan, H.S. Kim, B.C. De Cooman, A review of the physical metallurgy related to the hot press forming of advanced high strength steel, Steel Res. Int. 80 (2009) 241–248. https://doi.org/10.2374/SRI08SP131.

[7] H. Karbasian, A.E. Tekkaya, A review on hot stamping, J. Mater. Process. Technol. 210 (2010) 2103–2118. https://doi.org/10.1016/j.jmatprotec.2010.07.019.

[8] Norrbottens Jaernverk AB, Manufacturing a hardened steel article, 1977.

[9] G. Berglund, The history of hardening of boron steel in northern Sweden, in: 1st Int. Conf.

Hot Sheet Met. Form. High-Performance Steel, Kassel, Ger., 2008: p. 177.

[10] E. Billur, G. Berglund, T. Gustafsson, History and Future Outlook of Hot Stamping, in: Hot Stamp. Ultra High-Strength Steels, Springer International Publishing, 2019: pp. 31–44. https://doi.org/10.1007/978-3-319-98870-2.

[11] L. Vaissiere, J.P. Laurent, A. Reinhardt, Development of pre-coated boron steel for applications on PSA peugeot citroën and RENAULT bodies in white, SAE Tech. Pap. 111 (2002) 909–917. https://doi.org/10.4271/2002-01-2048.

[12] M. Merklein, M. Wieland, M. Lechner, S. Bruschi, A. Ghiotti, Hot stamping of boron steel sheets with tailored properties: A review, J. Mater. Process. Technol. 228 (2016) 11–24. https://doi.org/10.1016/j.jmatprotec.2015.09.023.

[13] E. Billur, V. Boškovi, Tailored Properties, in: Hot Stamp. Ultra High-Strength Steels, 2019. https://doi.org/10.1007/978-3-319-98870-2.

[14] D.W. Fan, B.C. De Cooman, State-of-the-knowledge on coating systems for hot stamped parts, Steel Res. Int. 83 (2012) 412–433. https://doi.org/10.1002/srin.201100292.

[15] H. Mohrbacher, Martensitic Automotive Steel Sheet - Fundamentals and Metallurgical Optimization Strategies, Adv. Mater. Res. 1063 (2015) 130–142. https://doi.org/10.4028/www.scientific.net/amr.1063.130.

[16] T. Taylor, G. Fourlaris, A. Clough, Effect of carbon and microalloy additions on hot-stamped boron steel, Mater. Sci. Technol. 33 (2017) 1964–1977. https://doi.org/10.1080/02670836.2017.1342018.

[17] B. Çetin, H. Meço, Metallurgy of Steels, in: Hot Stamp. Ultra High-Strength Steels, Springer International Publishing, 2019: pp. 19–29. https://doi.org/10.1007/978-3-319-98870-2.

[18] H. Mohrbacher, Influence of alloy modifications and microstructure on properties and

crash performance of press hardened steel components, in: 6th Int. Conf. Hot Steel Met. Form. High-Performance Steel, CHS2 2017-Proceedings, 2017: pp. 213–220.

[19] B. Hwang, D.W. Suh, S.J. Kim, Austenizing temperature and hardenability of low-carbon boron steels, Scr. Mater. 64 (2011) 1118–1120. https://doi.org/10.1016/j.scriptamat.2011.03.003.

[20] M. Sharma, I. Ortlepp, W. Bleck, Boron in Heat-Treatable Steels: A Review, Steel Res. Int. 90 (2019) 1–28. https://doi.org/10.1002/srin.201900133.

[21] X. Tingdong, S. Shenhua, Y. Zhexi, Y. Zongsen, Two types of boron segregation at austenite grain boundaries and their mutual relation, J. Mater. Sci. 25 (1990) 1739–1744. https://doi.org/10.1007/BF01045378.

[22] L. Karlsson, H. Norden, Non-Equlibrium Grain Boundary Segregation of Boron in Austenitic Stainless Steel, Acta Metall. 36 (1988) 35–48.

[23] Y.J. Li, D. Ponge, P. Choi, D. Raabe, Segregation of boron at prior austenite grain boundaries in a quenched martensitic steel studied by atom probe tomography, Scr. Mater. 96 (2015) 13–16. https://doi.org/10.1016/j.scriptamat.2014.09.031.

[24] J. Takahashi, K. Ishikawa, K. Kawakami, M. Fujioka, N. Kubota, Atomic-scale study on segregation behavior at austenite grain boundaries in boron- and molybdenum-added steels, Elsevier B.V., 2017. https://doi.org/10.1016/j.actamat.2017.05.021.

[25] D.J. Mun, E.J. Shin, K.C. Cho, J.S. Lee, Y.M. Koo, Cooling rate dependence of boron distribution in low carbon steel, Metall. Mater. Trans. A Phys. Metall. Mater. Sci. 43 (2012) 1639–1648. https://doi.org/10.1007/s11661-011-0997-0.

[26] Y.J. Li, D. Ponge, P. Choi, D. Raabe, Atomic scale investigation of non-equilibrium segregation of boron in a quenched Mo-free martensitic steel, Ultramicroscopy. 159 (2015) 240–247. https://doi.org/10.1016/j.ultramic.2015.03.009.

[27] M. Naderi, M. Ketabchi, M. Abbasi, W. Bleck, Analysis of microstructure and mechanical properties of different boron and non-boron alloyed steels after being hot stamped, in: Procedia Eng., Elsevier, 2011: pp. 460–465. https://doi.org/10.1016/j.proeng.2011.04.078.

[28] L. Lin, B. shun Li, G. ming Zhu, Y. lin Kang, R. dong Liu, Effect of niobium precipitation behavior on microstructure and hydrogen induced cracking of press hardening steel 22MnB5, Mater. Sci. Eng. A. 721 (2018) 38–46. https://doi.org/10.1016/j.msea.2018.02.021.

[29] B. Jian, L. Wang, H. Mohrbacher, H.Z. Lu, W.J. Wang, Development of Niobium Alloyed Press Hardening Steel with Improved Properties for Crash Performance, Adv. Mater. Res. 1063 (2014) 7–20. https://doi.org/10.4028/www.scientific.net/amr.1063.7.

[30] S. Zhang, J. Wan, Q. Zhao, J. Liu, F. Huang, Y. Huang, X. Li, Dual role of nanosized NbC precipitates in hydrogen embrittlement susceptibility of lath martensitic steel, Corros. Sci. 164 (2020) 108345. https://doi.org/10.1016/j.corsci.2019.108345.

[31] A.R. Marder, Metallurgy of zinc-coated steel, Prog. Mater. Sci. 45 (2000) 191–271. https://doi.org/10.1016/S0079-6425(98)00006-1.

[32] E.A. Silva, Private communication, (n.d.).

[33] S. Alibeigi, R. Kavitha, R.J. Meguerian, J.R. McDermid, Reactive wetting of high Mn steels during continuous hot-dip galvanizing, Acta Mater. 59 (2011) 3537–3549. https://doi.org/10.1016/j.actamat.2011.02.027.

[34] P. Namklang, V. Uthaisangsuk, Description of microstructures and mechanical properties of boron alloy steel in hot stamping process, J. Manuf. Process. 21 (2016) 87–100. https://doi.org/10.1016/j.jmapro.2015.11.008.

[35] D.A. da Costa Ximenes, L.P. Moreira, J.E.R. de Carvalho, D.N.F. Leite, R.G. Toledo, F.M. da Silva Dias, Phase transformation temperatures and Fe enrichment of a 22MnB5

Zn-Fe coated steel under hot stamping conditions, J. Mater. Res. Technol. (2019). https://doi.org/10.1016/j.jmrt.2019.11.003.

[36] M. Nikravesh, M. Naderi, G.H. Akbari, W. Bleck, Phase transformations in a simulated hot stamping process of the boron bearing steel, Mater. Des. 84 (2015) 18–24. https://doi.org/10.1016/j.matdes.2015.06.108.

[37] A. Barcellona, D. Palmeri, Effect of plastic hot deformation on the hardness and continuous cooling transformations of 22MnB5 microalloyed boron steel, Metall. Mater. Trans. A Phys. Metall. Mater. Sci. 40 (2009) 1160–1174. https://doi.org/10.1007/s11661-009-9790-8.

[38] J. Min, J. Lin, Y. Min, F. Li, On the ferrite and bainite transformation in isothermally deformed 22MnB5 steels, Mater. Sci. Eng. A. 550 (2012) 375–387. https://doi.org/10.1016/j.msea.2012.04.091.

[39] S. Chatterjee, H.S. Wang, J.R. Yang, H.K.D.H. Bhadeshia, Mechanical stabilisation of austenite, Mater. Sci. Technol. 22 (2006) 641–644. https://doi.org/10.1179/174328406X86128.

[40] R.H. Larn, J.R. Yang, The effect of compressive deformation of austenite on the bainitic ferrite transformation in Fe-Mn-Si-C steels, Mater. Sci. Eng. A. 278 (2000) 278–291. https://doi.org/10.1016/S0921-5093(99)00597-3.

[41] K. Tsuzaki, S. ichi Fukasaku, Y. Tomota, T. Maki, Effect of prior deformation of austenite on the γ → ε martensitic transformation in Fe-Mn alloys, Mater. Trans. JIM. 32 (1991) 222–228. https://doi.org/10.2320/matertrans1989.32.222.

[42] M. Nikravesh, M. Naderi, G.H. Akbari, Influence of hot plastic deformation and cooling rate on martensite and bainite start temperatures in 22MnB5 steel, Mater. Sci. Eng. A. 540 (2012) 24–29. https://doi.org/10.1016/j.msea.2012.01.018.

[43] L. Golem, L. Cho, J.G. Speer, K.O. Findley, Influence of austenizing parameters on microstructure and mechanical properties of Al-Si coated press hardened steel, Mater. Des. 172 (2019) 107707. https://doi.org/10.1016/j.matdes.2019.107707.

[44] J.W. Morris, On the ductile-brittle transition in lath martensitic steel, ISIJ Int. 51 (2011) 1569–1575. https://doi.org/10.2355/isijinternational.51.1569.

[45] H. Järvinen, M. Isakov, T. Nyyssönen, M. Järvenpää, P. Peura, The effect of initial microstructure on the final properties of press hardened 22MnB5 steels, Mater. Sci. Eng. A. 676 (2016) 109–120. https://doi.org/10.1016/j.msea.2016.08.096.

[46] T. Taylor, G. Fourlaris, P. Evans, G. Bright, New generation ultrahigh strength boron steel for automotive hot stamping technologies, Mater. Sci. Technol. 30 (2014) 818–826. https://doi.org/10.1179/1743284713Y.0000000409.

[47] D.W. Fan, R.B. Park, Y.R. Cho, B.C. De Cooman, Influence of isothermal deformation conditions on the mechanical properties of 22mnb5 hpf steel, Steel Res. Int. 81 (2010) 292–298. https://doi.org/10.1002/srin.201000008.

[48] C.W. Lee, W.S. Choi, L. Cho, Y.R. Cho, B.C. De Cooman, Liquid-Metal-Induced Embrittlement Related Microcrack Propagation on Zn-coated Press Hardening Steel, ISIJ Int. 55 (2015) 264–271. https://doi.org/10.2355/isijinternational.55.264.

[49] D.N. Hanlon, S.M.C. Van Bohemen, S. Celotto, Critical Assessment 10: Tensile elongation of strong automotive steels as function of testpiece geometry, Mater. Sci. Technol. (United Kingdom). 31 (2015) 385–388. https://doi.org/10.1179/1743284714Y.0000000707.

[50] J.R. Davis, Tensile Testing, 2nd Edition, ASM International, 2004. https://books.google.ca/books?id=5uRIb3emLY8C.

[51] M.H. Razmpoosh, A. Macwan, E. Biro, Y. Zhou, Effect of coating weight on fiber laser

welding of Galvanneal-coated 22MnB5 press hardening steel, Surf. Coatings Technol. 337 (2018) 536–543. https://doi.org/10.1016/j.surfcoat.2018.01.053.

[52] J. Jia, S.L. Yang, W.Y. Ni, J.Y. Bai, Microstructure and mechanical properties of fiber laser welded joints of ultrahigh-strength steel 22MnB5 and dual-phase steels, J. Mater. Res. 29 (2014) 2565–2575. https://doi.org/10.1557/jmr.2014.273.

[53] C. Allély, L. Dosdat, O. Clauzeau, K. Ogle, P. Volovitch, Anticorrosion mechanisms of aluminized steel for hot stamping, Surf. Coatings Technol. 238 (2014) 188–196. https://doi.org/10.1016/j.surfcoat.2013.10.072.

[54] M. Suehiro, K. Kusumi, T. Miyakoshi, J. Maki, M. Ohgami, Properties of aluminum-coated steels for hot-forming, Nippon Steel Tech. Rep. (2003) 16–21.

[55] F. Jenner, M.E. Walter, R. Mohan Iyengar, R. Hughes, Evolution of phases, microstructure, and surface roughness during heat treatment of aluminized low carbon steel, Metall. Mater. Trans. A Phys. Metall. Mater. Sci. 41 (2010) 1554–1563. https://doi.org/10.1007/s11661-009-0105-x.

[56] F. Borsetto, A. Ghiotti, S. Bruschi, Investigation of the high strength steel Al-Si coating during hot stamping operations, Key Eng. Mater. 410–411 (2009) 289–296. https://doi.org/10.4028/www.scientific.net/KEM.410-411.289.

[57] G. Zhong-Xiang, W. Kai, Z. Yi-Sheng, Z. Bin, Cracking and interfacial debonding of the Al-Si coating in hot stamping of pre-coated boron steel, Appl. Surf. Sci. 316 (2014) 595–603. https://doi.org/10.1016/j.apsusc.2014.08.043.

[58] L. Dosdat, J. Petitjean, T. Vietoris, O. Clauzeau, Corrosion resistance of different metallic coatings on press-hardened steels for automotive, Steel Res. Int. 82 (2011) 726–733. https://doi.org/10.1002/srin.201000291.

[59] P. Drillet, Coatings Dedicated to Press Hardened Steels for Automotive Applications, in:

Galvatech 2017 Conf. Proc., Tokyo, Japan, 2017: pp. 401–408.

[60] R.W. Richards, R.D. Jones, P.D. Clements, H. Clarke, Metallurgy of continuous hot dip aluminising, Int. Mater. Rev. 39 (1994) 191–212. https://doi.org/10.1179/imr.1994.39.5.191.

[61] R. Grigorieva, P. Drillet, J.M. Mataigne, A. Redjaïmia, Phase transformations in the Al-Si coating during the austenization step, Solid State Phenom. 172–174 (2011) 784–790. https://doi.org/10.4028/www.scientific.net/SSP.172-174.784.

[62] M. Windmann, A. Röttger, W. Theisen, Phase formation at the interface between a boron alloyed steel substrate and an Al-rich coating, Surf. Coatings Technol. 226 (2013) 130–139. https://doi.org/10.1016/j.surfcoat.2013.03.045.

[63] M. Windmann, A. Röttger, W. Theisen, Formation of intermetallic phases in Al-coated hot-stamped 22MnB5 sheets in terms of coating thickness and Si content, Surf. Coatings Technol. 246 (2014) 17–25. https://doi.org/10.1016/j.surfcoat.2014.02.056.

[64] W.K. Liang, W.J. Tao, B. Zhu, Y.S. Zhang, Influence of heating parameters on properties of the Al-Si coating applied to hot stamping, Sci. China Technol. Sci. 60 (2017) 1088–1102. https://doi.org/10.1007/s11431-016-0231-y.

[65] D.W. Fan, H.S. Kim, J.K. Oh, K.G. Chin, B.C. De Cooman, Coating degradation in hot press forming, ISIJ Int. 50 (2010) 561–568. https://doi.org/10.2355/isijinternational.50.561.

[66] K. Wang, Z. Gui, P. Liu, Y. Wang, Y. Zhang, Cracking behavior of Al-Si coating on hot stamping boron steel sheet, Procedia Eng. 81 (2014) 1713–1718. https://doi.org/10.1016/j.proeng.2014.10.218.

[67] K. Wang, Y. Jin, B. Zhu, Y. Zhang, Investigation on cracking characteristics of Al–Si coating on hot stamping boron steel parts based on surface strain analysis, Surf. Coatings

Technol. 309 (2017) 282–294. https://doi.org/10.1016/j.surfcoat.2016.11.046.

[68] J. Kondratiuk, P. Kuhn, Tribological investigation on friction and wear behaviour of coatings for hot sheet metal forming, Wear. 270 (2011) 839–849. https://doi.org/10.1016/j.wear.2011.02.011.

[69] K.R. Jo, L. Cho, D.H. Sulistiyo, E.J. Seo, S.W. Kim, B.C. De Cooman, Effects of Al-Si coating and Zn coating on the hydrogen uptake and embrittlement of ultra-high strength press-hardened steel, Surf. Coatings Technol. 374 (2019) 1108–1119. https://doi.org/10.1016/j.surfcoat.2019.06.047.

[70] V. Janik, Y. Lan, P. Beentjes, D. Norman, G. Hensen, S. Sridhar, Zn Diffusion and α-Fe(Zn) Layer Growth During Annealing of Zn-Coated B Steel, Metall. Mater. Trans. A Phys. Metall. Mater. Sci. 47 (2016) 400–411. https://doi.org/10.1007/s11661-015-3203-y.

[71] R. Autengruber, G. Luckeneder, S. Kolnberger, J. Faderl, A.W. Hassel, Surface and coating analysis of press-hardened hot-dip galvanized steel sheet, Steel Res. Int. 83 (2012) 1005–1011. https://doi.org/10.1002/srin.201200068.

[72] H. Järvinen, M. Honkanen, M. Patnamsetty, S. Järn, E. Heinonen, Press hardening of zinc-coated boron steels : Role of steel composition in the development of phase structures within coating and interface regions, Surf. Coat. Technol. 352 (2018) 378–391. https://doi.org/10.1016/j.surfcoat.2018.08.040.

[73] Y. Kim, J.R. McDermid, Microstructure and Phase Evolution of Galvanized Press Hardening Steel, in: Galvatech 2017 Conf. Proc., ISIJ International, Tokyo, Japan, 2017: pp. 501–505.

[74] J. Faderl, S. Kolnberger, M. Rosner, T. Kurz, Continuous Galvanizing Meets Press-Hardening, in: Galvatech 2011 Conf. Proc., Genova, Italy, 2011: pp. 2–9.

[75] C.W. Lee, D.W. Fan, S.J. Lee, I.R. Sohn, B.C. De Cooman, Galvanized Coating Evolution

During Hot Stamping, in: Galvatech 2011 Conf. Proc., Genova, Italy, 2011.

[76] Z. Ghanbari, J.G. Speer, K.O. Findley, Coating Evolution and Mechanical Behavior of Zn-Coated Press-Hardening Sheet Steel, 5th Int. Conf. Hot Sheet Met. Form. High-Performance Steel. (2015).

[77] J. Kondratiuk, P. Kuhn, E. Labrenz, C. Bischoff, Zinc coatings for hot sheet metal forming: Comparison of phase evolution and microstructure during heat treatment, Surf. Coatings Technol. 205 (2011) 4141–4153. https://doi.org/10.1016/j.surfcoat.2011.03.002.

[78] C. Dever, Effect of Coating Microstructure on the Electrochemical Properties of Continuous Galvanized Coatings on Press Hardened Steels, McMaster University, 2018.

[79] P. Pokorny, J. Kolisko, L. Balik, P. Novak, Description of structure of Fe-Zn intermetalic compounds present in hot-dip galvanized coatings on steel, Metalurgija. 54 (2015) 707–710.

[80] T.B. Massalski, Binary alloy phase diagrams, ASM Int. 3 (1992) 2874.

[81] C.W. Lee, W.S. Choi, Y.R. Cho, B.C. De Cooman, Surface oxide formation during rapid heating of Zn-coated press hardening steel, ISIJ Int. 54 (2014) 2364–2368. https://doi.org/10.2355/isijinternational.54.2364.

[82] M.G. Nicholas, C.F. Old, Liquid metal embrittlement, J. Mater. Sci. 14 (1979) 1–18.

[83] D.G. Kolman, A Review of Recent Advances in the Understanding of Liquid Metal Embrittlement, (2000).

[84] P. Gordon, H.H. An, The mechanisms of crack initiation and crack propagation in metal-induced embrittlement of metals, Metall. Trans. A. 13 (1982) 457–472. https://doi.org/10.1007/BF02643354.

[85] A.K. Huntington, Embrittlement of brass by mercury, J Inst Met. 11 (1914) 108–112.

[86] E. Heyn, Internal strains in cold-wrought metals, and some troubles caused thereby, J. Inst.

Met. 12 (1914) 1–37.

[87] H. Kang, L. Cho, C. Lee, B.C.D.E. Cooman, Zn Penetration in Liquid Metal Embrittled TWIP Steel, Metall. Mater. Trans. A. 47 (2016) 2885–2905. https://doi.org/10.1007/s11661-016-3475-x.

[88] B.C. De Cooman, W. Jung, K.R. Jo, D.H. Sulistiyo, L. Cho, Liquid metal embrittlement of advanced high strength steel, Galvatech 2017. (2017) 790–795.

[89] W. Rostoker, J.M. McCaughey, H. Markus, Embrittlement by Liquid Metals, Reinhold Publ. Corp., New York, 1960.

[90] N.S. Stoloff, T.L. Johnston, Crack propagation in a liquid metal environment, (1963).

[91] A.R.C. Westwood, M.H. Kamdar, Concerning liquid metal embrittlement , particularly of zinc monocrystals by mercury, Philos. Mag. (1963) 787–804. https://doi.org/10.1080/14786436308213836.

[92] W.M. Robertson, Propagation of a Crack Filled with Liquid Metal, North Am. Aviat. Sci. Cent. (1966).

[93] S.P. Lynch, Environmentally assisted cracking: Overview of evidence for an adsorption-induced localised-slip process, Acta Metall. 36 (1988) 2639–2661. https://doi.org/10.1016/0001-6160(88)90113-7.

[94] V. V. Popovich, Mechanisms of liquid-metal embrittlement, Fiz. Khimicheskaya Mekhanika Matertalov,. 15 (1979) 11–20. https://doi.org/10.1007/BF00729232.

[95] P.C. Hancock, M.B. Ives, The role of plastic deformation in liquid metal embrittlement, Can. Metall. Q. 10 (1971) 207–211. https://doi.org/10.1179/cmq.1971.10.3.207.

[96] M.A. Krishtal, The Formation of Dislocations in Metals on Diffusion of Surface-Active Substances in Connection with the Effect of Adsorption Embrittlement, Sov. Phys. Dokl. 15 (1970) 614.

[97] L. Klinger, E. Rabkin, Theory of the Kirkendall effect during grain boundary interdiffusion, Acta Mater. 59 (2011) 1389–1399. https://doi.org/10.1016/j.actamat.2010.10.070.

[98] L. Cho, H. Kang, C. Lee, B.C. De Cooman, Microstructure of liquid metal embrittlement cracks on Zn-coated 22MnB5 press-hardened steel, Scr. Mater. 90–91 (2014) 25–28. https://doi.org/10.1016/J.SCRIPTAMAT.2014.07.008.

[99] P. Drillet, R. Grigorieva, G. Leuillier, T. Vietoris, Study of Cracks Propagation Inside the Steel on Press Hardened Steel Zinc Based Coatings, in: Galvatech 2011, 2011: pp. 3–8.

[100] J. Li, H. Yang, S. Zhang, X. Liu, W. Hua, Study of Crack Generation and Propagation Mechanism Inside Zinc-coated Press-hardened Steel, in: Galvatech 2013 Conf. Proc., 2013: pp. 243–248.

[101] M.H. Razmpoosh, A. Macwan, E. Biro, D.L. Chen, Y. Peng, F. Goodwin, Y. Zhou, Liquid metal embrittlement in laser beam welding of Zn-coated 22MnB5 steel, Mater. Des. 155 (2018) 375–383. https://doi.org/10.1016/j.matdes.2018.05.065.

[102] D. Bhattacharya, Liquid metal embrittlement during resistance spot welding of Zn-coated high-strength steels, Mater. Sci. Technol. 0836 (2018) 1–21. https://doi.org/10.1080/02670836.2018.1461595.

[103] S.P. Lynch, Solid-metal-induced embrittlement of aluminium alloys and other materials, Mater. Sci. Eng. A. 108 (1989) 203–212. https://doi.org/10.1016/0921-5093(89)90421-8.

[104] J.C. Lynn, W.R. Warke, P. Gordon, Solid metal-induced embrittlement of steel, Mater. Sci. Eng. 18 (1975) 51–62. https://doi.org/10.1016/0025-5416(75)90072-5.

[105] K. Sadananda, A.K. Vasudevan, Review of environmentally assisted cracking, Metall. Mater. Trans. A Phys. Metall. Mater. Sci. 42 (2011) 279–295. https://doi.org/10.1007/s11661-010-0472-3.

[106] S.P. Lynch, Metal-induced embrittlement of materials, Mater. Charact. 28 (1992) 279–289. https://doi.org/10.1016/1044-5803(92)90017-C.

[107] K. Maleki, On the Origin of Micro-Cracking in Zn-Coated Press Hardened Steels, McMaster University, 2019.

[108] K. Maleki, J.R. McDermid, F.E. Goodwin, On the Origin of Microcracking in Zinc Coated Press Hardened Steels, in: Galvatech 2020, 2020.

[109] H. Peng, W. Peng, R. Lu, G. Wu, J. Zhang, Diffusion and cracking behavior involved in hot press forming of Zn coated 22MnB5, J. Alloys Compd. 806 (2019) 195–205. https://doi.org/10.1016/j.jallcom.2019.07.232.

[110] C.W. Lee, D.W. Fan, I.R. Sohn, S.J. Lee, B.C. De Cooman, Liquid-metal-induced embrittlement of Zn-coated hot stamping steel, Metall. Mater. Trans. A Phys. Metall. Mater. Sci. 43 (2012) 5122–5127. https://doi.org/10.1007/s11661-012-1316-0.

[111] M. Takahashi, M. Nakata, K. Imai, N. Kojima, N. Otsuka, Liquid Metal Embrittlement of Hot Stamped Galvannealed Boron Steel Sheet – Effect of Heating Time on Crack Formation –, ISIJ Int. 57 (2017) 1094–1101. https://doi.org/10.2355/isijinternational.ISIJINT-2016-730.

[112] J. Cui, G. Sun, J. Xu, X. Huang, G. Li, A method to evaluate the formability of high-strength steel in hot stamping, Mater. Des. 77 (2015) 95–109. https://doi.org/10.1016/j.matdes.2015.04.009.

[113] H. Järvinen, S. Järn, E. Lepikko, M. Järvenpää, P. Peura, ZnFe Coated 22MnB5 Steels in Direct Press Hardening: The Relationships between Coating Structure and Process Parameters, Key Eng. Mater. 674 (2016) 331–336. https://doi.org/10.4028/www.scientific.net/KEM.674.331.

[114] H.H. Seok, J.C. Mun, C. gil Kang, Micro-crack in zinc coating layer on boron steel sheet

in hot deep drawing process, Int. J. Precis. Eng. Manuf. 16 (2015) 919–927. https://doi.org/10.1007/s12541-015-0120-3.

[115] C. Dever, J. Kish, J. McDermid, Corrosion Properties of Hot Dip Zinc Galvanized Coatings on 22MnB5 Press Hardened Steels, in: Galvatech 2017 Conf. Proc., ISIJ International, Tokyo, Japan, 2017: pp. 385–392.

[116] T. Kurz, P. Larour, J. Lackner, T. Steck, G. Jesner, Press-hardening of zinc coated steel - Characterization of a new material for a new process, in: IOP Conf. Ser. Mater. Sci. Eng., 2016. https://doi.org/10.1088/1757-899X/159/1/012025.

[117] T. Kurz, H. Schwinghammer, G. Luckeneder, T. Manzenreiter, A. Sommer, Zinc coated press-hardening steel - challenges and solutions, 5th Int. Conf. Hot Sheet Met. Form. High-Performance Steel. (2015) 345–353. https://doi.org/10.4271/2015-01-0565.

[118] K. Isaksson, M. Jönsson, D. Berglund, The direct press hardening process for Zn-coated ultra-high strength steels, in: 2nd Int. Conf. Adv. High Strength Steel Press Hardening, Changsha, China, 2015: pp. 1–8.

[119] K. Hu, S. Zhou, R. Han, J. Gao, Y. Yang, Microstructure Evolution and Simulation in 22MnB5 Steel during Hot Stamping, J. Mater. Sci. Chem. Eng. 06 (2018) 9–14. https://doi.org/10.4236/msce.2018.68002.

[120] C.K. Chiuhuang, S.W. Wang, P.K. Lee, Investigation of the influence of forming parameters on the springback of hot-stamped hat-shaped parts, IOP Conf. Ser. Mater. Sci. Eng. 651 (2019) 0–7. https://doi.org/10.1088/1757-899X/651/1/012029.

[121] R. Autengruber, G. Luckeneder, A.W. Hassel, Corrosion of press-hardened galvanized steel, Corros. Sci. 63 (2012) 12–19. https://doi.org/10.1016/j.corsci.2012.04.048.

[122] R. Autengruber, G. Luckeneder, S. Kolnberger, J. Faderl, A.W. Hassel, Corrosion Behavior of Press-Hardened Hot-Dipped Galvanized Steel Sheet, in: Galvatech 2015 Conf.

Proc., Toronto, Canada, 2015: pp. 0–7.

[123] F. Zhu, D. Persson, D. Thierry, Formation of corrosion products an open and confined metal surfaces exposed to periodic wet/dry conditions - A comparison between zinc and electrogalvanized steel, Corrosion. 57 (2001) 582–590. https://doi.org/10.5006/1.3290385.

[124] C. Rémazeilles, P. Refait, On the formation of β-FeOOH (akaganéite) in chloride-containing environments, Corros. Sci. 49 (2007) 844–857. https://doi.org/10.1016/j.corsci.2006.06.003.

[125] R.A. Cottis, Interpretation of electrochemical noise data, Corrosion. 57 (2001) 265–285.

[126] F.H. Cao, Z. Zhang, J.X. Su, Y.Y. Shi, J.Q. Zhang, Electrochemical noise analysis of LY12-T3 in EXCO solution by discrete wavelet transform technique, Electrochim. Acta. 51 (2006) 1359–1364. https://doi.org/10.1016/j.electacta.2005.07.012.

CHAPTER 3 DEVELOPMENT OF A NEW GRADE OF ZN-COATED DIRECT PRESS-HARDENABLE STEEL

Chris Thomsen, Joseph McDermid – McMaster University, Hamilton, Ontario, Canada
Frank Goodwin – International Zinc Association

Authorship Contribution Statement

Chris Thomsen: Conceptualization, Investigation, Methodology, Formal analysis, Writing - original draft, Writing - review & editing.

Joseph McDermid: Conceptualization, Methodology, Formal analysis, Funding acquisition, Resources, Supervision, Writing - review & editing.

Frank Goodwin: Conceptualization, Funding provision.

DEVELOPMENT OF A NEW GRADE OF ZN-COATED DIRECT PRESS-HARDENABLE STEEL

Chris Thomsen, Joseph McDermid – McMaster University, Hamilton, Ontario, Canada

Frank Goodwin – International Zinc Association

ABSTRACT

Direct hot press forming (DHPF) of Zn-coated press hardening steels (PHS) presents significant challenges associated with avoiding liquid metal embrittlement (LME) while maintaining robust cathodic protection. In the present research, a prototype PHS which has an increased Mn content relative to the conventional 22MnB5 PHS was created to enable stamping below the Zn(Fe) (l) + Γ-Fe_3Zn_{10} peritectic temperature of 782 °C, thus potentially eliminating the liquid phase essential for LME. Experiments were performed over a range of austenization annealing times (30–180 s) at 900 °C and DHPF at temperatures of 600–700 °C. The new grade is exceptionally hardenable with a critical cooling rate of −10 °C/s, thus enabling DHPF below the peritectic temperature. The tensile strength of this steel met the target of 1500 MPa and total elongation at fracture of between 0.09–0.11. These properties were independent of DHPF temperature, indicating a large process window. In addition, the Zn coating met the target for robust cathodic protection of 15 vol% gamma phase. These experiments have demonstrated that it is possible to manufacture Zn-coated PHS with excellent properties and cathodic corrosion protection using the cost-effect DHPF process.

3.1 INTRODUCTION

Increasingly stringent fuel efficiency regulations placed on automotive manufacturers require designers to find solutions to lower the total weight of the body-in-white. One of the most efficient methods of accomplishing this goal is to reduce material cross-sections by using stronger materials. Press-hardened steels (PHS) are a particularly attractive option for vehicle mass reduction, as these steels offer an outstanding combination of high strength and formability at the direct hot press forming (DHPF) temperature while essentially eliminating spring-back.

PHSs must be galvanized or galvannealed in order to avoid decarburization during the austenization annealing prior to DHPF and to cathodically protect the final part from aqueous corrosion while in service. Currently, the dominant coating system for DHPF PHS is the Al-10%Si coating. However, after the DHPF process Al-Si coatings have been found to offer only barrier protection and not sacrificial cathodic protection [1,2]. Thus, a strong demand exists for Zn-based PHS coatings due to their barrier and sacrificial corrosion protection, good weldability, compatibility with paint systems and lower cost. However, problems associated with liquid-metal embrittlement (LME) during DHPF are well known and have constrained the use of Zn-coated PHS [3,4]. During austenization annealing at 850–950 °C, the as-received Zn coating transforms into a multiphase Zn-Fe coating consisting of zinc-ferrite (α-Fe(Zn)) containing 30 wt% Zn, in equilibrium with a liquid phase. Upon quenching, the coating undergoes the peritectic reaction at 782 °C whereby $\alpha\text{-Fe(Zn)} + \text{L} \rightarrow \alpha\text{-Fe(Zn)} + \Gamma\text{-Fe}_3\text{Zn}_{10}$. The presence of $\Gamma\text{-Fe}_3\text{Zn}_{10}$ in the DHPF coating microstructure has been found to provide significantly greater cathodic protection potential than coatings comprised solely of α-Fe(Zn) [5,6]. However, obtaining $\Gamma\text{-Fe}_3\text{Zn}_{10}$ in the final microstructure requires liquid to be present during the DHPF process, leading to conditions known to cause LME. Thus, the objectives of avoiding LME while achieving robust cathodic protection appear to be mutually exclusive.

One possible approach to alleviating this difficulty is to allow the steel to cool below the peritectic temperature before press forming [7]. This can be accomplished by using a dedicated pre-cooling step, or in the case of this study, an intentional increase in transfer time to the quenching die. Allowing the liquid zinc phase in the coating to solidify removes the conditions necessary for LME to occur. However, increasing the transfer time decreases the effective substrate cooling rate, necessitating the development of a grade of steel with hardenability superior to that of 22MnB5. Thus, the objective of this work is to develop a more hardenable PHS grade that can produce cathodically protective Zn-coated PHS with a minimum tensile strength of 1500 MPa using the direct hardening process.

3.2 EXPERIMENTAL METHOD

The chemical composition of the prototype grade is based on the composition of 22MnB5 and is shown in Table 3.1. The amount of Mn has been increased to 2.0 wt% in order to increase hardenability. The as-received cold-rolled steel had a thickness of 1.2 mm.

Table 3.1: Substrate compositions, transformation temperatures and critical cooling rates.

Substrate	C (wt%)	Mn (wt%)	Si (wt%)	B (ppm)	Ac_1 (°C)	Ac_3 (°C)	CCR (°C/s)
2.0% Mn	0.20	2.01	0.26	46	715	845	−10

Quench and deformation dilatometry were used to determine the critical temperatures – i.e. Ac_1, Ac_3, M_s, M_f – for the alloy and to develop a CCT diagram to determine the minimum cooling rates required to obtain a fully martensitic microstructure. All dilatometry experiments were conducted using a BÄHR DIL 805 dilatometer. The quench dilatometry samples comprised hollow cylinders taken from transfer bars and had dimensions of 4 mm OD × 3 mm ID × 10 mm. In order to determine the Ac_1 and Ac_3 temperature as a function of heating rate, samples were heated to 1000 °C at 5, 10 and 15 °C/s. Samples were then quenched to room temperature at −160 °C/s in order to determine the zero strain ($\varepsilon = 0$) M_f temperature. The assessed Ac_1 and Ac_3 temperatures are documented in Table 3.1. In order to determine the CCT diagram, a constant heating rate of 10 °C/s was used and the cooling rates varied from −1 to −75 °C/s. Samples were heated to a peak temperature of 865 °C (i.e. Ac_3 + 20 °C, Table 3.1) to ensure full austenization. The samples were held at 865 °C for 120 s before cooling at the targeted cooling rate.

Deformation dilatometry was carried out to determine the effect of deformation, if any, on the M_s and M_f temperatures. These experiments were performed using the same equipment as was used for as quench dilatometry. To avoid buckling under deformation, the deformation dilatometry samples were solid cylinders of dimensions 5 mm OD × 10 mm. The heating rates and peak annealing temperature for deformation dilatometry tests were the same as those used for CCT diagram construction. Following the peak temperature hold, the sample was cooled at −20 °C/s to the desired deformation temperatures, which were varied between 600–700 °C in 50 °C increments. Specimens were then strained at 1 s^{-1} to total strains of $\varepsilon = 0.10$–0.20 and quenched at −75 °C/s. The microstructures for all dilatometry samples were assessed using scanning electron microscopy (SEM) and microhardness measurements.

The McMaster Galvanizing Simulator, full details of which are available elsewhere [8], was used for galvanizing 120 mm × 200 mm panels of the experimental steel prior to austenization annealing and DHPF. Fig. 3.1 shows the thermal profile used for the galvanizing procedure. The panels were recrystallized at a peak annealing temperature (PAT) of 710 °C, resulting in a ferrite-pearlite microstructure. The panels were dipped in a 460 °C Fe saturated 0.20 wt % Al (dissolved) galvanizing bath for 4 s. Finally, the coated samples were cooled to room temperature at approximately −15 °C/s. The process atmosphere for all annealing treatments contained N_2-5 vol % H_2 and had at a dew point of −30 °C (i.e. $pO_2 = 2.71 \times 10^{-25}$ atm.).

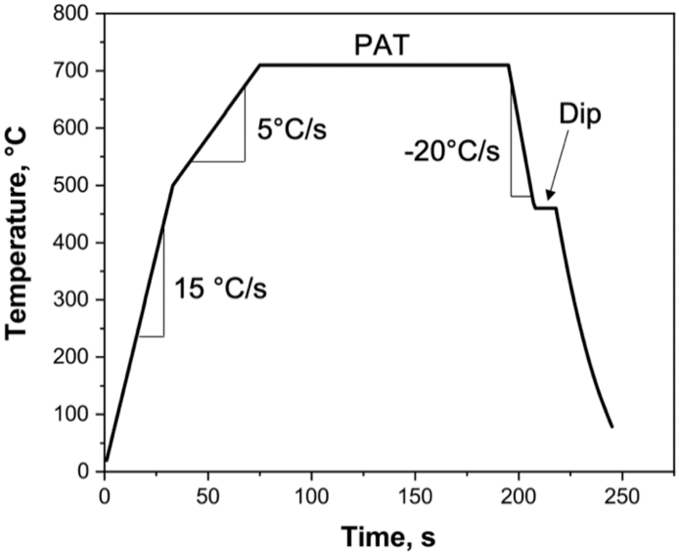

Fig. 3.1. Thermal profile used for coating in the McMaster galvanizing simulator.

Coated steel cross-sections were prepared for microstructural examination using standard metallographic methods. The microstructure of the substrate and the coating were analyzed by SEM, using a JEOL 6610-LV SEM. Secondary electron imaging (SEI) was used to acquire images using a working distance of 10 mm and an accelerating voltage of 10 keV. Immediately prior to sample insertion in the SEM, a thin layer of carbon was deposited on the sample surface to minimize charging.

Austenization of the Zn-coated steel blanks for press hardening trials utilized a conventional box furnace at 890℃ under ambient atmosphere. The thermal profile was characterised using a K-type thermocouple spot welded to the centre of a 110 × 110 mm panel excised from a coated sample. The cooling rate upon removal from the furnace was also recorded in the same manner. Heat/cooling tests were repeated six times in order to ensure reproducibility. Using water-cooled dies, panels were stamped into a “U-die” shape similar to the one described by Lee et al. [9]. Tensile coupons with a cross section of 3.2 mm ×1.2 mm and a gage length of 6.25 mm were used to determine mechanical properties of the DHPF steels. All tensile tests were performed on a 100 kN Instron tensile frame. Specimens were pulled at a crosshead speed of 1 mm/min and sample extension was measured using a contact extensometer.

X-ray diffraction (XRD) was used to quantitatively determine the phase make-up of the DHPF coatings as a function of austenization time and stamping temperature. A Bruker Mo Smart APEX2 diffractometer equipped with a Co Kα_1 source was used for all analyses. A slit size of 1 mm and a 1 mm collimator were used. Data were collected between $10° \leq 2\theta \leq 90°$. Analysis of diffraction data was completed in Diffrac Eva software along with TOPAS5. Error bars on the plots represent 95% confidence intervals of the mean value.

Galvanostatic polarization tests were performed with a Gamry Reference 600+ potentiostat. The electrolyte consisted of 100 g $ZnSO_4 \cdot 7H_2O$ and 200 g NaCl in 1000 mL of deionized water [10]. The tests were performed at room temperature and were naturally aerated. All samples were held for 600 s at open circuit potential (OCP) before starting the galvanostatic test to allow the sample to equilibrate with the solution. The current density used for all tests was 10 mA/cm^2.

3.3 RESULTS

The CCT diagram for the experimental steel, as determined using quench dilatometry, is shown in Fig. 3.2. Each coloured line represents a different cooling rate and at the end of each line is the average Vickers microhardness for that cooling rate. From Fig. 3.2, it can be clearly seen that, in order to generate fully martensitic microstructures, a critical (minimum) cooling rate of −10 °C/s is required. Cooling rates beyond this critical rate resulted in a slight increase in microhardness (Fig. 3.2). The effect of deformation on the martensite start (M_s) and finish (M_f) temperatures is shown in Fig. 3.3. Compared to undeformed (ε = 0) condition, both the M_s and M_f temperatures were significantly depressed, with no apparent effect of deformation strain or quenching temperature on either the deformation-induced M_s or M_f. In other words, straining the steel significantly reduced its hardenability. This result agrees with literature [11].

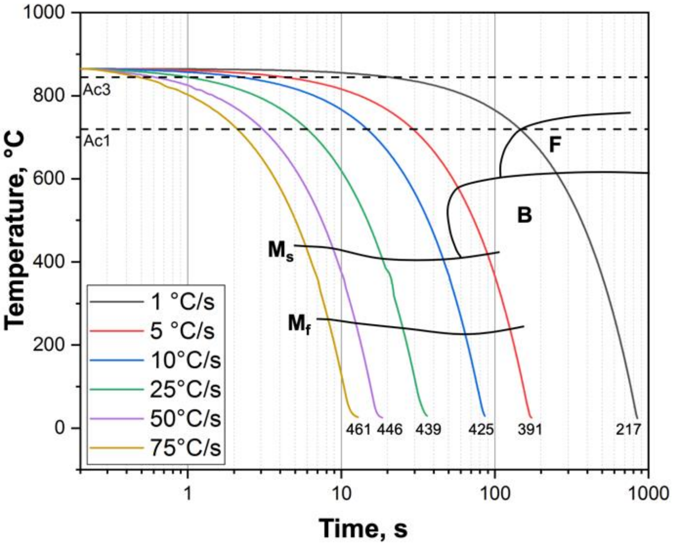

Fig. 3.2. CCT diagram with microhardness (HV) values at the end of each curve.

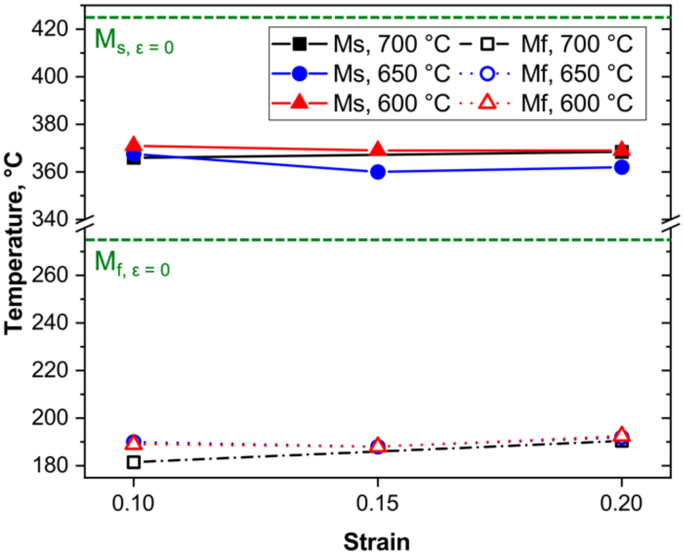

Fig. 3.3. Effect of applied strain on M_s and M_f.

Austenization heating as a function of time and cooling curves during transfer to the DHPF die are shown in Fig. 3.4 and Fig. 3.5, respectively. Experimental annealing times began when the panel reached 865 °C, approximately 160 s into the austenization heat treatment. For example, a 30 s annealing time corresponds to a total of 190 s in the furnace. After removing the panels from the furnace, they were allowed to cool in ambient air to the target DHPF temperature per the cooling curve shown in Fig. 3.5. From this figure, it was determined that the transfer times required for stamping at 700 °C, 650 °C and 600 °C were approximately 8 s, 11.5 s and 16 s, respectively. Upon reaching the target DHPF temperature, the samples were simultaneously formed and cooled at approximately −75 ℃/s, as shown in Fig. 3.5.

The substrate microstructures after U-die DHPF at 650℃ can be seen in Fig. 3.6. These microstructures are typical of all direct stamping temperatures. It can be seen that the microstructures of the samples annealed for 30 s and 60 s are not fully martensitic, but instead contained a mixture of ferrite and martensite. This is likely to have been due to the soaking time being insufficient for full austenization before quenching. It can also be seen that there was some microstructural banding in the 30 s and 60 s samples, indicative of some solute (Mn) segregation during substrate processing. However, the 120 s and 180 s austenization times were almost entirely martensitic, indicative of full austenization of the substrate prior to DHPF.

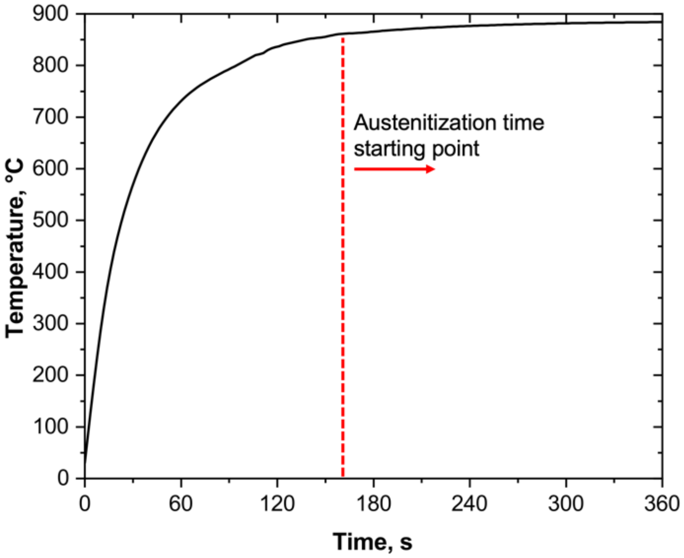

Fig. 3.4. Austenization anneal temperature versus time.

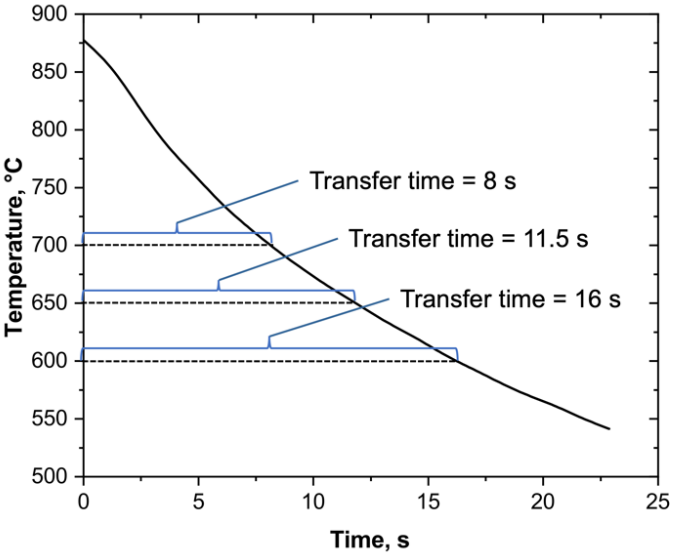

Fig. 3.5. Substrate cooling curves in ambient air upon removal from the annealing furnace

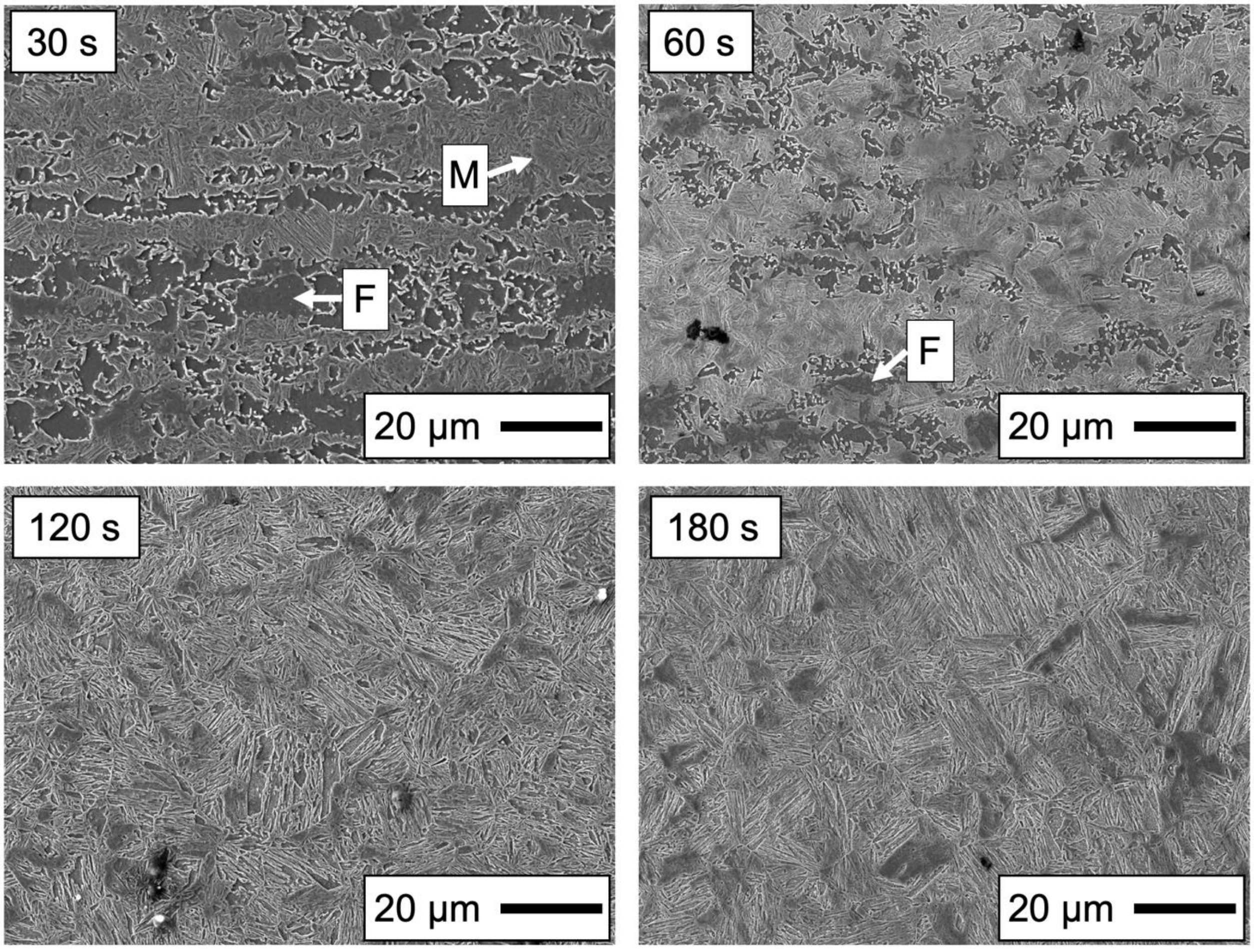

Fig. 3.6. Microstructures of DHPF specimens stamped at 650 °C as a function of annealing time (F = ferrite, M = martensite).

Fig. 3.7 summarizes the mechanical properties of the DHPF steels as a function of annealing time and stamping temperature. In each plot, the red data points show results from tensile coupons taken from the top of the U-die part, where there was very little forming strain (ε < 0.02) while black data points show results from the wall of the part, where there was slightly more forming strain (ε = 0.04–0.06). Each point on the plots represents data from four tensile tests (two coupons taken from two different panels). Examination of Fig. 3.7 will show that the mechanical properties from the wall samples are not significantly different from that from the top of the part. This indicates that the strain induced by forming does not significantly affect mechanical properties, at least for the strain levels and DHPF temperatures explored in this study.

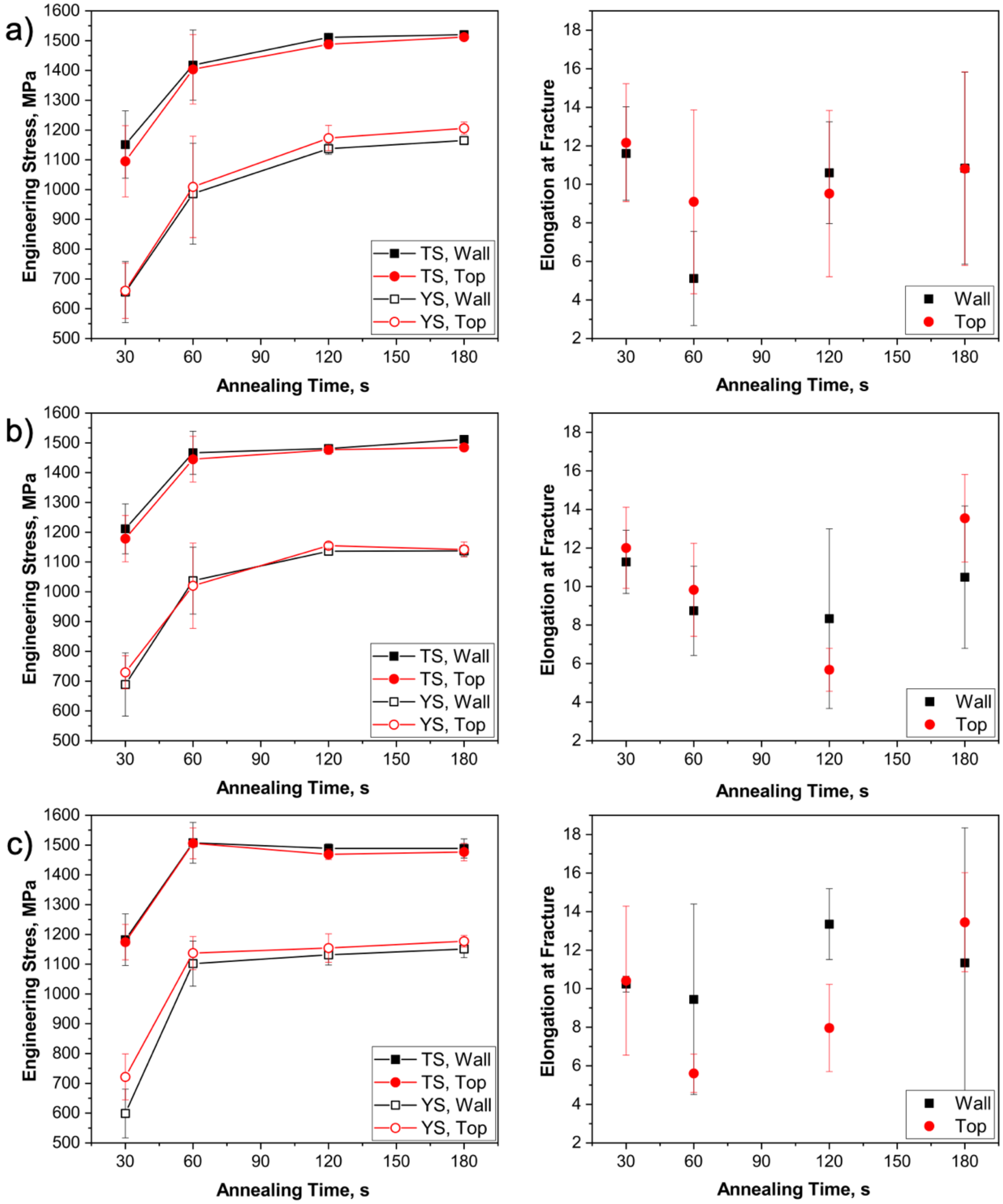

Fig. 3.7. Tensile strength (TS) and yield strength (YS) (left column) and total elongation at fracture (right column) of the DHPF at each stamping temperature. Rows a), b), and c) show results from stamping temperatures of 700 °C, 650 °C, and 600 °C.

The reduction of area for the DHPF tensile specimens is shown in Fig. 3.8. It can be seen that the reduction of area increased with austenization time and was roughly independent of stamping temperature, reaching a maximum of 0.25–0.30 after 120 s.

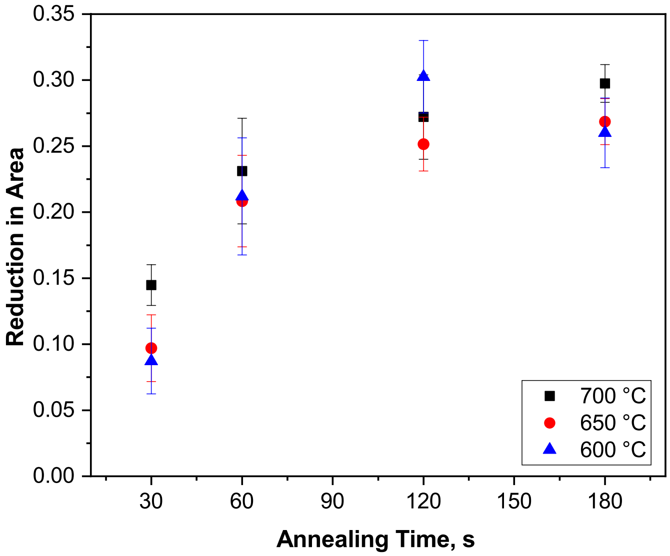

Fig. 3.8. Reduction of area for DHPF specimens after tensile testing.

Analysis of the coating microstructure *via* SEM, XRD and galvanostatic polarization testing showed that, for all tested DHPF conditions, the coating microstructural requirement for robust cathodic protection [6] was met. SEM showed qualitatively that significant fractions of Γ-Fe_3Zn_{10} (bright phase in Fig. 3.9) was present in all conditions. Increasing the annealing time lead to increased diffusional growth of the coating α-Fe(Zn) (light grey phase, Fig. 3.9), which caused an increase in average coating thickness from about 20 μm at 30 s to 30 μm at 180 s. It was also observed that there were no coating microcracks in samples taken from the top of the coating where there was an insignificant strain. At the corner of the U-die part, tensile strains tended 8to form large microcracks through the thickness of the coating along the α-Fe(Zn) grain boundaries. However, all through-thickness microcracks were arrested at the substrate with a blunt tip. This is in agreement with the observations by Lee et al. [9]. Qualitatively, XRD determined that the Γ-

Fe_3Zn_{10}/α-Fe(Zn) ratio decreased as annealing time was increased as shown in Fig. 3.10, where the squares, circles, and triangles represent data from panels which were stamped at 700 °C, 650 °C, and 600 °C, respectively. Clearly, the amount of the Γ-Fe_3Zn_{10} decreased with increasing annealing time at the expense of more α-Fe(Zn) being formed. Even at the longest annealing time of 180 s, the amount of Γ-Fe_3Zn_{10} exceeds the target of 15 vol % for robust corrosion protection. Also, it can be seen that the coating composition was relatively insensitive to the DHPF temperature, indicating that the austenization time was the most significant determinant of the coating microstructure.

Preliminary results for galvanostatic polarization tests (Fig. 3.11) indicate that for the 30 s and 180 s annealing times, similar galvanostatic responses are observed. The first plateau at approximately –0.800 V represents the dissolution of the Γ-Fe_3Zn_{10} phase. The dissolution of Γ-Fe_3Zn_{10} lasts for much longer in the 30 s than in the 180 s sample because of the former having significantly more Γ-Fe_3Zn_{10} present in the coating microstructure (Fig. 3.9, Fig. 3.10). Due to the significant phase mixing which is evident in Fig. 3.9, the dissolution potential is not constant. Instead, it increases gradually towards the potential for α-Fe(Zn), at approximately −0.670 V. Again, the effect of the Γ-Fe_3Zn_{10}/α-Fe(Zn) ratio is demonstrated: the specimen annealed for 180 s has a much longer dissolution time for α-Fe(Zn), consistent with more α-Fe(Zn) being present in the coating microstructure (Fig. 3.9, Fig. 3.10). For both samples the potential gradually increased in the α-Fe(Zn) dissolution region. This has been attributed to a compositional gradient existing in the coating where the Zn content is lower closer to the α-Fe(Zn)/steel interface. Finally, the dissolution of the bare steel is reached at approximately –0.530 V. Here, the dissolution potential is constant as no significant compositional gradients exists within the substrate. It is important to note that the coating is much thicker after the 180 s anneal versus the 30 s of annealing time.

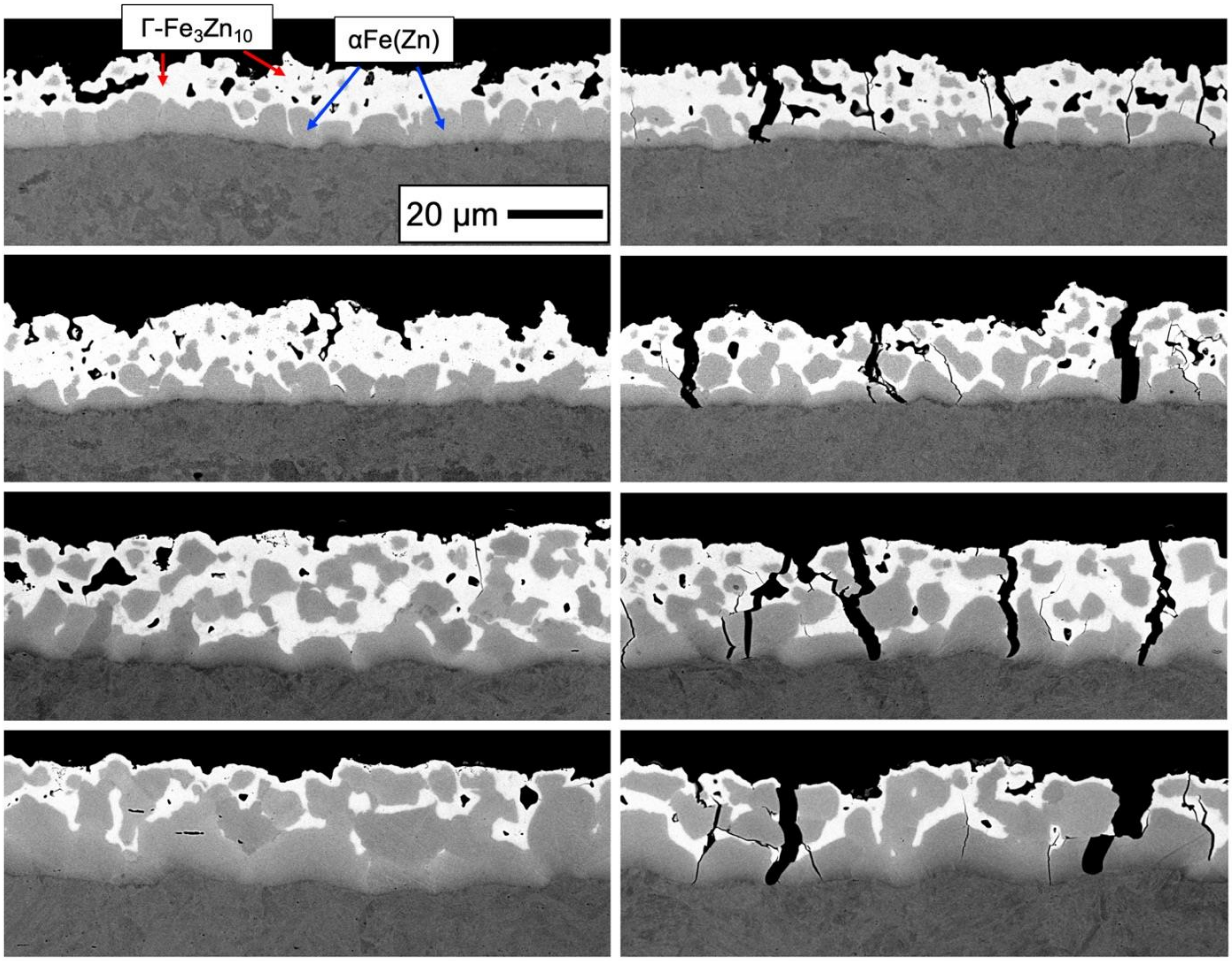

Fig. 3.9. Cross-sectional coating microstructures from steel stamped at 700 °C after each austenizing time. From top to bottom: 30 s, 60 s, 120 s, 180 s. The left and right column show images from the top and corner of the U-die part.

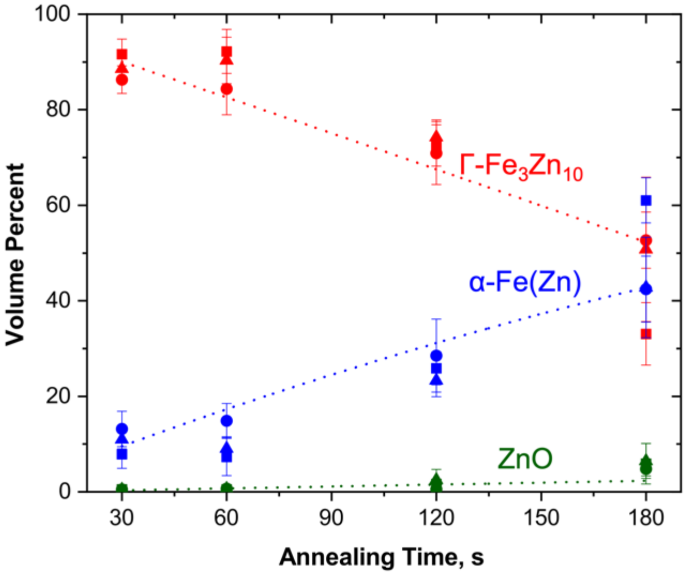

Fig. 3.10. XRD results showing the microstructural evolution of the coating.

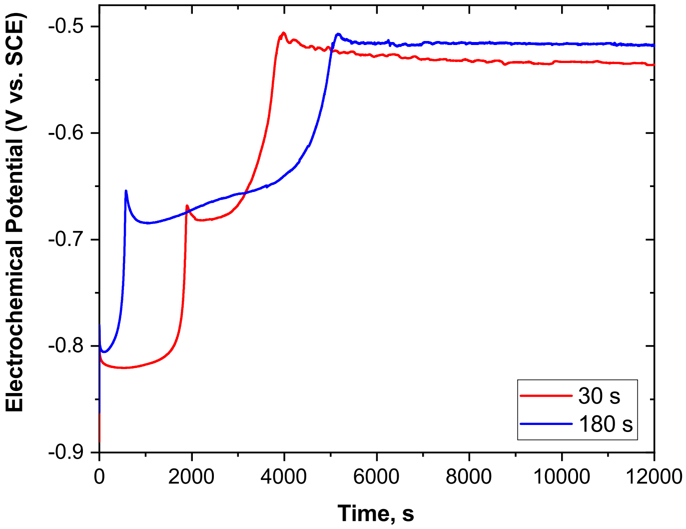

Fig. 3.11. Galvanostatic scans at 10 mA/cm^2.

3.4 DISCUSSION

This study builds on the work by Dever et al. [6], where the target of 15 vol % Γ-Fe_3Zn_{10} phase was proposed for the provision of robust cathodic corrosion protection for Zn-coated DHPF steels.

In that work, it was found that when using conventional Zn-coated 22MnB5 steel and DHPF methods, the process window for manufacturing Zn-coated PHS with robust cathodic corrosion protection while avoiding LME is prohibitively narrow. To expand the process window, the steel in this study was created with increased Mn content in order to improve on the hardenability of 22MnB5. The present study shows that this new grade is compatible with the microstructural targets for robust cathodic protection set by Dever et al. [6].

Results from quench dilatometry (Fig. 3.2) show that the critical cooling rate for the 2.0% Mn alloy is about −10 °C/s. This is a significant hardenability improvement over 22MnB5, for which a critical cooling rate of −25 to −40 °C/s is typically quoted in the literature [3,12]. This substantial improvement in hardenability enables the attainment of fully martensitic microstructures when quenching and forming below the peritectic temperature of 782 °C. Deformation dilatometry showed that compressing the part to strain levels of 0.1–0.2 at the DHPF temperatures of 600–700 °C caused a decrease in the M_s and M_f temperatures, indicating a loss in hardenability compared to undeformed specimens (Fig. 3.3). However, this suppression of the M_s and M_f temperatures did not adversely impact DHPF processing conducted in the present investigation.

The mechanical properties of the prototype PHS have been shown to match or slightly exceed the conventional 22MnB5 alloy. The tensile strength of the as-stamped specimens with fully martensitic microstructures was 1500 MPa and the yield strength was about 1100 MPa (Fig. 3.7), regardless of the stamping temperature. Elongation at fracture was usually approximately around 0.1, provided that the specimens did not fracture early. The measured reduction of area was about 0.25 (Fig. 3.8), indicative of significant plastic deformation before fracture. To offset the increase in strength by solid solution strengthening imparted by the increase in Mn content and to keep tensile strength levels around 1500 MPa, the level of C was lowered to 0.20 wt%, which is lower than is what is typically found in 22MnB5 grades. Therefore, there is room for strength levels to be enhanced towards 2000 MPa through the addition of more C.

Microstructural examination of the DHPF coatings demonstrated that the amount of Γ-Fe_3Zn_{10} phase decreased and the fraction of α-Fe(Zn) increased with increasing annealing time (Fig. 3.9 and Fig. 3.10) but were not a function of DHPF stamping temperature. In areas of the part where there was a high amount of strain, cracks were observed through the thickness of the coating. These cracks were all arrested at the substrate with a blunt tip. Galvanostatic testing (Fig. 3.11) showed three distinct dissolution potentials for the steels austenized at 30 s and 180 s. This demonstrates that there is still sufficient Γ-Fe_3Zn_{10} present in the coating after austenizing 180 s to provide a substantial driving force for cathodic protection of the DHPF alloy.

3.5 CONCLUSIONS

A prototype Zn-coated DHPF steel grade was studied with the objective of determining its suitability for achieving a tensile strength of 1500 MPa or greater while maintaining a dual phase Γ-Fe_3Zn_{10} + α-Fe(Zn) coating with robust cathodic protection potential. The conclusions from this study are:

- Dilatometry experiments showed that the new PHS grade containing 2.0% Mn exhibits significantly improved hardenability over 22MnB5, with a critical cooling rate of −10 °C/s.
- The mechanical properties of the prototype alloy matched those of the conventional 22MnB5 PHS. In fully martensitic specimens, tensile strength and yield strength were determined to be approximately 1500 MPa and 1100 MPa, respectively. Uniform elongation was on average 0.5–0.6 and significant post-uniform elongation (0.09–0.11) was observed.

- The mechanical properties were independent of the stamping temperatures tested, meaning that there is a stamping temperature process window of at least 100 °C.
- SEM and XRD results confirmed that, for all tested conditions, the coating meets the requirement of 15 vol% gamma phase for robust cathodic corrosion protection.

ACKNOWLEDGEMENTS

The authors would like to extend their gratitude the International Zinc Association – Galvanized Autobody Partnership (IZA-GAP) and the Natural Sciences and Engineering Research Council of Canada (NSERC, grant CRDPJ 522309 – 17) for their financial support. The authors would also like to thank U.S. Steel Corporation for the provision of the steel used in this study.

REFERENCES

[1] D.W. Fan, B.C. De Cooman, State-of-the-knowledge on coating systems for hot stamped parts, Steel Res. Int. 83 (2012) 412–433. https://doi.org/10.1002/srin.201100292.

[2] C. Allély, L. Dosdat, O. Clauzeau, K. Ogle, P. Volovitch, Anticorrosion mechanisms of aluminized steel for hot stamping, Surf. Coatings Technol. 238 (2014) 188–196. https://doi.org/10.1016/j.surfcoat.2013.10.072.

[3] T. Taylor, A. Clough, Critical review of automotive hot-stamped sheet steel from an industrial perspective, Mater. Sci. Technol. 0836 (2018) 1–53. https://doi.org/10.1080/02670836.2018.1425239.

[4] L. Cho, H. Kang, C. Lee, B.C. De Cooman, Microstructure of liquid metal embrittlement cracks on Zn-coated 22MnB5 press-hardened steel, Scr. Mater. 90–91 (2014) 25–28. https://doi.org/10.1016/J.SCRIPTAMAT.2014.07.008.

[5] R. Autengruber, G. Luckeneder, S. Kolnberger, J. Faderl, A.W. Hassel, Surface and coating analysis of press-hardened hot-dip galvanized steel sheet, Steel Res. Int. 83 (2012) 1005–1011. https://doi.org/10.1002/srin.201200068.

[6] C. Dever, J. Kish, J. McDermid, Corrosion Properties of Hot Dip Zinc Galvanized Coatings on 22MnB5 Press Hardened Steels, in: Galvatech 2017 Conf. Proc., ISIJ International, Tokyo, Japan, 2017: pp. 385–392.

[7] T. Kurz, P. Larour, J. Lackner, T. Steck, G. Jesner, Press-hardening of zinc coated steel - Characterization of a new material for a new process, in: IOP Conf. Ser. Mater. Sci. Eng., 2016. https://doi.org/10.1088/1757-899X/159/1/012025.

[8] E.M. Bellhouse, J.R. McDermid, Selective oxidation and reactive wetting during hot-dip galvanizing of a 1.0 pct Al-0.5 pct Si TRIP-assisted steel, Metall. Mater. Trans. A Phys. Metall. Mater. Sci. 43 (2012) 2426–2441. https://doi.org/10.1007/s11661-011-0983-6.

[9] C.W. Lee, W.S. Choi, L. Cho, Y.R. Cho, B.C. De Cooman, Liquid-Metal-Induced Embrittlement Related Microcrack Propagation on Zn-coated Press Hardening Steel, ISIJ Int. 55 (2015) 264–271. https://doi.org/10.2355/isijinternational.55.264.

[10] R. Autengruber, G. Luckeneder, A.W. Hassel, Corrosion of press-hardened galvanized steel, Corros. Sci. 63 (2012) 12–19. https://doi.org/10.1016/j.corsci.2012.04.048.

[11] M. Nikravesh, M. Naderi, G.H. Akbari, Influence of hot plastic deformation and cooling rate on martensite and bainite start temperatures in 22MnB5 steel, Mater. Sci. Eng. A. 540 (2012) 24–29. https://doi.org/10.1016/j.msea.2012.01.018.

[12] H. Mohrbacher, Martensitic Automotive Steel Sheet - Fundamentals and Metallurgical Optimization Strategies, Adv. Mater. Res. 1063 (2015) 130–142. https://doi.org/10.4028/www.scientific.net/amr.1063.130.

CHAPTER 4 DEVELOPMENT OF A 0.2C-2.0MN-0.26SI-0.005B ZN-COATED DIRECT PRESS-HARDENABLE STEEL

CHRIS THOMSEN[a] AND JOSEPH R. MCDERMID[a]

[a] Centre for Automotive Materials and Corrosion, McMaster University, 1280 Main Street West, Hamilton, ON L8S 4L7, Canada

Corresponding author’s email: mcdermid@mcmaster.ca

Authorship Contribution Statement

Chris Thomsen: Conceptualization, Investigation, Methodology, Formal analysis, Writing - original draft, Writing - review & editing.

Joseph McDermid: Conceptualization, Methodology, Formal analysis, Funding acquisition, Resources, Supervision, Writing - review & editing.

This draft manuscript has been prepared for submission in Materials Science and Engineering: A.

DEVELOPMENT OF A 0.2C-2.0MN-0.26SI-0.005B ZN-COATED DIRECT PRESS-HARDENABLE STEEL

CHRIS THOMSEN[a] AND JOSEPH R. MCDERMID[a]

[a] Centre for Automotive Materials and Corrosion, McMaster University, 1280 Main Street West, Hamilton, ON L8S 4L7, Canada

Corresponding author's email: mcdermid@mcmaster.ca

ABSTRACT

Direct press hardening, also known as direct hot press forming (DHPF), of Zn-coated steels remains challenging to implement due to the catastrophic loss of ductility associated with liquid metal embrittlement (LME) and the challenges associated with maintaining the desired robust cathodic corrosion protection associated with Zn-based metallic coatings. In the present research, a new grade of steel (0.20C-2.01Mn-0.26Si-0.005B) with superior hardenability relative to the conventional 22MnB5 substrate was created to enable stamping and quenching between 600 °C–700 °C, such that any $Zn(Fe)_{liq}$ in the coating was solidified before forming, thereby avoiding LME while attaining a fully martensitic microstructures. Dilatometry tests determined that the new 2Mn PHS has a critical cooling rate of approximately −10 °C/s to achieve a fully martensitic microstructure. DHPF experiments were performed over a range of austenization times (30 s–180 s) at 890 ℃ and stamping temperatures (600 °C–700 °C). It was found that samples austenized for 120 s or 180 s attained the desired fully martensitic microstructures after DHPF, regardless of the stamping temperature. The fully martensitic samples exhibited excellent mechanical properties, i.e. yield and tensile strengths of approximately 1125 MPa and 1500 MPa, respectively, with an average uniform elongation of 0.05 and an additional 0.04–0.05 of post-uniform elongation. LME

was not observed for any of the DHPF parameters employed, nor did any coating microcracks penetrate into the substrate. The DHPF coating met the target of ≥ 15 vol% Γ-Fe_3Zn_{10} for all tested DHPF conditions and, therefore, it is expected that the coating will offer excellent cathodic corrosion protection. In summary, it was determined that by using the prototype Zn-coated 0.20C-2.01Mn-0.26Si-0.005B steel with 120 s–180 s of austenization time and stamping temperatures between 600 °C–700 °C, it is possible to obtain tensile strengths ≥ 1500 MPa with a coating microstructure that offers robust cathodic corrosion protection.

4.1 INTRODUCTION

In response to ever-increasing demands placed on automotive materials to decrease the weight of the body-in-white while maintaining or improving passenger safety, the steel industry has spent significant resources on research and development of high strength steels [1–3]. One particular manufacturing method that has received much research attention and commercial implementation over recent years is press-hardening, for which the direct hot press forming (DHPF) is the favoured process due to its relative simplicity and low cost [2,4,5]. DHPF refers to a process where a steel blank is austenized in a furnace heated to 850 °C–950 °C and is then rapidly transferred to water-cooled dies that simultaneously form and quench the blank to form a fully martensitic microstructure. With the industry-standard 22MnB5 DHPF grade, tensile strengths (TS) of approximately 1500 MPa are expected, though modifications to the chemistry of these steels have resulted in TS approaching 2000 MPa [6–8]. The benefits of the DHPF process versus its alternatives are significant [2,4]. Due to its austenitic microstructure and the high temperatures of the blank during forming, the substrate formability is significantly enhanced versus the equivalent cold forming capability. Additionally, springback is essentially eliminated, improving dimensional accuracy. Due to the rapid cooling rates made possible by the water-cooled dies, fully martensitic microstructures are routinely achieved in the final part. For these reasons, DHPF is often used to manufacture complex parts with high geometrical accuracy and extremely high TS.

Inevitably, throughout the DHPF process, parts will be exposed to ambient air at high temperatures, leading to some substrate oxidation and decarburization. For acceptable paintability and surface appearance, it is necessary to remove the scale by shot-blasting, pickling, or other techniques which come at a significant increase in cost. In service, resistance to corrosion is also of great importance for automotive applications. For these reasons, it is necessary to protect the substrate from the environment. A variety of metallic coatings have been tested on PHS with varying success. The current coating standard for DHPF PHS is an Al-(7–11 wt%)Si coating with some minor alloying additions [9,10]. When put into service following DHPF processing, this coating provides acceptable barrier corrosion protection but does not provide the desired sacrificial cathodic protection associated with the widely used Zn-based metallic coatings [11–13]. Furthermore, the intermetallic phases formed in the Al-Si coatings as a result of the DHPF austenization step are extremely brittle and prone to microcracking during forming [9,14–16]. The inability of the Al-Si coating to offer sacrificial corrosion protection along with its forming limitations have provided a significant driving force for consideration of alternative coating systems, including Zn-based coatings [2,9].

Zn-based coatings are extensively used on sheet steels in automotive applications and are well known to offer outstanding cathodic corrosion protection, good weldability and paintability [9]. However, Zn-based coatings – in this case conventional galvanized (GI) and galvannealed (GA) – have found limited application in DHPF PHS. The fundamental cause of this DHPF incompatibility arises from the relatively low melting temperature of Zn (420 °C) and any Fe-Zn intermetallic phases that form during annealing of the Zn-based coating are well below typical

DPHF temperatures of 850–950 °C [17]. In particular, the peritectic reaction at 782 °C [17] results in the equilibrium Γ-Fe_3Zn_{10} coating intermetallic decomposing according to:

$$\Gamma\text{-}\mathrm{Fe_3Zn_{10}} \rightarrow \alpha\text{-}\mathrm{Fe(Zn)} + \mathrm{Zn(Fe)_{liq}} \qquad (4.1)$$

where α-Fe(Zn) is a solid solution Zn-enriched ferrite and $Zn(Fe)_{liq}$ is a Fe-enriched Zn liquid phase. The presence of liquid Zn(Fe) on the surface of the steel whilst it is subjected to a significant tensile strain (such as during DHPF) can lead to liquid metal embrittlement (LME) [2,18,19]. Thus, it is imperative that there be no Zn-based liquids present during the high temperature forming step in order to avoid catastrophic failure of the part.

There have been many studies on the evolution of the galvanized coating microstructure during austenization [20–27]. In the austenization furnace under ambient atmosphere, high temperatures and the diffusion-driven enrichment of the coating with Fe result in dramatic changes to the coating microstructure [20–26]. The final coating microstructure will depend on the heating rate, austenization time and temperature, and initial coating thickness [4,21]. As the substrate is heating to the austenization temperature (usually at an average rate of 10–12 °C/s [2]) a series of Zn-based intermetallic phases are formed [17,23], and it has been found that prior to passing through the peritectic reaction, the coating consists entirely of Γ-Fe_3Zn_{10} [21,22]. Meanwhile, an oxide layer is formed at the surface of the coating, typically consisting of ZnO and Al_2O_3 [23,26,28]. These two oxides prevent evaporation of Zn from the coating [20,26,28]. When the temperature rises above 782 °C, the Γ-Fe_3Zn_{10} coating transforms via the peritectic reaction in equation 4.1 such that α-Fe(Zn) and $Zn(Fe)_{liq}$ are formed. As austenization continues at 850 °C–950 °C, the coating grows thicker by solid state diffusion and it becomes continuously enriched with Fe, leading to an increase in the fraction of α-Fe(Zn) and a commensurate decrease in the fraction of $Zn(Fe)_{liq}$ [20,21,23]. When the blank is transferred to the water-cooled dies and quenched, the $Zn(Fe)_{liq}$ solidifies to Γ-Fe_3Zn_{10}. Thus, the amount of Γ-Fe_3Zn_{10} in the final microstructure is directly related to the amount of $Zn(Fe)_{liq}$ before quenching. Control of the microstructure of the coating is critical, as it has been found to have a determining effect on the capacity of the coating to provide sacrificial cathodic corrosion resistance to the steel [21,29,30], with a minimum of 15 vol% Γ-Fe_3Zn_{10} phase in the final coating being required for the provision of robust cathodic corrosion protection [21]. Considering a GI70 coating annealed at 900 °C before quenching, the fraction of Γ-Fe_3Zn_{10} decreased to below 15 vol% after 210 s of austenization, and after 240 s, the fraction of Γ-Fe_3Zn_{10} was negligible [21].

It is clear that in order to obtain robust cathodic protection, the liquid Zn(Fe) phase must be present in the coating before being quenched through the peritectic temperature to form Γ-Fe_3Zn_{10}. This presents a significant challenge where the objectives of attaining robust cathodic corrosion protection while avoiding LME are ostensibly in fundamental conflict. One approach to satisfying both of these objectives is to solidify any residual coating liquid before forming occurs [31–33], thus removing a necessary condition for LME. Whether this task is performed using a dedicated pre-cooling step or an increase in transfer time, there is a corresponding decrease in the effective cooling rate, meaning that the standard 22MnB5 grade (0.22C–1.23Mn–0.23Si–0.003B (wt%)) does not have sufficient hardenability to produce fully martensitic microstructures and meet target properties while avoiding LME.

The objective of the present study is to define a process window in which a prototype 0.20C-2.01Mn-0.26Si-0.005B (wt%) galvanized press-hardening steel grade may be produced using the direct press-hardening method, such that it has a fully martensitic microstructure with TS ≥ 1500 MPa and with ≥ 15 vol% Γ-Fe_3Zn_{10} in the coating microstructure for the provision of robust cathodic protection while avoiding liquid metal embrittlement. The prototype grade will be assessed in the context of meeting these targets by determining the microstructural evolution of the substrate and the coating, the development of mechanical properties and fracture modes, and the corrosion protection potential as a function of austenization time and direct hot press forming temperature.

4.2 MATERIALS AND METHODS

The substrate material examined in this study was a novel grade similar to typical PHS grades but with additional Mn to increase hardenability such that DHPF could be carried out at temperatures below the Fe-Zn peritectic temperature of 782 °C, thus avoiding the presence of liquid in the coating and allowing for the presence of the significant volume fractions of Γ-Fe_3Zn_{10} in the coating microstructure, known to promote robust cathodic protection in the final part. The chemical composition of the prototype PHS is listed in Table 4.1. The substrate was fabricated at United States Steel Research via vacuum melting, hot rolling and cold rolling to a final thickness of 1.2 mm. A thermomechanical processing summary for the prototype alloy is provided in Fig. 4.1.

Table 4.1. Chemical composition of the alloy (wt%).

C	Mn	Si	B	P	Al
0.20	2.01	0.26	0.005	0.01	0.04

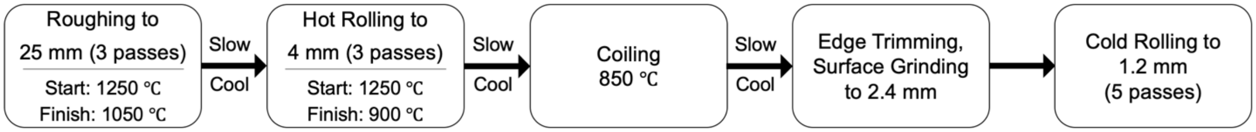

Fig. 4.1. Thermomechanical processing route for the production of the prototype PHS steel.

4.2.1 Dilatometry

Phase transformation temperatures and the continuous cooling transformation (CCT) diagram for the prototype PHS alloy were determined by quench dilatometry, along with limited use of deformation dilatometry, using a BÄHR DIL 805 dilatometer. Quench dilatometry samples consisted of hollow cylinders with dimensions of 3 mm ID × 4 mm OD × 10 mm. It was first determined that the Ac_1 and Ac_3 temperatures for the prototype steel were approximately 710 °C and 845 °C, respectively, where the Ac_1 and Ac_3 temperatures were found to be insensitive to the heating rates of between 5–15 °C/s typical of DHPF operations. In order to construct a continuous cooling transformation (CCT) diagram for the prototype alloy to determine the minimum cooling rate required to produce the target fully martensitic structure for the prototype PHS, quench dilatometry samples were heated at 10 °C/s to a peak temperature of 865 °C (i.e. Ac_3 + 20 °C), held for 120 s and then cooled at rates between −1 and −75 °C/s. The CCT diagram was then constructed using the dilatometry data, an examination of the substrate microstructures and microhardness values. In all cases, microhardness measurements were performed using a Clemex CMT.HD 1000 gf load and dwell time of 10 s.

Deformation dilatometry was conducted to determine the effect, if any, of deformation strain during the DHPF process on the martensite start (M_s) and finish (M_f) temperatures. In this case, samples consisted of solid cylinders of 5 mm OD × 10 mm. The heating rate, peak annealing temperature and soak time were the same as were used for CCT diagram construction. After a 120 s dwell time at the peak annealing temperature, samples were cooled to the desired deformation temperature at −20 °C/s and were compressed at a strain rate of 1 s^{-1} to true strains of $\varepsilon = 0.10$, 0.15, and 0.20 followed by quenching at −75 °C/s through the M_f temperature.

4.2.2 Galvanizing

The experimental steel was galvanized using the McMaster Galvanizing Simulator, details of which are provided elsewhere [34]. Prior to undergoing the galvanizing treatment, panels of dimensions 120 mm × 200 mm were degreased and cleaned using a nylon brush and a 2 % NaOH solution at 80 °C, rinsed in warm water, followed by a final rinse in isopropanol and drying using a warm air stream. As seen in Fig. 4.2, the panels were heated to a peak annealing temperature (PAT) of 710 °C (i.e. just below the Ac_1 temperature) and isothermally held for 120 s in order to produce a microstructure consisting of recrystallized ferrite and pearlite. The panel was then cooled to 460 °C and dipped in a Fe saturated 0.20 wt% Al (dissolved) [35] 460 °C galvanizing bath for 4 s. Finally, the coated panels were cooled to room temperature at approximately −15 °C/s using flowing N_2. The coating thickness was measured by X-ray fluorescence and was determined to be an average of 9.3 μm, corresponding to an average coating weight of 66 g/m^2/side.

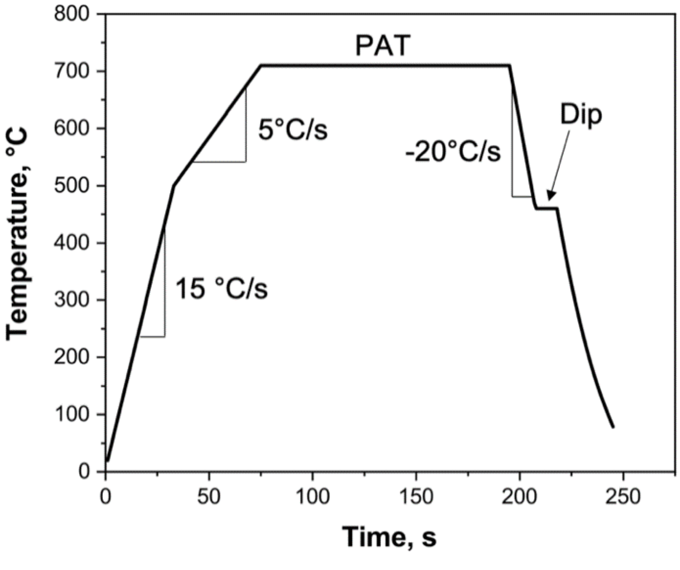

Fig. 4.2. Galvanizing heat treatment schematic.

4.2.3 Direct Hot-Press Forming

Square blanks of dimensions 100 mm × 100 mm were cut from the uniform coating region of the galvanized panel [34] for DHPF tests. Austenization of the blanks was executed in a conventional box furnace in ambient atmosphere at 890 °C. A K-type thermocouple spot-welded to the centre of a blank was used to determine the blank heating curves (Fig. 4.3), and the cooling rate in ambient atmosphere upon blank removal from the box furnace (Fig. 4.4). To ensure heating/cooling profile reproducibility, heating/cooling curve calibration experiments were repeated six times. The experimental austenization time was defined as starting once the panel reached 865 ℃ - i.e. Ac_3 + 20 °C. From Fig. 4.3, this occurred 160 s after the panel was inserted into the furnace. Thus, the reported experimental austenization times of 30, 60, 120, and 180 s correspond to the panels being in the furnace for a total of 190, 220, 280, and 340 s, respectively. DHPF was carried out at 700 ℃, 650 ℃ and 600 ℃ by varying the transfer time from the box furnace to the quenching dies. Using the cooling curves in Fig. 4.4, it was determined that the transfer times required to stamp at 700, 650, and 600 °C were 8, 11.5, and 16 s, respectively. A 100 kN Instron tensile frame equipped with water cooled dies was used to form the U-die DHPF part, the dimensions of which are shown in Fig. 4.5.

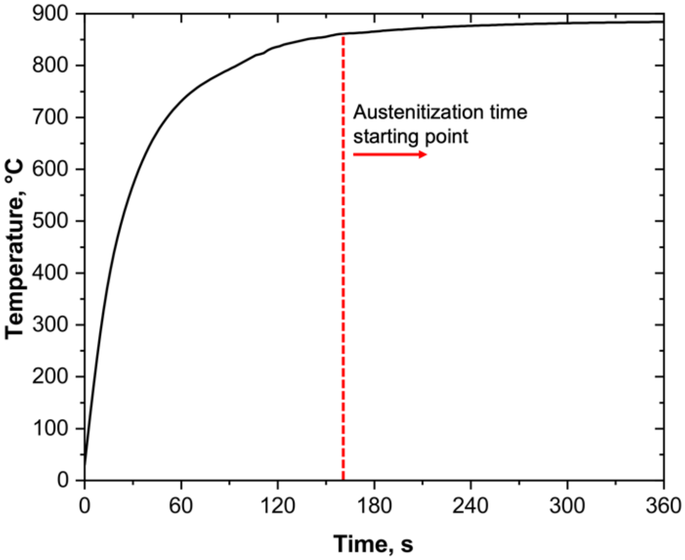

Fig. 4.3. Heating in the austenization furnace.

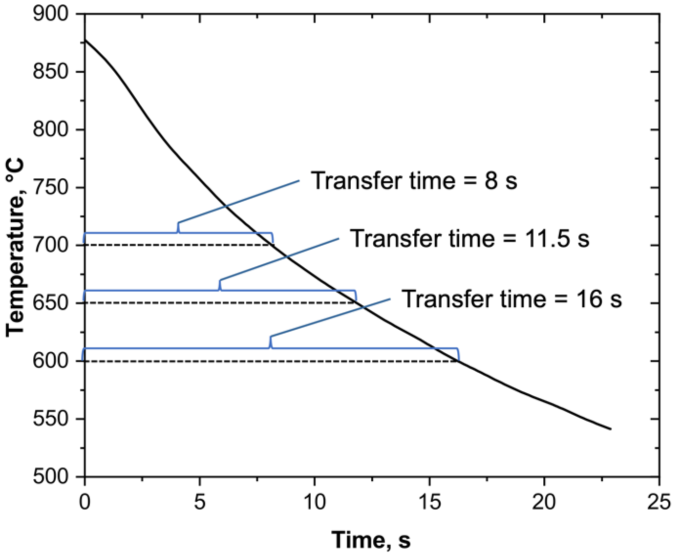

Fig. 4.4. Cooling in ambient air upon removal from the austenization furnace and the required transfer times to stamp at desired temperatures.

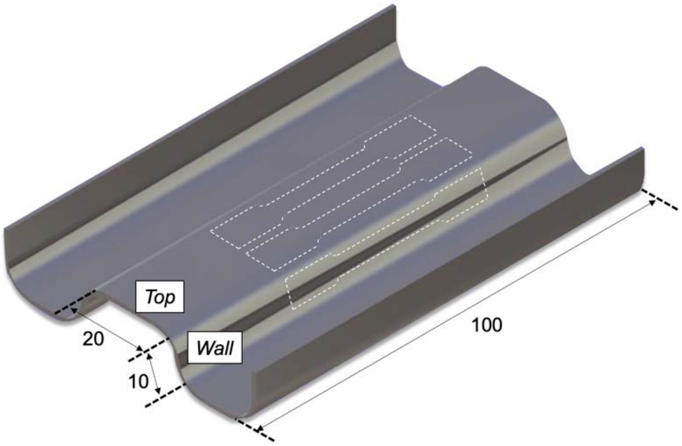

Fig. 4.5. Schematic of the DHPF part with locations of tensile coupons, dimensions in mm.

4.2.4 Tensile Testing

Uniaxial tensile tests were conducted to determine the yield strength (YS), tensile strength (TS), uniform elongation (UE), and total elongation (TE) of the die quenched prototype steel as a function of austenization time, stamping temperature and DHPF strain. All tensile coupons were taken with the tensile axis aligned in the sheet transverse direction. Due to geometric constraints, it was not possible to excise standard ASTM E8 sub-size specimens from the U-die DHPF part (Fig. 4.5). Instead, a custom tensile coupon geometry was used, the dimensions of which are shown in Fig. 4.6. In all cases, tensile testing was conducted using a 100 kN Instron tensile frame and a cross-head speed of 1 mm/min. Sample elongation was measured using a conventional contact extensometer in all cases. The mechanical property data quoted in the subsequent text is based on the average of six measurements (two coupons taken from three different panels subjected to the same processing route) to ensure reproducibility and the mechanical properties reported are the average of the measurements. Error bars for the mechanical property data represent the 95% confidence limit of the mean. The reduction of area, Z, of each tensile coupon was calculated according to ASTM E8 standards [36]:

$$Z = \frac{A_0 - A_f}{A_0} \tag{4.2}$$

where A_0 is the original area measured by calipers before the tensile test and A_f is the area of the fracture surface as measured by light microscopy.

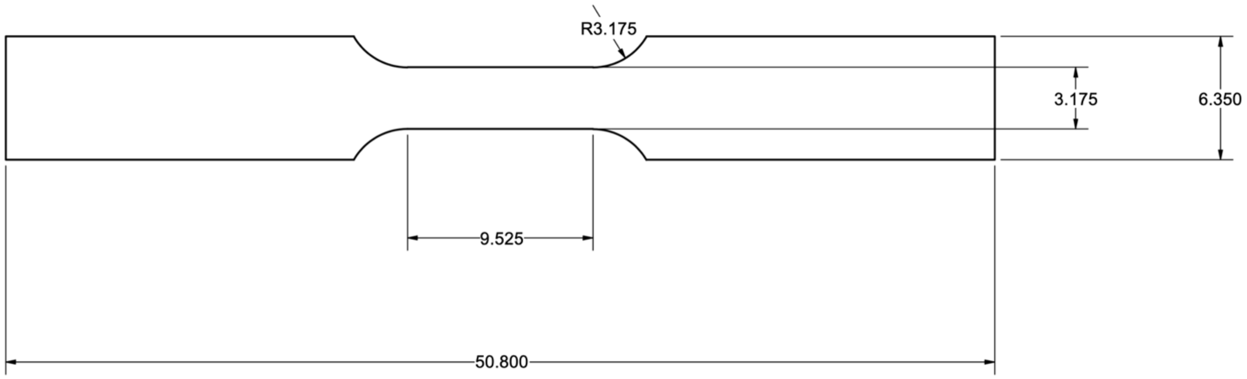

Fig. 4.6. Dimensions of tensile specimens taken from U-die DHPF parts, in mm.

4.2.5 X-ray Diffraction

X-ray Diffraction (XRD) was used to determine the fraction of each phase present in the coating as a function of austenization time and stamping temperature. All XRD tests were performed with a Bruker D8 DISCOVER with DAVINCI.DESIGN diffractometer equipped with a Co Kα1 (λ = 1.79026 Å) source to minimize the effect of Fe fluorescence. A slit size of 1 mm and a 1 mm collimator were used for all spectra. Data were collected between $10° \leq 2\theta \leq 90°$. Analysis of diffraction data was done using the resident Diffrac Eva software, and the volume fraction of each phase was calculated through Rietveld refinement using TOPAS5 software. As was the case for the tensile testing data, error bars for XRD measurements represent the 95% confidence intervals based on the measurement of two specimens from three different panels, for a total of six measurements per condition.

4.2.6 Substrate and Coating Microstructures

In order to determine the substrate and coating microstructures, samples were cold mounted in epoxy resin and polished according to standard metallographic procedures. All microstructural examinations were carried out in a JEOL 6610-LV scanning electron microscope (SEM) using an acceleration voltage of 15 keV and working distance of 10 mm. All samples for microstructural analysis were carbon coated to avoid sample charging while in the SEM. Fractographs of fractured tensile coupons employed the same SEM and settings, with the exception that a larger working distance (25 mm) was used to improve the depth of field.

Samples for substrate microstructural analysis were etched using a solution of 2 vol% nitric acid in ethanol (nital). Substrate microstructure images were captured using secondary electron imaging (SEI) mode. Samples for coating analysis were not etched. To enhance phase contrast between the coating phases, coating microstructures were acquired using backscattered electron imaging (BEI) mode.

4.3 RESULTS

4.3.1 As-Received and As-Galvanized PHS Microstructure

The as-received, cold-rolled microstructure for the prototype PHS is shown in Fig. 4.7 (a) and the as-galvanized microstructure is shown in Fig. 4.7 (b). The as-received cold-rolled microstructure (Fig. 4.7 (a)) consisted of a mixture of elongated grains of ferrite and pearlite with strong microstructural banding, like as a result of Mn segregation during casting. It can also be seen that there were some cementite particles present along the grain boundaries. The as-galvanized microstructure – which subsequently entered the DHPF process – consisted of a recrystallized version of the as-received microstructure, as was expected owing to the annealing temperature being below the Ac_1.

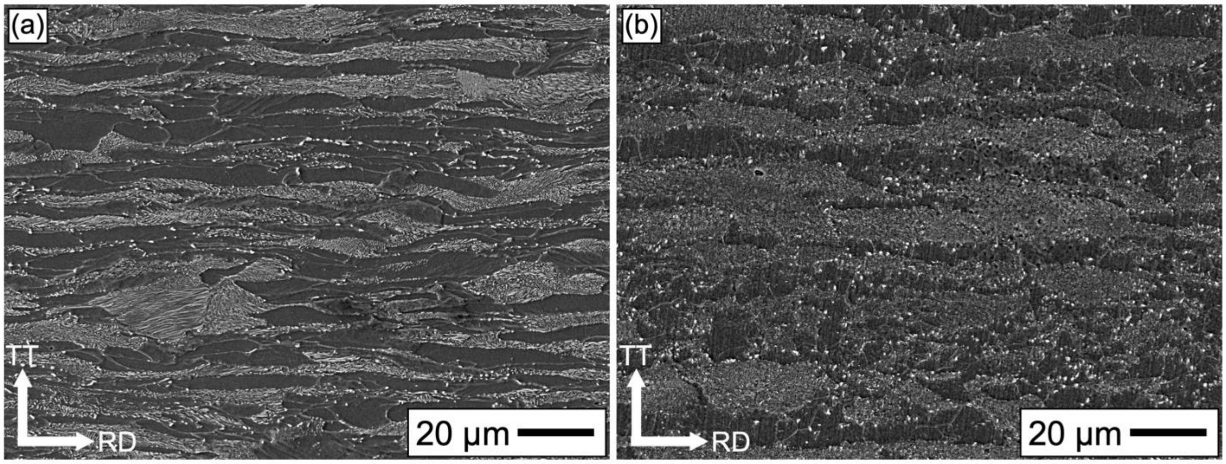

Fig. 4.7. Microstructures of the steel sheet in the (a) as-received and (b) as-galvanized condition. RD and TT denote the rolling and through thickness directions, respectively.

4.3.2 Dilatometry

As discussed in the introduction, hardenability is of critical importance when considering candidate steel grades for the DHPF process, particularly given that increasing the transfer time to perform press forming below 750 °C significantly decreases the effective cooling rate. The CCT diagram for the prototype alloy arising from the quench dilatometry investigation is documented in Fig. 4.8. It should be noted that the microhardness values determined for each cooling rate are documented at the end of each cooling curve. As stated above, the Ac_3 temperature for the alloy was determined to be approximately 845 °C and was invariant for heating rates of 5–15 °C/s. As can be seen from Fig. 4.8, the critical cooling rate to obtain fully martensitic microstructures was approximately −10 °C/s with a resultant substrate hardness of approximately 425 HV. It can also be seen that the microhardness increased with increasing cooling rate and that the M_s and M_f temperatures were determined to be approximately 405 °C and 230 °C, respectively, for cooling rates between −10 and −25 °C/s (Fig. 4.8). Fig. 4.8 also shows that the M_s and M_f temperatures increased slightly with increasing cooling rate, rising to approximately 425 °C and 275 °C, respectively, for the highest cooling rate of −75 °C/s. This was also accompanied by an increase in the microhardness of the samples to approximately 460 HV.

Deformation dilatometry with a post-deformation cooling rate of −75 °C/s was performed to determine the effect of deformation and die quenching on the M_s and M_f temperatures as a function of the targeted stamping temperatures of 600–700 °C. As seen in Fig. 4.9, the M_s and M_f temperatures were significantly reduced when compared to the undeformed condition by approximately 55 °C and 85 °C, respectively. Fig. 4.9 also shows that the deformation temperatures did not have an appreciable effect on the M_s and M_f temperatures, nor did the amount of strain.

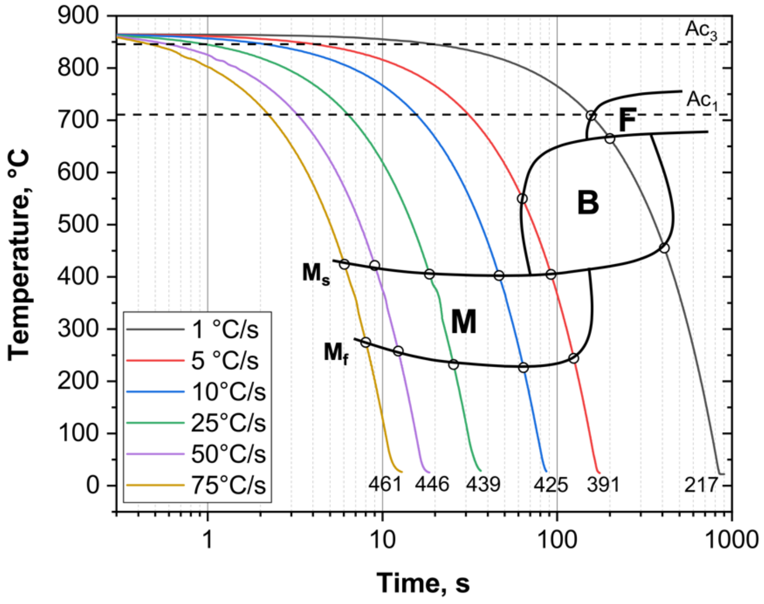

Fig. 4.8. CCT diagram for the prototype steel. Sample microhardness values (HV) are shown at the end of each curve.

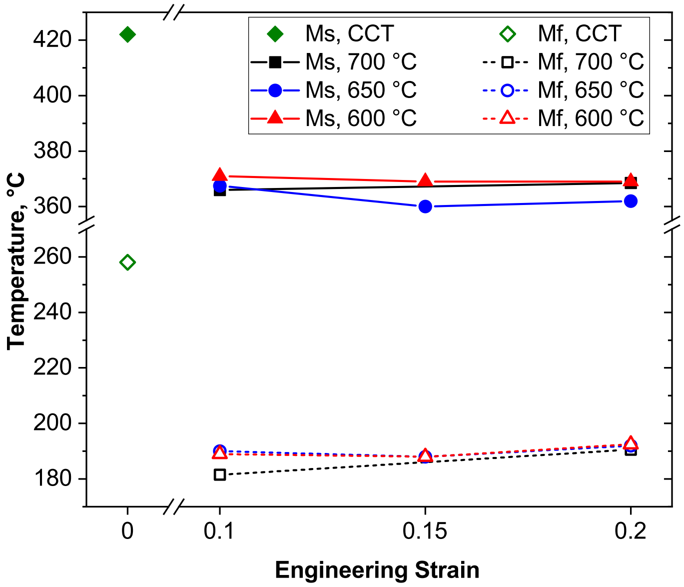

Fig. 4.9. M_s and M_f temperatures as a function of compressive strain and deformation temperature.

4.3.3 U-die DHPF Substrate Microstructures

The substrate microstructures and microhardness after U-die DHPF as a function of austenization time and stamping temperature are shown in Fig. 4.10. Observation of Fig. 4.10 (a-c) will show that after 30 s of austenization, significant fractions of ferrite remained in the microstructure. This was likely due to insufficient time for full austenization. It is clear on comparison of the images from samples austenized for 30 s that stamping at 700 °C resulted in a greater fraction of ferrite in the final microstructure than that observed for stamping at 600 °C (i.e. compare Fig. 4.10 (a) and (c)). This was likely due to the additional 8 seconds at elevated temperatures that samples stamped at 600 °C experienced before being quenched (see Fig. 4.4), allowing for additional austenite formation. It should also be noted that some of the microstructural banding and elongated grain structure from the as-received material (Fig. 4.7) remained in as-quenched microstructure, supporting the hypothesis of having an incomplete austenization reaction for the 30 s austenization time.

When the steel was austenized for 60 s before DHPF, the resultant microstructure largely consisted of martensite with small fractions of ferrite (Fig. 4.10 (d-f)). Compared to the 30 s austenization time samples, the ferrite grains were considerably smaller and evenly dispersed, as opposed to having formed bands oriented along the rolling direction. Again, there appeared to be slightly more ferrite in the 700 °C DHPF microstructure than in the 600 °C microstructure (i.e. Fig. 4.10 (d) vs. (f)). The microhardness of the samples austenized for 60 s is much higher than that of the samples austenized for 30 s, consistent with the increase in martensite fraction.

The shortest austenization time which resulted in a fully martensitic microstructure for all DHPF temperatures was 120 s (Fig. 4.10 (g-i)). Comparison of the microstructures and microhardness of the samples austenized for 120 s (Fig. 4.10 (g-i)) to those austenized for 180 s (Fig. 4.10 (j-l)) will show that there were no significant differences in between the two. From these results, it is clear that the objective of attaining fully martensitic microstructures whilst stamping at temperatures that avoid LME was met only in samples austenized for 120 or 180 s, and that these results were independent of stamping temperature. These findings are further supported by the microhardness results for the 120 s and 180 s austenization time samples (Fig. 4.10 (g-l)), which showed relatively insignificant variation and no definitive trends with the stamping temperature.

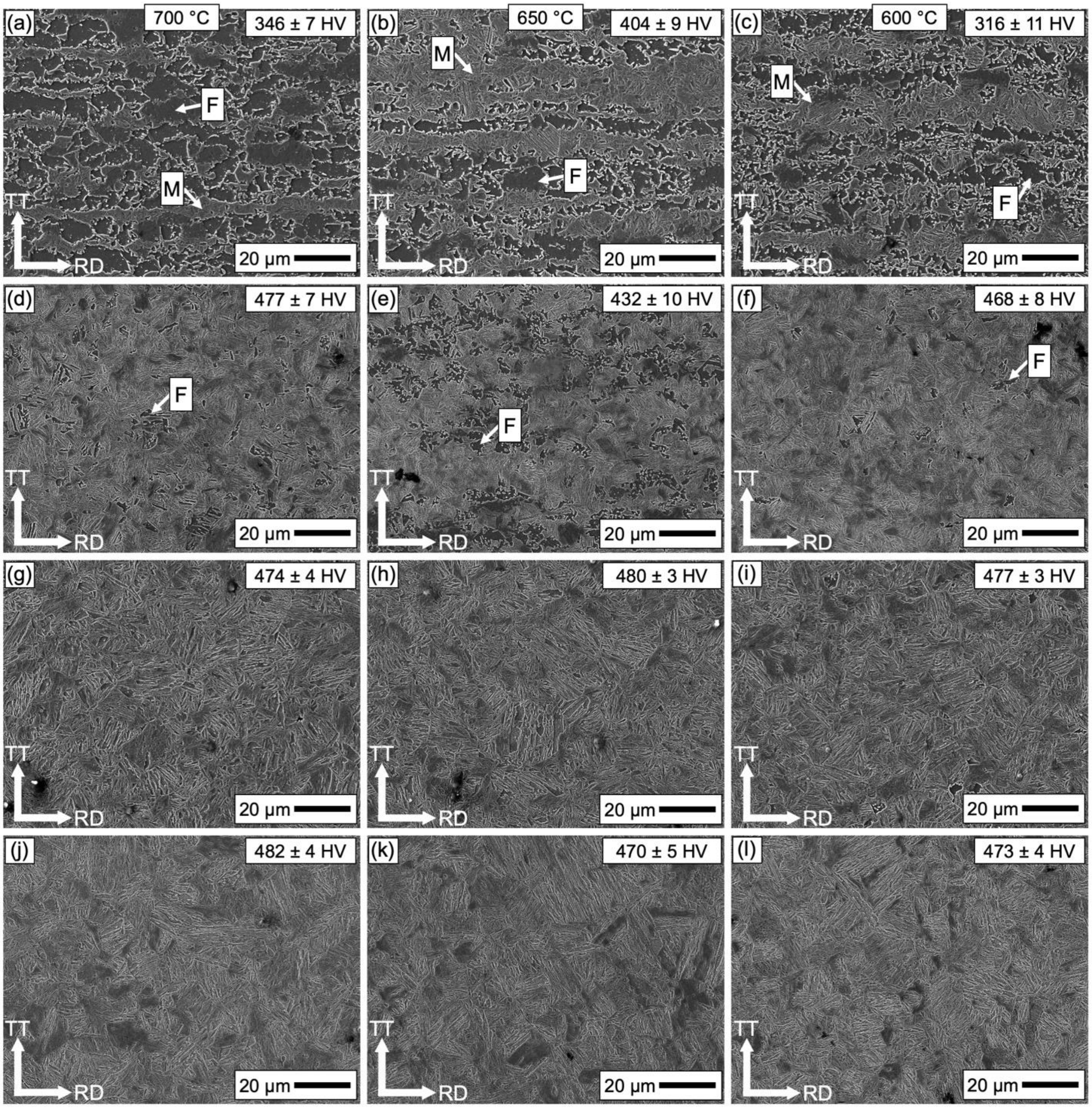

Fig. 4.10. Substrate microstructures and microhardness values excised from the top of the part after DHPF as a function of austenization time: (a–c) 30 s, (d–f) 60 s, (g–i) 120 s, and (j–l) 180 s and stamping temperature, indicated at the top of each column.

4.3.4 U-die DHPF Mechanical Properties

Representative uniaxial engineering stress-strain tensile curves from Zn-coated panels of the prototype alloy stamped at 700 °C are plotted in Fig. 4.11. It should be noted that the samples excised from the top of the part (red points) experienced minimal strain during DHPF ($\varepsilon < 0.02$) whereas samples taken from the wide wall (black data points) were subjected to higher DHPF strains ($\varepsilon = 0.04$–0.06) [27]. These curves may be categorized into two groups, i.e. those that reached approximately 1500 MPa TS and those that did not. This distinction becomes clearer when observing the trends in summative engineering mechanical properties, shown in Fig. 4.12. The left column in Fig. 4.12 shows TS and YS as a function of austenization time for each DHPF temperature. The difference in TS and YS between the U-channel top and the side wall were insignificant in all cases, implying that the strains induced during DHPF did not result in a problematic suppression of the martensitic transformation temperatures for the range of process parameters explored in this study. It is clear that the mechanical properties for the all of the samples austenized for 30 s and for the samples austenized for 60 s and then stamped at 700 °C or 650 °C did not meet the minimum TS of 1500 MPa. Correlation of the mechanical properties with the microstructural information in Fig. 4.10 reveals that the substrate microstructure after 30 s of austenization was not fully martensitic, leading to TS values below 1500 MPa. However, for the samples austenized for 60 s and stamped at 600 °C and for all samples austenized for 120 s or longer, the YS was between 1100–1200 MPa and TS was approximately 1500 MPa, thereby meeting the target properties for the PHS.

The right column in Fig. 4.12 shows the UE and TE at fracture, also as a function of austenization time and DHPF temperature. Again, there was no significant difference between samples taken from the top and wall, indicating that elongation at fracture was not a function of the strain imposed by the forming process. Compared to the samples austenized for 60 s or more, the UE was much greater in the sample austenized for 30 s due to the significant volume fractions of ferrite in their dual-phase microstructure (Fig. 4.10). For austenization times greater than 30 s, the UE decreased significantly. It can be seen that in nearly all cases, a UE of at least 5% was reached, which was often followed by significant post-uniform elongation.

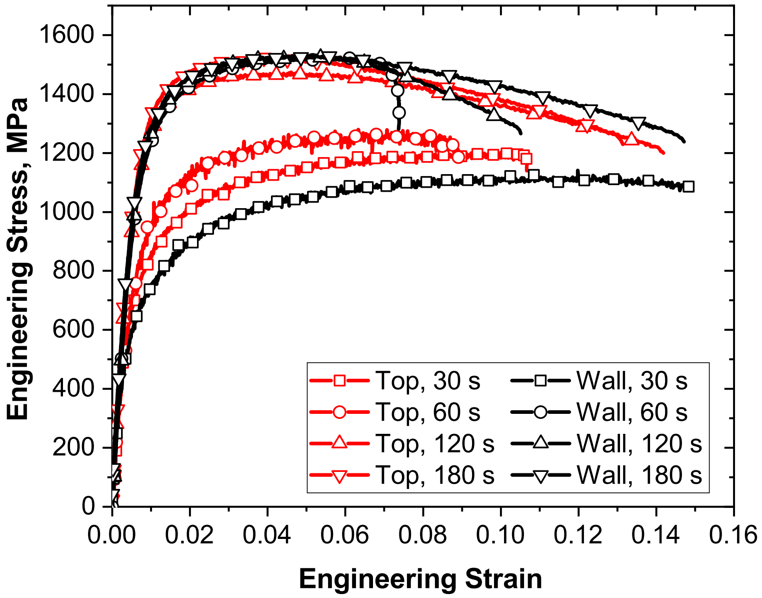

Fig. 4.11. Stress-strain curves for the prototype alloy after DHPF, stamped at 700 °C.

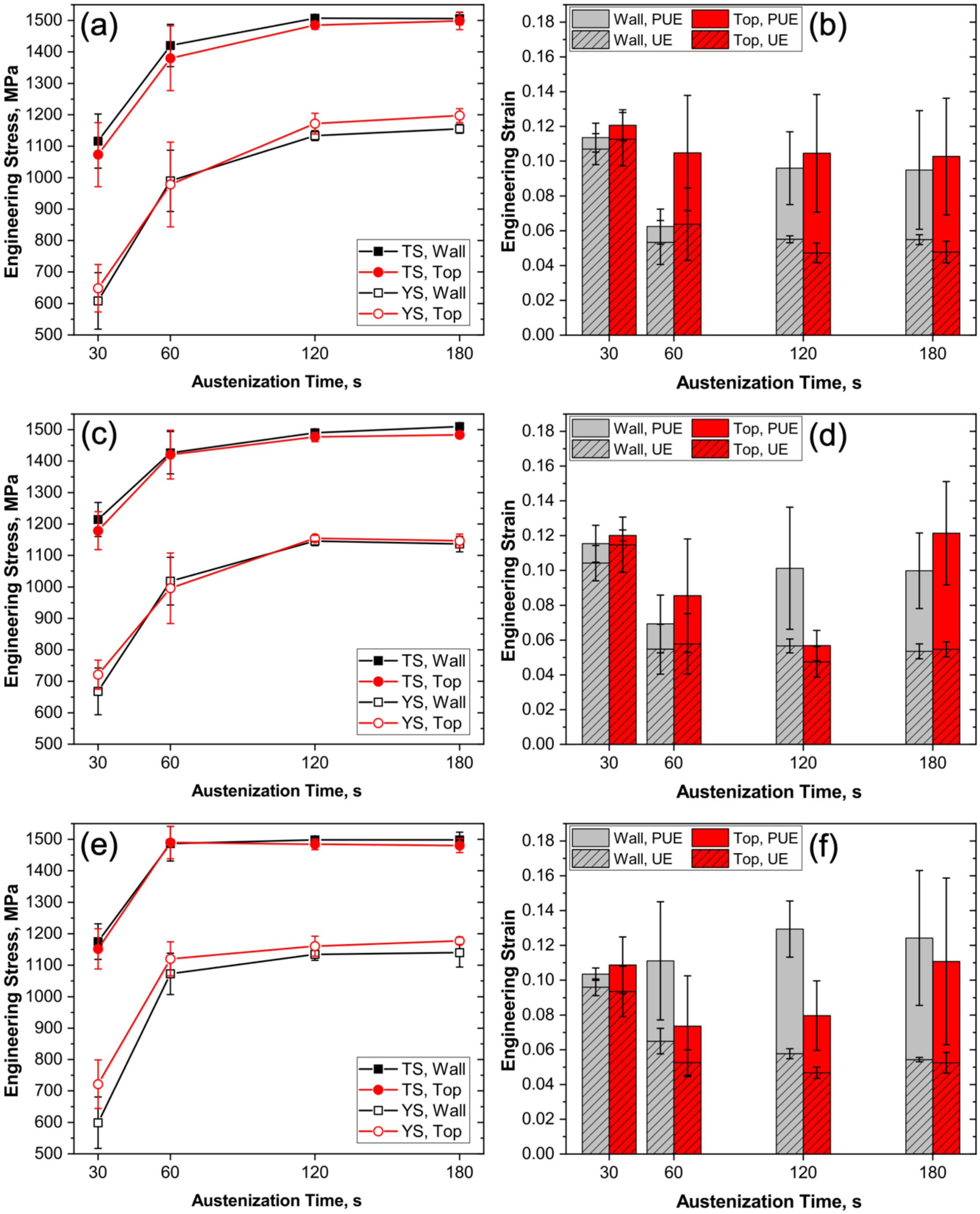

Fig. 4.12. Mechanical properties of the prototype PHS steel for each combination of austenization time and stamping temperature, and from the top and side wall of the DHPF part, per Fig. 4.5. Each row shows results from one of the DHPF temperatures (a-b) 700 °C, (c,d) 650 °C, (e,f) 600 °C.

4.3.5 Fracture

Fractographic examination of the tensile coupons demonstrated that fracture clearly occurred in a ductile manner. On the macroscopic level, a classic “cup and cone” structure was observed for all experimental conditions, indicating significant amounts of necking and plastic deformation before fracture. Investigation of the fracture surface using SEM showed shear lips at the edges of the specimen and microscopic voids or dimples consistent with void nucleation and coalescence expected from ductile fracture in the bulk substrate. A typical fracture surface for the processing conditions which resulted in the target TS ≥ 1500 MPa – in this case the 120 s-700 °C condition – is shown in Fig. 4.13 (a). This fractograph shows three distinct regions in the facture surface: (i) the α-Fe(Zn) + Γ-Fe_3Zn_{10} coating, (ii) a Zn-enriched martensite layer [27], and (iii) the martensitic substrate. In the coating, intergranular cracks and the blocky appearance of the fracture surface in this microstructural zone clearly indicate brittle fracture. These cracks were arrested at the coating–substrate interface. The Zn-enriched martensite layer (α’-Fe(Zn)) appears slightly darker and smoother than the rest of the substrate. Small parabolic dimples are seen in this region due to fracture by shear, as opposed to the triaxial stress state found in the centre of the fracture surface. In the bulk martensitic substrate (Fig. 4.13 (b)) the dimples became larger and more equiaxed, characteristic of ductile tearing. It should be noted that there was evidence of void nucleation from alumina particles, titanium nitrides, and MnS stringers. These observations did not depend on austenization time or stamping temperature.

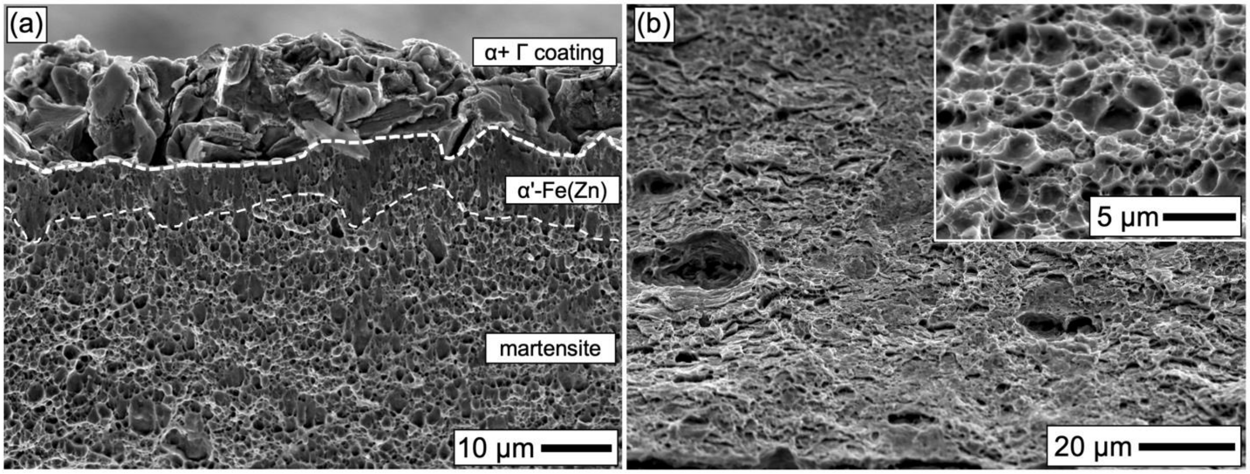

Fig. 4.13. Fracture surfaces of a sample austenized for 120 s and stamped at 700 °C showing (a) the coating, Zn-enriched transition layer, and the martensitic substrate and (b) the centre, showing some large voids.

The reduction of area (Fig. 4.14) calculated from equation 4.2 increased from 0.09–0.15 for the samples austenized for 30 s to 0.25–0.30 for those austenized for 120 or 180 s. This significant post-uniform plastic deformation agrees with the observation of ductile fracture (Fig. 4.13) as a function of austenization time and DHPF temperature (Fig. 4.10). Additionally, it is worth noting that the processing routes that resulted in properties that met the target of TS ≥ 1500 MPa – i.e. austenization times of 120 and 180 s and stamping temperatures between 600 °C and 700 °C – also resulted in the greatest reduction of area. The significant plastic deformation corresponding to the 0.25–0.30 reduction of area shows that failure could not have occurred as a result of LME, which induces catastrophic brittle failure. This result also indicates that material produced from this processing route should exhibit reasonable formability in addition to their excellent strength properties.

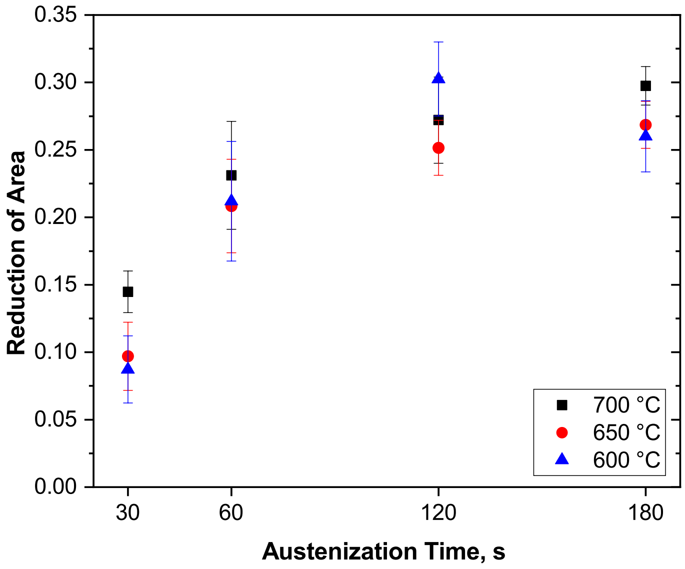

Fig. 4.14. Reduction of area of DHPF tensile coupons as a function of annealing time and stamping temperature.

4.3.6 Coating Evolution

During austenization, the Zn coating grew through diffusion with the substrate and became continuously more enriched with Fe and grew into the substrate. Results from XRD show that the coating mainly consists of two phases after DHPF: α-Fe(Zn) and Γ-Fe_3Zn_{10}, in agreement with other studies [20,21,23,24,27]. Additionally, the data show that, as the austenization time increased, the fraction of α-Fe(Zn) grew steadily at the expense of Γ-Fe_3Zn_{10} (Fig. 4.15). The amount of ZnO also increased slightly with increasing austenization time, to a maximum of about 5 vol%. The fraction of Γ-Fe_3Zn_{10} in the coating was well above the target of ≥ 15 vol% in all cases; for the samples austenized for 120 s and 180 s, the Γ-Fe_3Zn_{10} content was between 71–74 vol% and 33–53 vol% respectively. It is clear that the phase fractions were very sensitive to austenization time, while DHPF stamping temperature had an insignificant effect. The presence of Γ-Fe_3Zn_{10} indicates that $Zn(Fe)_{liq}$ had formed due to austenization, however, no LME was detected from during DHPF or tensile testing (Fig. 4.12), from analysing fracture surfaces (Fig. 4.13), or from searching for cracks at the coating–substrate interface (Fig. 4.16). These results show that in addition to forming ≥ 15 vol% Γ-Fe_3Zn_{10}, the objective of doing so while avoiding LME has been achieved.

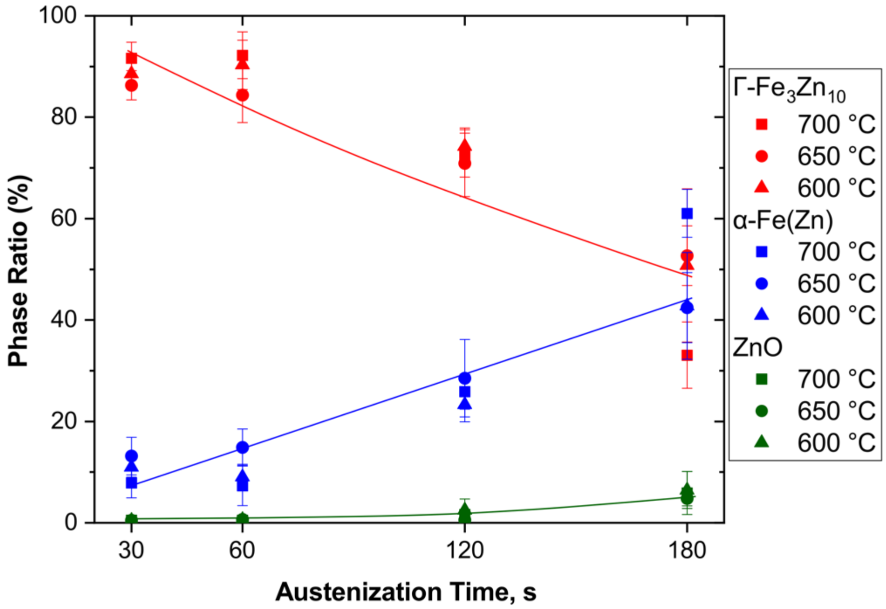

Fig. 4.15. XRD phase analysis results as a function of austenization time and DHPF stamping temperature.

The evolution of the coating microstructure for different strain conditions in the U-channel DHPF part is shown in Fig. 4.16. Results from specimens austenized for 30 s and 60 s are excluded from these data as these processing routes did not meet the TS target. As discussed, the coating microstructure consists of two phases; Γ-Fe_3Zn_{10} and α-Fe(Zn), the former of which appears lighter in the BEI mode images due to its higher Zn concentration. The coating grew from an average of 17 μm after 30 s to 23 μm after 180 s. In agreement with the XRD data (Fig. 4.15), it can be seen qualitatively that the amount of Γ-Fe_3Zn_{10} decreases from 120 s to 180 s of austenization. The intergranular coating crack characteristics follow the results from several investigations [19,27,37]. At the top of the formed part, very little strain was present (i.e. $\varepsilon < 0.02$) [27], leading to a crack-free coating. The outside wall of the part showed thin through-thickness intergranular α-Fe(Zn) cracks in the coating. However, these did not penetrate into the substrate in any case, an important difference between the present results and the results of Lee et. al. [19] for the conventional 22MnB5 substrate. In the inner wall, where the part was exposed to friction against the die, some intergranular α-Fe(Zn) coating cracks were observed. The outside corner of the part experienced the highest strain, where significant tensile forces forced a number of large cracks to open up, which can also be seen to have propagated along α-Fe(Zn) grain boundaries. Finally, on the inside of the corner, compressive forces tended to close or prevent cracks from occurring. More importantly, the die friction at the inner wall appears to have stripped the thin layer of Γ-Fe_3Zn_{10} that had formed after the 180 s austenization time.

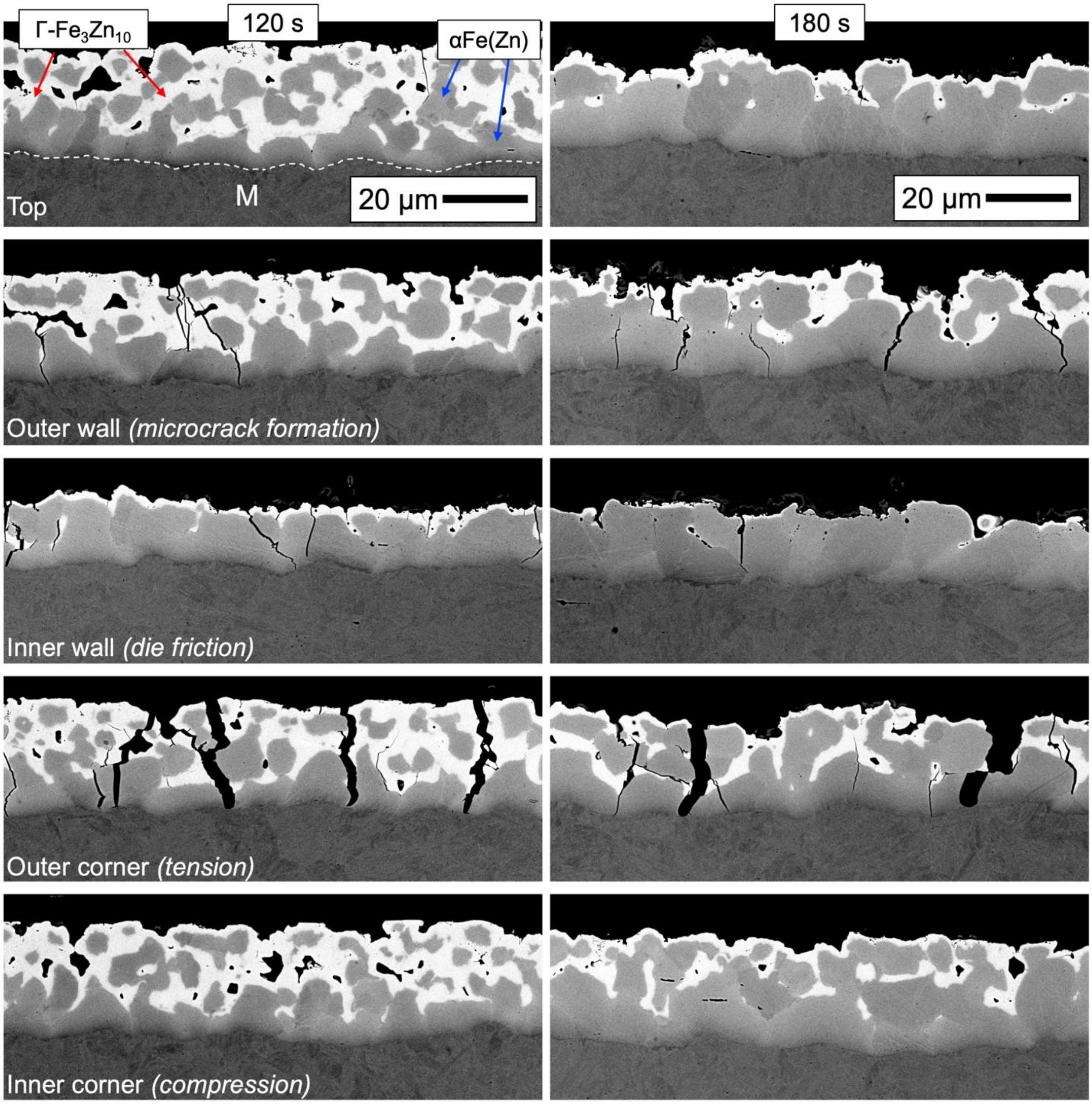

Fig. 4.16. Coating microstructural evolution at different areas and austenization times. The left and right columns show the final microstructures after 120 s and 180 s of austenization respectively, both stamped at 700 °C.

4.4 DISCUSSION

The increased Mn content in the prototype PHS grade proved to increase the hardenability of the prototype PHS substantially relative to the industry standard 22MnB5, thus allowing formation of fully martensitic microstructures at the stamping temperatures of between 600–700℃ required to avoid LME. The effect of Mn on hardenability has been linked to its segregation to austenite during austenization, which increases hardenability both by retarding the formation of ferrite and bainite and increasing the solubility of C in austenite [38]. Through dilatometric tests, it was found that, in the absence of applied strain, the critical cooling rate to form fully martensitic microstructures for the new steel grade is −10 °C/s. Deformation dilatometry (Fig. 4.9) showed that the application of compressive strain at the target stamping temperatures had a strong effect on the martensitic transformation temperatures, decreasing M_s and M_f by approximately 55 °C and 85 °C, respectively, relative to the unstrained condition. This result indicates that the actual critical cooling rate for the formation of fully martensitic microstructures by DHPF is likely to be higher than −10 °C/s, in agreement with the general trends found in the literature [39,40]. Additionally, varying the amount of strain between 0.1–0.2 did not significantly affect the deformation-induced martensitic transformation temperatures. The reduction of martensitic transformation temperatures has been observed in the literature and is commonly attributed to the mechanical stabilization of austenite due to the strain imposed by deformation [41–43]. Overall, dilatometry tests have shown that the increased hardenability of the prototype grade enabled the formation of fully martensitic microstructures (Fig. 4.10) and the attainment of the target TS of approximately 1500 MPa (Fig. 4.12), despite the prolonged transfer time (slower cooling rate) and the suppression of martensitic transformation due to mechanical stabilization of austenite.

The substrate microstructure (Fig. 4.10) and summative mechanical properties (Fig. 4.12) for the prototype steel in the DHPF condition were determined for each combination of austenization time and stamping temperature. Austenization time significantly influenced the microstructure and mechanical properties, while stamping temperature and the amount of strain induced by forming had a minor, if not insignificant, impact. It was found that only samples austenized for 120 s and 180 s were fully austenitic before stamping and, therefore, only these samples satisfied the objectives of having a fully martensitic microstructures and TS $\geq$ 1500 MPa. Upon observation of the fracture surfaces of tensile samples that met these targets (Fig. 4.13), it was determined that ductile fracture occurred with void nucleation and growth originating at second phase particles. Furthermore, the fully martensitic samples experienced a significant reduction of area (0.25–0.30) when pulled to fracture, as shown in Fig. 4.14. The consistent observation of ductile fracture and significant reduction of area in all samples austenized for 120 and 180 s indicates that the method of avoiding LME by extending the transfer time to solidify $Zn(Fe)_{liq}$ before stamping was successful. Considering all these results together, it can be concluded that processing routes for this grade consisting of 120–180 s of austenization time followed by stamping at 600–700 °C met the microstructure and mechanical property targets, i.e. a fully martensitic substrate with TS $\geq$ 1500 MPa that avoids LME and fails in a ductile manner.

Significant changes occurred to the coating during austenization. The microstructural evolution (Fig. 4.15) and growth of the coating are consistent with previous studies [20,21,23,24,27]. During heating, the coating transformed to a mixture of α-Fe(Zn), $Zn(Fe)_{liq}$, and ZnO. The coating was then cooled to stamping temperatures between 600–700 °C to allow for $Zn(Fe)_{liq}$ to solidify to Γ-Fe_3Zn_{10} via the peritectic reaction (equation 4.1). In this manner, the presence of $Zn(Fe)_{liq}$ during forming and the associated LME was avoided. Furthermore, significant fractions Γ-Fe_3Zn_{10} were retained in the final coating microstructure for all processing conditions which met the substrate mechanical property targets (Fig. 4.15). Specifically, samples austenized for 120 s and 180 s that met the mechanical property targets also had coating Γ-Fe_3Zn_{10} fractions much greater than the target of ≥ 15 vol% required for robust cathodic protection, as determined by Dever et al. [21].

Microscopy of the coating–substrate interface at different areas of the DHPF part revealed through-thickness intergranular cracks in the coating α-Fe(Zn) at the outer corner and wall sections of the part; however, these cracks were arrested at the substrate. No indications of LME-assisted cracks were observed, which is in agreement with the features of the fracture surfaces (Fig. 4.13), the good ductility observed during tensile tests (Fig. 4.12), and the measured reduction of area (Fig. 4.14).

4.5 CONCLUSIONS

This study has shown that it is possible to process the prototype Zn-coated 0.2C-2.0Mn-0.26Si-0.005B (wt%) PHS using the DHPF process such that the dual targets of TS ≥ 1500 MPa and possessing a coating that is consistent with providing robust cathodic corrosion protection can be achieved. The threat of liquid metal embrittlement was avoided by performing the stamping and quenching step between 600–700 °C such that all liquid left in the Zn-based coating system solidified via the reaction $\alpha\text{-Fe(Zn)} + \text{Zn(Fe)}_{liq} \rightarrow \alpha\text{-Fe(Zn)} + \Gamma\text{-Fe}_3\text{Zn}_{10}$. The findings of this study are summarized below.

- As a result of the increased Mn content, the critical cooling rate for the formation of fully martensitic microstructures for this prototype grade without deformation was determined to be −10 °C/s. This increase in hardenability enabled DHPF at 600–700 °C while still meeting the microstructural and mechanical property targets.

- The samples austenized for 120 s or 180 s, i.e. those that had fully martensitic microstructures after DHPF, met the target of TS ≥ 1500 MPa. These samples exhibited 0.05 UE typically followed by 0.04–0.05 PUE, though the extent of PUE was greatly variable.
- No LME was observed for the DHPF parts or in the fracture surface images of tensile coupons taken from DHPF parts. Microcracks seen in the coating were arrested at the substrate-coating interface.
- The reduction of area for DHPF tensile specimens that met the mechanical property targets was 0.25-0.30. This significant extent of necking before failure is further confirmation that LME was avoided.
- The phase fraction of Γ-Fe_3Zn_{10} in the DHPF coating decreased with austenization time; however, the coating microstructure met the target for robust cathodic corrosion protection of containing a minimum of 15 vol% of Γ-Fe_3Zn_{10} set by Dever et al. [21] for all processing routes which met the substrate mechanical property targets.
- By austenizing the galvanized prototype 0.2C-2.0Mn-0.26Si-0.005B (wt%) PHS for 120 s or 180 s followed by DHPF between 600–700 °C, it is possible to meet the specified mechanical property target of TS ≥ 1500 MPa while avoiding LME and providing the required coating microstructure of ≥ 15 vol% Γ-Fe_3Zn_{10} to provide robust cathodic protection for the underlying substrate.

ACKNOWLEDGEMENTS

The authors would like to thank the International Zinc Association – Galvanized Autobody Partnership (IZA-GAP) and the Natural Sciences and Engineering Research Council of Canada

(NSERC, grant CRDPJ 522309 – 17) for their financial support. The authors would also like to thank U.S. Steel Research (Munhall, USA) for the provision of the prototype PHS steel used in this study. The authors also the Canadian Centre for Electron Microscopy, and the McMaster Analytical X-Ray Diffraction Facility for their technical assistance.

REFERENCES

[1] S. Keeler, M. Kimchi, P. J. Mooney, Advanced High-Strength Steels Apllication Guidelines Version 6.0, World Auto Steel. 6 (2017) 314. http://www.worldautosteel.org/download_files/AHSS Guidelines V6/00_AHSSGuidelines_V6_20170430.pdf.

[2] T. Taylor, A. Clough, Critical review of automotive hot-stamped sheet steel from an industrial perspective, Mater. Sci. Technol. 0836 (2018) 1–53. https://doi.org/10.1080/02670836.2018.1425239.

[3] O. Bouaziz, H. Zurob, M. Huang, Driving force and logic of development of advanced high strength steels for automotive applications, Steel Res. Int. 84 (2013) 937–947. https://doi.org/10.1002/srin.201200288.

[4] D.W. Fan, H.S. Kim, B.C. De Cooman, A review of the physical metallurgy related to the hot press forming of advanced high strength steel, Steel Res. Int. 80 (2009) 241–248. https://doi.org/10.2374/SRI08SP131.

[5] H. Karbasian, A.E. Tekkaya, A review on hot stamping, J. Mater. Process. Technol. 210 (2010) 2103–2118. https://doi.org/10.1016/j.jmatprotec.2010.07.019.

[6] T. Taylor, G. Fourlaris, P. Evans, G. Bright, New generation ultrahigh strength boron steel for automotive hot stamping technologies, Mater. Sci. Technol. 30 (2014) 818–826.

https://doi.org/10.1179/1743284713Y.0000000409.

[7] T. Taylor, G. Fourlaris, A. Clough, Effect of carbon and microalloy additions on hot-stamped boron steel, Mater. Sci. Technol. 33 (2017) 1964–1977. https://doi.org/10.1080/02670836.2017.1342018.

[8] A. Tokizawa, K. Yamamoto, Y. Takemoto, T. Senuma, Development of 2000MPa class hot stamped steel components with good toughness and high resistance against delayed fracture, in: 4th Int. Conf. Hot Sheet Met. Form. High Perform. Steel, CHS2, Luleå, Sweden, 2013: pp. 9–12.

[9] D.W. Fan, B.C. De Cooman, State-of-the-knowledge on coating systems for hot stamped parts, Steel Res. Int. 83 (2012) 412–433. https://doi.org/10.1002/srin.201100292.

[10] R.W. Richards, R.D. Jones, P.D. Clements, H. Clarke, Metallurgy of continuous hot dip aluminising, Int. Mater. Rev. 39 (1994) 191–212. https://doi.org/10.1179/imr.1994.39.5.191.

[11] P. Drillet, Coatings Dedicated to Press Hardened Steels for Automotive Applications, in: Galvatech 2017 Conf. Proc., Tokyo, Japan, 2017: pp. 401–408.

[12] C. Allély, L. Dosdat, O. Clauzeau, K. Ogle, P. Volovitch, Anticorrosion mechanisms of aluminized steel for hot stamping, Surf. Coatings Technol. 238 (2014) 188–196. https://doi.org/10.1016/j.surfcoat.2013.10.072.

[13] J. Maki, M. Kurosaki, K. Kusumi, Effect of heating condition and hot forming on corrosion resistance of hot stamped aluminized steels, in: 3th Int. Conf. Proc. Hot Sheet Met. Form. High-Performance Steel, Kassel: Association for Iron & Steel Technology, 2011.

[14] G. Zhong-xiang, L. Wei-kang, L. Yong, Z. Yi-sheng, Thermo-mechanical behavior of the Al – Si alloy coated hot stamping boron steel, Mater. Des. 60 (2014) 26–33.

https://doi.org/10.1016/j.matdes.2014.03.011.

[15] K. Wang, Z. Gui, P. Liu, Y. Wang, Y. Zhang, Cracking behavior of Al-Si coating on hot stamping boron steel sheet, Procedia Eng. 81 (2014) 1713–1718. https://doi.org/10.1016/j.proeng.2014.10.218.

[16] G. Zhong-Xiang, W. Kai, Z. Yi-Sheng, Z. Bin, Cracking and interfacial debonding of the Al-Si coating in hot stamping of pre-coated boron steel, Appl. Surf. Sci. 316 (2014) 595–603. https://doi.org/10.1016/j.apsusc.2014.08.043.

[17] J. Nakano, D. V. Malakhov, G.R. Purdy, A crystallographically consistent optimization of the Zn-Fe system, Calphad Comput. Coupling Phase Diagrams Thermochem. 29 (2005) 276–288. https://doi.org/10.1016/j.calphad.2005.08.005.

[18] L. Cho, H. Kang, C. Lee, B.C. De Cooman, Microstructure of liquid metal embrittlement cracks on Zn-coated 22MnB5 press-hardened steel, Scr. Mater. 90–91 (2014) 25–28. https://doi.org/10.1016/J.SCRIPTAMAT.2014.07.008.

[19] C.W. Lee, W.S. Choi, L. Cho, Y.R. Cho, B.C. De Cooman, Liquid-Metal-Induced Embrittlement Related Microcrack Propagation on Zn-coated Press Hardening Steel, ISIJ Int. 55 (2015) 264–271. https://doi.org/10.2355/isijinternational.55.264.

[20] Y. Kim, J.R. McDermid, Microstructure and Phase Evolution of Galvanized Press Hardening Steel, in: Galvatech 2017 Conf. Proc., ISIJ International, Tokyo, Japan, 2017: pp. 501–505.

[21] C. Dever, J. Kish, J. McDermid, Corrosion Properties of Hot Dip Zinc Galvanized Coatings on 22MnB5 Press Hardened Steels, in: Galvatech 2017 Conf. Proc., ISIJ International, Tokyo, Japan, 2017: pp. 385–392.

[22] C. Dever, Effect of Coating Microstructure on the Electrochemical Properties of Continuous Galvanized Coatings on Press Hardened Steels, McMaster University, 2018.

[23] R. Autengruber, G. Luckeneder, S. Kolnberger, J. Faderl, A.W. Hassel, Surface and coating analysis of press-hardened hot-dip galvanized steel sheet, Steel Res. Int. 83 (2012) 1005–1011. https://doi.org/10.1002/srin.201200068.

[24] V. Janik, Y. Lan, P. Beentjes, D. Norman, G. Hensen, S. Sridhar, Zn Diffusion and α-Fe(Zn) Layer Growth During Annealing of Zn-Coated B Steel, Metall. Mater. Trans. A Phys. Metall. Mater. Sci. 47 (2016) 400–411. https://doi.org/10.1007/s11661-015-3203-y.

[25] J. Kondratiuk, P. Kuhn, E. Labrenz, C. Bischoff, Zinc coatings for hot sheet metal forming: Comparison of phase evolution and microstructure during heat treatment, Surf. Coatings Technol. 205 (2011) 4141–4153. https://doi.org/10.1016/j.surfcoat.2011.03.002.

[26] C.W. Lee, D.W. Fan, S.J. Lee, I.R. Sohn, B.C. De Cooman, Galvanized Coating Evolution During Hot Stamping, in: Galvatech 2011 Conf. Proc., Genova, Italy, 2011.

[27] K. Maleki, On the Origin of Micro-Cracking in Zn-Coated Press Hardened Steels, McMaster University, 2019.

[28] C.W. Lee, W.S. Choi, Y.R. Cho, B.C. De Cooman, Surface oxide formation during rapid heating of Zn-coated press hardening steel, ISIJ Int. 54 (2014) 2364–2368. https://doi.org/10.2355/isijinternational.54.2364.

[29] A.W. Hassel, Fundamental Aspects of Corrosion of Press Hardened Galvanized Steel, in: Galvatech 2017 Conf. Proc., ISIJ International, Tokyo, Japan, 2017.

[30] R. Autengruber, G. Luckeneder, A.W. Hassel, Corrosion of press-hardened galvanized steel, Corros. Sci. 63 (2012) 12–19. https://doi.org/10.1016/j.corsci.2012.04.048.

[31] T. Kurz, P. Larour, J. Lackner, T. Steck, G. Jesner, Press-hardening of zinc coated steel - Characterization of a new material for a new process, in: IOP Conf. Ser. Mater. Sci. Eng., 2016. https://doi.org/10.1088/1757-899X/159/1/012025.

[32] T. Kurz, H. Schwinghammer, G. Luckeneder, T. Manzenreiter, A. Sommer, Zinc coated

press-hardening steel - challenges and solutions, 5th Int. Conf. Hot Sheet Met. Form. High-Performance Steel. (2015) 345–353. https://doi.org/10.4271/2015-01-0565.

[33] K. Isaksson, M. Jönsson, D. Berglund, The direct press hardening process for Zn-coated ultra-high strength steels, in: 2nd Int. Conf. Adv. High Strength Steel Press Hardening, Changsha, China, 2015: pp. 1–8.

[34] E.M. Bellhouse, J.R. McDermid, Selective oxidation and reactive wetting during hot-dip galvanizing of a 1.0 pct Al-0.5 pct Si TRIP-assisted steel, Metall. Mater. Trans. A Phys. Metall. Mater. Sci. 43 (2012) 2426–2441. https://doi.org/10.1007/s11661-011-0983-6.

[35] J.R. McDermid, M.H. Kaye, W.T. Thompson, Fe solubility in the Zn-rich corner of the Zn-Al-Fe system for use in continuous galvanizing and galvannealing, Metall. Mater. Trans. B Process Metall. Mater. Process. Sci. 38 (2007) 215–230. https://doi.org/10.1007/s11663-007-9028-3.

[36] ASTM E8 / E8M-16ae1, Standard Test Methods for Tension Testing of Metallic Materials, ASTM International, West Conshohocken, PA, 2016. https://doi.org/10.1520/E0008_E0008M-13A.

[37] C. Dever, J.R. Kish, J.R. Mcdermid, Electrochemical Properties of Continuous Galvanized Coatings on Press Hardened Steels Introduction Press hardened steels (PHS) used for vehicle light-weighting and Use 22MnB5 for direct hot press forming (DHPF) of complex parts Liquid Metal Embrittlem, 83 (2018).

[38] M. Calcagnotto, D. Ponge, D. Raabe, On the effect of manganese on grain size stability and hardenability in ultrafine-grained ferrite/martensite dual-phase steels, Metall. Mater. Trans. A Phys. Metall. Mater. Sci. 43 (2012) 37–46. https://doi.org/10.1007/s11661-011-0828-3.

[39] M. Nikravesh, M. Naderi, G.H. Akbari, Influence of hot plastic deformation and cooling

rate on martensite and bainite start temperatures in 22MnB5 steel, Mater. Sci. Eng. A. 540 (2012) 24–29. https://doi.org/10.1016/j.msea.2012.01.018.

[40] M. Naderi, A. Saeed-Akbari, W. Bleck, The effects of non-isothermal deformation on martensitic transformation in 22MnB5 steel, Mater. Sci. Eng. A. 487 (2008) 445–455. https://doi.org/10.1016/j.msea.2007.10.057.

[41] M. Nikravesh, M. Naderi, G.H. Akbari, W. Bleck, Phase transformations in a simulated hot stamping process of the boron bearing steel, Mater. Des. 84 (2015) 18–24. https://doi.org/10.1016/j.matdes.2015.06.108.

[42] A. Barcellona, D. Palmeri, Effect of plastic hot deformation on the hardness and continuous cooling transformations of 22MnB5 microalloyed boron steel, Metall. Mater. Trans. A Phys. Metall. Mater. Sci. 40 (2009) 1160–1174. https://doi.org/10.1007/s11661-009-9790-8.

[43] J. Min, J. Lin, Y. Min, F. Li, On the ferrite and bainite transformation in isothermally deformed 22MnB5 steels, Mater. Sci. Eng. A. 550 (2012) 375–387. https://doi.org/10.1016/j.msea.2012.04.091.

CHAPTER 5 DEVELOPMENT OF A 0.19C-2.5MN-0.26SI-0.005B ZN-COATED DIRECT PRESS-HARDENABLE STEEL

CHRIS THOMSEN[a] AND JOSEPH R. MCDERMID[a]

[a] Centre for Automotive Materials and Corrosion, McMaster University, 1280 Main Street West, Hamilton, ON L8S 4L7, Canada

Corresponding author’s email: mcdermid@mcmaster.ca

Authorship Contribution Statement

Chris Thomsen: Conceptualization, Investigation, Methodology, Formal analysis, Writing - original draft, Writing - review & editing.

Joseph McDermid: Conceptualization, Methodology, Formal analysis, Funding acquisition, Resources, Supervision, Writing - review & editing.

This draft manuscript has been prepared for submission in a peer-reviewed academic journal.

DEVELOPMENT OF A 0.19C-2.5MN-0.26SI-0.005B ZN-COATED DIRECT PRESS-HARDENABLE STEEL

CHRIS THOMSEN[a] AND JOSEPH R. MCDERMID[a]

[a] Centre for Automotive Materials and Corrosion, McMaster University, 1280 Main Street West, Hamilton, ON L8S 4L7, Canada

Corresponding author's email: mcdermid@mcmaster.ca

ABSTRACT

Direct hot press forming (DHPF) of Zn-coated press-hardenable steels (PHS) presents significant challenges associated with avoiding liquid metal embrittlement (LME) while attaining robust cathodic protection. The present research uses a novel galvanized 0.19C-2.5Mn-0.26Si-0.005B PHS grade and DHPF with an extended transfer time (lower stamping temperature) to overcome these challenges. The increased Mn content of this prototype grade significantly improved hardenability and enabled fully martensitic microstructures to be achieved even when stamping at 600–700 °C instead of the usual 800–850 °C. The experimental stamping temperatures of 600, 650, and 700 °C were chosen to be well below the Γ-$Fe_3Zn_{10} \rightarrow \alpha$-Fe(Zn) + $Zn(Fe)_{liq}$ peritectic temperature of 782 °C, such that no $Zn(Fe)_{liq}$ would remain in the coating to cause LME by the time forming strain was applied. The prototype grade was characterized with a focus on the objectives of achieving tensile strengths ≥ 1500 MPa and achieving robust cathodic protection by attaining ≥ 15 vol% Γ-Fe_3Zn_{10}, while avoiding LME. Dilatometry tests have confirmed that the critical cooling rate for formation of fully martensitic microstructures for the prototype alloy is only −5 °C/s. Uniaxial tensile tests showed excellent mechanical properties, with TS >1550 MPa and uniform elongation of 0.05. No indications of LME were found, and ductile fracture was

observed with significant post-uniform elongation and reduction of area before failure. It was concluded that austenization times of 60–180 s combined with any of the tested DHPF stamping temperatures between 600–700 °C led to properties which met the targets of TS ≥ 1500 MPa and ≥ 15 vol% Γ-Fe_3Zn_{10}.

5.1 INTRODUCTION

Automotive lightweighting and safety requirements continue to drive demand for materials that can provide ultra-high strengths while possessing adequate formability [1,2]. Press-hardened steel (PHS) has become a material of choice for the anti-intrusion zone of vehicles due to its ultra-high strength and formability at reasonable cost [2,3]. The industry standard PHS grade is known as 22MnB5 and has a range of compositions, typically about 0.22C-1.2Mn-0.25Si-0.003B wt% [2–4]. PHS components are typically manufactured using the direct hot press forming (DHPF) method, which involves three main steps: austenization, transfer, and forming and quenching. Austenization involves heating the blank to 850–950 °C for 3–8 minutes in order to fully transform the as-received ferrite and pearlite microstructure into austenite [2–5]. The austenized blank is then immediately transferred to water-cooled dies which simultaneously form and quench the blank. The main benefits of the DHPF method are that it takes advantage of the high formability of the high-temperature austenitic steel and, by quenching in the forming dies to form martensite, final strengths of 1500 MPa or higher can be produced with tight geometric tolerances [2,3,5].

The DHPF process can be performed with bare or coated steel, but decarburization and scaling will occur without a coating. Decarburization will lead to non-uniform hardenability and the oxide scale must be removed by shot-peening to allow for adequate paintability and weldability [2]. Pre-coated steel is commonly used to mitigate these problems; the most common coating applied to PHS is an Al-Si coating with a near-eutectic composition of 7–11 wt% Si [2,6]. The Al-

Si coating offers excellent protection from decarburization and oxidation during austenization, however, significant changes to the Al-Si coating during austenization create undesirable characteristics such as high surface roughness [7], brittleness [8], and inadequate cathodic corrosion resistance [4,9,10].

Zn-based coatings are the most common coating applied to sheet steel because these coatings can provide excellent barrier and cathodic corrosion resistance in addition to good weldability and paintability [2,4]. During the austenization step of DHPF, the Zn coating increases in temperature and becomes enriched with Fe through counterdiffusion with the substrate, causing the formation and dissolution of a series of Zn-based intermetallic phases as austenization continues [11]. Previous studies have demonstrated that just prior to passing through the peritectic point at 782 °C, the coating consisted entirely of Γ-Fe_3Zn_{10} [12,13]. Further austenization time then causes the Γ-Fe_3Zn_{10} to transform via the peritectic reaction [14]:

$$\Gamma\text{-}\mathrm{Fe_3Zn_{10}} \rightarrow \alpha\text{-}\mathrm{Fe(Zn)} + \mathrm{Zn(Fe)_{liq}} \tag{5.1}$$

forming a phase of Zn in solid solution with ferrite, α-Fe(Zn), and a Zn-rich liquid phase, $Zn(Fe)_{liq}$. When the blank is then quenched in the DHPF process, the $Zn(Fe)_{liq}$ solidifies back into Γ-Fe_3Zn_{10}. It has been found that a minimum of 15 vol% Γ-Fe_3Zn_{10} is required in the coating to obtain robust cathodic corrosion resistance [12,13], thus it is essential to form $Zn(Fe)_{liq}$ during austenization if robust cathodic protection of the substrate is desired. However, having $Zn(Fe)_{liq}$ in contact with the substrate during the application of a significant stress leads to conditions likely to cause liquid metal embrittlement (LME), which causes catastrophic brittle failure of the substrate [15]. Indeed, LME has been observed in many studies on PHS [16–20], and the prospect of LME during DHPF has severely limited the industrial application of Zn-coated PHS. Nevertheless, automotive manufacturers are interested in expanding the use of PHS into more corrosion prone areas of the body-in-white (BIW) to further reduce weight, creating a demand for PHS coatings that can offer cathodic corrosion resistance [2,21]. This demand has prompted efforts to define processing routes to produce Zn-coated PHS [2].

All of the currently available solutions to avoid LME in galvanized PHS are based on ensuring no liquid is present during forming. One method involves utilizing an extended transfer time or a pre-cooling step to solidify any $Zn(Fe)_{liq}$ present before stress is applied during the forming step [21,22]. This way, a relatively short austenization time can be used so that a certain amount of Γ-Fe_3Zn_{10} will be present in the final coating microstructure to provide robust cathodic resistance. Extending the transfer time of the DHPF process lowers the effective cooling rate, which has been shown to render the hardenability of the conventional 22MnB5 PHS grade insufficient to produce a fully martensitic microstructure [22,23]. Therefore, the hardenability of the substrate must be improved in order to enable this process.

To this end, a prototype steel with composition 0.19C-2.5Mn-0.26Si-0.005B (wt%) was developed. The objective of this study is to define a processing route with which this prototype grade can be produced such that after DHPF it simultaneously satisfies the strength and corrosion protection targets previously mentioned, i.e. fully martensitic microstructures and TS $\geq$ 1500 MPa, fraction of Γ-Fe_3Zn_{10} in the coating microstructure $\geq$ 15 vol%, while avoiding LME.

5.2 MATERIALS AND METHODS

The material used in this study was a novel grade based on the composition of 22MnB5 but with additional Mn to increase hardenability. The chemical composition is listed in Table 5.1. The substrate was fabricated at United States Steel Research (Munhall, Pennsylvania) via hot rolling and cold rolling to a final sheet thickness of 1.2 mm, as shown in Fig. 5.1.

Table 5.1. Chemical composition of the alloy (wt%).

C	Mn	Si	B	P	Al
0.19	2.48	0.26	0.005	0.01	0.04

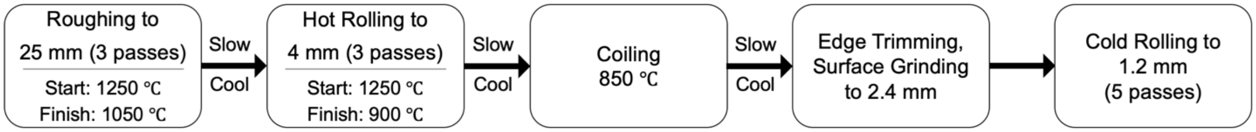

Fig. 5.1. Processing route steps for producing the prototype alloy.

5.2.1 Dilatometry

The austenitic transformation temperatures during heating (Ac_1 and Ac_3) and the phase transformation temperatures upon cooling were determined using a BÄHR DIL 805 dilatometer. For tests not involving deformation, test specimens from transfer bars were machined into 3 mm ID x 4 mm OD x 10 mm hollow cylinders. A thermocouple was welded to the middle of each specimen before the test and dilation was measured by recording the displacement of quartz rods which move with the expansion of the test specimen. Quench dilatometry tests were utilized to collect the data necessary to create a continuous cooling transformation (CCT) diagram. First, tests were performed to determine the Ac_1 and Ac_3 temperatures, which were found to be 700 °C and 835 °C respectively. These temperatures were found to be independent of heating rate between 5–15 °C/s. To collect the data required for the construction of the CCT diagram, specimens were heated at a rate of 10 °C/s to a peak temperature of 875 °C, held at the peak temperature for 120 s, then quenched to room temperature at a variety of cooling rates between −1 and −75 °C/s. Inflection points on the dilation vs. time curves at various cooling rates were used to identify phase transformation temperatures for this material. The points were then assigned to a specific phase transformation start or finish by using microstructure images, microhardness results, and by consulting the literature.

Dilatometry tests with a compression step at the desired stamping temperatures (referred to as deformation dilatometry) were completed to determine the effect of strain on the M_s and M_f transformation temperatures during cooling to room temperature. As compression could cause buckling in the thin-walled quench dilatometry specimens, solid cylinders with dimensions of 5 mm OD x 10 mm were used instead. The same dilatometer was used, along with identical heating rate, peak temperature, and peak temperature soak time as the dilatometry tests for the construction of the CCT diagram. After 120 s of soak time at the peak temperature, samples were cooled to the stamping temperatures of interest (700, 650, and 600 °C) at a rate of −20 °C/s using controlled gas flow and then compressed at a strain rate of 1 s^{-1} to total strains of $\varepsilon = 0.10$ and 0.20. Finally, specimens were quenched past the M_f temperature at −75 °C/s.

5.2.2 Galvanizing

The prototype steel was acquired without a coating and was galvanized using the McMaster Galvanizing Simulator (MGS), full details of which are provided elsewhere [24]. Large sheets of the steel were cut using a shear into the 120 mm x 200 mm panels required for the simulator. Prior to galvanizing, the panels were immersed and brushed in a 2 wt% NaOH solution at 80 °C in order to remove residual oils and other contaminants. The panels were then quickly rinsed in warm deionized water, followed by a final rinse in isopropanol. Before being placed in the MGS, a K-type thermocouple was welded to the surface of the sample to accurately record temperature throughout the process. As seen in Fig. 5.2, the panels were heated to a peak annealing temperature (PAT) of 710 °C and held for 120 s in order to produce a microstructure consisting of ferrite and pearlite. The atmosphere consisted of N_2-5 vol% H_2 and was set to a controlled dewpoint of −30 °C to mimic typical industrial practices. Following the heat treatment, the panel was cooled to 460 °C at −20 °C/s and dipped in a Fe saturated 0.20 wt% Al (dissolved) galvanizing bath held at 460 °C for 4 s. After dipping, the coated panels were cooled to near room temperature at approximately −15 °C/ using N_2 gas jets. The galvanized coating weight was measured by X-ray fluorescence to be approximately 9 μm, corresponding to 66 gm^{-2}.

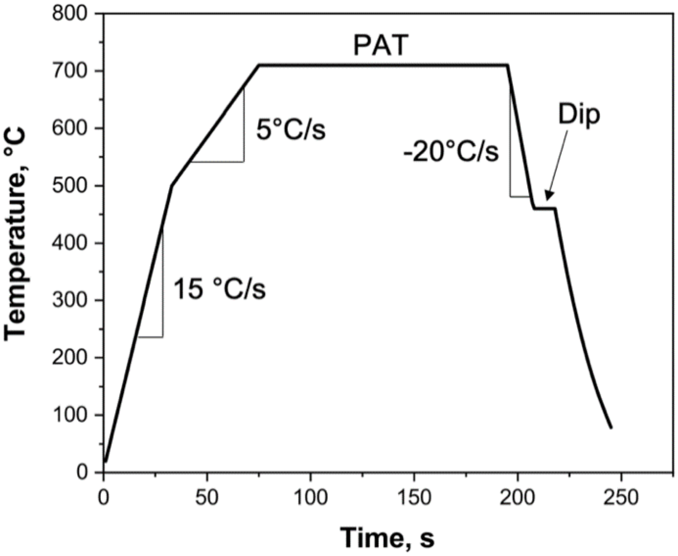

Fig. 5.2. Galvanizing heat treatment schematic.

5.2.3 Direct Hot Press Forming

Square blanks with dimensions of 100 mm x 100 mm were used for DHPF. The coated blanks were excised out of a section of the galvanized panel identified in a previous study to have the most uniform heating history [24]. Austenization of the blanks was executed in a conventional box furnace in ambient atmosphere held at 890 °C, imitating the industrial process. To determine the heating rate once the blank was inserted into the furnace, a K-type thermocouple was spot-welded to the centre of a blank and the temperature was recorded (Fig. 5.3). Likewise, when the sample was removed from the furnace its temperature was recorded as the blank was allowed to cool to room temperature in order to determine the transfer time necessary to perform stamping at the desired temperatures (Fig. 5.4). This procedure was performed six times in order to ensure reproducibility. The beginning of austenization was defined to start once the blank reached its Ac_3 temperature + 20 °C. As seen in Fig. 5.3, this occurred approximately 160 s after the blank was inserted into the furnace. Therefore, the reported austenization times of 30, 60, 120, and 180 s in this study correspond to the blanks being in the furnace for total times of 190, 220, 280, and 340 s respectively.

Since the heating and cooling rates were very consistent between tests, it was not necessary to monitor the temperature in-situ during DHPF experiments. After the prescribed austenization time was reached when executing the DHPF process, austenized blanks were removed from the furnace and allowed to cool in ambient air until the desired stamping temperature was met before being transferred to the water-cooled die set. It was determined that the transfer times required to stamp at the desired temperatures of 700, 650, and 600 °C were 8, 11.5, and 16 s respectively (Fig. 5.4). A 250 kN Instron frame was used to bring the die and punch together. A schematic of the DHPF part is shown in Fig. 5.5, with dimensions provided in mm.

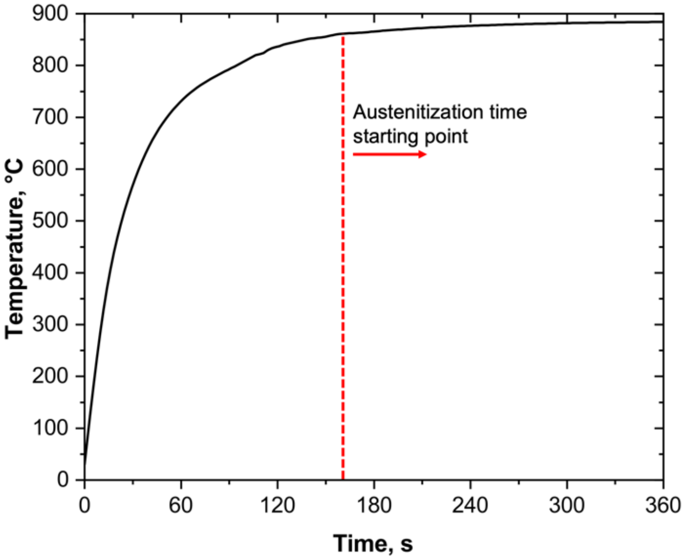

Fig. 5.3. Heating rate in the austenization furnace.

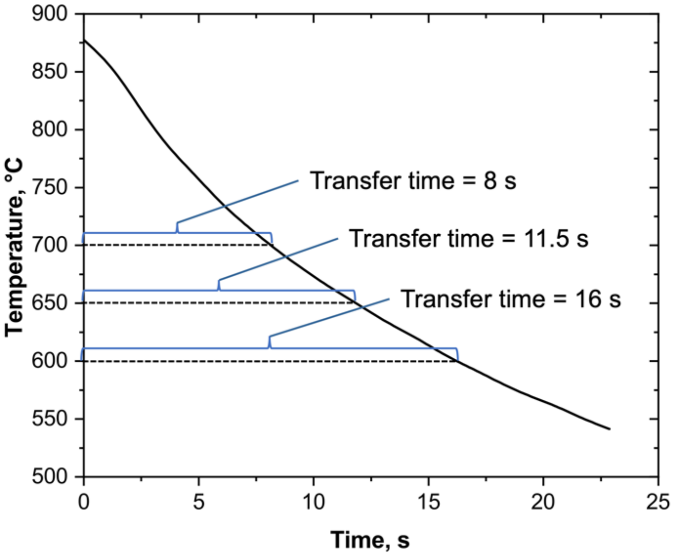

Fig. 5.4. Cooling in ambient air upon removal from the austenization furnace and the required transfer times to stamp at desired temperatures.

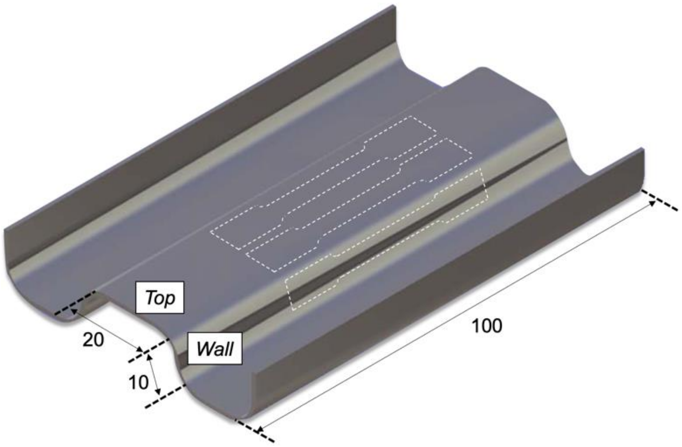

Fig. 5.5. Schematic of DHPF part with locations of tensile coupons.

5.2.4 Tensile Testing

Uniaxial tensile tests were conducted in order to determine the yield strength (YS), TS, uniform elongation (UE), post-uniform elongation (PUE), and total elongation (TE) of the material as a function of austenization time, DHPF stamping temperature, and strain imposed by the forming process. Tensile coupons were taken from the top and the wall of the DHPF part (Fig. 5.5) to determine mechanical properties as a function of strain imposed by the forming process [25]. To improve statistical results and ensure reproducibility, three DHPF parts were produced for each combination of austenization time and stamping temperature. Therefore, a total of six tensile tests were performed at each combination of austenization time, stamping temperature, and section of the DHPF part. Due to small size of the DHPF part, it was not possible to excise ASTM E8 sub-size specimens [26]. Instead, a smaller tensile coupon geometry was used [25], the dimensions of which are shown in Fig. 5.6. Tensile tests were conducted using a 100 kN Instron testing machine and a crosshead speed of 1 mm/min, and strain was measured using a contact extensometer. The reduction of area of each fractured tensile coupon was measured according to ASTM E8 [26]:

$$Z = \frac{A_0 - A_f}{A_0} \tag{5.2}$$

where A_0 is the original gauge area as measured by calipers, and A_f is the final area measured by light optical microscopy.

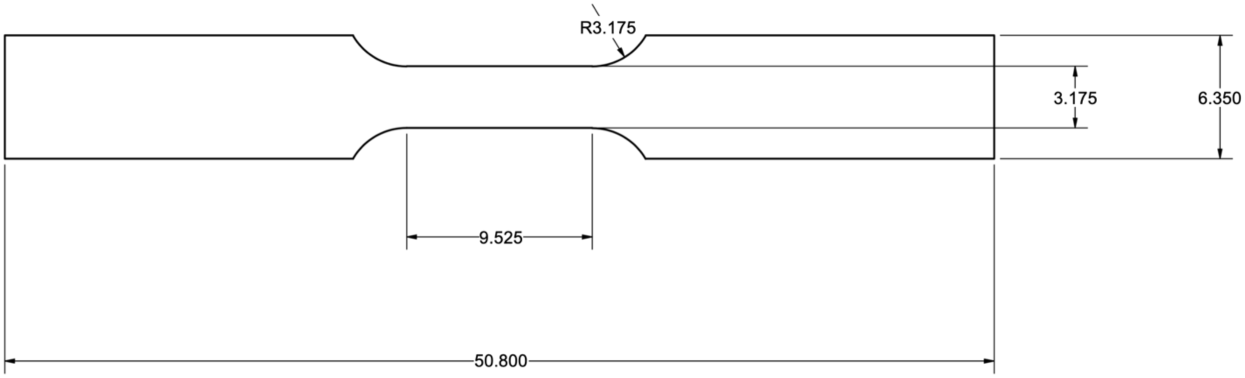

Fig. 5.6. Dimensions of tensile specimens taken from DHPF parts, in mm.

5.2.5 Substrate and Coating Microstructures

Samples for substrate and coating microstructural images were cold mounted in epoxy resin, then ground and polished according to standard metallographic procedures. The substrate and coating microstructures were imaged using a JEOL 6610-LV scanning electron microscope (SEM). In all cases, an accelerating voltage of 15 kV was used with a working distance of 10 mm. The working distance was increased to 25 mm for taking fractographs to improve the depth of field. Prior to being placed in the SEM, all samples except fracture surfaces were coated in a thin layer of carbon in order to minimize charging.

For substrate imaging, the microstructure was revealed by etching with 2 vol% nital for approximately 5 s. Samples for substrate imaging and fractography were imaged using the secondary electron detector. Samples for coating analysis and fractography were not etched. To reveal phase contrast, coating microstructures used the backscattered electron detector.

5.3 RESULTS

5.3.1 As-Received Microstructure

The as-received microstructure is shown in Fig. 5.7. It consisted of a roughly even mixture of ferrite and pearlite with cementite decorating grain boundaries. The grains were elongated in the rolling direction (RD), which is often a consequence of the segregation of Mn during casting.

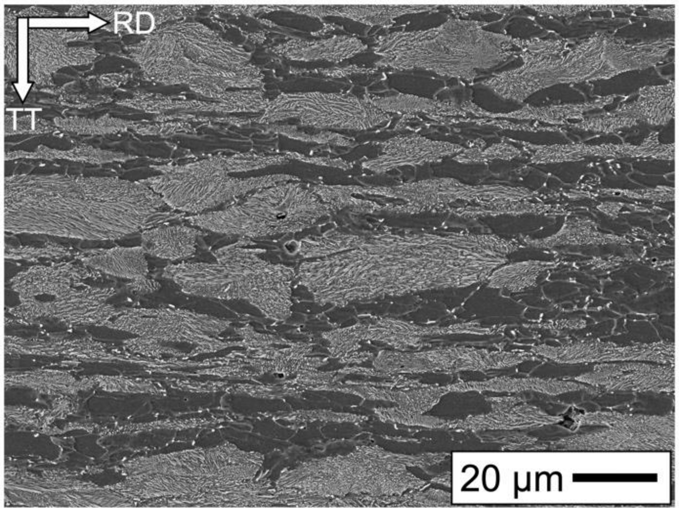

Fig. 5.7. As-received microstructure of the prototype alloy.

5.3.2 Dilatometry

Fig. 5.8 displays the CCT diagram constructed for this prototype grade based on the dilatometry results. At the end of each curve, microhardness values (HV) are presented. It can be seen that the critical cooling rate in order to attain a fully martensitic microstructure for this alloy is −5 °C/s. Cooling at −5 °C/s produced a microhardness of 435 HV, which steadily increased to 474 HV at the maximum tested cooling rate of −75 °C/s. This result proves that the hardenability has successfully been improved by the additional Mn content and suggests a robust processing window where fully martensitic microstructures can be achieved even when performing the DHPF at reduced temperatures, i.e. slow cooling rates.

Deformation dilatometry was executed to determine the effect of deformation on the martensitic transformation temperatures when compression was applied at the target stamping temperatures of 600, 650, and 700 °C. A summary of these results is presented in Fig. 5.9. It is clear that deformation significantly reduced the M_s and M_f temperatures relative to the undeformed condition, however, stamping temperature and the amount of strain applied had a negligible effect on the deformed values of M_s and M_f. This result indicates that the hardenability of the prototype grade decreased as a result of deformation. This is consistent with other reports in the literature [27–29], where this effect has been attributed to the mechanical stabilization of austenite [27–29].

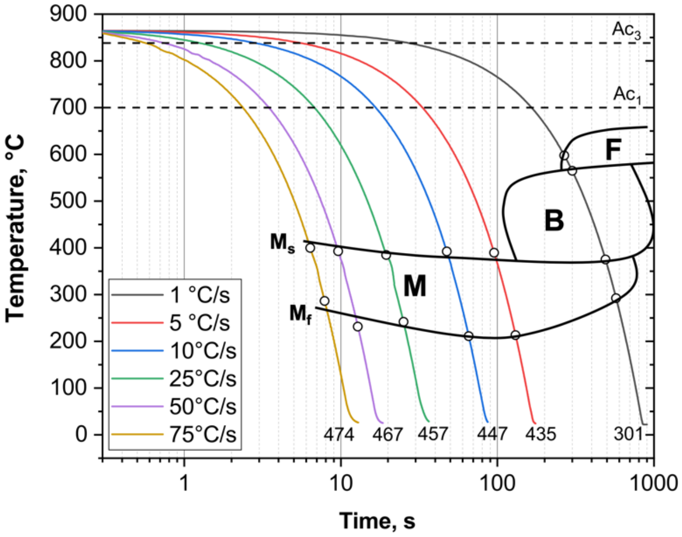

Fig. 5.8. Continuous cooling transformation diagram for the prototype steel. Microhardness values (HV) for the resulting steel are shown at the end of each curve.

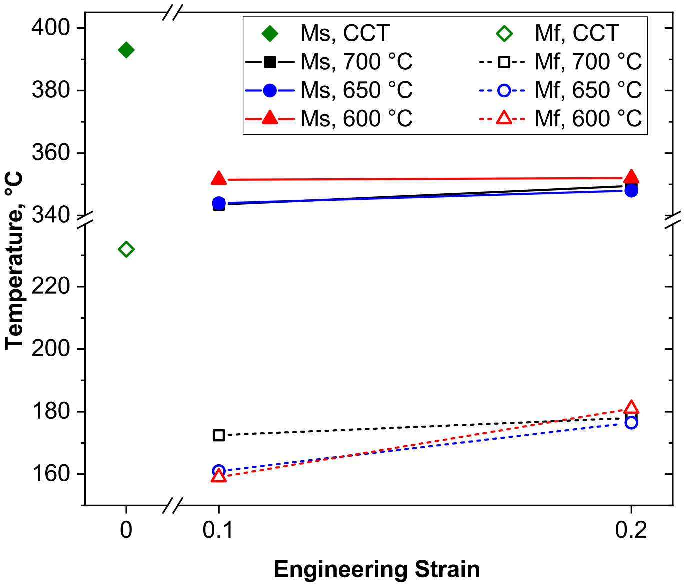

Fig. 5.9. M_s and M_f temperatures for undeformed specimens and deformed specimens as a function of compressive strain and deformation temperature.

5.3.3 DHPF Substrate Microstructures

The substrate microstructures after DHPF are shown in Fig. 5.10. The samples austenized for only 30 s (a-c) show small amounts of ferrite, which was likely a result of insufficient austenization time. The rest of the microstructures are fully martensitic with no visual differences between austenization times of 60–180 s and stamping temperatures from 600–700 °C.

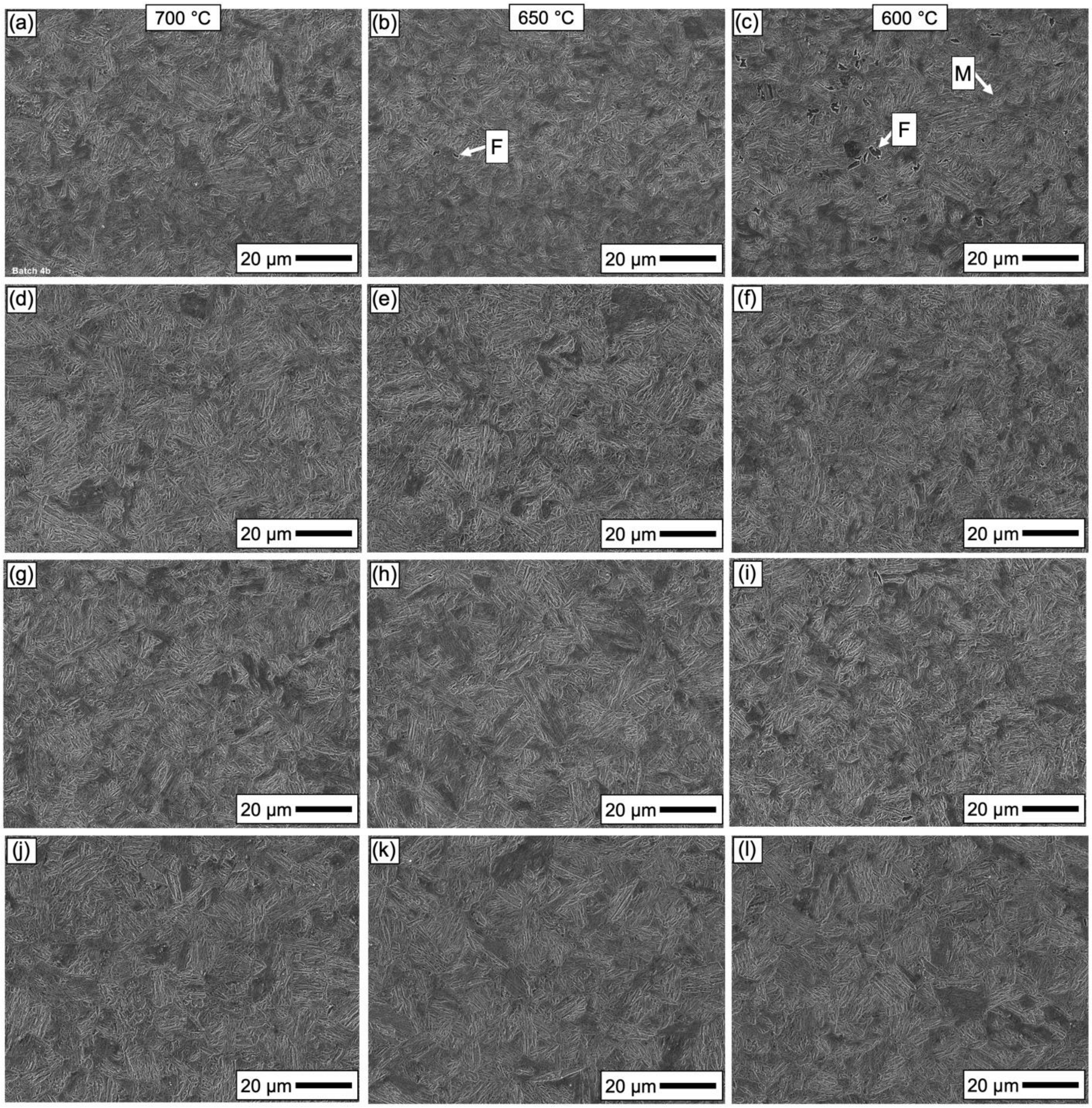

Fig. 5.10. Substrate microstructures after DHPF as a function of stamping temperature (as indicated at the top of each column) and austenization time: (a-c) 30 s, (d-f) 60 s, (g-i) 120 s, and (j-l) 180 s.

5.3.4 DHPF Mechanical Properties

The mechanical properties of the prototype alloy after DHPF were tested as a function of austenization time, stamping temperature, and strain imposed by the location on the formed part. Representative stress-strain curves for a stamping temperature of 700 °C are shown in Fig. 5.11. Red and black lines correspond to data from the top and the wall of the DHPF part, respectively. Owing to the fully or nearly fully martensitic microstructures observed over all austenization times and stamping temperatures (Fig. 5.10), the stress-strain response is very similar over all conditions. It is also noted that the stress-strain curves of all of the samples which correspond to fully martensitic microstructures meet the target of TS ≥ 1500 MPa while exhibiting significant UE and PUE. To more clearly decipher the evolution of mechanical behaviour with austenization time and stamping temperature, it is useful to compare summative properties.

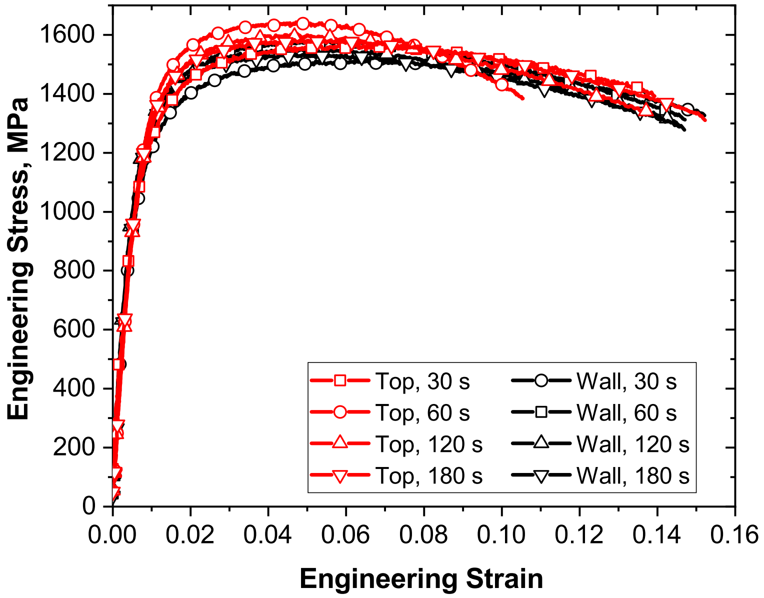

Fig. 5.11. Representative stress-strain curves (tested in TD orientation) for the prototype alloy in the DHPF condition stamped at 700 °C.

Summative properties for the prototype alloy in the DHPF condition are shown in Fig. 5.12. It is again evident that stamping after only 30 s of austenization did not yield full strength properties relative to the longer austenization times. Although the specimens austenized for 30 s exhibit approximately 1500 MPa TS, it is clear that austenization was not quite completed and some ferrite was retained in the microstructure after quenching (Fig. 5.10 (a-c)). When the austenization time was at least 60 s, the TS was over 1500 MPa at every tested stamping temperature, regardless of whether samples were excised from the top or the wall. At every tested condition, the mean TS was higher for samples taken from the top of the DHPF part; on average, over all conditions, the YS and TS were approximately 46 MPa and 32 MPa higher for the top than for the wall. For each stamping temperature, the average TS peaks after 60 s of austenization. The mean peak TS values are 1586, 1645, and 1628 MPa for stamping temperatures of 700, 650, and 600 °C, respectively. The TS at the top then slightly declines with further austenization to mean values of 1552, 1607, and 1598 MPa for stamping temperatures of 700, 650, and 600 °C, respectively. Based on these results, it is concluded that austenization times of at least 60–180 s met the strength target of TS ≥ 1500 MPa, regardless of stamping temperature.

The TE at fracture for the prototype alloy at each combination of austenization time and stamping temperature are shown in Fig. 5.12 (b), (d), and (f). For each austenization time, results from the top and wall are split into two different bars. The TE is split into components of UE and PUE. Similar to the TS and YS, a slight difference can be observed between values from the top and the wall; in 10 out of 12 of the tested conditions, the average TE was lower for the top than for the wall. Once the austenization time was 60 s or longer the elongation properties did not change significantly. The significant extent of PUE observed in all conditions implies that LME has been avoided, since LME would have resulted in little to no plastic deformation before fracture.

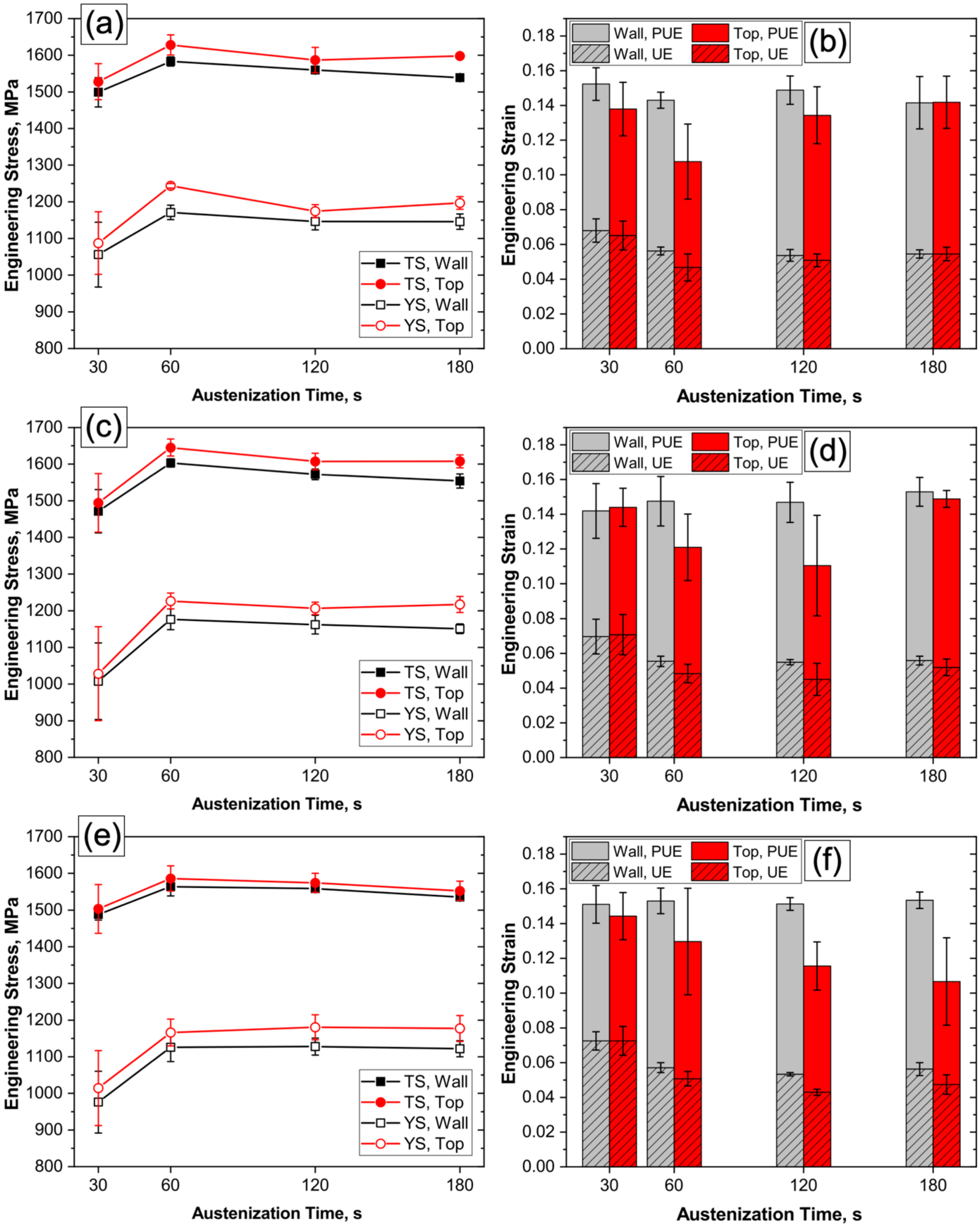

Fig. 5.12. Summative mechanical properties of the prototype steel at the top and the wall of the DHPF part at each combination of austenization time and stamping temperature. Each row shows results from a different stamping temperature: (a,b) 700 °C, (c,d) 650 °C, and (e,f) 600 °C.

5.3.5 Fracture

Macroscopically, it was observed that all fracture coupons exhibited the classic "cup and cone" appearance characteristic of ductile failure. Some tensile coupons which resulted in representative stress-strain curves were selected for fractography, shown in Fig. 5.13. Large spherical inclusions and horizontal tears (parallel to the gauge width) can also be observed, such as in the lower half of Fig. 5.13 (a) and near the top of Fig. 5.13 (b). Most importantly, the fracture surfaces feature void nucleation and growth characteristic of ductile failure, which supports the conclusion that brittle fracture by LME has been avoided.

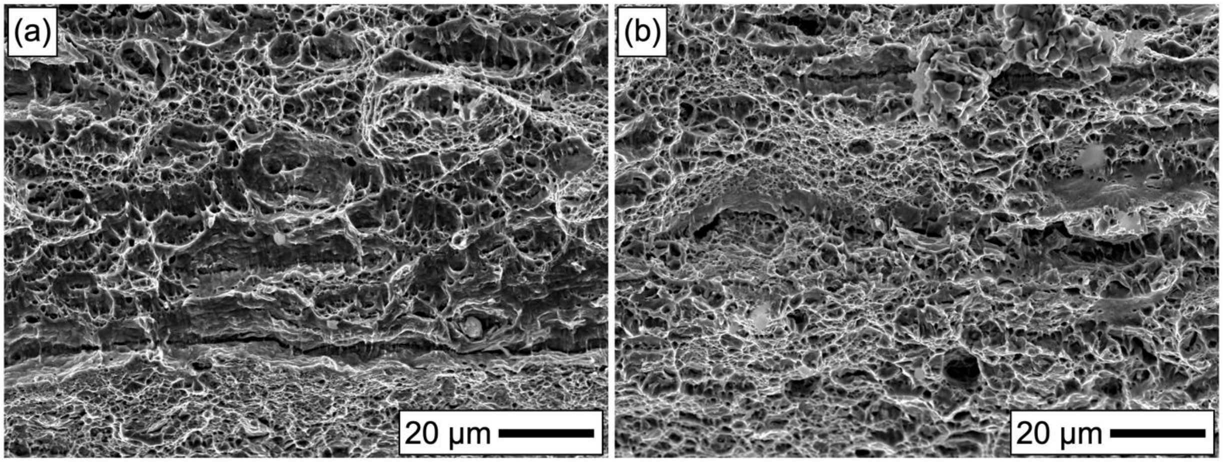

Fig. 5.13. SEM images taken from the centre of fracture surfaces after an austenization time of 60 s, stamped at (a) 700 °C and (b) 600 °C.

The reduction of area of the fractured surface relative to the original gauge area of the tensile specimen is shown in Fig. 5.14. Each point includes data from both the top and the wall, as these values were very similar. As expected based on the results of the tensile tests, the reduction of area was not a function of stamping temperature. The mean reduction of area for samples austenized for only 30 s was between 0.12–0.17 for all stamping temperatures; increasing austenization time to 60 s or longer resulted in reduction of area of 0.23–0.26. Although the average

TE remained relatively constant across all austenization temperatures, the reduction of area for samples austenized for only 30 s was lower than the rest. This can again be correlated to the microstructures (Fig. 5.10), where small amounts of ferrite were observed only in samples austenized for 30 s. These high amount of reduction of area is consistent with the significant amount of PUE observed in tensile tests (Fig. 5.12) and the observation of ductile fracture features on the fracture surfaces of failed tensile coupons (Fig. 5.13).

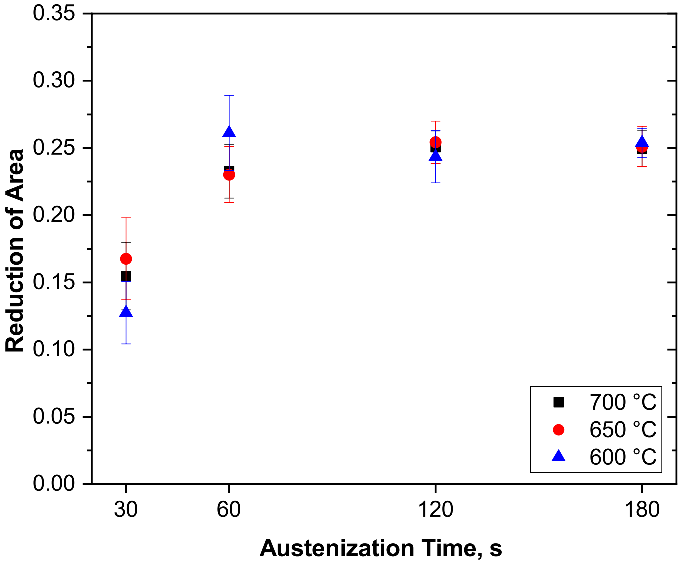

Fig. 5.14. Reduction of area of DHPF tensile coupons as a function of annealing time and stamping temperature.

5.3.6 Coating Evolution

The microstructural evolution of the coating at different austenization times and regions of the DHPF part is shown in Fig. 5.15 and Fig. 5.16. The micrographs were taken using the backscattered electron detector and were taken from the DHPF part locations indicated by Lee et al. [17] to visualize the effect of strain applied during DHPF on the coating. The Γ-Fe_3Zn_{10} phase has a higher Zn concentration and thus a higher average atomic number than α-Fe(Zn), giving it a greater backscatter electron coefficient. This enabled phase contrast by making Γ-Fe_3Zn_{10} appear brighter than α-Fe(Zn). First, it can be seen that the average thickness of the coating increased with respect to austenization time. This was expected as the Zn coating is well known to grow through counter-diffusion with the substrate [4,11–13]. Diffusion into the substrate also means that the average Fe content of the coating increases with austenization time. This has the effect of shifting the phase equilibrium towards α-Fe(Zn) from Γ-Fe_3Zn_{10}, which can be confirmed qualitatively by comparing Fig. 5.15 and Fig. 5.16.

The top region of the parts experienced minimal amounts of strain during the forming process and therefore exhibits a lower concentration of cracks relative to the outer wall. The inner wall, noted to be a region of die-friction [17], displayed some cracks and typically had a slightly lower coating thickness compared to other regions of the part. In the inner corner where the part was deformed in compression, no cracks were observed; this is contrasted by the outer corner which showed wide cracks that opened up due to the large tensile forces at this location during forming. Most importantly, no LME-type cracks were seen, and all observed coating micro-cracks were observed terminating at the coating-substrate interface.

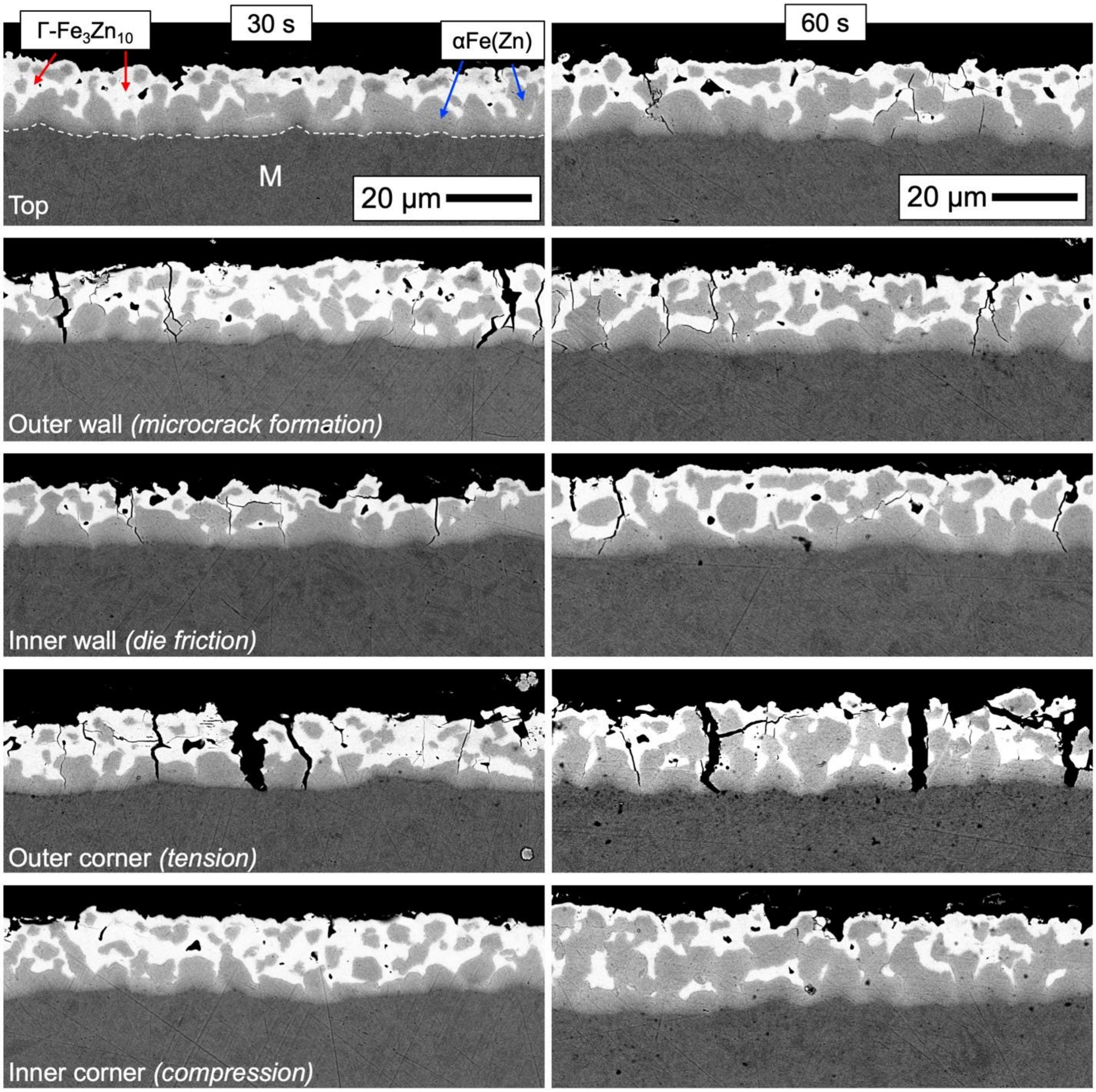

Fig. 5.15. Coating microstructural evolution at different locations on the formed part, as indicated. The left and right columns show the final microstructures after 30 s and 60 s of austenization respectively, both stamped at 700 °C.

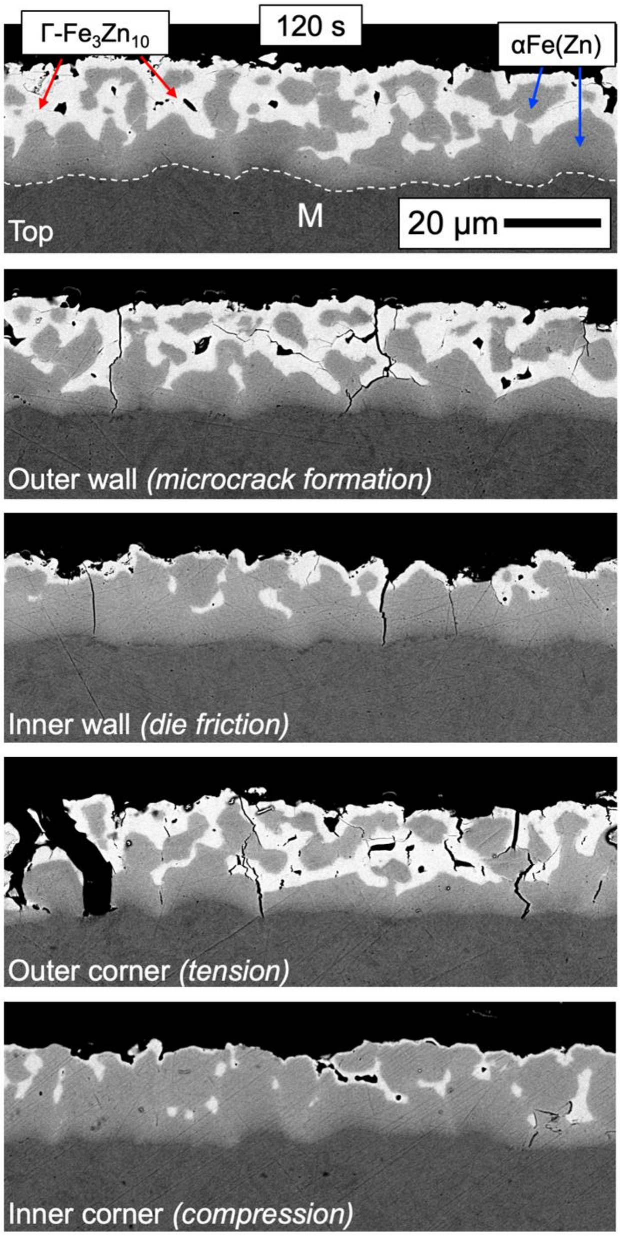

Fig. 5.16. Coating microstructures at different areas of the DHPF part after 120 s of austenization time and stamped at 700 °C.

5.4 DISCUSSION

In order to avoid LME, the transfer time of the DHPF process was intentionally extended to allow the peritectic reaction to occur such that $Zn(Fe)_{liq}$ solidified before the forming step, a method that has been shown to be feasible in other studies [21,22,30]. This successfully prevented LME by removing the liquid during the application of tensile stress. However, extending the transfer time renders the hardenability of 22MnB5 insufficient to produce a fully martensitic microstructure [23,31]. To this end, a new grade of PHS with increased Mn content was created with the aim of creating a reasonable process window for attainment of fully martensitic microstructures when stamping below the peritectic temperature.

Results from dilatometry tests have shown that the hardenability of this prototype grade has been significantly improved compared to that of 22MnB5. Fig. 5.8 shows that the critical cooling rate has been reduced to only −5 °C/s, much lower than the −27 to −35 °C/s often quoted for 22MnB5 [2,32–34]. Deformation dilatometry revealed that the M_s and M_f temperatures were significantly reduced by the application of deformation (Fig. 5.9), representing a decrease in hardenability relative to the undeformed condition. This finding has also been reported in other studies on PHS grades subjected to the DHPF process [27–29,35] and is attributed to the mechanical stabilization of austenite, whereby dislocations generated by deformation or forming act as barriers to martensitic transformation fronts, and therefore have the effect of decreasing hardenability [36–38]. However, testing on formed parts showed fully martensitic microstructures (Fig. 5.10) and TS > 1500 MPa (Fig. 5.12), indicating that this loss in hardenability was not enough to cause the formation of ferrite in the final microstructure.

Microstructural imaging indicated that 30 s of austenization was slightly too short to fully austenize the blank. This resulted in some ferrite in the final microstructure and slightly reduced mechanical properties relative to the fully martensitic samples (Fig. 5.11 and Fig. 5.12). With 60 s of austenization or more, fully martensitic microstructures and TS of approximately 1550–1600 MPa were attained. The minor decrease in TS with increasing austenization time could be due to an increase in prior austenite grain size as was observed by Golem et al. [39]. Most importantly, it is evident from these results that processing conditions that involved an austenization time of 60–180 s and any stamping temperature between 600–700 °C met the targets for formation of fully martensitic microstructures and TS ≥ 1500 MPa.

The dominant fracture mode of all samples was ductile fracture. The trend in reduction of area measured from fractured tensile coupons (Fig. 5.14) is consistent with the microstructural and fracture surface observations. The samples austenized for only 30 s contained minute fractions of ferrite displayed approximately 15% reduction of area, compared to the 25% reduction of area for austenization times of 60 s or more. This difference can be attributed to the additional cleavage-type failure caused by decohesion at ferrite-martensite interfaces. The observations of ductile fracture and significant necking before failure show that LME was avoided at every combination of DHPF parameters tested.

As austenization time increased, the coating continued to interdiffuse with the substrate causing an increase in thickness and bulk Fe content. The fraction of Γ-Fe_3Zn_{10} appears to decrease with austenization time, an observation which has also been made in numerous other studies [4,11,25,40–43]. It has been determined by Dever et al. [12] that a minimum of 15 vol% Γ-Fe_3Zn_{10} is required for robust cathodic protection, which appears to have been met based on comparing the coating micrographs in Fig. 5.15 and Fig. 5.16 to images from previous studies [13,43] and considering quantitative X-ray diffraction (XRD) testing from other studies [13,25,43], though XRD testing on these samples is required to confirm this. Microstructural images at different areas of the DHPF part show very similar results to those reported by Lee et al. [17], with the important distinction that in the present study no LME-type cracks were observed. Thin through-thickness coating cracks were observed at the inner and outer wall, corner, as well as sometimes the top of the part. However, these cracks terminated at the substrate in all cases. Strictly, no assertion can be made on whether or not ≥ 15 vol% Γ-Fe_3Zn_{10} is attained in the coating microstructure as XRD tests have not yet been completed. However, the coating images, early XRD results, and comparisons to previous studies [13,25,43] suggest that the Γ-Fe_3Zn_{10} target will be met at all austenization times.

5.5 CONCLUSIONS

A new grade of Zn-coated PHS containing 2.5 wt% Mn was characterized on the basis of compatibility with the DHPF process with an extended transfer time while meeting the targets of attaining fully martensitic microstructures, TS ≥ 1500 MPa, ≥ 15 vol% Γ-Fe_3Zn_{10}, and avoiding LME. The most important conclusions are:

- The additional Mn significantly improved the hardenability of this prototype grade relative to conventional PHS grades. The critical cooling rate for formation of a fully martensitic microstructure was determined to be −5 °C/s, much lower than for conventional grades.
- Tensile tests on DHPF material showed that the microstructure and mechanical properties of the grade were mainly a function of austenization time. With samples austenized for 30 s, small amounts of ferrite were observed in the microstructure and TS was approximately 1500 MPa. Austenization times of 60–180 s resulted in properties which met the targets of fully martensitic microstructures and TS ≥ 1500 MPa.
- No evidence of LME was detected at any austenization time or stamping temperature. Ductile fracture was the dominant failure mechanism observed in all tensile coupons and reduction of area before fracture was significant, about 0.20–0.25. Cracks were observed in the coating of the formed parts, but these cracks were arrested at the substrate in all cases.
- The microstructural evolution of the coating was a strong function of austenization time with the amount of the cathodically-protective Γ-Fe_3Zn_{10} phase decreasing as austenization

time increased. It is likely that the requirement of ≥15 vol% Γ-Fe_3Zn_{10} has been met based on the limited results available and comparison to other very similar studies.

- It has been determined that a process window that meets the requirements of fully martensitic microstructures with TS ≥ 1500 MPa and ≥15 vol% Γ-Fe_3Zn_{10} in the coating for robust cathodic protection while avoiding LME exists, and includes austenization times of 60–180 s and DHPF stamping temperatures of 600–700 °C.

ACKNOWLEDGEMENTS

The authors would like to thank the International Zinc Association – Galvanized Autobody Partnership (IZA-GAP) and the Natural Sciences and Engineering Research Council of Canada (NSERC, grant CRDPJ 522309 – 17) for their financial support. The authors would also like to thank U.S. Steel Corporation for the provision of the steel used in this study and the Canadian Centre for Electron Microscopy.

REFERENCES

[1] S. Keeler, M. Kimchi, P. J. Mooney, Advanced High-Strength Steels Apllication Guidelines Version 6.0, World Auto Steel. 6 (2017) 314. http://www.worldautosteel.org/download_files/AHSS Guidelines V6/00_AHSSGuidelines_V6_20170430.pdf.

[2] T. Taylor, A. Clough, Critical review of automotive hot-stamped sheet steel from an industrial perspective, Mater. Sci. Technol. 0836 (2018) 1–53. https://doi.org/10.1080/02670836.2018.1425239.

[3] H. Karbasian, A.E. Tekkaya, A review on hot stamping, J. Mater. Process. Technol. 210

(2010) 2103–2118. https://doi.org/10.1016/j.jmatprotec.2010.07.019.

[4] D.W. Fan, B.C. De Cooman, State-of-the-knowledge on coating systems for hot stamped parts, Steel Res. Int. 83 (2012) 412–433. https://doi.org/10.1002/srin.201100292.

[5] D.W. Fan, H.S. Kim, B.C. De Cooman, A review of the physical metallurgy related to the hot press forming of advanced high strength steel, Steel Res. Int. 80 (2009) 241–248. https://doi.org/10.2374/SRI08SP131.

[6] R.W. Richards, R.D. Jones, P.D. Clements, H. Clarke, Metallurgy of continuous hot dip aluminising, Int. Mater. Rev. 39 (1994) 191–212. https://doi.org/10.1179/imr.1994.39.5.191.

[7] F. Jenner, M.E. Walter, R. Mohan Iyengar, R. Hughes, Evolution of phases, microstructure, and surface roughness during heat treatment of aluminized low carbon steel, Metall. Mater. Trans. A Phys. Metall. Mater. Sci. 41 (2010) 1554–1563. https://doi.org/10.1007/s11661-009-0105-x.

[8] G. Zhong-Xiang, W. Kai, Z. Yi-Sheng, Z. Bin, Cracking and interfacial debonding of the Al-Si coating in hot stamping of pre-coated boron steel, Appl. Surf. Sci. 316 (2014) 595–603. https://doi.org/10.1016/j.apsusc.2014.08.043.

[9] L. Dosdat, J. Petitjean, T. Vietoris, O. Clauzeau, Corrosion resistance of different metallic coatings on press-hardened steels for automotive, Steel Res. Int. 82 (2011) 726–733. https://doi.org/10.1002/srin.201000291.

[10] C. Allély, L. Dosdat, O. Clauzeau, K. Ogle, P. Volovitch, Anticorrosion mechanisms of aluminized steel for hot stamping, Surf. Coatings Technol. 238 (2014) 188–196. https://doi.org/10.1016/j.surfcoat.2013.10.072.

[11] R. Autengruber, G. Luckeneder, S. Kolnberger, J. Faderl, A.W. Hassel, Surface and coating analysis of press-hardened hot-dip galvanized steel sheet, Steel Res. Int. 83 (2012)

1005–1011. https://doi.org/10.1002/srin.201200068.

[12] C. Dever, J. Kish, J. McDermid, Corrosion Properties of Hot Dip Zinc Galvanized Coatings on 22MnB5 Press Hardened Steels, in: Galvatech 2017 Conf. Proc., ISIJ International, Tokyo, Japan, 2017: pp. 385–392.

[13] C. Dever, Effect of Coating Microstructure on the Electrochemical Properties of Continuous Galvanized Coatings on Press Hardened Steels, McMaster University, 2018.

[14] J. Nakano, D. V. Malakhov, G.R. Purdy, A crystallographically consistent optimization of the Zn-Fe system, Calphad Comput. Coupling Phase Diagrams Thermochem. 29 (2005) 276–288. https://doi.org/10.1016/j.calphad.2005.08.005.

[15] M.G. Nicholas, C.F. Old, Liquid metal embrittlement, J. Mater. Sci. 14 (1979) 1–18.

[16] L. Cho, H. Kang, C. Lee, B.C. De Cooman, Microstructure of liquid metal embrittlement cracks on Zn-coated 22MnB5 press-hardened steel, Scr. Mater. 90–91 (2014) 25–28. https://doi.org/10.1016/J.SCRIPTAMAT.2014.07.008.

[17] C.W. Lee, W.S. Choi, L. Cho, Y.R. Cho, B.C. De Cooman, Liquid-Metal-Induced Embrittlement Related Microcrack Propagation on Zn-coated Press Hardening Steel, ISIJ Int. 55 (2015) 264–271. https://doi.org/10.2355/isijinternational.55.264.

[18] P. Drillet, R. Grigorieva, G. Leuillier, T. Vietoris, Study of Cracks Propagation Inside the Steel on Press Hardened Steel Zinc Based Coatings, in: Galvatech 2011, 2011: pp. 3–8.

[19] J. Li, H. Yang, S. Zhang, X. Liu, W. Hua, Study of Crack Generation and Propagation Mechanism Inside Zinc-coated Press-hardened Steel, in: Galvatech 2013 Conf. Proc., 2013: pp. 243–248.

[20] Z. Ghanbari, J.G. Speer, K.O. Findley, Coating Evolution and Mechanical Behavior of Zn-Coated Press-Hardening Sheet Steel, 5th Int. Conf. Hot Sheet Met. Form. High-Performance Steel. (2015).

[21] K. Isaksson, M. Jönsson, D. Berglund, The direct press hardening process for Zn-coated ultra-high strength steels, in: 2nd Int. Conf. Adv. High Strength Steel Press Hardening, Changsha, China, 2015: pp. 1–8.

[22] T. Kurz, P. Larour, J. Lackner, T. Steck, G. Jesner, Press-hardening of zinc coated steel - Characterization of a new material for a new process, in: IOP Conf. Ser. Mater. Sci. Eng., 2016. https://doi.org/10.1088/1757-899X/159/1/012025.

[23] K. Hu, S. Zhou, R. Han, J. Gao, Y. Yang, Microstructure Evolution and Simulation in 22MnB5 Steel during Hot Stamping, J. Mater. Sci. Chem. Eng. 06 (2018) 9–14. https://doi.org/10.4236/msce.2018.68002.

[24] E.M. Bellhouse, J.R. McDermid, Selective oxidation and reactive wetting during hot-dip galvanizing of a 1.0 pct Al-0.5 pct Si TRIP-assisted steel, Metall. Mater. Trans. A Phys. Metall. Mater. Sci. 43 (2012) 2426–2441. https://doi.org/10.1007/s11661-011-0983-6.

[25] K. Maleki, On the Origin of Micro-Cracking in Zn-Coated Press Hardened Steels, McMaster University, 2019.

[26] ASTM E8 / E8M-16ae1, Standard Test Methods for Tension Testing of Metallic Materials, ASTM International, West Conshohocken, PA, 2016. https://doi.org/10.1520/E0008_E0008M-13A.

[27] M. Nikravesh, M. Naderi, G.H. Akbari, W. Bleck, Phase transformations in a simulated hot stamping process of the boron bearing steel, Mater. Des. 84 (2015) 18–24. https://doi.org/10.1016/j.matdes.2015.06.108.

[28] A. Barcellona, D. Palmeri, Effect of plastic hot deformation on the hardness and continuous cooling transformations of 22MnB5 microalloyed boron steel, Metall. Mater. Trans. A Phys. Metall. Mater. Sci. 40 (2009) 1160–1174. https://doi.org/10.1007/s11661-009-9790-8.

[29] J. Min, J. Lin, Y. Min, F. Li, On the ferrite and bainite transformation in isothermally deformed 22MnB5 steels, Mater. Sci. Eng. A. 550 (2012) 375–387. https://doi.org/10.1016/j.msea.2012.04.091.

[30] T. Kurz, H. Schwinghammer, G. Luckeneder, T. Manzenreiter, A. Sommer, Zinc coated press-hardening steel - challenges and solutions, 5th Int. Conf. Hot Sheet Met. Form. High-Performance Steel. (2015) 345–353. https://doi.org/10.4271/2015-01-0565.

[31] C.K. Chiuhuang, S.W. Wang, P.K. Lee, Investigation of the influence of forming parameters on the springback of hot-stamped hat-shaped parts, IOP Conf. Ser. Mater. Sci. Eng. 651 (2019) 0–7. https://doi.org/10.1088/1757-899X/651/1/012029.

[32] H. Mohrbacher, Martensitic Automotive Steel Sheet - Fundamentals and Metallurgical Optimization Strategies, Adv. Mater. Res. 1063 (2015) 130–142. https://doi.org/10.4028/www.scientific.net/amr.1063.130.

[33] P. Namklang, V. Uthaisangsuk, Description of microstructures and mechanical properties of boron alloy steel in hot stamping process, J. Manuf. Process. 21 (2016) 87–100. https://doi.org/10.1016/j.jmapro.2015.11.008.

[34] D.A. da Costa Ximenes, L.P. Moreira, J.E.R. de Carvalho, D.N.F. Leite, R.G. Toledo, F.M. da Silva Dias, Phase transformation temperatures and Fe enrichment of a 22MnB5 Zn-Fe coated steel under hot stamping conditions, J. Mater. Res. Technol. (2019). https://doi.org/10.1016/j.jmrt.2019.11.003.

[35] D.W. Fan, R.B. Park, Y.R. Cho, B.C. De Cooman, Influence of isothermal deformation conditions on the mechanical properties of 22mnb5 hpf steel, Steel Res. Int. 81 (2010) 292–298. https://doi.org/10.1002/srin.201000008.

[36] S. Chatterjee, H.S. Wang, J.R. Yang, H.K.D.H. Bhadeshia, Mechanical stabilisation of austenite, Mater. Sci. Technol. 22 (2006) 641–644.

https://doi.org/10.1179/174328406X86128.

[37] R.H. Larn, J.R. Yang, The effect of compressive deformation of austenite on the bainitic ferrite transformation in Fe-Mn-Si-C steels, Mater. Sci. Eng. A. 278 (2000) 278–291. https://doi.org/10.1016/S0921-5093(99)00597-3.

[38] K. Tsuzaki, S. ichi Fukasaku, Y. Tomota, T. Maki, Effect of prior deformation of austenite on the γ → ε martensitic transformation in Fe-Mn alloys, Mater. Trans. JIM. 32 (1991) 222–228. https://doi.org/10.2320/matertrans1989.32.222.

[39] L. Golem, L. Cho, J.G. Speer, K.O. Findley, Influence of austenizing parameters on microstructure and mechanical properties of Al-Si coated press hardened steel, Mater. Des. 172 (2019) 107707. https://doi.org/10.1016/j.matdes.2019.107707.

[40] H. Peng, W. Peng, R. Lu, G. Wu, J. Zhang, Diffusion and cracking behavior involved in hot press forming of Zn coated 22MnB5, J. Alloys Compd. 806 (2019) 195–205. https://doi.org/10.1016/j.jallcom.2019.07.232.

[41] V. Janik, Y. Lan, P. Beentjes, D. Norman, G. Hensen, S. Sridhar, Zn Diffusion and α-Fe(Zn) Layer Growth During Annealing of Zn-Coated B Steel, Metall. Mater. Trans. A Phys. Metall. Mater. Sci. 47 (2016) 400–411. https://doi.org/10.1007/s11661-015-3203-y.

[42] Y. Kim, J.R. McDermid, Microstructure and Phase Evolution of Galvanized Press Hardening Steel, in: Galvatech 2017 Conf. Proc., ISIJ International, Tokyo, Japan, 2017: pp. 501–505.

[43] C. Thomsen, J. McDermid, F. Goodwin, Development of a New Grade of Zn-Coated Press-Hardenable Steel, in: Galvatech 2020 Conf. Proc., Vienna, Austria, 2020.

CHAPTER 6 GLOBAL DISCUSSION

The characterization results of the prototype press-hardening alloys were presented in detail in Chapters 3–5. This section provides a brief summary of the main findings and compares results from the two alloys – 0.20C-2.0Mn-0.26Si-0.005B and 0.19C-2.5Mn-0.26Si-0.005B – on the basis of phase transformation kinetics, microstructural and mechanical property evolution of the substrate, and microstructural evolution and micro-cracking characteristics of the coating. The results are discussed in context of defining DHPF processing routes that enable these two grades to meet the mechanical property target of TS ≥ 1500 MPa and the coating microstructure target for robust cathodic protection of ≥ 15 vol% Γ-Fe_3Zn_{10} [1,2], while avoiding LME.

6.1 PHASE TRANSFORMATION KINETICS

The CCT diagram for both alloys superimposed on a single plot is shown in Fig. 6.1. The increased Mn content clearly has the effect of shifting the start of the bainite and ferrite transformations to lower temperatures and longer times, i.e. it delays the onset of diffusional transformations and hence increases hardenability. This effect is well known in the literature [3–6]. The critical cooling rates for the formation of fully martensitic microstructures for the 2Mn and 2.5Mn alloy were determined to be −10 °C/s and −5 °C/s, respectively (Fig. 6.1). A comprehensive set of microstructural images from the dilatometry study are available in Appendix A (Fig. A.1 and Fig. A.2). This represents a substantial increase in hardenability over 22MnB5, which is often quoted in the literature to have a critical cooling rate of between −27 and −35 °C/s [4,6–8]. This increase in hardenability is critical because it made it possible to achieve a fully martensitic microstructures despite the extended transfer times, i.e. lower effective cooling rates. Using 22MnB5 with the DHPF process with extended transfer time employed in this work would likely have resulted in the formation of bainite and ferrite and the deterioration of mechanical properties, per other studies in the literature [9–11].

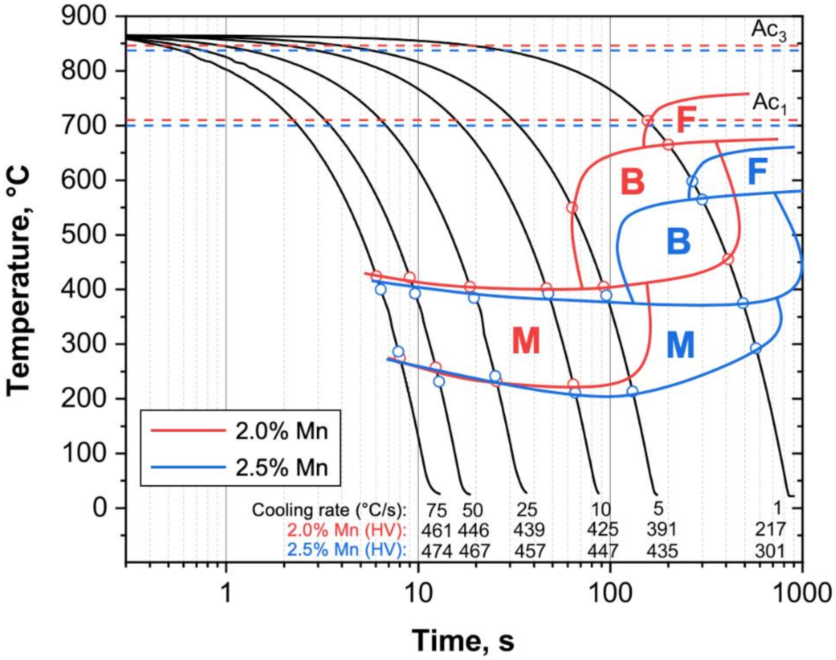

Fig. 6.1. Superposition of the continuous cooling transformation diagrams for both alloys.

Another way of evaluating the hardenability of the two prototype alloys is to determine the evolution of microhardness as a function of cooling rate, which is directly related to the fraction of martensite in the microstructure. This is shown in Fig. 6.2 where data from the two prototype grades used in this study are compared to data for 22MnB5 sourced from the literature [3,8,12–14]. The increase in hardenability due to the increased Mn content of the prototype grades is clear as both the 2Mn and 2.5Mn alloys began to reach maximum hardness at lower cooling rates than 22MnB5. The evolution of microhardness found in the literature usually follows a sigmoidal evolution; this was not captured in the present work because low cooling rates (i.e. between −0.1 and −5 °C/s) were not tested. This sigmoidal evolution of the microhardness curve is directly related to the evolved phase fraction of martensite which follows the same kinetics [15,16].

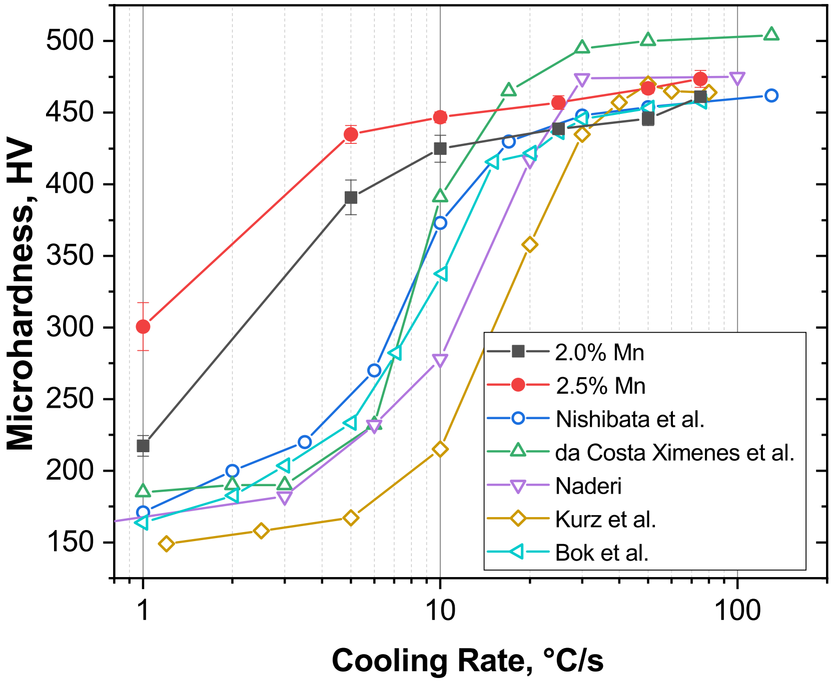

Fig. 6.2. Microhardness vs. cooling rate for the 2Mn and 25.Mn alloys compared to data for 22MnB5 compiled from the literature [3,8,12–14].

Deformation dilatometry showed that the martensitic transformation temperatures were supressed by the application of strain during the forming process, as shown in Fig. 6.3. This has also been observed in the literature and is attributed to the mechanical stabilization of austenite [17–19]. Mechanical stabilization of austenite occurs when new dislocations generated by the forming process act as barriers to motion of glissile transformation interfaces, resulting in a higher driving force required for the martensitic transformation and a corresponding downward shift in M_s and M_f temperatures [20]. However, it is clear from the microstructural images (Fig. 4.10 and Fig. 5.10) and measured mechanical properties (Fig. 4.12 and Fig. 5.12) that the reduction of hardenability due to the mechanical stabilization of austenite was not sufficient to result in the formation of bainite or ferrite. Some evidence for dynamic recrystallization and subsequent grain refinement is found when comparing the microstructures of the deformation dilatometry specimens

(Fig. A.3 and Fig. A.4) to the microstructures of the undeformed (CCT) specimens (Fig. A.1 and Fig. A.2). This could explain the higher microhardness measured from the DHPF samples (Fig. 4.10) compared to the dilatometry samples. Although it is clear that deformation decreased the hardenability of both grades due to the mechanical stabilization of austenite, the increase in hardenability imparted from the Mn additions enabled the formation of fully martensitic microstructures by DHPF, as evidenced in Fig. 4.10 and Fig. 5.10.

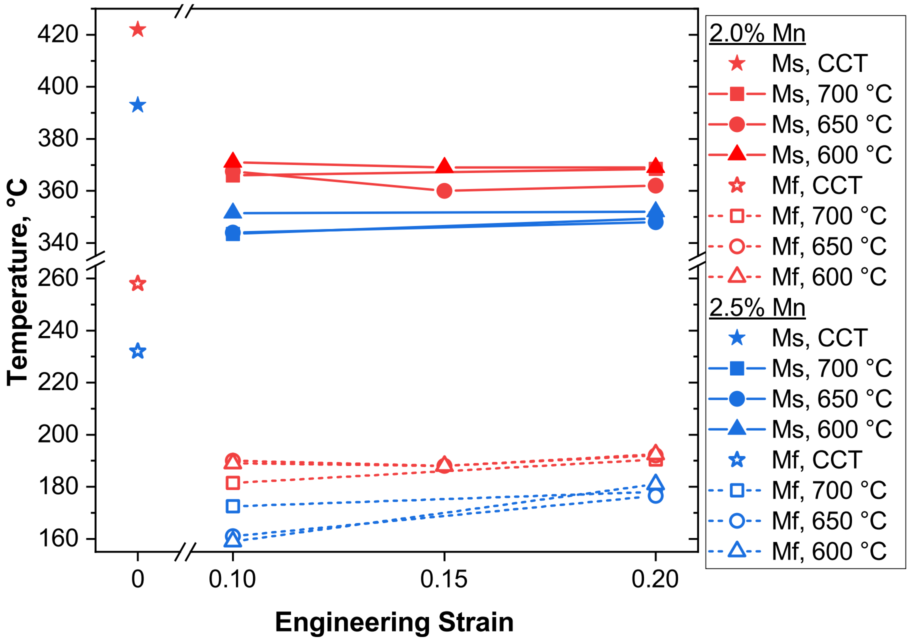

Fig. 6.3. M_s and M_f temperatures for both alloys with deformation for the experimental DHPF target temperatures.

6.2 MECHANICAL PROPERTIES

Representative stress-strain curves for both prototype alloys are shown in Fig. 6.4. A complete set of tensile curves across all processing conditions can be found in Appendix B (Fig. B.3–Fig. B.6). At short austenization times (30 and 60 s), there is a marked difference between the stress-strain response of the two alloys. This is related to the presence of ferrite in the microstructure. For the 2Mn alloy, an austenization time of 30 s resulted in a significant amount of ferrite in the microstructure after DHPF and mean microhardness over all three stamping temperatures between 316–404 HV (Fig. 4.12 (a-c)). When 60 s of austenization was used a small amount of ferrite was present, and microhardness values increased to between 432–477 HV (Fig. 4.12 (d-f)). The onset of necking during tensile testing occurred at higher strains in the specimens with these dual phase microstructures. With 120 or 180 s, any differences in microstructure became undetectable, and microhardness values were all between 470–482 HV (Fig. 4.12 (g-l)). On the other hand, the microstructure of the 2.5Mn alloy was very nearly fully martensitic after 30 s of austenization (Fig. 5.12 (a-c)), and fully martensitic after 60 s of austenization (Fig. 5.12 (d-f)).

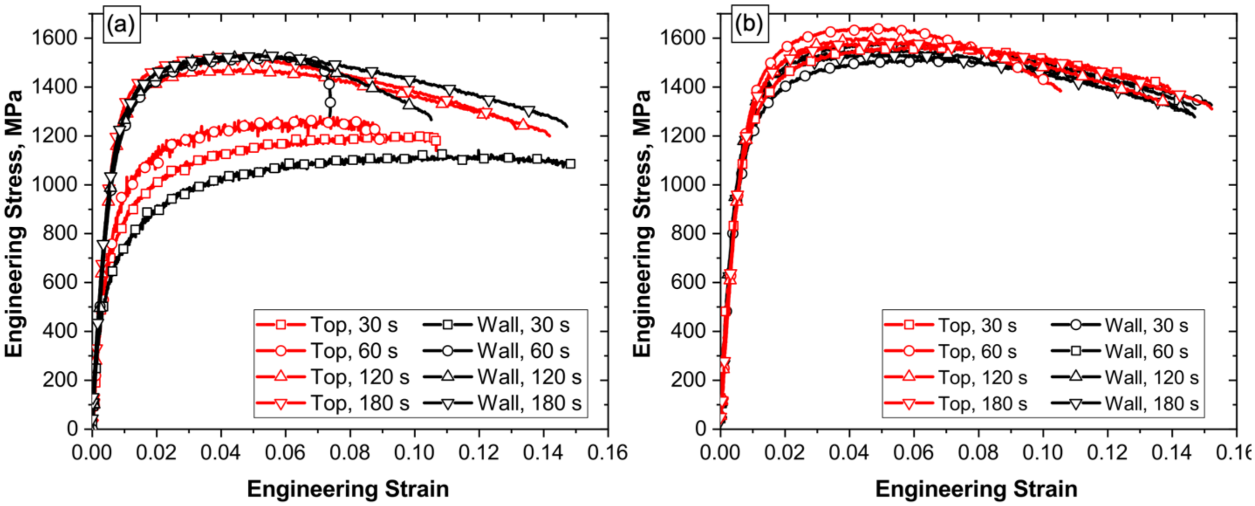

Fig. 6.4. Representative stress-strain curves for DHPF stamped at 700 °C for (a) 2Mn and (b) 2.5Mn.

Summarized YS and TS as a function of austenization time for the DHPF 2Mn and 2.5Mn prototype alloys are shown in Fig. 6.5. As noted in Chapters 3–5, the effect of stamping temperature between 600–700 °C on YS and TS was negligible. In light of this negligible dependence, and for ease of comparison, data from all stamping temperatures were compiled to generate the data points shown in Fig. 6.5. The error bars in Fig. 6.5 represent the 95% confidence intervals calculated from all 18 tensile tests performed at each combination of substrate material, austenization time, and section of the DHPF part. For the 2Mn alloy, an austenization time of 30 s yielded inferior mechanical properties that did not meet of TS ≥ 1500 MPa. As noted, examination of Fig. 4.10 (a-c) shows that the sample austenized for 30 s exhibited a dual-phase microstructure with roughly equal amounts of ferrite and martensite, which explains the low strength values. A small amount of ferrite was still present after 60 s of austenization (Fig. 4.10 (d-f)), leading to TS slightly lower than the target TS ≥ 1500 MPa. With 120 s or 180 s of austenization, the microstructure became fully martensitic (Fig. 4.10 (g-l)) and the mechanical properties levelled off at approximately 1150 MPa YS and 1500 MPa TS. Based on this information, it was concluded in Chapters 3 and 4 that when using the Zn-coated 0.20C-2.0Mn-0.26Si-0.005B steel, the objective of TS ≥ 1500 MPa can be successfully achieved if austenization time is between 120–180 s and DHPF stamping temperatures are between 600–700 °C.

The YS and TS of the 2.5Mn alloy were less sensitive to this range of austenization times. After 30 s of austenization, the mechanical properties were nearly fully developed and only a very small amount of ferrite can be observed in the microstructures in Fig. 5.10 (a-c). For austenization times between 60–180 s, the TS exceeds the 1500 MPa target. The TS and YS then peak after 60 s and decrease slightly as austenization time increases. This could be due to the increase of prior austenite grain size caused by increased austenization time, as shown by Golem et al. [21]. Comparing fully martensitic specimens, the TS of the 2.5Mn is 50 to 100 MPa higher than that of the 2Mn alloy, while the YS are the same. It was concluded in Chapter 5 that a processing window for producing Zn-coated 0.19C-2.5Mn-0.26Si-0.005B steel that meets the target of TS ≥ 1500 MPa can be achieved when using austenization times of 60–180 s and DHPF stamping temperatures between 600–700 °C.

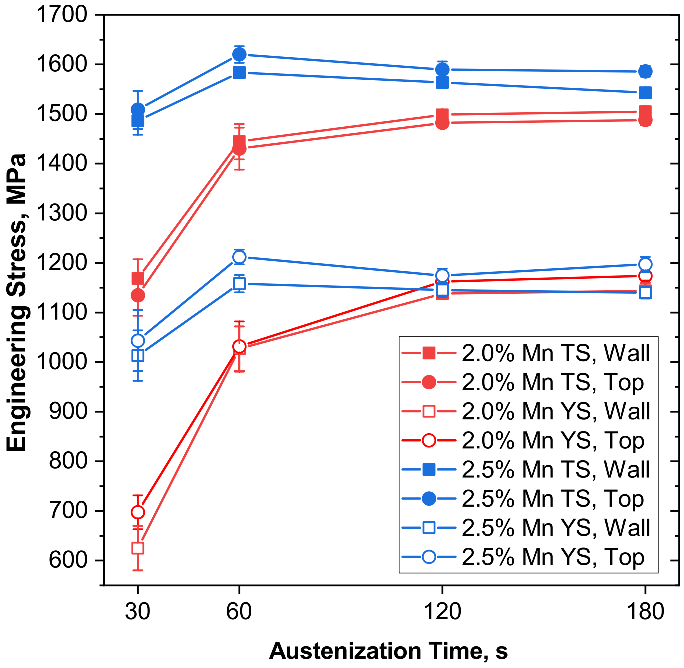

Fig. 6.5. Average mechanical properties for the 2Mn and 2.5Mn prototype PHS alloys for all experimental stamping temperatures.

Fig. 6.6 shows the average elongation at fracture for both prototype alloys for all three stamping temperatures and from both regions of the DHPF part (top and wall). Error bars are based on the results of 36 tensile tests that were executed at each austenization time and represent the 95% confidence interval of the mean. For each bar, the total elongation is split into the components of uniform elongation (UE) and post-uniform elongation (PUE). The UE followed the expected trend versus the evolution of mechanical properties (Fig. 6.5), i.e. as TS increased, UE decreased. The alloy and DHPF processing combination which resulted in large amounts of microstructural ferrite (i.e. the 2Mn alloy austenized for 30 s) exhibited by far the highest UE – approximately 0.11 UE followed by only 0.01 PUE. After 60 s of austenization, the UE dropped to 0.06 and the UE became constant at slightly greater than 0.05 for the samples austenized for 120 s and 180 s, respectively. However, the amount of PUE steadily increased with increasing austenization time, reaching a maximum of approximately 0.06 after 180 s. For the 2.5Mn alloy, UE after 30 s of austenization was 0.07 and, for austenization times between 60–180 s, the UE dropped to a constant value of about 0.05. This difference can again be related to the microstructure, which shows a small amount of ferrite remaining after 30 s of austenization (Fig 4.10), Unlike the 2Mn alloy, the 2.5Mn alloy showed consistent values of PUE (0.07–0.08) at every austenization time. From these results, it is seen that the elongations of fully martensitic samples for the 2 or 2.5 Mn grade match or slightly exceed typical values for PHS [5,6] (Chapter 2.5).

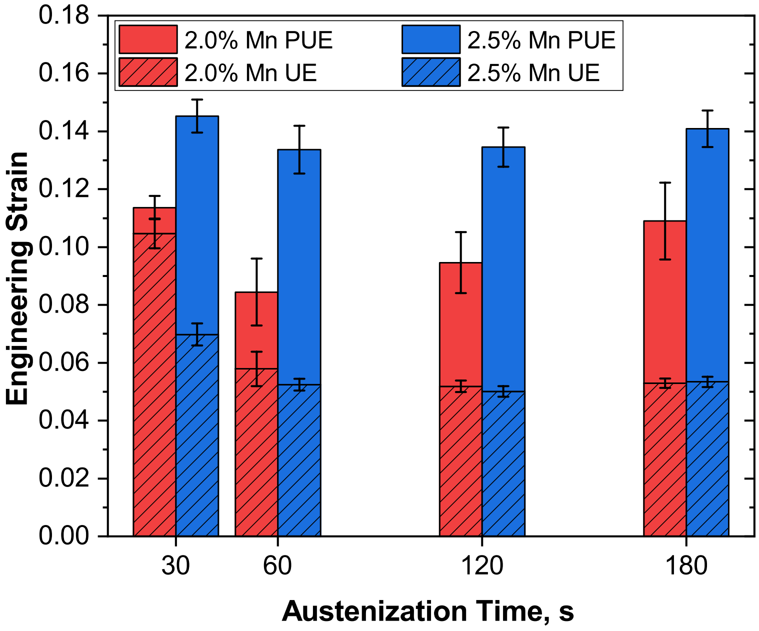

Fig. 6.6. Average elongation at fracture for the 2Mn and 2.5Mn alloys over all stamping temperatures and both regions of the DHPF part.

A comparison of the reduction of area results for the prototype alloys is shown in Fig. 6.7. Both alloys exhibit a very similar reduction of area dependence on austenization time, the main difference being that the reduction of area of the 2Mn alloy becomes constant after 120 s while the reduction of area of the 2.5Mn alloy becomes constant after 60 s. These austenization times are consistent with the lowest austenization times required for each alloy for the formation of fully martensitic microstructures upon DHPF. The reduction of area generally follows the same trend as the PUE (Fig. 6.6), where fully martensitic samples experienced greater extents of PUE before fracture than ferrite-containing samples did. The significant amount of necking that occurred before failure indicates that the technique of stamping at temperatures between 600–700 °C to solidify Zn(Fe)$_{liq}$ and avoid LME was successful. In addition, there is a favourable relationship between microstructure and reduction of area – samples that were fully martensitic and met the TS ≥ 1500 MPa target also experienced the greatest reduction of area.

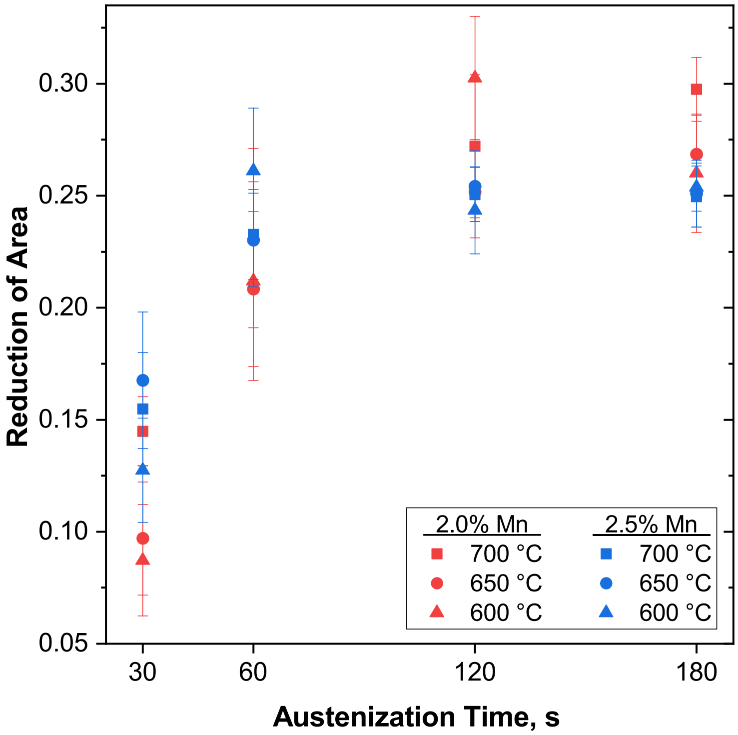

Fig. 6.7. Comparison of reduction of area of both alloys as a function of annealing time and stamping temperature.

For both alloys in all tested conditions, the fracture surfaces (Fig. 4.13 and Fig. 5.13) indicated primarily ductile fracture in the bulk substrate through void nucleation and growth. Equiaxed dimples were seen at the centre of the fracture surface where a triaxial stress state was present as well as some larger voids caused by second phase particles. These results are consistent with the reduction of area findings that for every tested combination of austenization time and DHPF stamping temperature, LME has been avoided and samples have fractured in a much more desirable ductile manner.

6.3 COATING PROPERTIES

The prototype PHS alloys used in this work were galvanized using the MGS and the average coating thickness was approximately 9 μm (66 gm^{-2}). The microstructural evolution of the coating for both alloys is shown in Fig. 6.8. More detailed results for coatings stamped at 700 °C may be found in Fig. 4.16, Fig. 5.15, and Fig. 5.16, and results from stamping temperatures of 650 °C and 600 °C are shown in Appendix C (Fig. C.1–Fig. C.7). No difference between the two alloys with respect to coating growth kinetics, phase evolution, or the extent of cracking was expected as the initial coating thickness, austenization treatment, and DHPF process was the same for both. Fig. 6.8 shows that after 30 s of austenization, the coating quantitatively looks to be mostly Γ-Fe_3Zn_{10}. This was proven by XRD measurements which showed Γ-Fe_3Zn_{10} concentrations of about 90 vol% (Fig. 4.15). After 180 s of austenization time, the coating thickened to about 23 μm and contained 33–53 vol% Γ-Fe_3Zn_{10} (Fig. 4.15). In all measured cases, the amount of Γ-Fe_3Zn_{10} in the DHPF coating was above the 15 vol% target required for robust cathodic protection. This agrees well with the growth kinetics and phase evolution studies by Dever [1,2] discussed in Chapter 2.6.2 and other studies on Zn-coated PHS [22–29]. In Fig. 4.16, Fig. 5.15, and Fig. 5.16 some through-thickness cracks were seen in the coating in the wall and outer corner of the DHPF part. However, all observed cracks were arrested at the coating/substrate interface, typically with a blunt tip. Unlike the present work, in the study by Lee et al. [30] Zn-enriched cracks were seen penetrating deep into the substrate. This difference could be related to the stamping temperature – Lee et al. [30] performed DHPF at 750 °C and it is possible that even though this is below the peritectic temperature of 782 °C, some liquid Zn may have still been present due to the rapid cooling rates employed. The stamping temperatures of 600–700 °C employed in the present work make it much more likely that the liquid Zn(Fe) would have fully solidified when forming took place, thereby removing the liquid necessary for LME to occur. It is clear that any austenization time between 30–180 s followed by any DHPF stamping temperature between 600–700 °C will result in attainment of the ≥ 15 vol% Γ-Fe_3Zn_{10} required for robust cathodic protection while avoiding LME, indicating a wide process window that is easily compatible with realizing the mechanical property targets.

The amount of Γ-Fe_3Zn_{10} is above the target for robust cathodic protection of ≥ 15 vol% [1] for all tested DHPF conditions. Early electrochemical testing results on the 2Mn grade after 30 s and 180 s of austenization that were shown in Fig. 3.11 indicate that the Γ-Fe_3Zn_{10} phase is indeed providing cathodic corrosion resistance for the substrate. Therefore, although the cathodic corrosion resistance has not been directly tested, preliminary results indicate that it is promising based on the early electrochemical testing results and the electrochemical data from Dever et. al [1] and other studies [1,2,29,31].

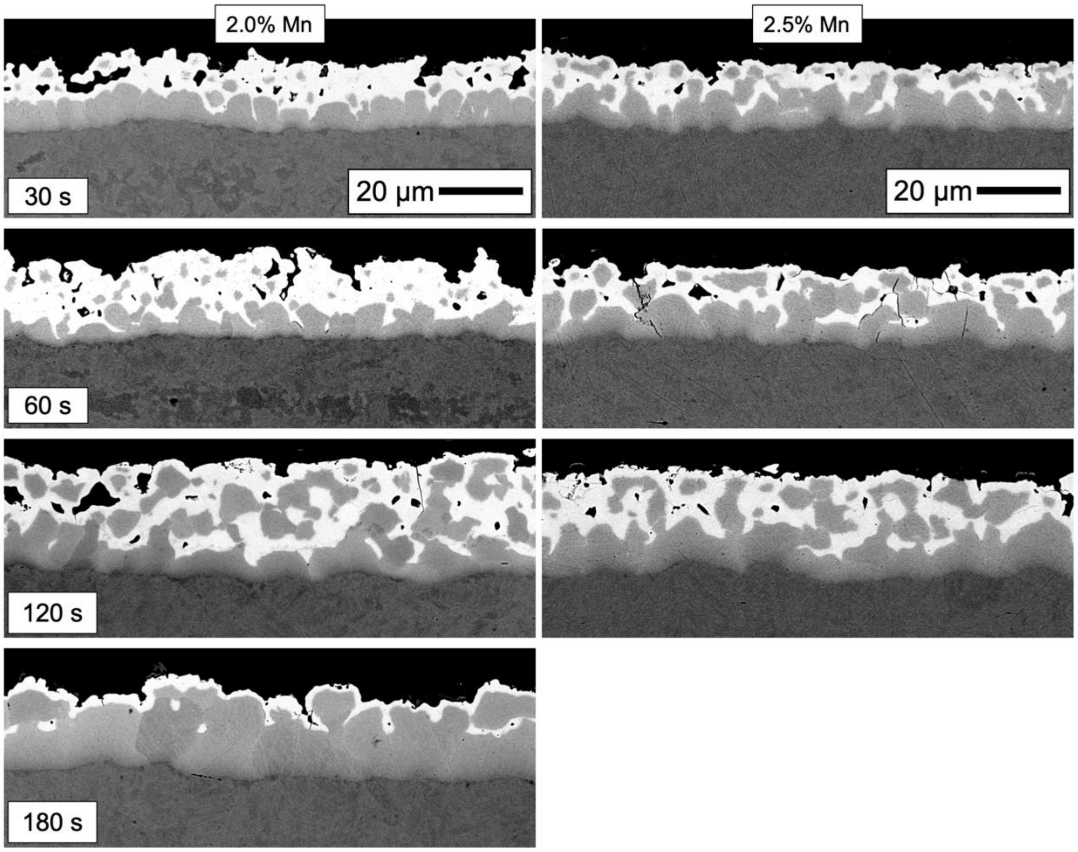

Fig. 6.8. Comparison of the microstructure of the coating at the top of the DHPF part for both alloys.

REFERENCES

[1] C. Dever, J. Kish, J. McDermid, Corrosion Properties of Hot Dip Zinc Galvanized Coatings on 22MnB5 Press Hardened Steels, in: Galvatech 2017 Conf. Proc., ISIJ International, Tokyo, Japan, 2017: pp. 385–392.

[2] C. Dever, Effect of Coating Microstructure on the Electrochemical Properties of Continuous Galvanized Coatings on Press Hardened Steels, McMaster University, 2018.

[3] T. Kurz, P. Larour, J. Lackner, T. Steck, G. Jesner, Press-hardening of zinc coated steel - Characterization of a new material for a new process, in: IOP Conf. Ser. Mater. Sci. Eng., 2016. https://doi.org/10.1088/1757-899X/159/1/012025.

[4] H. Mohrbacher, Martensitic Automotive Steel Sheet - Fundamentals and Metallurgical Optimization Strategies, Adv. Mater. Res. 1063 (2015) 130–142. https://doi.org/10.4028/www.scientific.net/amr.1063.130.

[5] D.W. Fan, H.S. Kim, B.C. De Cooman, A review of the physical metallurgy related to the hot press forming of advanced high strength steel, Steel Res. Int. 80 (2009) 241–248. https://doi.org/10.2374/SRI08SP131.

[6] T. Taylor, A. Clough, Critical review of automotive hot-stamped sheet steel from an industrial perspective, Mater. Sci. Technol. 0836 (2018) 1–53. https://doi.org/10.1080/02670836.2018.1425239.

[7] P. Namklang, V. Uthaisangsuk, Description of microstructures and mechanical properties of boron alloy steel in hot stamping process, J. Manuf. Process. 21 (2016) 87–100. https://doi.org/10.1016/j.jmapro.2015.11.008.

[8] D.A. da Costa Ximenes, L.P. Moreira, J.E.R. de Carvalho, D.N.F. Leite, R.G. Toledo, F.M. da Silva Dias, Phase transformation temperatures and Fe enrichment of a 22MnB5 Zn-Fe coated steel under hot stamping conditions, J. Mater. Res. Technol. (2019).

https://doi.org/10.1016/j.jmrt.2019.11.003.

[9] D.W. Fan, R.B. Park, Y.R. Cho, B.C. De Cooman, Influence of isothermal deformation conditions on the mechanical properties of 22mnb5 hpf steel, Steel Res. Int. 81 (2010) 292–298. https://doi.org/10.1002/srin.201000008.

[10] K. Hu, S. Zhou, R. Han, J. Gao, Y. Yang, Microstructure Evolution and Simulation in 22MnB5 Steel during Hot Stamping, J. Mater. Sci. Chem. Eng. 06 (2018) 9–14. https://doi.org/10.4236/msce.2018.68002.

[11] C.K. Chiuhuang, S.W. Wang, P.K. Lee, Investigation of the influence of forming parameters on the springback of hot-stamped hat-shaped parts, IOP Conf. Ser. Mater. Sci. Eng. 651 (2019) 0–7. https://doi.org/10.1088/1757-899X/651/1/012029.

[12] T. Nishibata, N. Kojima, Effect of quenching rate on hardness and microstructure of hot-stamped steel, J. Alloys Compd. 577 (2013) 1–6. https://doi.org/10.1016/j.jallcom.2011.12.154.

[13] M. Naderi, Hot Stamping of Ultra High Strength Steels, Aachen University, 2007. http://publications.rwth-aachen.de/record/49929.

[14] H.H. Bok, S.N. Kim, D.W. Suh, F. Barlat, M.G. Lee, Non-isothermal kinetics model to predict accurate phase transformation and hardness of 22MnB5 boron steel, Mater. Sci. Eng. A. 626 (2015) 67–73. https://doi.org/10.1016/j.msea.2014.12.008.

[15] J. Huang, W.J. Poole, M. Militzer, Austenite formation during intercritical annealing, Metall. Mater. Trans. A Phys. Metall. Mater. Sci. 35 A (2004) 3363–3375. https://doi.org/10.1007/s11661-004-0173-x.

[16] K. Bräutigam-Matus, G. Altamirano, A. Salinas, A. Flores, F. Goodwin, Experimental determination of continuous cooling transformation (CCT) diagrams for dual-phase steels from the intercritical temperature range, Metals (Basel). 8 (2018).

https://doi.org/10.3390/met8090674.

[17] M. Nikravesh, M. Naderi, G.H. Akbari, W. Bleck, Phase transformations in a simulated hot stamping process of the boron bearing steel, Mater. Des. 84 (2015) 18–24. https://doi.org/10.1016/j.matdes.2015.06.108.

[18] A. Barcellona, D. Palmeri, Effect of plastic hot deformation on the hardness and continuous cooling transformations of 22MnB5 microalloyed boron steel, Metall. Mater. Trans. A Phys. Metall. Mater. Sci. 40 (2009) 1160–1174. https://doi.org/10.1007/s11661-009-9790-8.

[19] J. Min, J. Lin, Y. Min, F. Li, On the ferrite and bainite transformation in isothermally deformed 22MnB5 steels, Mater. Sci. Eng. A. 550 (2012) 375–387. https://doi.org/10.1016/j.msea.2012.04.091.

[20] R.H. Larn, J.R. Yang, The effect of compressive deformation of austenite on the bainitic ferrite transformation in Fe-Mn-Si-C steels, Mater. Sci. Eng. A. 278 (2000) 278–291. https://doi.org/10.1016/S0921-5093(99)00597-3.

[21] L. Golem, L. Cho, J.G. Speer, K.O. Findley, Influence of austenizing parameters on microstructure and mechanical properties of Al-Si coated press hardened steel, Mater. Des. 172 (2019) 107707. https://doi.org/10.1016/j.matdes.2019.107707.

[22] V. Janik, Y. Lan, P. Beentjes, D. Norman, G. Hensen, S. Sridhar, Zn Diffusion and α-Fe(Zn) Layer Growth During Annealing of Zn-Coated B Steel, Metall. Mater. Trans. A Phys. Metall. Mater. Sci. 47 (2016) 400–411. https://doi.org/10.1007/s11661-015-3203-y.

[23] H. Järvinen, M. Honkanen, M. Patnamsetty, S. Järn, E. Heinonen, Press hardening of zinc-coated boron steels : Role of steel composition in the development of phase structures within coating and interface regions, Surf. Coat. Technol. 352 (2018) 378–391. https://doi.org/10.1016/j.surfcoat.2018.08.040.

[24] Y. Kim, J.R. McDermid, Microstructure and Phase Evolution of Galvanized Press Hardening Steel, in: Galvatech 2017 Conf. Proc., ISIJ International, Tokyo, Japan, 2017: pp. 501–505.

[25] J. Faderl, S. Kolnberger, M. Rosner, T. Kurz, Continuous Galvanizing Meets Press-Hardening, in: Galvatech 2011 Conf. Proc., Genova, Italy, 2011: pp. 2–9.

[26] C.W. Lee, D.W. Fan, S.J. Lee, I.R. Sohn, B.C. De Cooman, Galvanized Coating Evolution During Hot Stamping, in: Galvatech 2011 Conf. Proc., Genova, Italy, 2011.

[27] Z. Ghanbari, J.G. Speer, K.O. Findley, Coating Evolution and Mechanical Behavior of Zn-Coated Press-Hardening Sheet Steel, 5th Int. Conf. Hot Sheet Met. Form. High-Performance Steel. (2015).

[28] J. Kondratiuk, P. Kuhn, E. Labrenz, C. Bischoff, Zinc coatings for hot sheet metal forming: Comparison of phase evolution and microstructure during heat treatment, Surf. Coatings Technol. 205 (2011) 4141–4153. https://doi.org/10.1016/j.surfcoat.2011.03.002.

[29] R. Autengruber, G. Luckeneder, S. Kolnberger, J. Faderl, A.W. Hassel, Surface and coating analysis of press-hardened hot-dip galvanized steel sheet, Steel Res. Int. 83 (2012) 1005–1011. https://doi.org/10.1002/srin.201200068.

[30] C.W. Lee, W.S. Choi, L. Cho, Y.R. Cho, B.C. De Cooman, Liquid-Metal-Induced Embrittlement Related Microcrack Propagation on Zn-coated Press Hardening Steel, ISIJ Int. 55 (2015) 264–271. https://doi.org/10.2355/isijinternational.55.264.

[31] R. Autengruber, G. Luckeneder, S. Kolnberger, J. Faderl, A.W. Hassel, Corrosion Behavior of Press-Hardened Hot-Dipped Galvanized Steel Sheet, in: Galvatech 2015 Conf. Proc., Toronto, Canada, 2015: pp. 0–7.

CHAPTER 7 CONCLUSIONS AND RECOMMENDATIONS FOR FUTURE WORK

7.1 CONCLUSIONS

This research detailed the development of two new grades of Zn-coated PHS with nominal compositions of 0.20C-2.0Mn-0.26Si-0.005B and 0.19C-2.5Mn-0.26Si-0.005B. These prototype grades were designed with increased Mn content to improve hardenability relative to typical PHS and facilitate DHPF with an extended transfer time such that stamping was performed between 600–700 °C. By doing so, the presence of Zn(Fe) liquid during forming was eliminated and LME was prevented while allowing for attainment of high volume fractions of Γ-Fe_3Zn_{10} in the final coating microstructure. Characterization was carried out in the context of defining a process window in which these grades can meet targets of $TS \geq 1500$ MPa and ≥ 15 vol % Γ-Fe_3Zn_{10} in the coating microstructure for robust cathodic protection while avoiding LME. The main conclusions are:

- The additional Mn in these grades successfully improved hardenability relative to conventional PHS grades. The critical cooling rates for the 2Mn and 2.5Mn alloy were determined to be −10 °C/s and −5 °C/s, respectively. This increase in hardenability is critical to the objective of stamping at 600–700 °C while attaining fully martensitic microstructures.
- Deformation dilatometry showed that deformation caused a reduction in hardenability due to the mechanical stabilization of austenite, however, fully martensitic microstructures were still attained in the DHPF part.
- It was found that for both alloys the microstructure after DHPF was a strong function of austenization time at 890 °C. For the 2Mn alloy, austenization times of 120 s or 180 s

resulted in fully martensitic microstructures after DHPF. The 2.5Mn alloy was less sensitive to austenization time, with fully martensitic microstructures in the DHPF parts being formed after 60–180 s of austenization time.

- Tensile tests showed that the fully martensitic samples met the target of TS ≥ 1500 MPa regardless of stamping temperature for both the 2Mn and 2.5Mn grades. Therefore, processing routes that are compatible with satisfying TS ≥ 1500 MPa for the 2Mn alloy include 120–180 s of austenization time followed by stamping between 600–700 °C. For the 2.5Mn grade, the DHPF process window was widened to include 60–180 s of austenization time and stamping between 600–700 °C.
- Fracture surfaces of tensile specimens excised from DHPF parts were analyzed and, in all cases, ductile fracture was observed to be the failure mechanism. This was consistent with the significant extent of PUE and reduction of area of fractured tensile specimens. No evidence of brittle fracture by LME was seen, leading to the conclusion that the method of performing stamping between 600–700 °C to solidify $Zn(Fe)_{liq}$ before forming and thereby avoid LME was successful.
- The amount of Γ-Fe_3Zn_{10} in the final coating microstructure decreased with increasing austenization time and was not dependent on stamping temperature. For all DHPF conditions, the coating met the requirement of a minimum of 15 vol% Γ-Fe_3Zn_{10}, so it can be expected that the coatings will provide robust cathodic corrosion for the substrate. However, proper corrosion testing including electrochemical tests and long-term exposure tests will need to be carried out to verify this expectation. This result implies a wide process window such that any austenization time between 60–180 s combined with stamping

temperatures between 600–700 °C will satisfy the requirement of $\geq$ 15 vol% Γ-Fe_3Zn_{10} for robust cathodic protection.

- No LME-type cracks or microcracks penetrating into the substrate were observed when imaging the coating-substrate interface of the DHPF part at any combination of austenization time and stamping temperature. This result, along the ductile fracture surfaces and the significant PUE and reduction of area proves that the threat of LME has been avoided.
- In summary, the above findings show that it is possible to use either of the 0.20C-2.0Mn-0.26Si-0.005B or 0.19C-2.5Mn-0.26Si-0.005B prototype grades to satisfy the objectives of TS $\geq$ 1500 MPa and $\geq$ 15 vol% Γ-Fe_3Zn_{10} for robust cathodic protection while avoiding LME. For the 2Mn alloy, the successful processing route included austenization times of 120–180 s and stamping temperatures of 600–700 °C. For the 2.5Mn alloy, the processing window was slightly wider, including austenization times of 60–180 s and stamping temperatures of 600–700 °C.

7.2 FUTURE WORK

Based on the aforementioned conclusions, a number of recommendations for future work may be made. These recommendations include:

- Determining the limits of the process windows, testing for prolonged austenization times could be performed to determine after what austenization time the fraction of Γ-Fe_3Zn_{10} in the coating decreases to below 15 vol%.
- The scope of mechanical testing on these steels could be broadened. As PHS must be able to withstand very high strain rates in automotive applications, fracture toughness tests should be performed to determine the crashworthiness of these grades. Bending tests such

as VDA238-100 could be conducted as an indication of the ability of the DHPF steel to deform in impact conditions.

- Thorough evaluation of the corrosion properties after DHPF for the conditions corresponding to the process window that was defined for both alloys is needed in order to confidently state that these coatings provide robust cathodic corrosion protection. Such testing would include electrochemical tests such as potentiodynamic and galvanostatic polarization tests to determine the driving force for cathodic protection and the corrosion kinetics, as well as accelerated cyclic corrosion tests (SAE J2334).
- The two prototype grades should be subjected to pilot-scale testing in order to determine the robustness of the defined process windows. This would require the procurement of larger sheets of galvanized substrate material as well as collaboration with industry sponsors.
- Given that the industry is shifting its focus towards PHS with even higher TS than 1500 MPa, future iterations of this project should involve a target of TS $\geq$ 1800 MPa which may be met by a new prototype alloy with increased C content.

APPENDIX A: MICROSTRUCTURE OF DILATOMETRY SPECIMENS

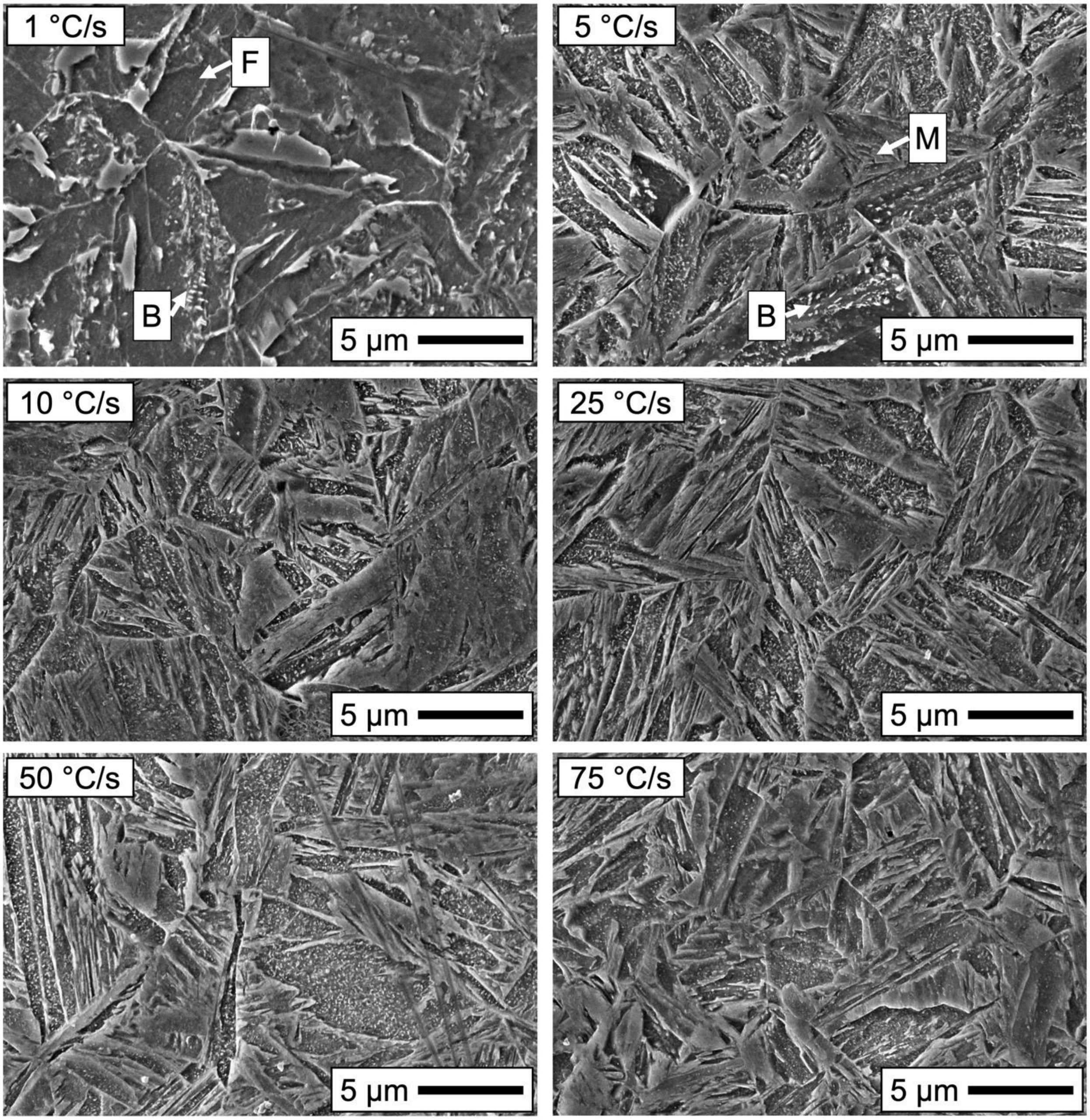

Fig. A.1. Microstructures obtained from CCT dilatometry tests for the 2.0Mn alloy labeled with cooling rate.

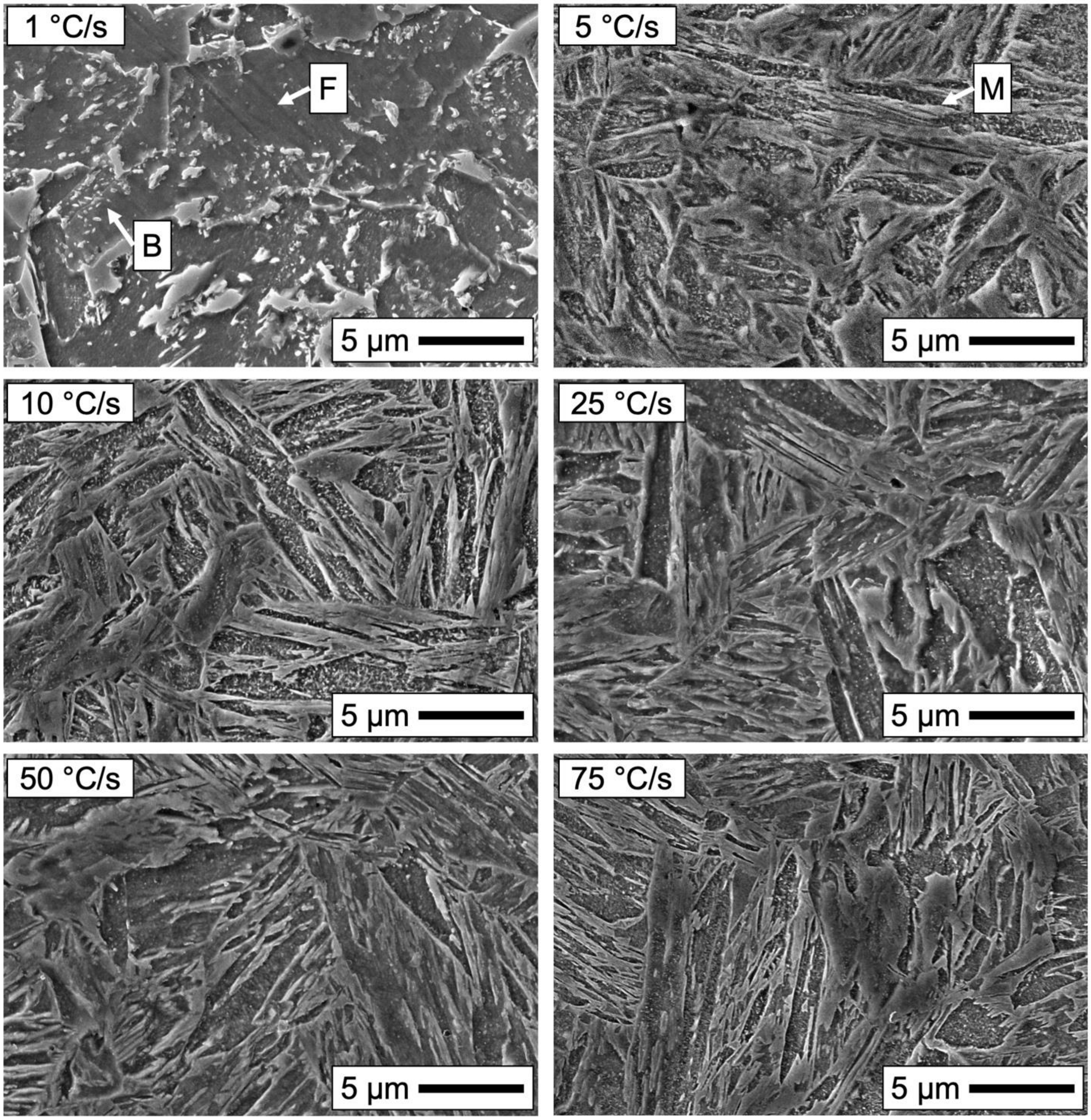

Fig. A.2. Microstructures obtained from CCT dilatometry tests for the 2.5Mn alloy labeled with cooling rate.

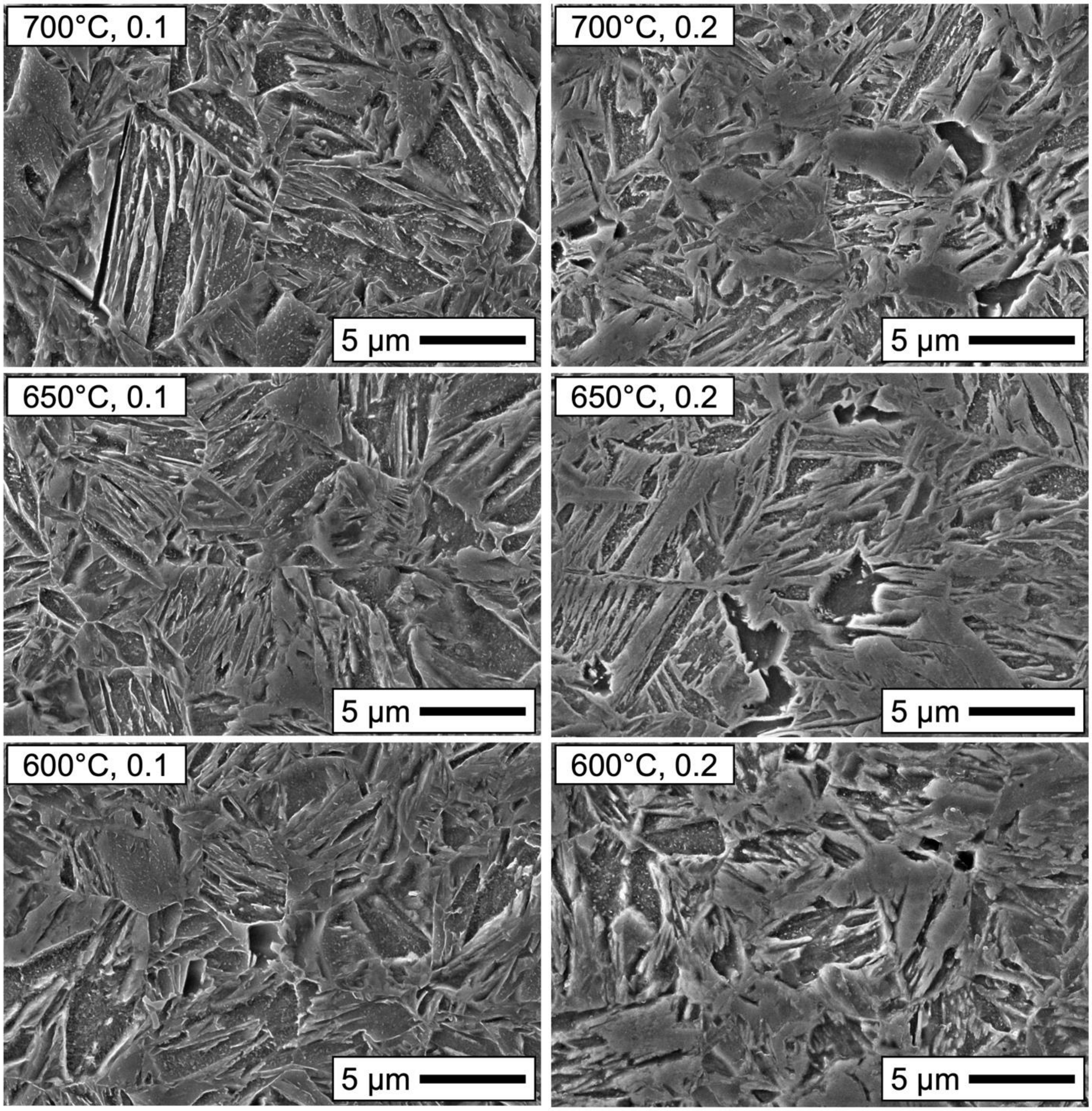

Fig. A.3. Microstructures obtained from deformation dilatometry tests for the 2.0Mn alloy labeled with deformation temperature and amount of strain.

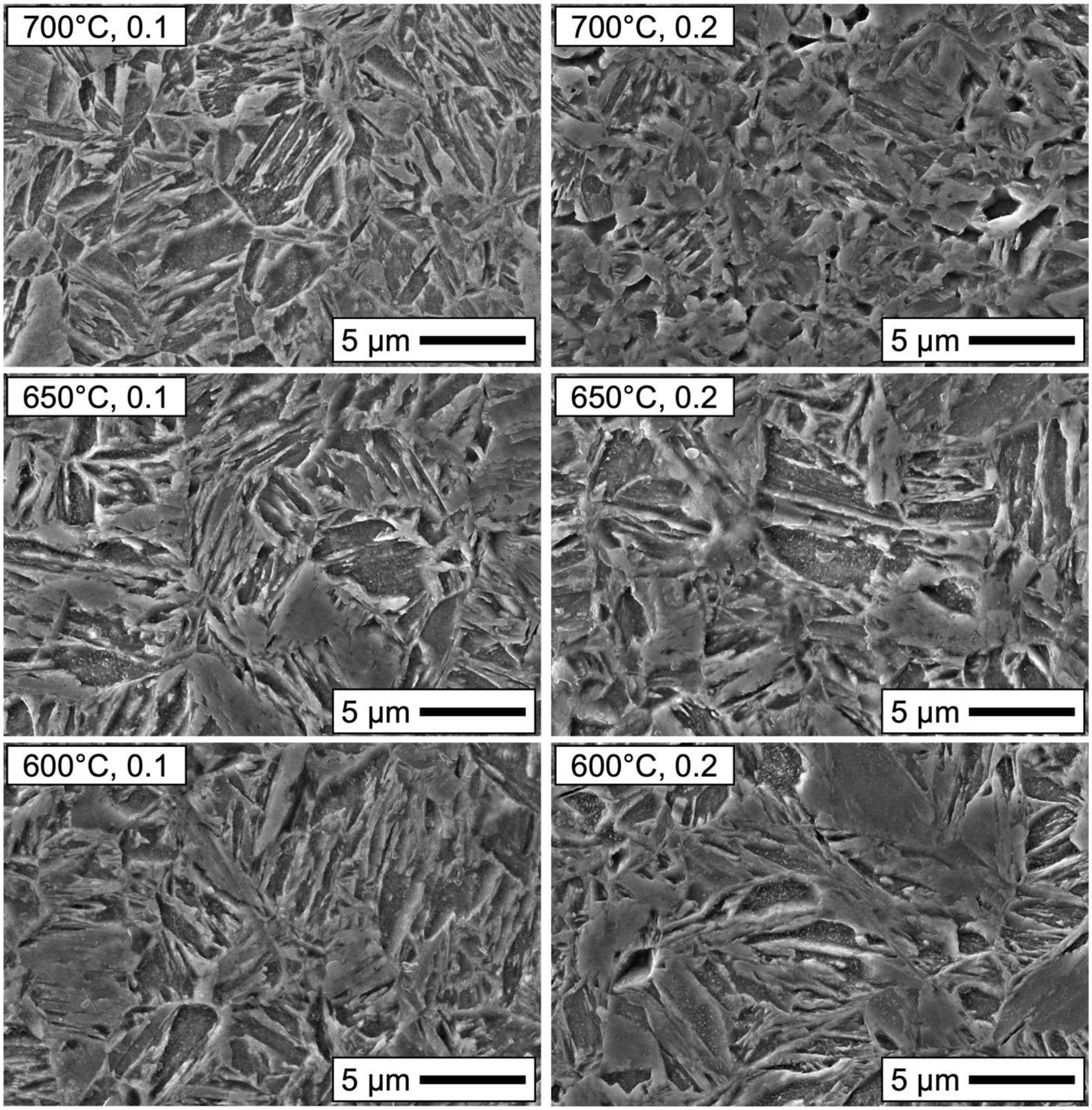

Fig. A.4. Microstructures obtained from deformation dilatometry tests for the 2.5Mn alloy labeled with deformation temperature and amount of strain.

APPENDIX B: STRESS-STRAIN CURVES

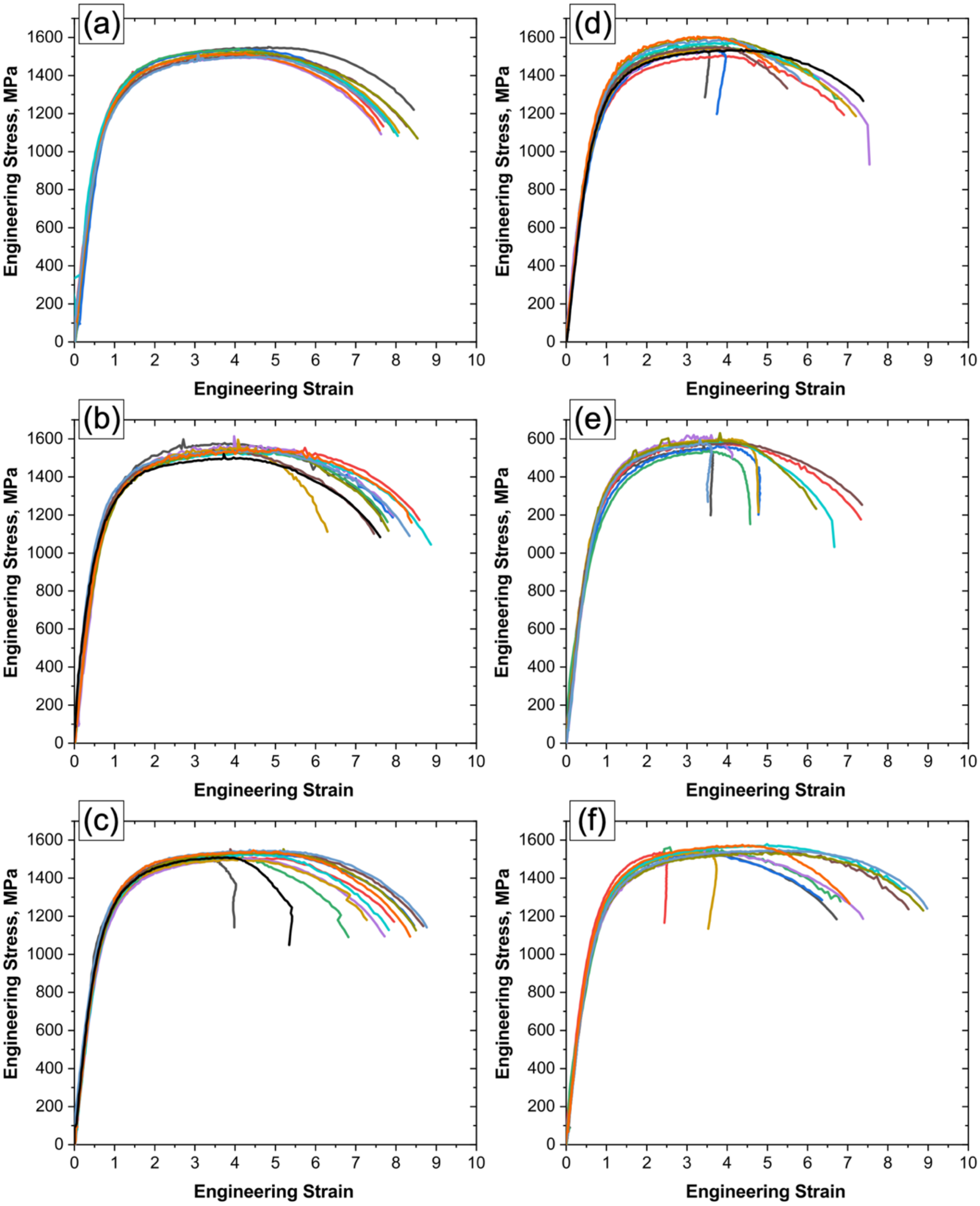

Fig. B.1. Stress-strain curves for bare and coated samples in the LD-orientation taken from PDQ 2.0Mn alloy after 120 s of austenization time and various stamping temperatures: (a) Bare, 700 °C (b) Bare, 650 °C, (c) Bare, 600 °C, (d) Coated, 700 °C, (e) Coated, 650 °C, (f) Coated, 600 °C.

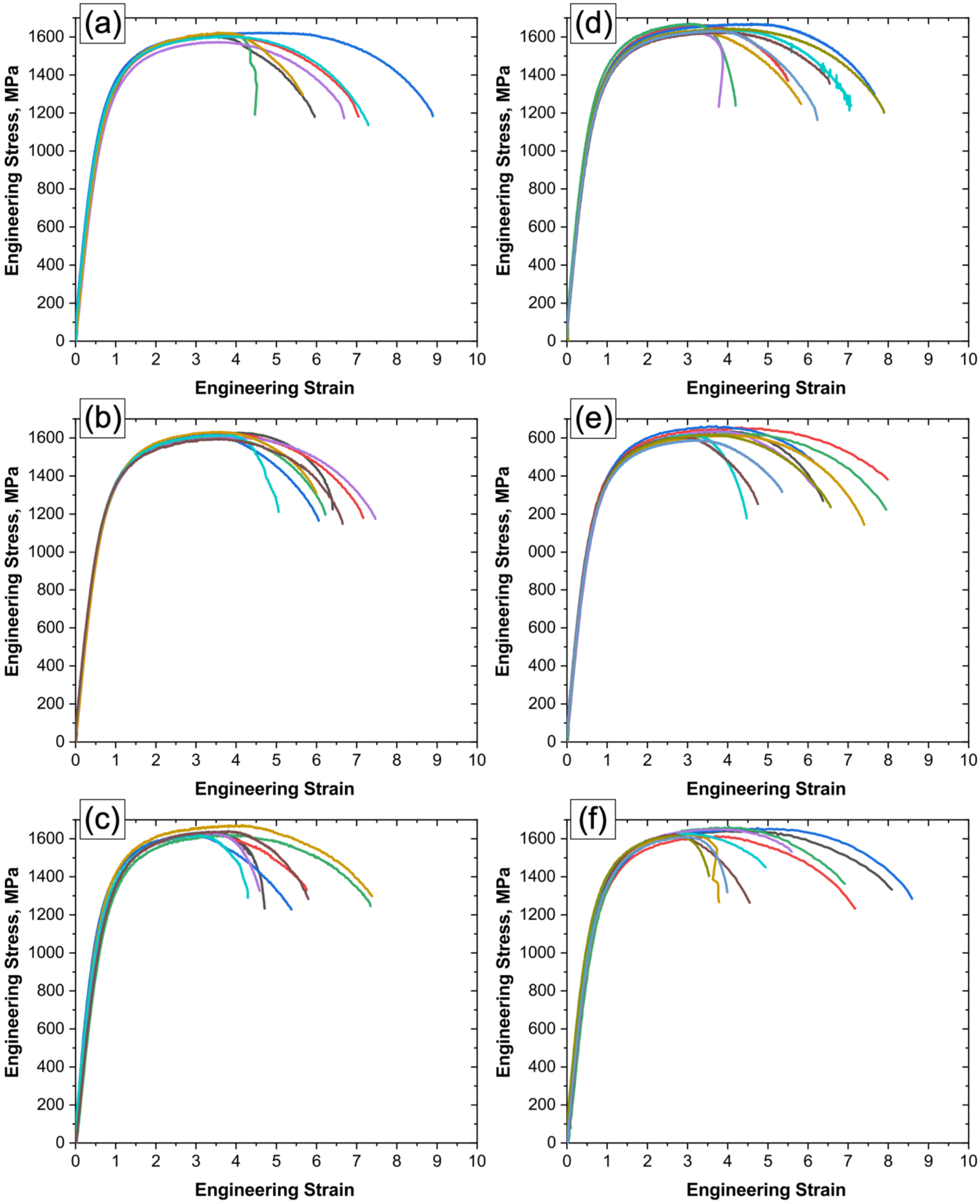

Fig. B.2. Stress-strain curves for bare and coated samples in the LD-orientation taken from PDQ 2.5Mn alloy after 120 s of austenization time and various stamping temperatures: (a) Bare, 700 °C (b) Bare, 650 °C, (c) Bare, 600 °C, (d) Coated, 700 °C, (e) Coated, 650 °C, (f) Coated, 600 °C.

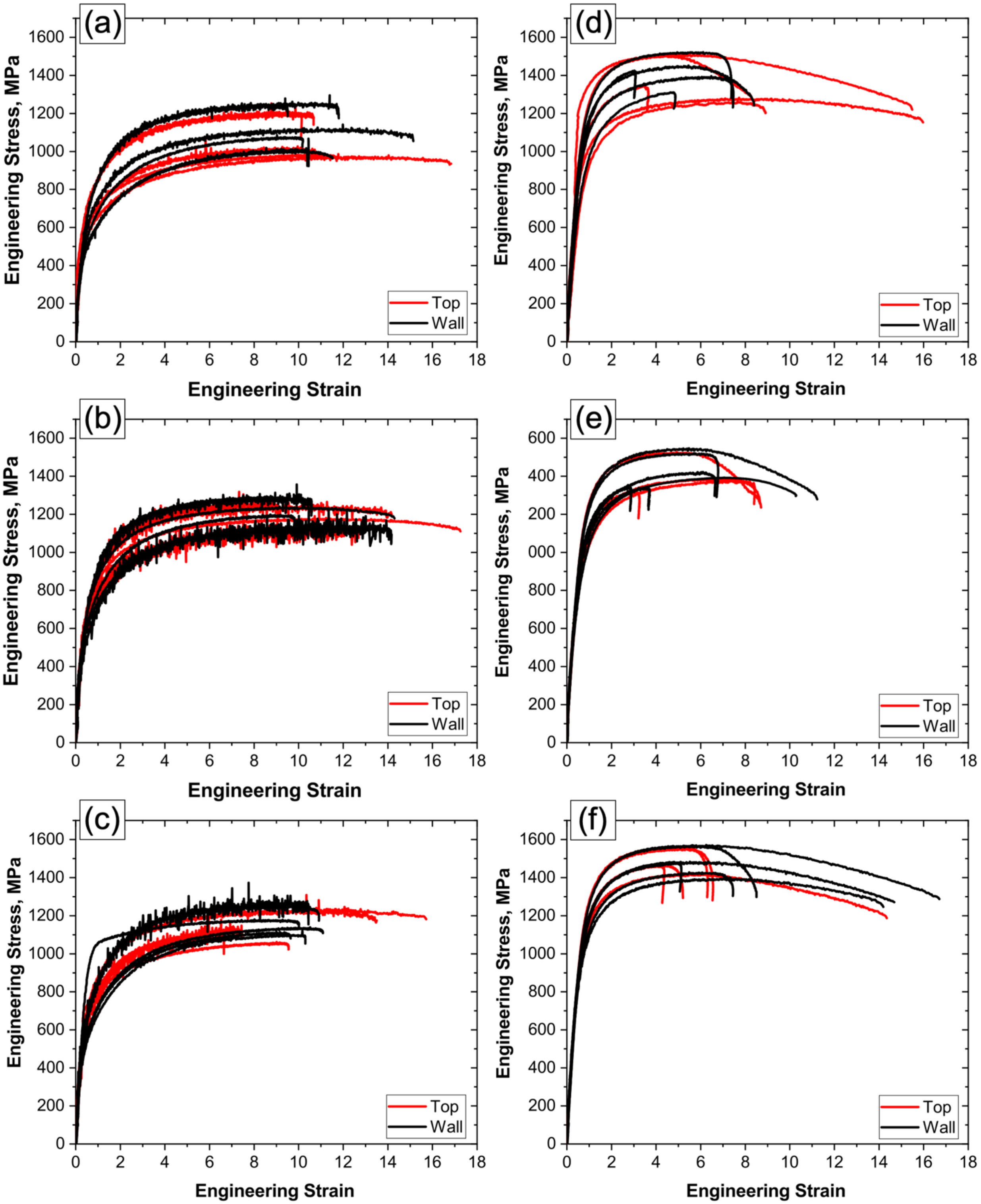

Fig. B.3. Stress-strain curves in the TD-orientation taken from DHPF 2.0Mn alloy at various austenization times and stamping temperatures: (a) 30 s–700 °C (b) 30 s–650 °C, (c) 30 s–600 °C, (d) 60 s–700 °C, (e) 60 s–650 °C, (f) 60 s–600 °C.

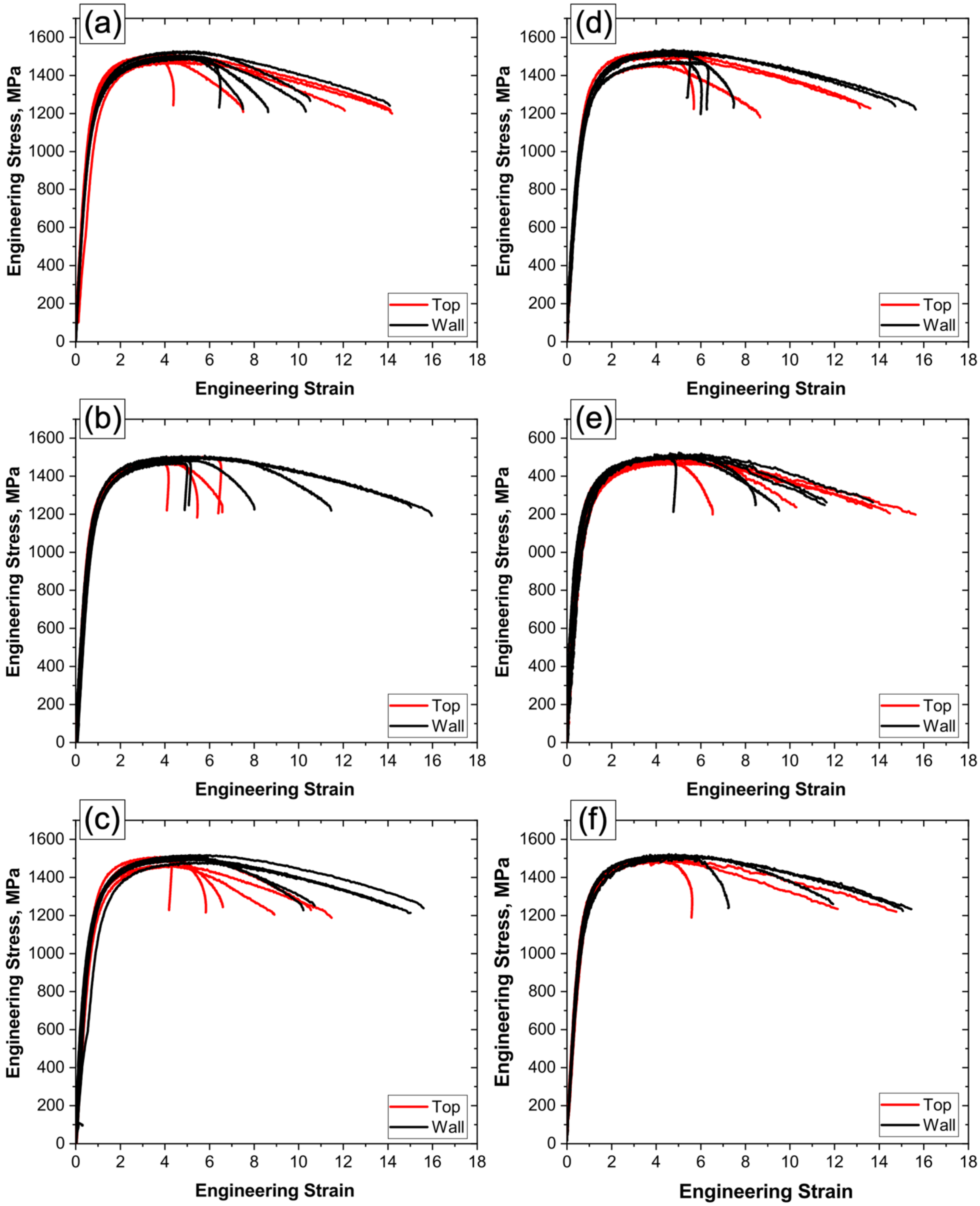

Fig. B.4. Stress-strain curves in the TD-orientation taken from DHPF 2.0Mn alloy at various austenization times and stamping temperatures: (a) 120 s–700 °C (b) 120 s–650 °C, (c) 120 s–600 °C, (d) 180 s–700 °C, (e) 180 s–650 °C, (f) 180 s–600 °C.

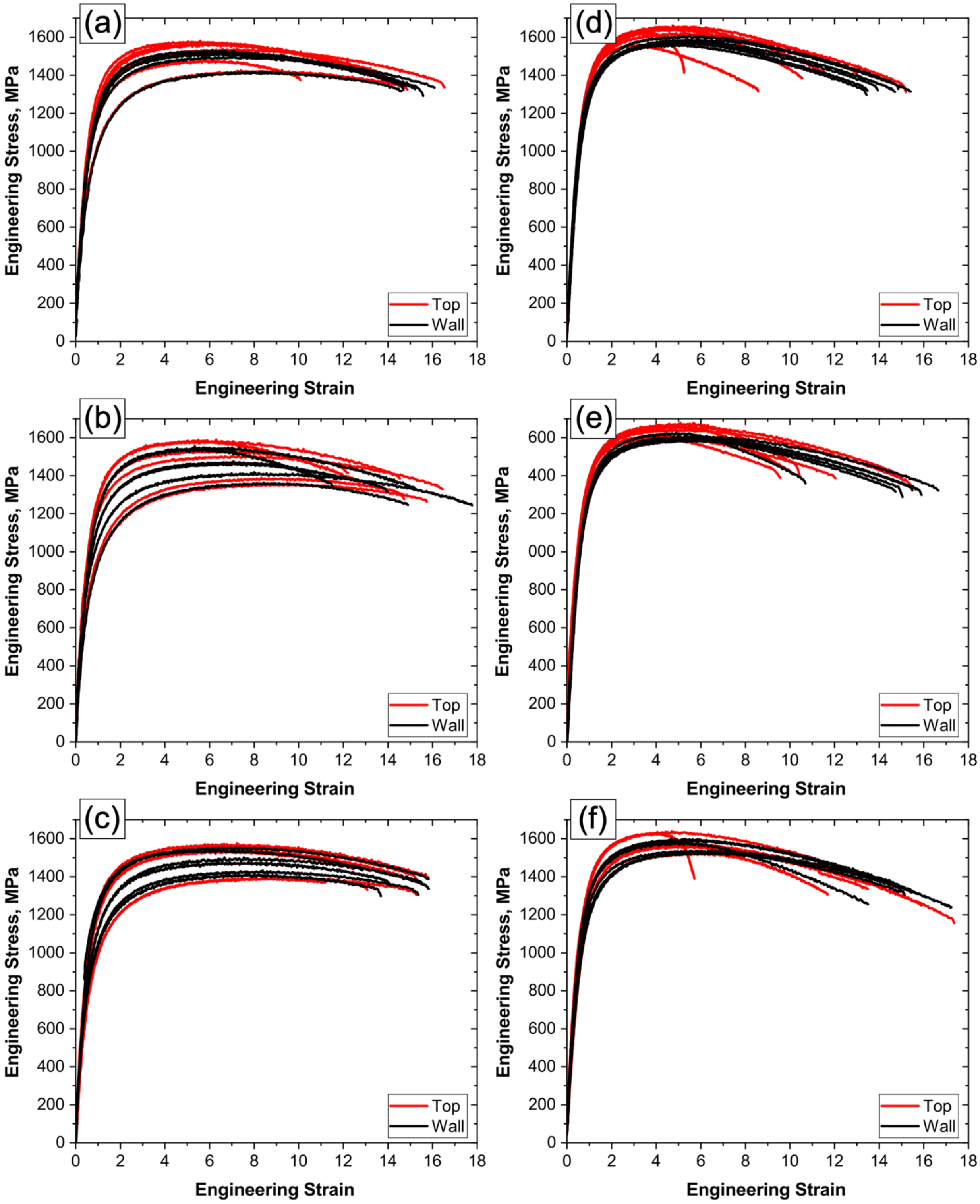

Fig. B.5. Stress-strain curves in the TD-orientation taken from DHPF 2.5Mn alloy at various austenization times and stamping temperatures: (a) 30 s–700 °C (b) 30 s–650 °C, (c) 30 s–600 °C, (d) 60 s–700 °C, (e) 60 s–650 °C, (f) 60 s–600 °C.

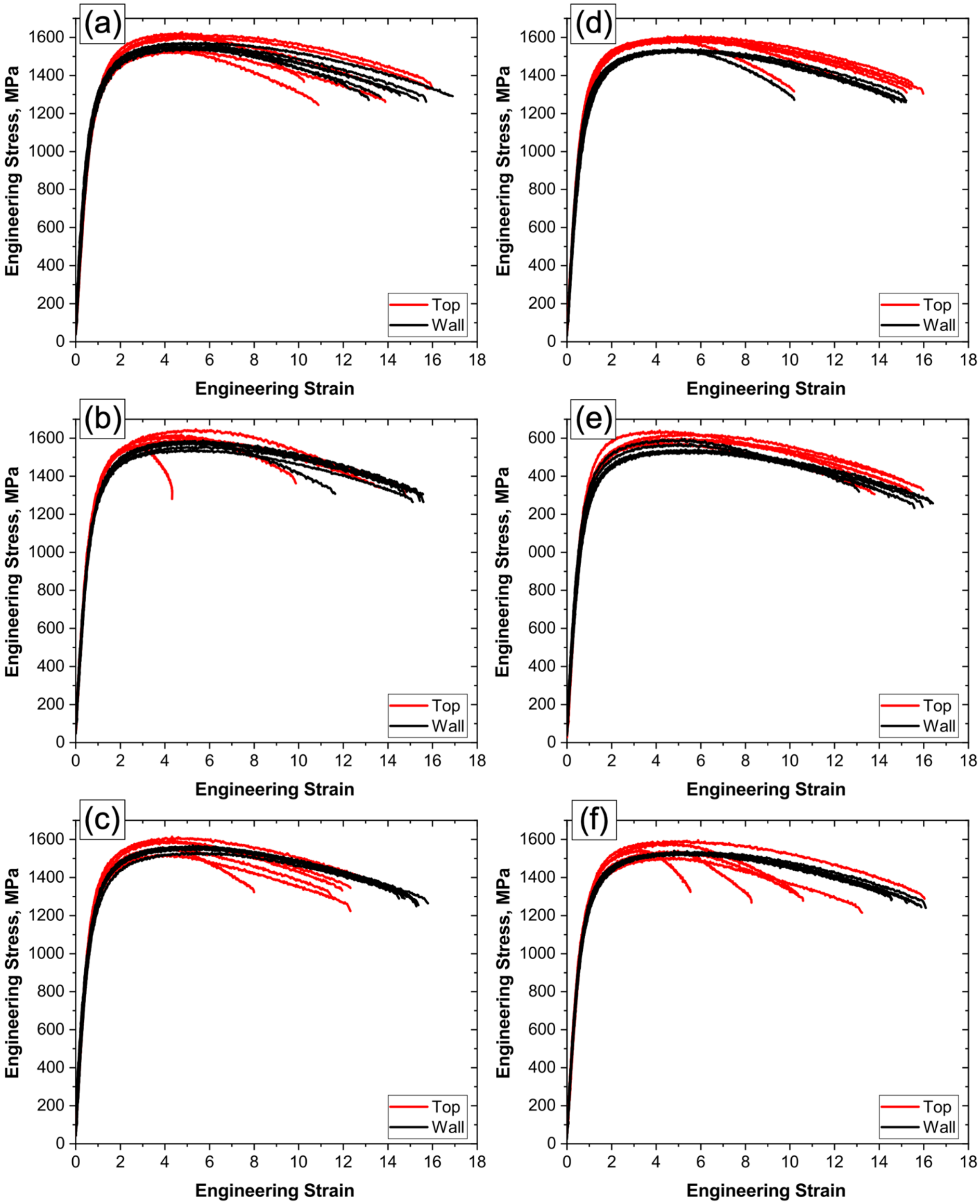

Fig. B.6. Stress-strain curves in the TD-orientation taken from DHPF 2.5Mn alloy at various austenization times and stamping temperatures: (a) 120 s–700 °C (b) 120 s–650 °C, (c) 120 s–600 °C, (d) 180 s–700 °C, (e) 180 s–650 °C, (f) 180 s–600 °C.

APPENDIX C: COATING MICROSTRUCTURAL EVOLUTION

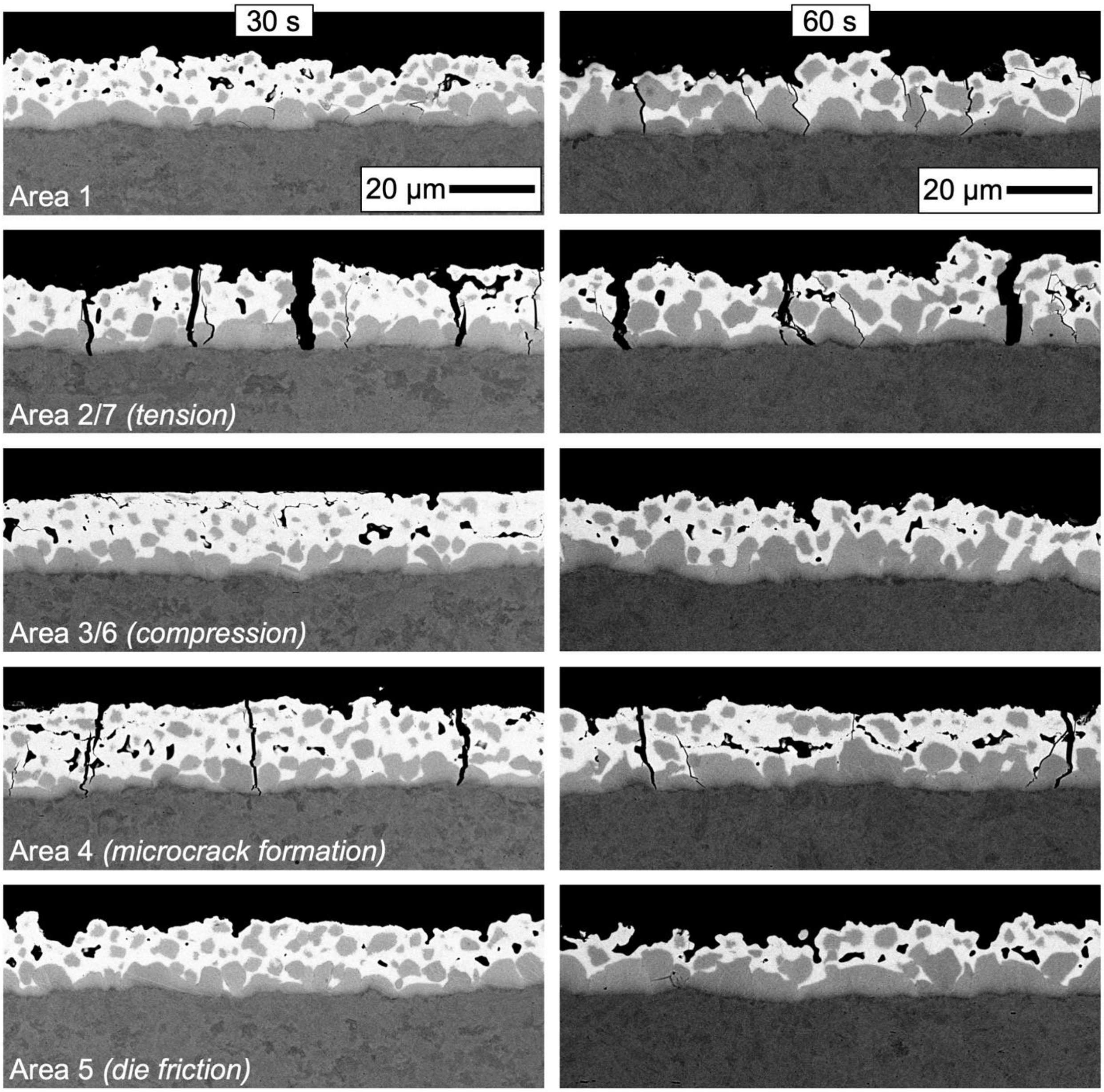

Fig. C.1. Coating microstructural images of the 2.0Mn alloy at different regions of the DPHF part. Austenization times of 30 s (left) and 60 s (right), all stamped at 650 °C.

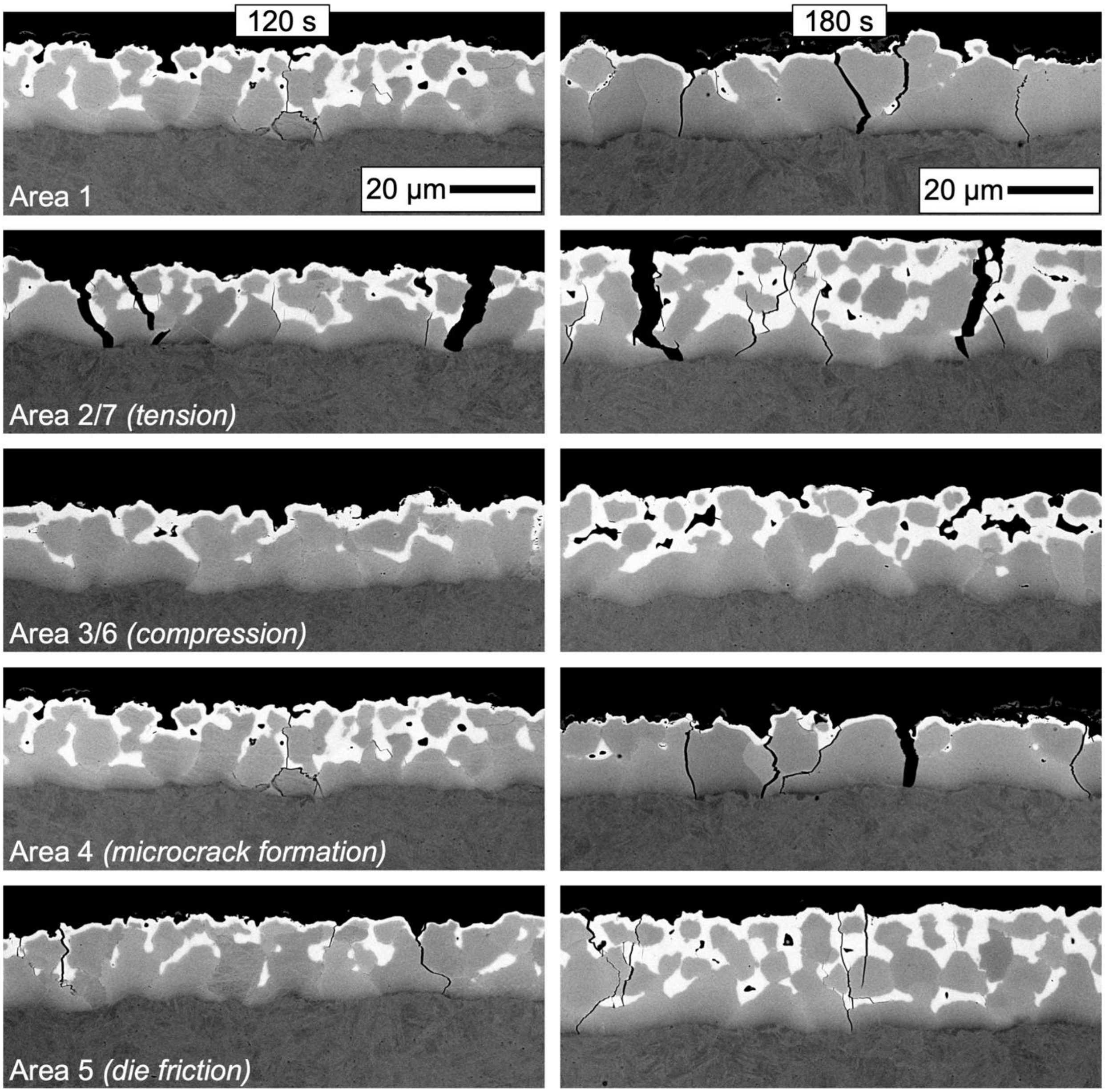

Fig. C.2. Coating microstructural images of the 2.0Mn alloy at different regions of the DPHF part. Austenization times of 120 s (left) and 180 s (right), all stamped at 650 °C.

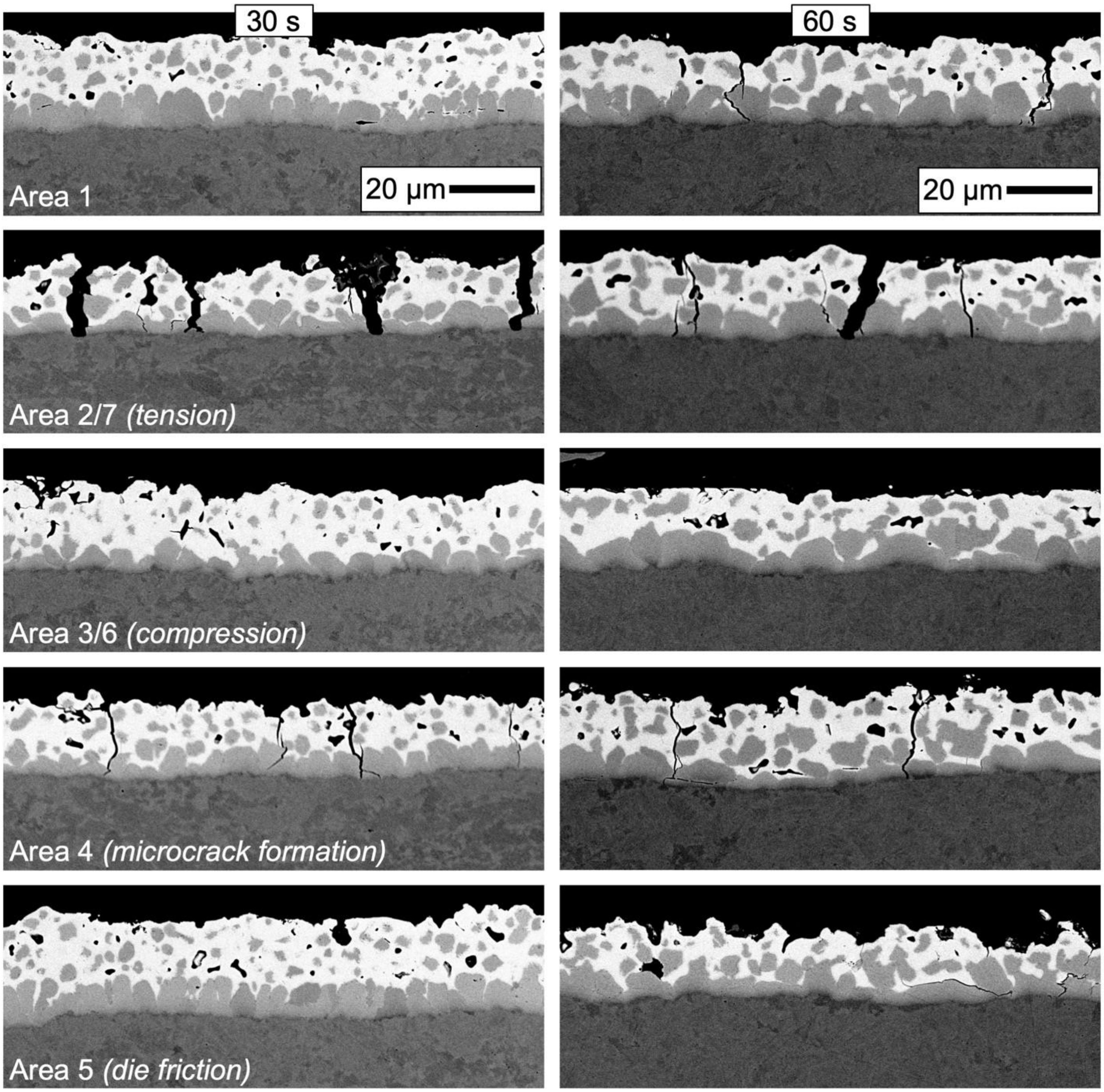

Fig. C.3. Coating microstructural images of the 2.0Mn alloy at different regions of the DPHF part. Austenization times of 30 s (left) and 60 s (right), all stamped at 600 °C.

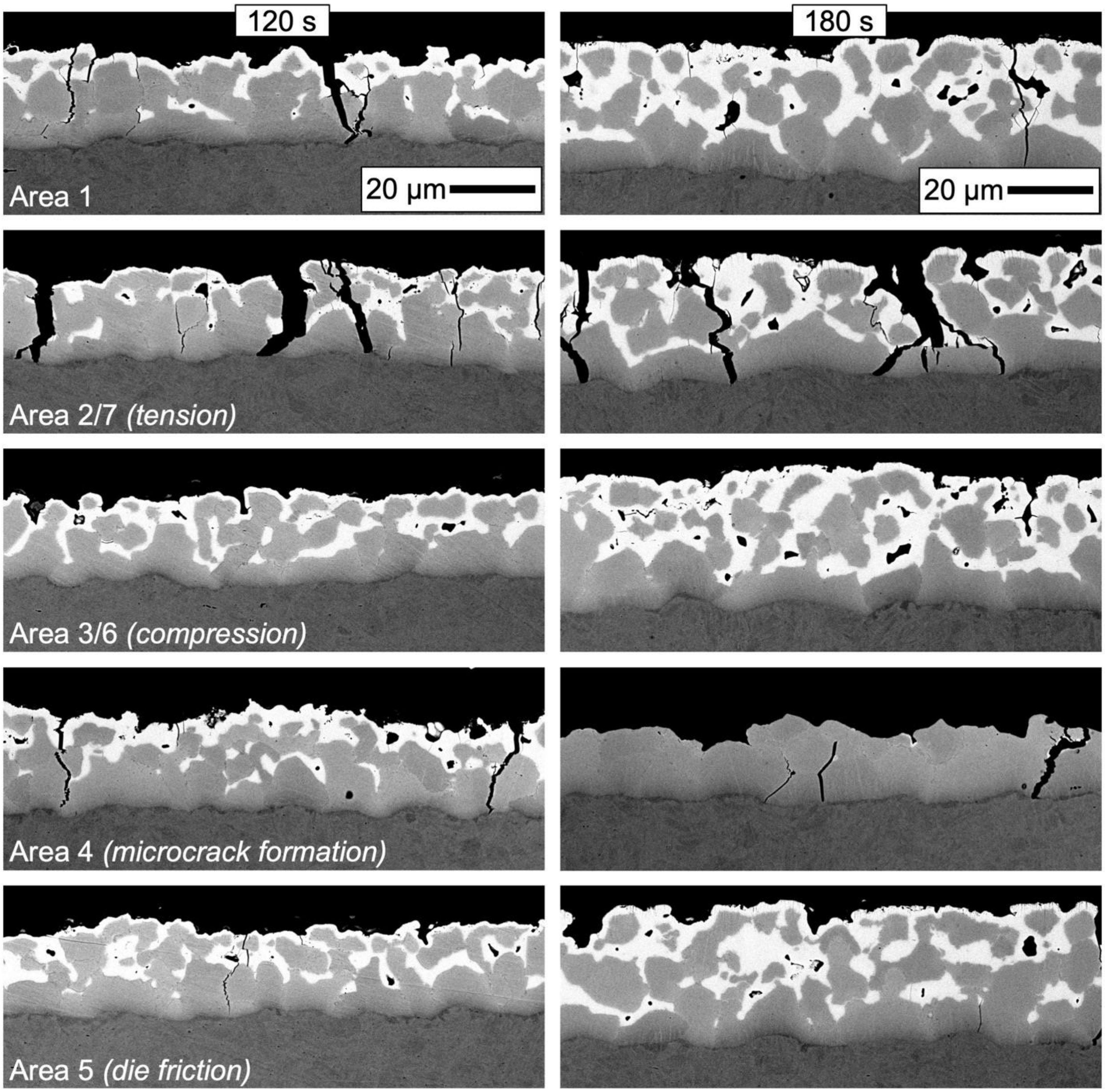

Fig. C.4. Coating microstructural images of the 2.0Mn alloy at different regions of the DPHF part. Austenization times of 120 s (left) and 180 s (right), all stamped at 600 °C.

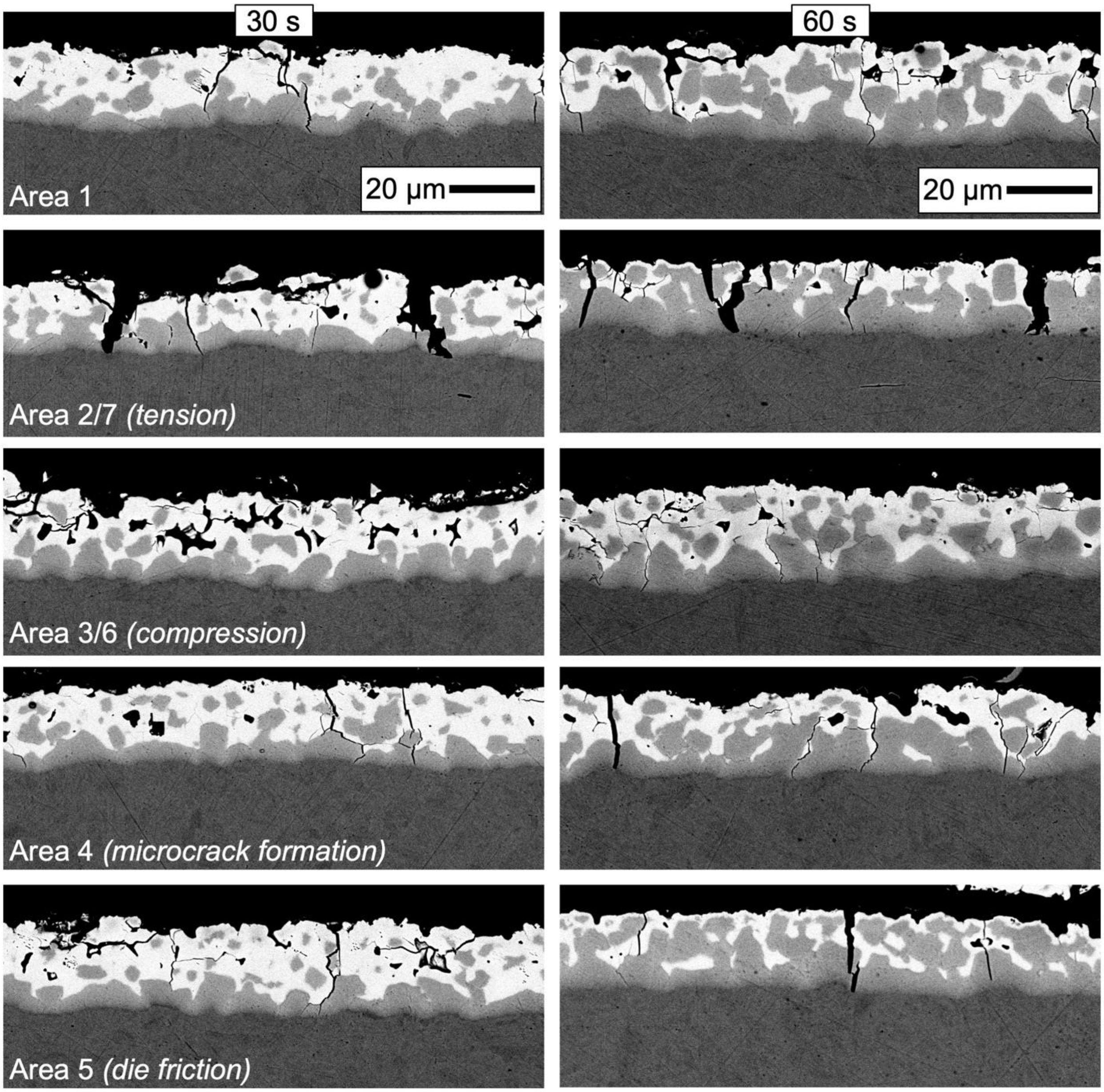

Fig. C.5. Coating microstructural images of the 2.5Mn alloy at different regions of the DPHF part. Austenization times of 30 s (left) and 60 s (right), all stamped at 650 °C.

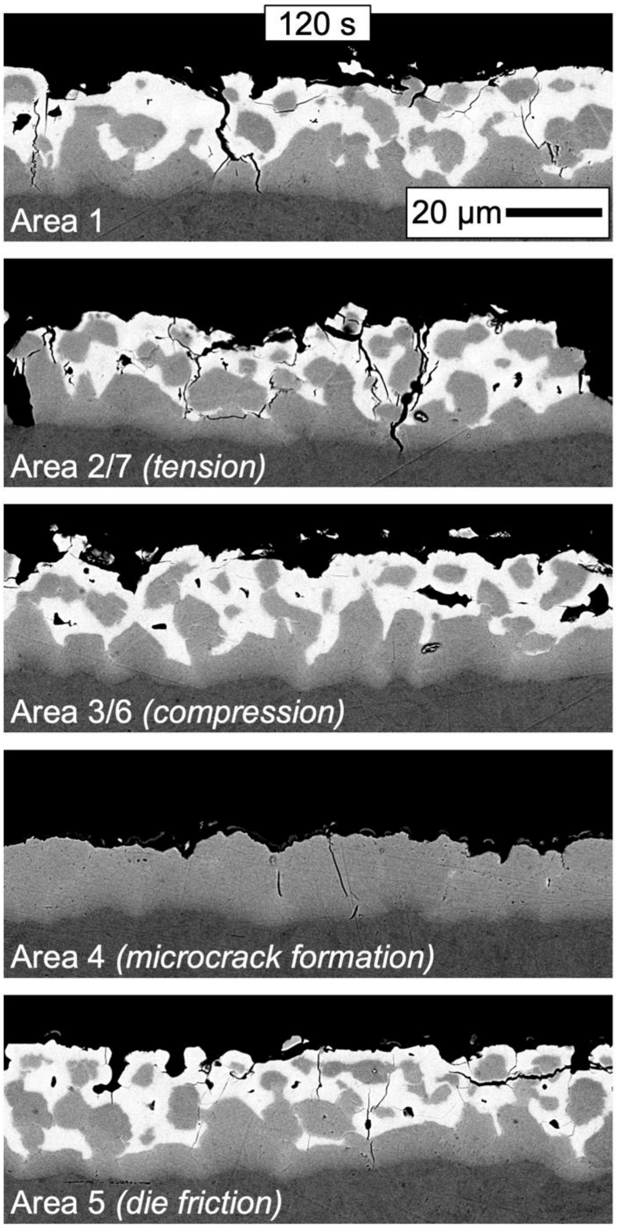

Fig. C.6. Coating microstructural images of the 2.5Mn alloy at different regions of the DPHF part. Austenization time of 120, stamped at 650 °C.

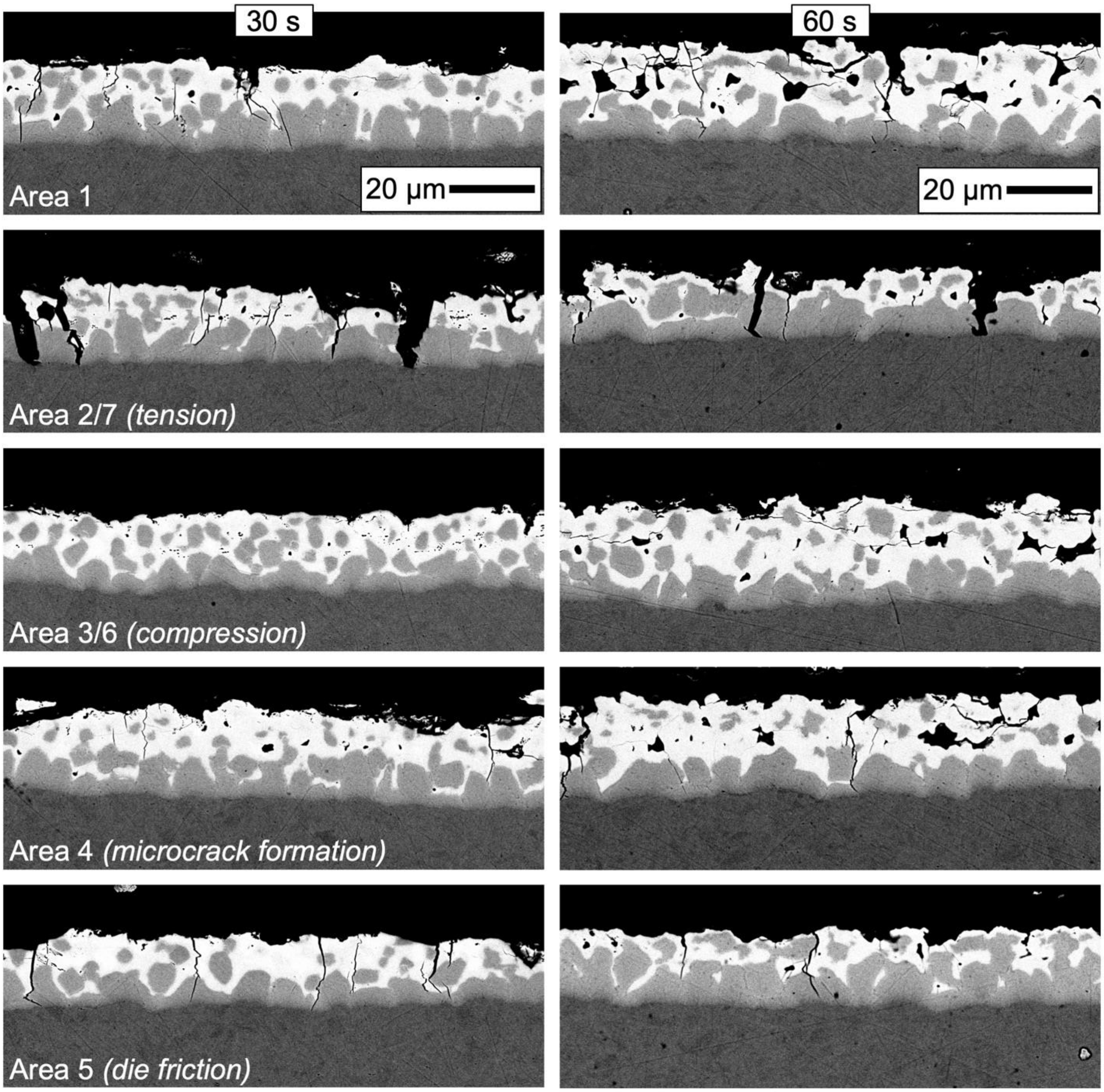

Fig. C.7. Coating microstructural images of the 2.5Mn alloy at different regions of the DPHF part. Austenization times of 30 s (left) and 60 s (right), all stamped at 600 °C.